JAERI-M
87-134

REPORT OF THE SECOND JOINT SEMINAR ON ATOMIC PHYSICS, SOLID STATE PHYSICS AND MATERIAL SCIENCES IN THE ENERGY REGION OF TANDEM ACCELERATORS

September 1987

Department of Physics

日本原子力研究所
Japan Atomic Energy Research Institute

JAERI-Mレポートは，日本原子力研究所が不定期に公刊している研究報告書です。
入手の問合わせは，日本原子力研究所技術情報部情報資料課（〒319-11茨城県那珂郡東海村）あて，お申しこしください。なお，このほかに財団法人原子力弘済会資料センター（〒319-11 茨城県那珂郡東海村日本原子力研究所内）で複写による実費頒布をおこなっております。

JAERI-M reports are issued irregularly.
Inquiries about availability of the reports should be addressed to Information Division Department of Technical Information, Japan Atomic Energy Research Institute, Tokai-mura, Naka-gun, Ibaraki-ken 319-11, Japan.

編集兼発行　日本原子力研究所
印　　刷　いばらき印刷㈱

JAERI-M 87-134

Report of the Second Joint Seminar on Atomic Physics, Solid State Physics and Material Sciences in the Energy Region of Tandem Accelerators

Department of Physics
Tokai Research Establishment
Japan Atomic Energy Research Institute
Tokai-mura, Naka-gun, Ibaraki-ken

(Received August 10, 1987)

The Second Joint Seminar on Atomic Physics, Solid State Physics and Material Sciences in the Energy Region of Tandem Accelerators was held on January 8-10, 1987 at the Tokai Research Establishment of JAERI.

The Seminar was attended by approximately 80 scientists from many Universities and Institutes as well as from JAERI. This Report includes 33 of the papers presented at the Seminar.

We wish to express our appreciation to all the participants for their cooperation at the Seminar and for their contributions to this Report.

Organizing Committee
T. Iwata (JAERI)
Y. Nakai (JAERI)
H. Watanabe (JAERI)
Y. Kazumata (JAERI)
S. Ishino (Univ. of Tokyo)

Keywords: Atomic Physics, Radiation Damage, Accelerators, Proceedings, Solid State Physics, Material Science

第2回「タンデム領域の重イオンによる物性・材料および原子分子物理の研究」研究会報告書

日本原子力研究所東海研究所物理部

（1987年8月10日受理）

タンデム加速器のエネルギー領域における物性・材料および原子分子物理の第2回研究会が1987年1月8日から10日まで日本原子力研究所東海研究所において開催された。研究会には約80名の研究者が参加した。本報告書は研究会で発表された論文33篇をまとめたものである。

研究会世話人
岩田忠夫（日本原子力研究所）
中井洋太（〃）
渡辺斉（〃）
数又幸生（〃）
石野栞（東京大学）

CONTENTS

PART I

ATOMIC PHYSICS

I.1 ATOMIC COLLISIONS UNDER EXTREME CONDITIONS IN SPACE

Yukikazu ITIKAWA

Institute of Space and Astronautical Science
Komaba, Meguroku, Tokyo 153

In space, atoms and molecules are often placed under the extreme conditions which are very difficult to be realized on Earth. For instance, extremely hot and dense plasmas are found in and around various stellar objects (e.g., neutron stars) on one hand and extremely cold and diffuse gases prevail in interstellar space on the other. There is so strong a magnetic field that electron clouds in atoms and molecules are distorted. The study of atomic collisions under the extreme conditions is not only helpful in understanding the astrophysical environment but also reveals new aspects of the physics of atoms and molecules. This paper is an invitation to the study. (References are not exhaustive but only provide a clue with which more details can be found.)

(1) Extremely high temperature

Now it is known that many celestial objects consist of plasmas of high temperature. For instance, a flare region of the solar corona has been found to have the temperature as high as 4×10^7 K. (1) Cosmic X-ray comes mostly from hot plasmas of similar temperature. The presence of highly charged ions in such astrophysical plasmas has been confirmed through the observation of line spectra in the UV to X-ray regions. (2) In this sense, the space is 'a natural source' of highly charged ions. A variety of collisions involving the highly-charged ions, therefore, take place in space.

Highly-charged ions exist even in a low-temperature plasma (gas). Strong UV light emitted by a star ionizes atoms in the surrounding gas (its temperature being normally below 1 eV). Low energy ($\lesssim$ 1 eV) collisions between the ions and the gaseous particles (e.g., H and He) play a significant role there. (3) In this respect, a recent measurement of the charge transfer cross section for $N^{3+} + H_2$ at 0.1 eV/amu (4) gives a new insight into the physics of the low-energy collisions involving highly-charged ions.

(2) Extremely low temperature

Space between stars is not completely empty but is filled with gas. A rather dense region is called interstellar cloud. A number of molecules, ranging from the simplest one H_2 to the very complicated organic one CH_3CH_2CN, have been found in the interstellar cloud. (5,6) Most of them are detected through their radio emission or absorption. How are the molecules formed in such a low temperature (10 - 100 K) and low density (1 - 10^6 cm^{-3}) gas ? Now many people have proposed models based on two-body gaseous reactions of atoms and molecules (especially ion-molecule reactions). (7,8) For the modeling, we need to know the relevant collision processes at the low temperature of the interstellar space. It should be mentioned that a few groups in the world have recently started to measure rate coefficients for the reactions at the temperature range of 10 K. (9,10)

(3) Extremely low density

In the interstellar space, collisions are so rare that any atoms or molecules once formed can survive for a long time (unless their radiative lifetime is short). Many radicals are present and unstable isomers (e.g., HNC) are sometimes abundant there. (11) Another example is a highly excited (Rydberg) atom. Through the detection of recombination lines, (12) a Rydberg atom with the principal quantum number up to 732 has been confirmed to exist. (13) It is not clearly known, however, what a role the collision involving the highly excited atom plays in space.

(4) Extremely high density

Space provides typical examples of high density plasmas. For instance, the outer layer of a neutron star has a mass density of 10^4 - 10^8 g/cm^3. In relation to the development of the inertial confinement fusion system, atomic processes in dense-hot plasmas have been studied extensively. A useful bibliography on the subject was prepared (14) and a review was published. (15)

(5) Extremely strong magnetic field

Magnetic field often plays a decisive role in astrophysical phenomena. Very strong field has been confirmed to exist around the peculiar stars such as white dwarfs ($\sim 10^4$ T) (16) and neutron stars ($\sim 10^8$ T) (17). Atomic collisions are affected by a strong magnetic field in two ways. First atoms and molecules themselves are deformed. (18) Atomic properties like energy levels are changed. Secondly collision dynamics are modified if charged particles are involved. (19) As a consequence we might encounter in the strong magnetic field atomic processes of a completely different nature from those on Earth.

References

(1) K. Tanaka: Publ. Astron. Soc. Jpn. 38 (1986) 225.
(2) G.A. Doschek: Autoionization, ed. A. Temkin (Plenum, 1985) p.171.
(3) R. McCarroll, P. Valiron and L. Opradolce: Planetary Nebulae, ed. D.R. Flower (D. Reidel, 1983) p.187.
(4) H.-Y. Wang and D.A. Church: J. Phys. B 19 (1986) L799.
(5) G.H.F. Diercksen, W.F. Huebner and P.W. Langhoff, ed.: Molecular Astrophysics (D. Reidel, 1985).
(6) C.M. Walmsley: Phys. Scripta T11 (1985) 27.
(7) S.S. Prasad and W.T. Huntress, Jr.: Astrophys. J. Suppl. 43 (1980) 1.
(8) C.M. Leung, E. Herbst and W.F. Huebner: Astrophys. J. Suppl. 56 (1984) 231.
(9) J.A. Luine and G.H. Dunn: Astrophys. J. 299 (1985) L67.
(10) J.B. Marquette, B.R. Rowe, G. Dupeyrat and E. Roueff: Astron. Astrophys. 147 (1985) 115.
(11) S. Green: Ann. Rev. Phys. Chem. 32 (1981) 103.
(12) P.A. Shaver, ed.: Radio Recombination Lines (D. Reidel, 1980).
(13) W.D. Watson: Nature 315 (1985) 630.
(14) T. Kato, J. Hama, T. Kagawa, S. Karashima, N. Miyanaga, H. Tawara, N. Yamaguchi, K. Yamamoto and K. Yonei: Bibliography on Atomic Processes in Hot Dense Plasmas, IPPJ-AM-29 (Inst. Plasma Phys., Nagoya Univ., 1983).

(15) T. Kagawa, T. Kato, T. Watanabe and S. Karashima: Atomic Processes in Hot Dense Plasmas, IPPJ-AM-31 (Inst. Plasma Phys., Nagoya Univ., 1983).

(16) J.R.P. Angel, J. Liebert and H.S. Stockman: Astrophys. J. 292 (1985) 260.

(17) J. Trümper, W. Pietsch, C. Reppin, W. Voges, R. Staubert and E. Kendziorra: Astrophys. J. 219 (1978) L105.

(18) W. Rösner, G. Wunner, H. Herold and H. Ruder: J. Phys. B 17 (1984) 29.

(19) A. Ohsaki: J. Phys. Soc. Jpn. 52 (1983) 431, 442.

I.2 IONIZATION OF RYDBERG ATOMS IN THERMAL COLLISIONS WITH POLAR MOLECULES

Toshizo SHIRAI
Department of Physics, Japan Atomic Energy Research Institute

I. INTRODUCTION

In the recent ten years numerous experimental and theoretical studies[1] have been made of collisional depopulation of Rydberg, or highly excited, atoms in thermal collisions with polar molecules. The experimental results[2] show that the collisional depopulation occurs by three distinct processes, namely, n-changing collisions, ℓ-changing collisions, and ionization collisions. In order to elucidate the mechanisms of these processes theoretically, not only the approximate quantum mechanical approaches[3] within the impulse approximation but also the purely classical treatment[4] have been applied.

In this paper ionization collision between a Rydberg atom R and a rotationally excited polar molecule M(J) at room temperature (i.e. T=300K),

$$R^{+}\text{-}e_R(n,\ell) + M(J) \rightarrow R^{+} + e + M(J'),\ J > J' \qquad (1.1)$$

is examined theoretically. Here R^{+} denotes the ion core of R and $e_R(n,\ell)$ the Rydberg electron in the state with specified principal (n) and azimuthal (ℓ) quantum numbers. Ionization occurs mainly owing to the energy transfer from molecular rotation to atomic excitation, because the energy transfer from relative translational motion to atomic excitation is much less effective. Therefore the key mechanism for the ionization is the rotational deexcitation process,

$$e_R(n,\ell) + M(J) \rightarrow e + M(J'). \qquad (1.2)$$

As far as the authors know, the approximate quantum mechanical calculations carried out so far employed the dipole-Born approximation[5] for the process (1.2)。 In order to take into account the higher-order corrections, however, the dipole-Born approximation should be replaced by a more sophisticated one. Especially when the molecule is strongly polar, the validity of the Born approximation becomes questionable. We employed here the Glauber approximation. The dipole-Glauber differential cross section[6] (DCS) becomes the same as the dipole-Born DCS when the molecular dipole moment is weak, and also reproduces well

the results of the close-coupling calculations even when the molecular dipole moment becomes large. Besides, it should be noted that the dipole fordidden transitions can also be dealt with by the dipole-Glauber approximation. In a recent paper[7], Pesnelle et al. reported the importance of the rotational deexcitaion with $\Delta J \equiv J-J>1$ in the ionization collisions of low Rydberg He atoms with NH_3. Using the semiquantal approximation,[8] we have carried out the calculations of the ionization collisions between the Rydberg Xe atoms and the polar molecules CO, HF, HCl, and LiF. Both Glauber and Born DCS's for the rotational deexcitation process (1.2) were employed for comparison.

In a previous paper[9] (referred to as I hereafter) we proposed a new semiquantal cross-section formula to be applicable to the general case where the DCS for electron-neutral atom/molecule scattering depends not only on the momentum transfer but also on the relative velocity. Brief summary of the formula is given in Sec. II。 In Sec. III the calculated results and discussions are presented for the Xe(n)+CO, HCl, HF, and LiF systems. Experimental[10,11] and theoretical[4] ionization rates for Xe(27f) + HF and Xe(31f) + HCl at 300K are compared with the present results. In the present treatment, the Rydberg atom is assumed to be hydrogenic and the polar molecule is taken to be a rigid rotor.

II。 THEORY

During the collision between a Rydberg atom and a neutral particle (atom/molecule), the neutral particle does not interact simultaneously with both of the Rydberg electron and its parent ion core. Owing to the charge neutrality, the interaction between the Rydberg atom and the neutral particle becomes effective only in a small region compared to the dimension of the Rydberg atom. The Rydberg electron and the parent ion are thus assumed to be independent scattering centers. The impulse approximation is appropriate to describe such a characteristic collision. The binary-encounter approximation for the form-factor of the Rydberg atom is employed as an additional approximation.[12] This approximation is considered to be quite good, because the momentum transferred to the Rydberg electron is large compared to its own momentum. In the present treatment the parent ion does not play any important role in the collision other than the role of determining the momentum distribution of the Rydberg electron. Thus, the semiquantal approximation used in the present calculations is a kind of combination

of the impulse and the binary-encounter approximations.

The semiquantal cross-section formula proposed by Flannery[8] was rewritten in I in the form more useful in practice. A mass-disparity approximation (i.e., neglect of the ratio of mass of electron to that of R and M) is used without introducing any serious error. The following is a summary of the notations used in this paper: m: mass of electron; μ: reduced mass of the (R-M) system; $p_{i,f}$: initial and final momentum of the relative motion in the (R-M) system; p: momentum transfer;

$$p_{max,min} = |p_i \pm p_f| = |p_i \pm [p_i^2 - 2(\varepsilon_n + \Delta)]^{1/2}|;$$

ε_n: ionization potential of R(n,ℓ); Δ: difference of the initial and final rotational energies (Δ>0 for excitation and Δ<0 for deexcitation); $\sigma_{JJ'}(p,v)$: DCS for the collision (1.2); V: initial velocity of the relative motion of the (R-M) system; ε: internal energy transferred to R;

$$\varepsilon_{max} = -p^2/2\mu + Vp - \Delta;$$

$$\varepsilon_{min} = \begin{cases} -p^2/2\mu - Vp - \Delta \text{ for } 0 \le p \le p_{min}, \\ \varepsilon_n \text{ for } p_{min} \le p \le p_{max}; \end{cases}$$

$\mathcal{F}_{n\ell}(u)$: velocity(u) distribution function of $e_R(n,\ell)$; u_n: average orbital velocity of $e_R(n,\ell)$.

The cross-section formula, Eq.(2.37) of I, for the ionization collision (1.1) is expressed within the mass-disparity approximation as follows:

$$\sigma_{n\ell,J,J'}(V) = \frac{2\pi}{(mV)^2} \int_0^{p_{max}} pdp \int_{v_m^2}^{\infty} \sigma_{J,J'}(p,v)dv^2 \int_{\varepsilon_{min}}^{\varepsilon_{max}} \frac{d^2F_{n\ell}(p,v,\varepsilon)}{d\varepsilon dv^2} d\varepsilon, \tag{2.1}$$

where the last integrand is newly introduced and defined by

$$\frac{d^2F_{n\ell}(p,v,\varepsilon)}{d\varepsilon dv^2} = \frac{1}{2\pi p} \int_{u_-}^{u_+} \frac{u\,\mathcal{F}_{n\ell}(u)\,du}{[(u_+^2 - u^2)(u^2 - u_-^2)]^{1/2}}. \tag{2.2}$$

The other quantities are the same as in I: $v_m = p/2m + \Delta/p$, $u_\pm = v^2 + C \pm 2[B(v^2 - v_m^2)]^{1/2}$, $C = V^2 - 2v(p,\varepsilon)v_m$, $B = V^2 - v(p,\varepsilon)^2$, and $v(p,\varepsilon) = p/2\mu + (\varepsilon+\Delta)/p$. If the DCS's $\sigma_{J,J'}(p,v)$ are independent of v, the order of the integrals with respect to v and ε can be changed, and the integral over v^2 can be carried out analytically. Integrating Eq.(2.2) over v^2, we can obtain the following expression for the density of the binary-encounter

form-factor:

$$\frac{d^2F_{n\ell}(p,\varepsilon)}{d\varepsilon} = \int_{v_m^2}^{\infty} \frac{d^2F_{n\ell}(p,v,\varepsilon)}{d\varepsilon dv^2}\, dv^2 = \frac{1}{2p}\int_{u(p,\varepsilon)}^{\infty} u\, \mathcal{F}_{n\ell}(u)\, du, \tag{2.3}$$

where

$$u(p,\varepsilon) = |\varepsilon/p - p/2m|$$

Taking an average of Eq. (2.3) with respect to ℓ (see Eq. (2.42) of I), we have

$$\frac{dF_n(p,\varepsilon)}{d\varepsilon} = \frac{1}{n^2}\sum_{\ell}(2\ell+1)\frac{dF_{n\ell}(p,\varepsilon)}{d\varepsilon}$$

$$= \frac{2^4}{3\pi}\frac{1}{2pu_n}[u(p,\varepsilon)^2/u_n^2 + 1]^{-3}. \tag{2.4}$$

Thus the quantity defined in Eq. (2.2) can be regarded as a velocity-dependent density of the binary-encounter form-factor.

In the dipole-Glauber approximation, not only the dipole transition $\Delta J=J-J'=1$ but also other non-dipole transitions $\Delta J>1$ can occur and induce the ionization of the Rydberg atom. Therefore, a summation with respect to ΔJ and an average over the rotational distribution at a given temperature T are necessary to be taken to obtain the thermally averaged ionization cross section,

$$\bar{\sigma}_{n\ell}(V) = \sum_{\Delta J=1}\ \sum_{J=\max(\Delta J,J^*)} f_J \sigma_{n\ell,J,J-\Delta J}(V), \tag{2.6}$$

where

$$f_J = (2J+1)\exp(-BJ(J+1)/kT) / \sum_{J=0}^{\infty}(2J+1)\exp(-BJ(J+1)/kT) \tag{2.5}$$

with B the rotational constant of the polar molecule and k the Boltzmann's constant. Here J* is the smallest rotational quantum number which satisfies the condition,

$$\Delta J(2J^*+1-\Delta J)B \geq \varepsilon_n, \tag{2.7}$$

where the left-hand side means the deexcitation energy in the transition from J* to J*-ΔJ。

The ionization rate constant is given as follows:

$$K_{n\ell}(T) = \int_0^{\infty} V\bar{\sigma}_{n\ell}(V) f(V) dV, \tag{2.8}$$

where f(v) is the Boltzmann distribution function given by

$$f(V) = (\mu/2\pi kT)^{3/2} 4\pi V^2 \exp(-\mu V^2/2kT)。 \tag{2.9}$$

It is useful for later discussion to briefly summarize the findings in I concerning the ionization with simultaneous deexcitation in the low-energy collisions (see section III B of I). By taking into account the fact that the electron-velocity distribution function $\mathcal{F}_{n\ell}(u)$ with high n reaches a maximum at $u\simeq u_n$, and rapidly decreases when $u>u_n$, we estimated an effective integral domain of p. Since the integral over u in Eq. (2.2) becomes significant only when u_- can be zero, the effective domain of p is determined from a condition that the minimum value of $u_-(=|\vec{v}-\vec{V}|)$ is equal to zero. Finally, we obtain the following effective domain of p (see Eq. (3.11) of I),

$$p^+ \geq p \geq p^-, \tag{2.10}$$

where

$$p^\pm = m[(V^2-2\Delta/m)^{1/2} \pm V]. \tag{2.11}$$

Since the thermal velocity $V_{th}[=(8kT/\pi\mu)^{1/2}$ and T=300K] satisfies the condition, $mV_{th}^2/2<<\Delta$, $p^\pm$ can be approximated by

$$p^\pm \sim p_0 \pm mV_{th} \tag{2.12}$$

with $p_0=(-2m\Delta)^{1/2}$. Since the range $(2mV_{th})$ of the integration over p is narrow and $v_m(p=p_0)=0$, we can roughly estimate the integral over v by putting $v_m=0$ in Eq. (2.1)。 The analysis made above indicates that p_0 can be used as a useful measure to comprehend the behaviour of the cross sections against n and V.

III. RESULTS OF NUMERICAL APPLICATIONS AND DISCUSSION

Analytic expressions for the dipole-Born $[\sigma^B_{J,J-1}(p)]$ and dipole-Glauber $[\sigma^G_{J,J'}(p,v)]$ DCS's are available in Refs. 5 and 6, respectively. For the convenience of later discussion, it is instructive to compare them by the ratio $R_{J,J'}(\xi)[=\sigma^G_{J,J'}(p,v)/\sigma^B_{J,J-1}(p)]$, which is expressed in terms of the reduced momentum transfer $\xi[=(2D/ea_0)p/mv]$. Here D is the molecular dipole moment, e the electronic charge, and a_0 the Bohr radius. The values of $R_{J,J'}(\xi)$ for the rotational deexcitations with $\Delta J=1$, 2, and 3 are shown in Figs. 1a, b, and c. For $\xi<0.3$, the dipole allowed transition ($\Delta J=1$) occurs most predominantly. In this region, $\sigma^G_{J,J-1}(p,v)$ is, therefore, well approximated by $\sigma^B_{J,J-1}(p)$. For $0.3\leq\xi<6$, $R_{J,J-1}(\xi)$ decreases rapidly and becomes as small as $R_{J,J'}(\xi)$ with $\Delta J>1$. In this region the use of the Born approximation is questionable, because the dipole forbidden transitions can be expected to contribute to the same extent as the dipole allowed transition. For $\xi\geq6$, there appears an oscillatory

structure in the curve $R_{J,J'}(\xi)$ vs. ξ, which might not be true and might disappear in a more sophisticated treatment including short range potentials. However, this structure gives no serious influence on the final results of the present application.

Molecular data are listed in Table I for four polar molecules studied here. These molecules have been selected for the case studies to examine the applicability of the dipole-Born DCS. The Boltzmann

TABLE I Dipole moment D and rotational constant B used in the calculation. All values are given in atomic units. Values in parenthesis are the power of ten by which the entry is to be multiplied.

	CO	HCl	HF	LiF
D	4.41(-2)	4.36(-1)	7.19(-1)	2.49
B	8.76(-6)	4.76(-5)	9.37(-5)	6.08(-6)

TABLE II The Boltzmann average J_{av} of the initial rotational quantum number J at 300K.

	CO	HCl	HF	LiF
J_{av}	8.7	3.4	2.3	10.6

average of the initial J at 300K is also given in Table II. It is discerned that the J distribution becomes broader for molecules with smaller rotational constant (see Fig. 2).

We have calculated the ionization cross sections for collisions between the Rydberg Xe atom and these polar molecules. The dependences of the cross sections on n, D, and collision velocity V are obtained, and are analyzed in the subsequent subsections.

A. Dependence on n and D (dipole moment)

The n-dependence has been investigated for the cross sections averaged over ℓ, i.e.,

$$\bar{\sigma}_n(V) = \frac{1}{n^2} \sum_{\ell} (2\ell+1)\bar{\sigma}_{n\ell}(V).$$

Calculations have been carried out for the Xe(n)+CO, HCl, HF, and LiF systems with $n \leq 100$ at V_{th}. It is noted that the dipole moments D of the molecules studied here satisfies the relation, $D_{CO} < D_{HCl} < D_{HF} < D_{LiF}$ (see

TABLE I)。

The results $\bar{\sigma}_n^B(V_{th})$ and $\bar{\sigma}_n^G(V_{th})$ obtained with use of the dipole-Born and dipole-Glauber DCS's are shown as a function of n in Figs. 3 to 6. It is seen that the dipole-Glauber DCS brings about a decrease in the cross section and yields a saw-like n-dependence in contrast to a clear step-like n-dependence[13] in the case of the dipole-Born DCS. This sudden increase of the cross section appears at each n at which the binding energy of the Rydberg electron ($1/2n^2$ a.u.) becomes equal to the molecular rotational energy (2BJ) released in the dipole allowed deexcitation transition. In other words, as n increases, the molecules with lower J can take part in the ionization, and thus the cross section takes a rapid increase. The values of $\bar{\sigma}_n^B(V_{th})$ and $\bar{\sigma}_n^G(V_{th})$ become larger with increasing D, and the difference between them becomes more prominent. These features come from the sharp decrease of $R_{J,J-1}(\xi)$ in the range $1<\xi<6$. Since the reduced momentum transfer ξ is inversely proportional to v and is proportional to D, $\xi_0[=(2D/ea_0)p_0/v$ and $v=v_n]$, being a measure to estimate the effective domain of the twofold integral with respect to p and v, becomes larger with n and/or D。 This explains the prominent difference in $\bar{\sigma}_n^B(V_{th})$ and $\bar{\sigma}_n^G(V_{th})$。

B. Dependence on V (relative collision velocity)

The calculated results of $\bar{\sigma}_{n\ell}(V)$ defined by Eq. (2.6) are shown in Figs. 7 and 8 for the Xe(27f)+HF and Xe(31f)+HCl systems, respectively. Both results indicate that $\bar{\sigma}_{n\ell}(V)$ can be expressed as $\bar{\sigma}_{n\ell}(V)=C_{n\ell}/V$ with $C_{n\ell}$ a proportionality constant. The value of $C_{n\ell}$ depends on the approximation employed for the scattering amplitude of the process (1.2)。

It is shown in a previous paper[12] that the V dependence of the cross sections is generally given as 1/V in the low-velocity limit when the electron-neutral atom/molecule DCS depends, as in the case of the Born DCS, only on the momentum transfer. In the case of the Glauber DCS, we can provide the following qualitative interpretation in terms of $p^{\pm}(\sim p_0 \pm mV)$ given by Eq. (2.12). For $V/V_{th}<10$, the relative velocity $v(=|\vec{V}-\vec{u}|)$ between e_R and M(J) is nearly equal to the velocity u of e_R. This means that the energy transfer from relative translational motion to atomic excitation is much less effective. Therefore, ionization occurs mainly due to the energy transfer from molecular rotation to

atomic excitation in the thermal-energy collisions. Because of this, p_0 is determined only by the rotational deexcitation energy. Since the integration range $[p^-,p^+]$ is narrow in proportion to V, we can use p_0 as a representative point to estimate the integral over v in Eq. (2.1). Since v_m is zero at $p=p_0$, we can roughly estimate the integral over v by putting $v_m=0$. Then the velocity dependence of the cross section can again be shown to be 1/V. Substituting an expression $V\bar{\sigma}_{n\ell}(V)=C_{n\ell}$ into the Eq. (2.8), we can easily see that rate constant is independent of the temperature T, i.e., $K_{n\ell}(T)=C_{n\ell}$.

C. Comparison with experiment

In TABLE III, the calculated ionization rate constants at 300K for Xe(27f)+HF and Xe(31f)+HCl are compared with the experimental values[10,11] and theoretical values obtained by the classical Monte Calro approach.[4] The classical results are obtained simply by $V\bar{\sigma}_{n\ell}(V)$, though the classical cross section $\bar{\sigma}_{n\ell}(V)$ is not well in proportion to 1/V (e.g., Fig. 7(b) in Ref. 4 shows a more moderate V dependence than 1/V). It is seen that the Born result agrees quite well with the experimental value for Xe(27f)+HF, but not well for Xe(31f)+HCl. The contrary applies to the classical results. The results of the Glauber approximation, on the other hand, are smaller in both cases, although the ratio between the two cases agrees very well with that of the experiment (see the last row of TABLE III).

TABLE III Experimental and theoretical ionization rates (in $10^{-7}cm^3/s$) at 300K for the Xe(27f)+HF and Xe(31f)+HCl systems. The figures in parentheses are the experimental and theoretical (statistical) uncertainties. The values marked "(Born)" and "(Glauber)" are obtained with use of the dipole-Born and dipole-Glauber approximations to e + HF (or HCl) scattering amplitude, respectively.

	Experiment	Theory		
Xe(27f)+HF	1.5(±0.8)[a]	1.36 (Born)	0.480(Glauber)	0.22(±0.02)[c]
Xe(31f)+HCl	0.9(±0.4)[b]	0.480(Born)	0.265(Glauber)	0.76(±0.08)[c]
ratio	1.7	2.8	1.8	0.29

[a] Reference 10.
[b] Reference 11.
[c] Reference 4.

REFERENCES

1. A recent comprehensive review is found in Rydberg States of Atoms and Molecules, edited by R. F. Stebbings and F. B. Dunning (Cambridge University, Cambridge, New York,1983).
2. F. G. Kellert, K. A. Smith, R. D. Rundle, F. B. Dunning, and R. F. Stebbings, J. Chem. Phys. 72, 3179 (1980); F. B. Dunning and R. F. Stebbings in Ref. 1, p. 315, and references therein.
3. M. Matsuzawa in Ref. 1, p. 267 and references therein.
4. S. Preston and N. F. Lane, Phys. Rev. A 33, 148 (1986).
5. K. Takayanagi, J. Phys. Soc. Jpn 21, 507 (1966); O. H. Crawford, J. Chem. Phys. 47, 1100 (1967).
6. O. Ashihara, I. Shimamura, and K. Takayanagi, J. Phys. Soc. Jpn. 38, 1732 (1975); I. Shimamura in Electron-Molecule Collisions, edited by I. Shimamura and K. Takayanagi (Plenum, Yew York,1984), p. 89.
7. A. Pesnelle, C. Ronge, M. Perdrix, and G. Watel, Phys. Rev. A 34, 5146 (1986).
8. M. R. Flannery in Ref. 1, p. 393 and references therein.
9. T. Shirai, Y. Nakai, and H. Nakamura, Phys. Rev. A 30, 1672 (1984) to be referred to as I.
10. C. Higgs, K.A. Smith, G.B. McMillian, F.B. Dunning, and R.F. Stebbings, J. Phys. B 14, L285 (1981).
11. R.F. Stebbings F.B. Dunning, and C. Higgs, J. Electron Spectrosc. Relat. Phenom. 23, 333 (1981).
12. H. Nakamura, T. Shirai, and Y. Nakai, Phys. Rev. A 17, 1892 (1978).
13. M. Matsuzawa and W.A. Chupka, Chem. Phys. Lett. 50, 373 (1977).

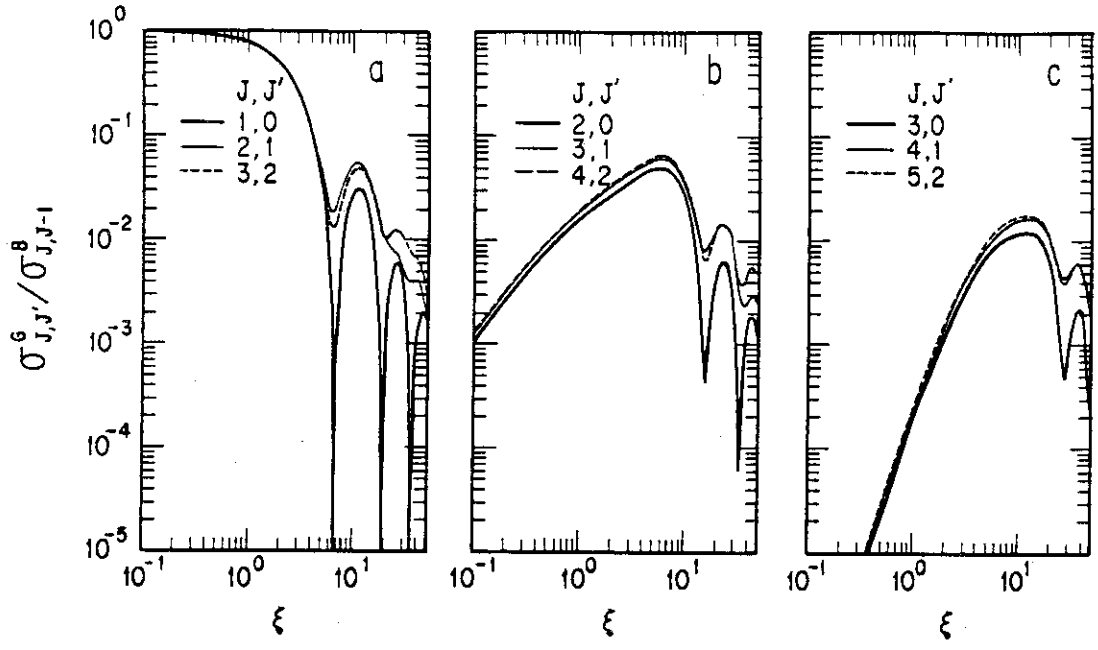

Fig. 1 Ratio of $\sigma^{G}_{J,J'}(p,v)$ (Glauber approximation) to $\sigma^{B}_{J,J-1}(p)$ (Born approximation) against the reduced momentum transfer $\xi[=(2D/ea_0)p/mv]$ for $\Delta J=1$ (a), $\Delta J=2$ (b), and $\Delta J=3$ (c). The other cases with higher J can not be drawn in a distinguishable way.

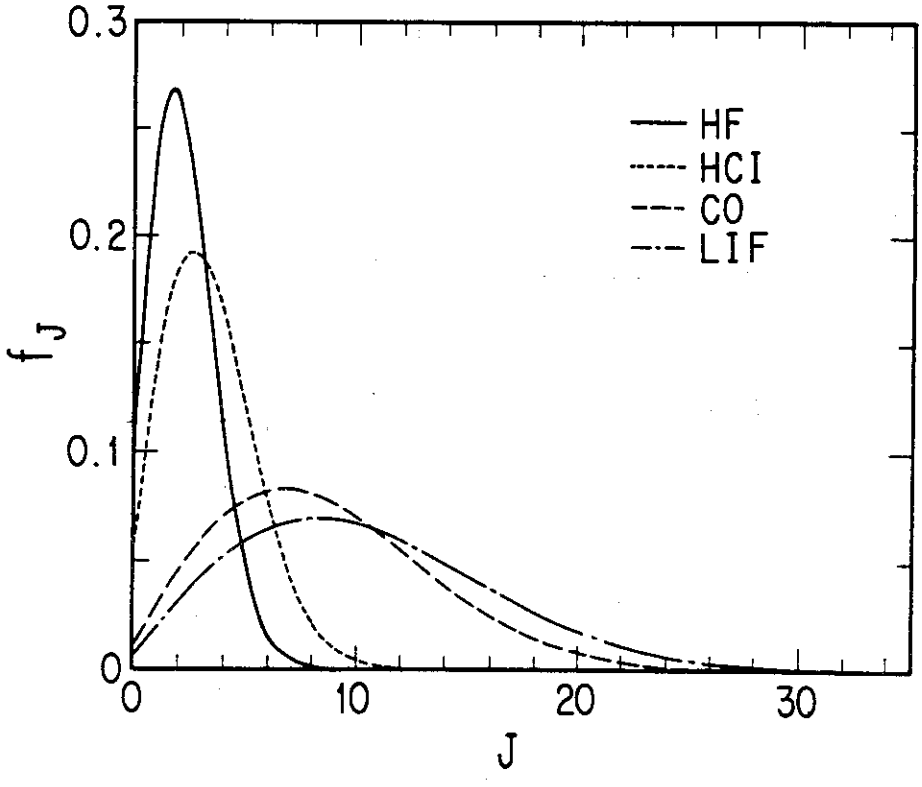

Fig. 2 Rotational distribution at 300K for the CO, HF, HCl, and LiF molecules as a function of rotational quntum number (J).

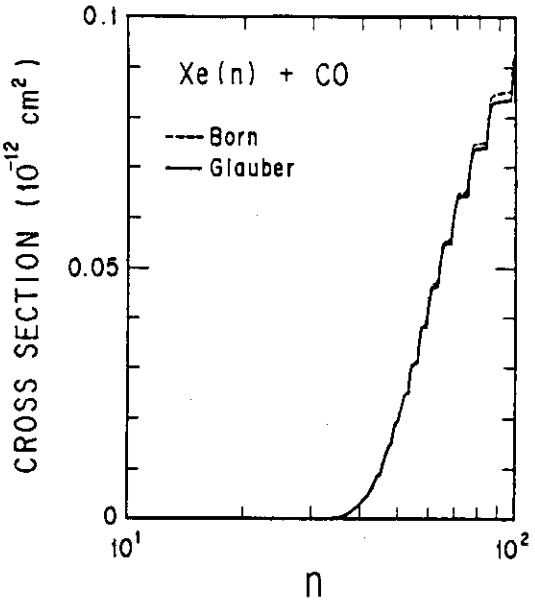

Fig. 3 Principal quantum number (n) dependence of cross sections for $Xe(n)+CO \rightarrow Xe^{+}+e+CO$ at thermal velocity (5.2×10^4cm/s).

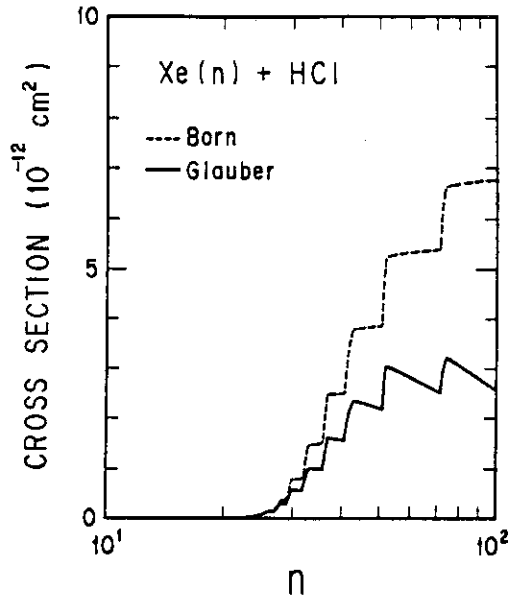

Fig. 4 The same as in Fig. 6 for $Xe(n)+HCl \rightarrow Xe^{+}+e+HCl$ at thermal velocity (4.7×10^4cm/s).

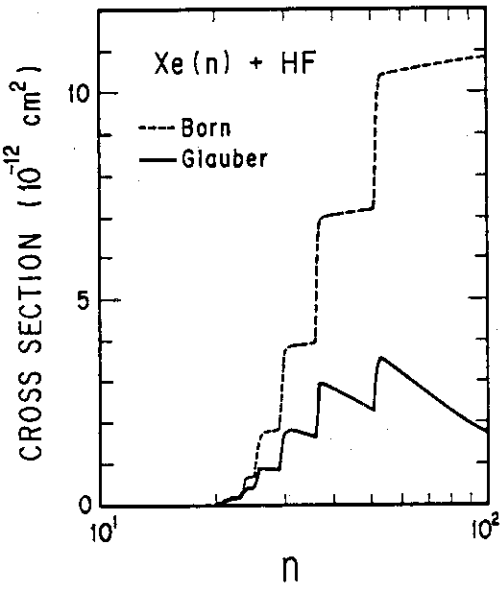

Fig. 5 The same as in Fig. 6 for $Xe(n)+HF \rightarrow Xe^{+}+e+HF$ at thermal velocity (6.0×10^4cm/s).

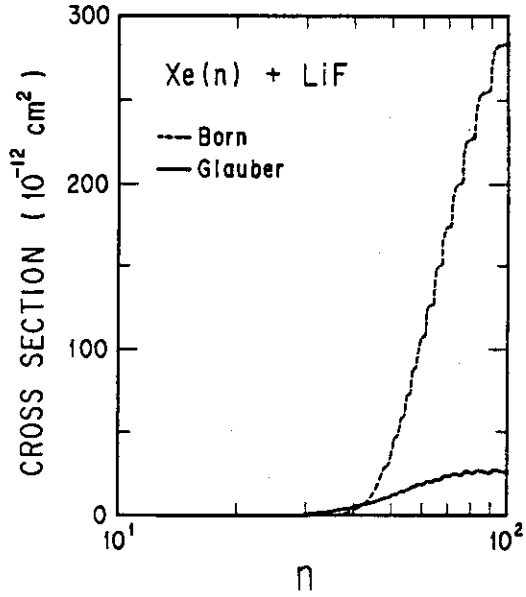

Fig. 6 The same as in Fig. 6 for $Xe(n)+LiF \rightarrow Xe^{+}+e+LiF$ at thermal velocity (5.4×10^4cm/s).

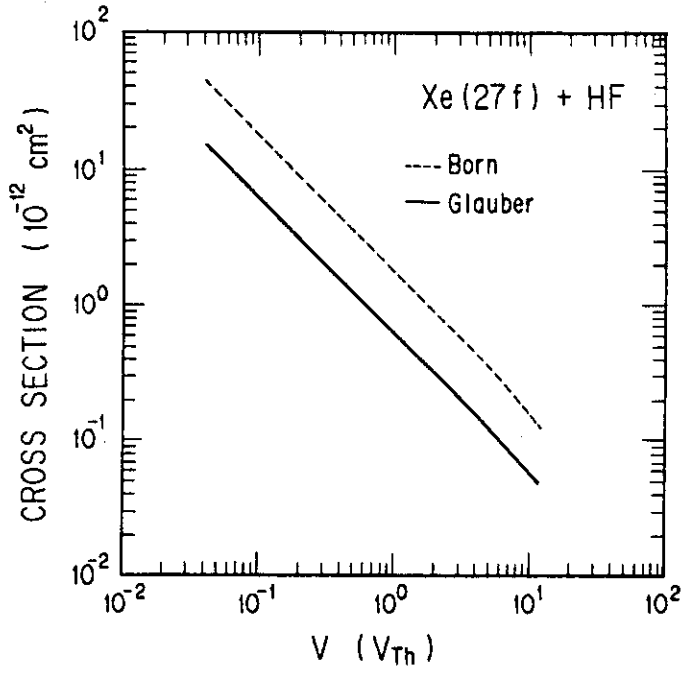

Fig. 7 Relative velocity (V) dependence of cross sections for Xe(27f)+HF→Xe^++e+HF。 V is given in units of thermal velocity V_{th}(=6.0×10^4cm/s)。

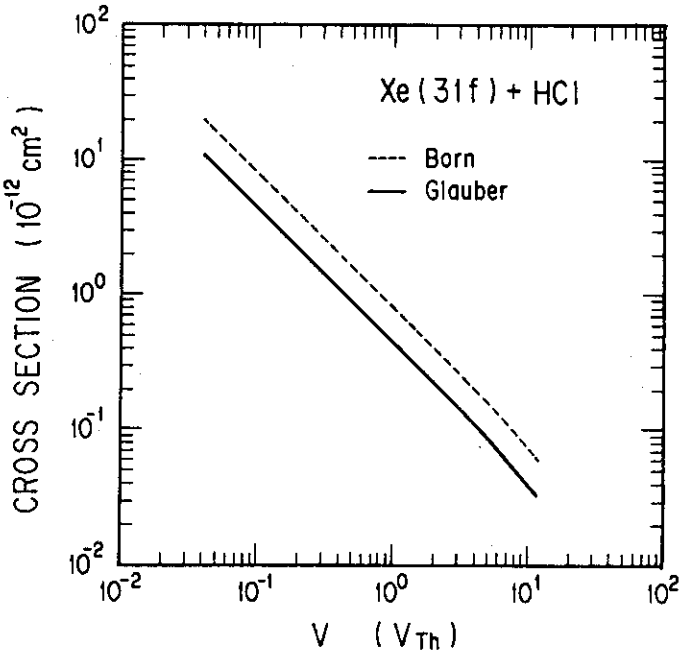

Fig. 8 The same as in Fig. 10 for Xe(31f)+HCl→ Xe^++e+HCl and V_{th}(=4.7×10^4cm/s).

I.3 OBSERVATION OF RESONANT COHERENT EXCITATION OF HIGHLY CHARGED HEAVY IONS

Ken-ichiro KOMAKI, Akio OOTUKA, Eugeni VILALTA, Fuminori FUJIMOTO, Yasuo HIRAO*, Akira MIZOBUCHI*, Takeo HASEGAWA*, Masayuki SEKIGUCHI*, Toshiyuki HATTORI**, Kenji KIMURA***, Michihiko MANNAMI***, Hiroshi KUDO**** and Kiyoshi KAWATSURA*****

College of Arts and Sciences, University of Tokyo,
*Institute for Nuclear Study, University of Tokyo,
**Research Laboratory of Nuclear Reactors, Tokyo Institute of Technology, ***Faculty of Engineering, Kyoto University,
****Institute of Applied Physics, Tsukuba University and
*****Department of Physics, Japan Atomic Energy Research Institute

1. Introduction

An axially channeled ion feels the periodic potential of a crystal as an oscillatory electric field with a frequency which is the ion velocity divided by the atomic spacing along the axis. When this frequency (or one of the higher harmonics) matches the exicitation energy of the ion, selective excitation(Resonant Coherent Excitation) and subsequent emission of a photon(Okorokov Effect) can be expected. Since the prediction of the effect(1) and the first report on the deexcitation photons(2), many workers have tried to confirm the result, but no positive results were obtained. It is considered that the excited electron of the ion has a larger orbital radius than that of the crystal channel and, consequently, is easily stripped. The coherent excitation, itself, is in fact detected as changes in charge state distribution of emerging ions(3). On the other hand, electrons excited resonantly and then stripped are considered to travel with the same verocity as the ion. Such electrons may contribute to the 'convoy electrons' of which origin is not known. The purposes of the present work are [1] to detect the deexcitation photons emitted from the resonantly excited ions and [2] to obtain knowledges on the origin of the convoy electrons. The final purpose of the present experiment was to

obtain a beam of excited ions. If a beam of resonantly excited ions is extracted from a crystal, it will provide ion-atom collision studies with a new tool.

2. Resonant excitation of highly charged heavy ions

To avoid any stripping of excited electrons, it is necessory to keep their orbital diameters well below the inter atomic row distance of the crystal. This condition can be satisfied in the case of the inner-shell electrons of heavy ions. In the present, we report some preliminary results of the experiment performed using the SF-cyclotron at Institute for Nuclear Study, University of Tokyo.

Figure 1 shows an arrangement of beam lines in the experimental area. A beam of $^{20}Ne^{6+}$ was accelerated up to 85 MeV and then charge stripped to 9+(hydrogen-like) by a 40 $\mu g/cm^2$ carbon foil and was introduced to the scattering chamber in the CAVE 3A after charge and energy analyzed by a pair of Beam Analyzer magnets. Two sets of 4-jaw slits were attached in front of the scattering chamber in order to limit the irradiated area of the target, to obtain required parallelity and to satisfy a faint beam condition.

A self-supported thin single crystal of (111) gold was prepared by vacuum evaporation on a mica substrate. Crystal thickness was about 2000 Å. The crystal was mounted on a goniometer capable of rotating around two axes and translating along two directions. The alignment of the crystal

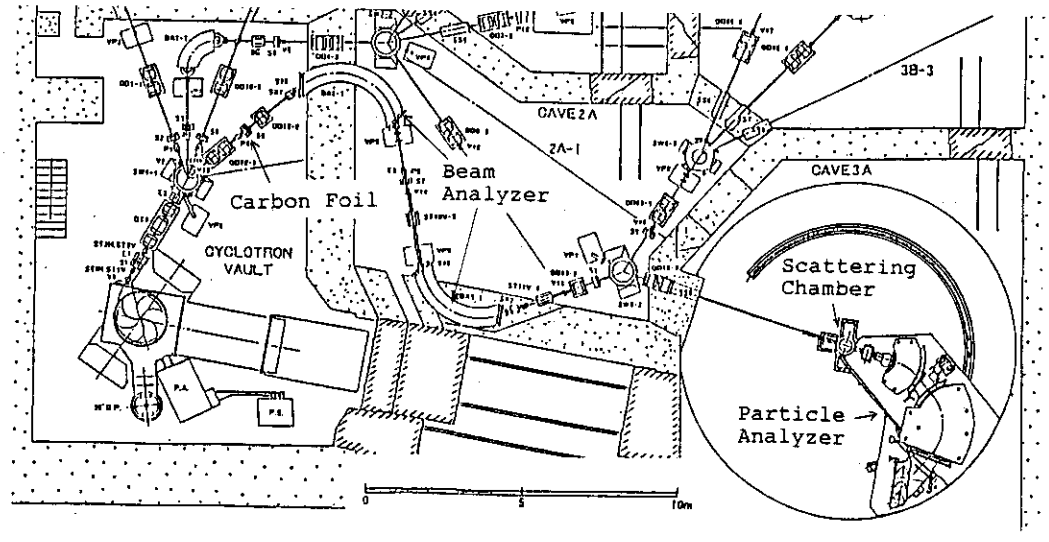

Fig. 1 Top view of the SF-cyclotron facility at Institute for Nuclear Study, University of Tokyo.

axis to the beam was achieved by detecting channeled ions using a silicon surface barrier detector placed at a zero scattering angle. Ratios of the low-energy loss ions to total transmitted ions were measured while changing the crystal orientation. Fig. 2 shows the change in the low-loss ion count for total transmission of 2000 ions while rotating the crystal across the <111> axis. The half width of the peak is consistent with the theoretical critical angle of 0.35°.

The incident energy was changed by the step of 0.5∿1.0 MeV around the resonance energy(87.3 MeV, 6th harmonic) for the <111> channeling. The charge state distribution was measured with the Particle Analyzer for random and <111> aligned incidences at each incident energy. Fig. 3 shows the change in the ratios of 9+ to 9+ plus 10+ charge state fractions for the random and aligned incidences. While the ratio for random incidence shows a smooth tendency, that for aligned incidence shows a dip around incident energy of 88 to 89 MeV. If we take acount of the energy loss, 0.75 MeV, of the incident ion in the target, this energy agrees with the calculated resonance energy, 87.3 MeV. The resonance curve is similar to that of 6th order resonance of N^{6+} ions for Au <111> channeling(3).

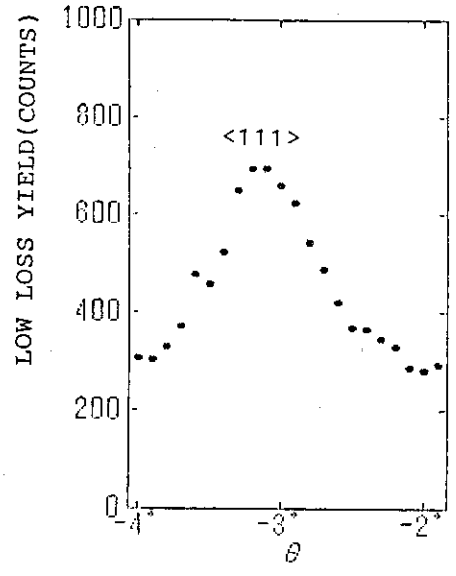

Fig. 2 Rotation angle dependence of number of low-energy loss ions transmitted through a thin Au single crystal. The total number of transmitted ions for each point was 2000.

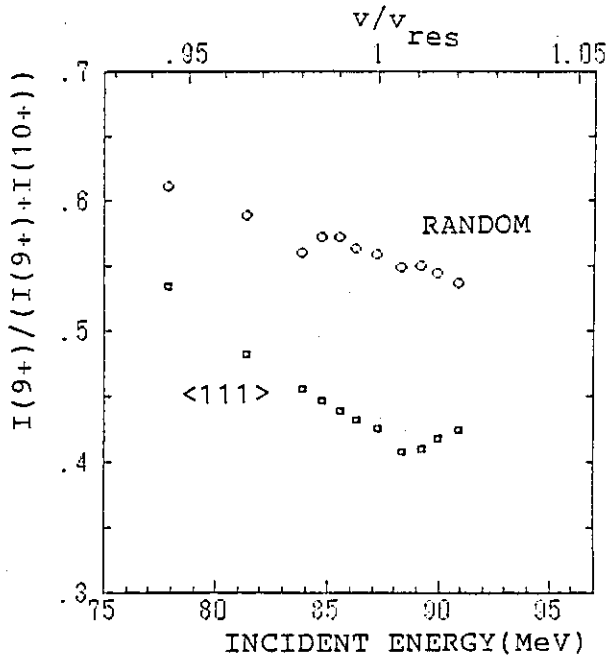

Fig. 3 Ratios of 9+ and 9+ plus 10+ charge state fractions transmitted through a Au foil for random and <111> aligned incidences at various energy.

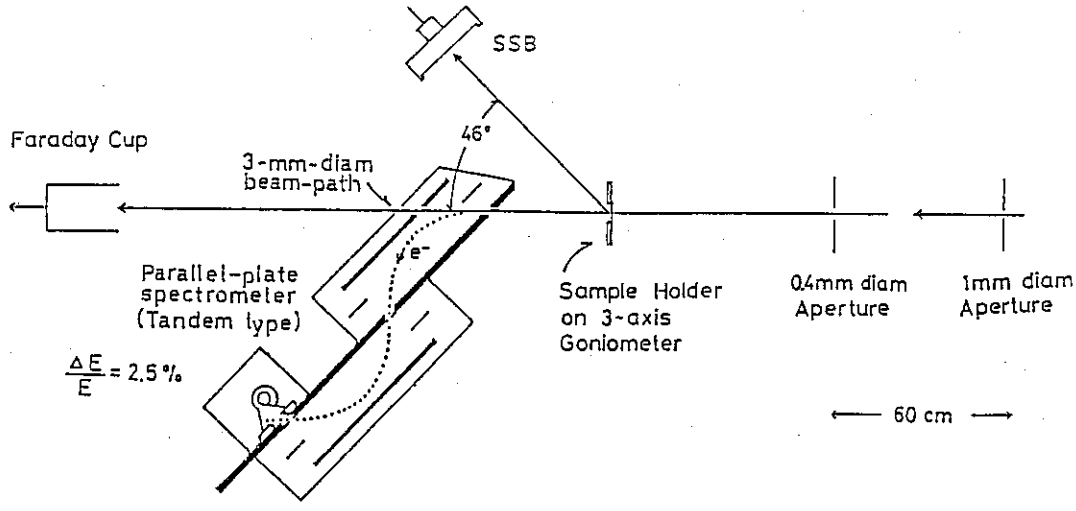

Fig. 4 Experimental arrangement for spectrometry of ion induced secondary electrons.

Work is still in progress. The next step is to observe the change in the intensity of the deexcitation X-ray(1.02 keV) using a Si(Li) detector at 45° to the incident direction.

3. Convoy electrons caused by reosonantly excited ions

Figure 4 shows the experimental arrangement for the convoy electron measurement. A beam of 0.6- to 1.6-MeV He^+ ions from the 2-MV van de Graaff accelerator at JAERI was collimated by two apertures and transmitted a thin foil of Au single crystal parallel to the <111> axis. The crystal was prepared by the same way as described above and was aligned by detecting foreward scattering using a Si detector at 46° to the beam. The energy spectraum of the 0° secondary electrons was measured with a doubly folded parallel plate energy analyzer. Partial spectra for 1.0- and 1.1-MeV He^+ incidences are given in Fig. 5, where convoy peaks are clearly seen. As the convoy electron intensity, total count of 5 channels at the peak was chosen. Fig. 6 shows

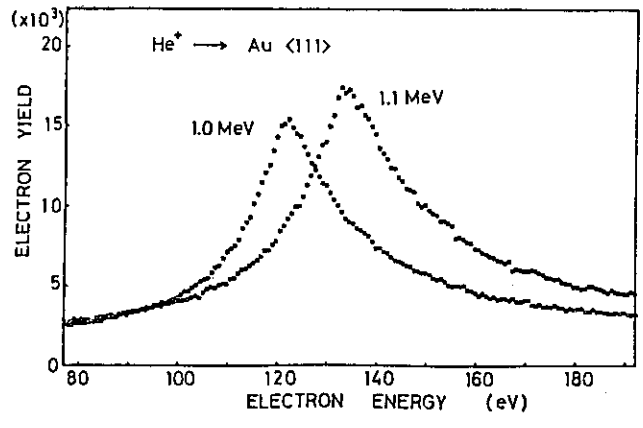

Fig. 5 Energy spectra of secondary electrons caused by the <111> channeling of 1.0- and 1.1-MeV He^+ ions.

the change in the convoy intensity with the incident energy. In the present case, the expected resonance energy is 1.01 MeV. In the figure, however, no distinct change in the convoy intensity is found at the resonance energy even if we take account of the energy loss of the incident ions in the target crystal. This situation might be caused by the fact that the radius of the excited state of He^+ has an orbital radius of 1.1 Å which is larger than the inter string distance of the Au <111> atomic rows and consequently the resonance width may be too large to be observed.

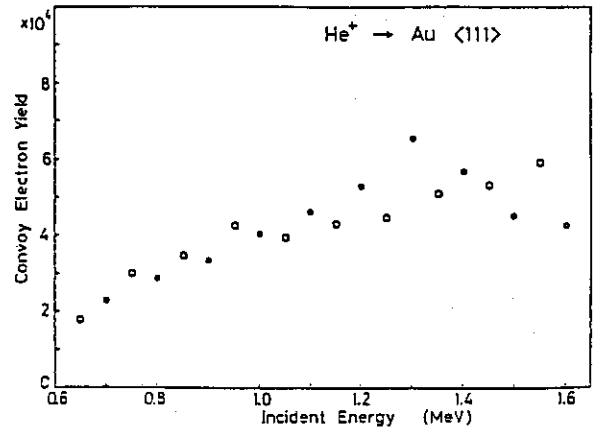

Fig. 6 Convoy electron intensity for Au <111> channeling of He^+ ions as a function of the incident energy. Open and closed circles were mesured by increasing and decreasing the incident energy, respectively.

In order to clarify this situation, a measurement of the charge state change of the transmitted ions and an experiment using heavier ions such as C^{5+} ions are planned.

References

(1) V.V. Okorokov: JETP Lett. 2(1965) 1111.

(2) V.V. Okorokov, D.T. Tolchenkov, I.S. Khizhnyakov, Yu.N. Cheblukov, Yu.Ya. Lapitski, G.A. Iferov and Yu.N. Zhukova: Phys. Lett. A 43(1973) 485.

(3) S. Datz, C.D. Moak, O.H. Crawford, H.F. Krause, P.F. Dittner, J. Gomez del Campo, J.A. Biggerstaff, P.D. Miller, P. Hvelplund and H. Knudsen: Phys. Rev. Lett. 40(1978) 843.

I.4 ION-INDUCED SECONDARY ELECTRONS EMITTED UNDER CHANNELING CONDITIONS

Hiroshi KUDO, Kunihiro SHIMA, Seiji SEKI[+], Koki TAKITA[#]
Kohzoh MASUDA[#], Kouichi MURAKAMI[#], and Takashi IPPOSHI[#]

Institute of Applied Physics, University of Tsukuba, [+]Tandem Accelerator Center, University of Tsukuba, [#]Institute of Materials Science, University of Tsukuba

1. Introduction

It has been reported by several authors(1-4) that the ion-induced emission of secondary electrons from single-crystal targets strongly depends on the incident direction of projectile ions. By using low-energy (less than hundred keV) ions of noble gases, they found that the total electron yield reflects the areal density of the atomic rows or planes that are parallel to the ion-beam direction. This effect, however, has not been extensively studied mainly because of the difficulty in treating the complicated scattering of electrons in solids, which produces observed secondary electrons. This situation is in contrast to the simple case of Rutherford backscattering or characteristic x-ray emission under channeling conditions(5).

A necessary approach to investigate this phenomenon should be the energy analysis of the emitted electrons. Such energy spectra under channeling (shadowing) conditions have been measured recently by Macdonald et al.(6), and by Kudo et al.(7-9) with a particular interest in the emission of Auger electrons. However, they have not interpreted the decrease in the electron yield over a wide energy range, as is clearly observed for low-index axial channeling (roughly 50% decrease for high-energy electrons). It is still unknown how the electron spectrum under channeling conditions depends, e.g., on the structure of the crystal channel, and on the ion species.

With such a background, this letter reports on an experimental study of the electron emission under channeling conditions, with a technical interest in the structure analysis of thin surface layers by using

secondary electrons.

2. Experimental

The apparatus used in this experiment has been described in a previous paper(8). The parallel-plate electron spectrometer of the double-deflection type, with a relative energy resolution of 2.5% full width at half maximum, is effective in stopping stray electrons from entering the electron multiplier. Since the electrons were analyzed in energy at 180° with respect to the ion-beam direction, it was easy to avoid the error associated with a misalignment of the spectrometer axis. Actually, even 20° tilt of the sample surface caused no noticeable change in the electron yield. The measurements were carried out at room temperature (290-295K) under the pressure of about 5×10^{-6} Pa. The (110), (111), and (100) wafers of Si crystals (0.3-0.5 mm thick) were chemically etched. Under these experimental conditions, the Si surfaces were covered with contaminant layers (a few monolayers thick) consisting of carbon and oxygen atoms, as identified previously(8). Such thin layers, however, could hardly affect the decrease in the high-energy electron yield since under channeling conditions those electrons are originated from collisions between the projectile and target electrons in the surface region of more than twenty nanometers thick , as will be estimated later (Fig. 5).

3. Results

Figure 1 shows energy spectra of secondary electrons induced by 15- and 30-MeV He^{++}, measured for <110> and random (nonchanneling) incidences.

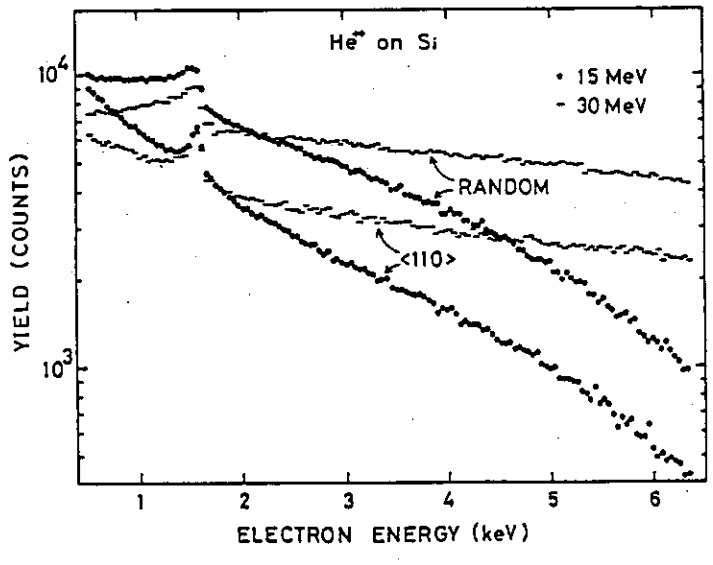

Fig. 1 Secondary electron spectra for He^{++}.

Figure 2 shows the dependece of the spectra on various axial incidences of 15-MeV He^{++}. A characteristic trend is seen in Figs. 1 and 2 if we

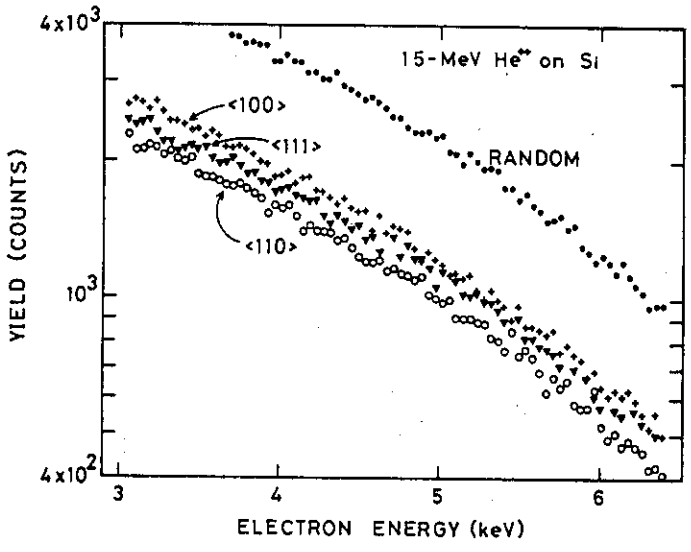

Fig. 2 Secondary electron spectra for <110>, <111>, and <100> incidences of He^{++} on Si targets.

compare the pairs of spectra for axial and random cases; the logarithmic plots of each pair can be well overlapped by vertical translation at electron energies above 3 keV. This means that the number of high-energy electrons emitted under channeling conditions decreases at a constant rate, independent of the electron energy E. This was also observed for carbon and oxygen ions, as shown in Fig. 3. The charge state of the ions only

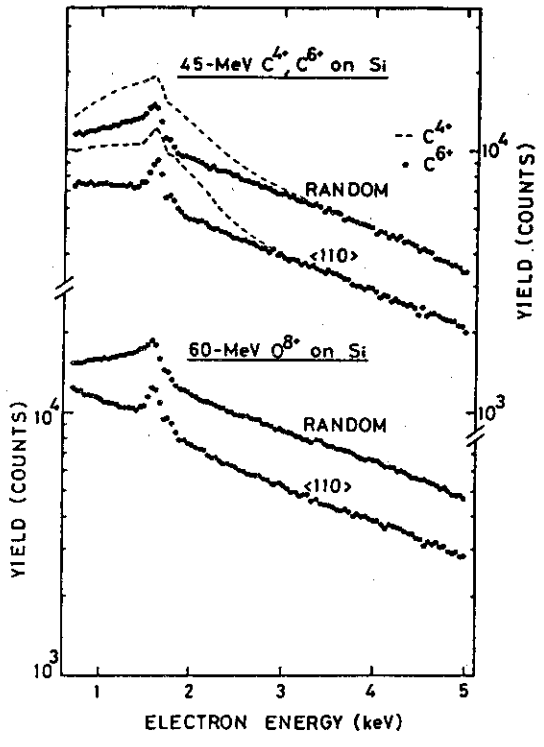

Fig. 3 Secondary electron spectra for 3.75-MeV/amu carbon and oxygen ions.

affects the low-energy yield in the spectra. This is typically seen in Fig. 3 for C^{4+} and C^{6+}, for which the electron yields are normalized to the same number of the incident carbon ions. For C^{4+} case, the enhanced portion of the electron yield observed below about 3 keV results from the electron loss of C^{4+}.

Since the maximum energy transferred from a projectile of 3.75 MeV/amu to a stationary free electron (in a head-on collision) is 8.2 keV, the present measurements mostly covered the energy region where sufficient electron yields for measurements are obtained.

4. Discussion

The decrease in the electron yield observed under channeling conditions can be interpreted in terms of the ion-beam shadowing effect, i.e., as the decrease in the effective target thickness responsible for the production of scattered electrons. We demonstrate this by confirming a scaling law of the data, which is expected from the shadowing effect. The scaling law essentially corresponds to a special case of the universal plot found by Feldman for the surface-peak intensity observed in ion backscattering spectra.(10,11)

The shadowing effect is described as the successive increase in the impact parameter in a sequence of soft collisions between the ion and aligned atoms, although this increase is somewhat disturbed by the thermal displacement of atoms. In the collision sequence, each soft collision of impact parameter b causes the increase in the impact parameter for the next soft collision by $\phi(b)d$, where $\phi(b)$ is the scattering angle in the laboratory frame and d is the interatomic distance along the row. In a Coulomb approximation which is applicable to fast ions as in the present case, $\phi(b)d$ is given by(11)

$$\phi(b)d = \frac{Z_1 Z_2 e^2 d}{b E_0 (1 + M_1/M_2)} = R_s^2/4b \ , \qquad [1]$$

where Z_1 and Z_2 are the atomic numbers of the projectile and target, respectively, e is the electronic charge, E_0 is the ion energy, M_1/M_2 is the mass ratio between the projectile and target, and R_s $(=[4Z_1Z_2e^2d/E_0(1+M_1/M_2)]^{1/2})$ is the shadow cone radius. The factor $1+M_1/M_2$ comes from the laboratory-frame expression of a small scattering angle.

Equation [1] indicates that the shadowing effect, i.e., the impact-parameter increase with depth is determined through the parameter R_s. Next, we obtain an expression of the constant reduction rate of the high-energy electron yield, W, observed for channeling incidences. Because the number of target atoms that are effective for producing scattered electrons is restricted from the shadowing effect, the effective number of target atoms, N (atoms/row), is a function of R_s. Therefore, the effective target thickness for the shadowing case is given by $N(R_s)d$. We assume that the observed yield of secondary electrons is proportional to the number of the scattered electrons near the surface. This linearity enables a treatment of W without discussing the detail of the production of observed secondary electrons. Actually, we may write

$$W=N(R_s)d/t, \quad \text{i.e.,} \quad W/d=N(R_s)/t, \qquad [2]$$

where t is the effective target thickness for random incidences. The thickness t corresponds to the depth over which the ion-induced electrons do not contribute to the observed electron yield, as a result of elastic and inelastic scattering suffered in the target. Since such scattering smears the correspondence between the depth where the collision (between the projectile and a terget electron) occurs and the energy distribution of the secondary electrons originated from the collision , the thickness t should be independent of the measured electron energy over a wide energy range. This causes a constant W through eq.[2], as observed in the experiments. For low-energy electrons, however, the scattering in the target prevents the electron's escape from a deep region, and therefore, decreases t. This effect results in an increase in W for low-energy electrons, as typically observed below 3 keV in Fig. 1.

For fast ions (e.g., MeV/amu energy range), the parameter t in eq.[2] is determined only through the ion's velocity v irrespective of ion species, according to the semiclassical approximation model(12). In this model, the ion-induced transition probability of a target electron from the initial to the final state (corresponding to the production of a scattered electron) is expressed as $Z_1^2 f(v)$ with f(v) being the corresponding transition probability for protons with the same velocity, so that the parameter Z_1 gives only the scaling factor for the number of scattered electrons. Therefore, we can expect from eq.[2] that the values of W/d

obtained for various ions with a same velocity can be universally scaled against the parameter R_s. Figure 4 shows the plot of W/d as a function of R_s^{-1}, which was obtained for various axial incidences of 3.75-MeV/amu ions of helium, carbon and oxygen on the Si targets. In this plot, we see that

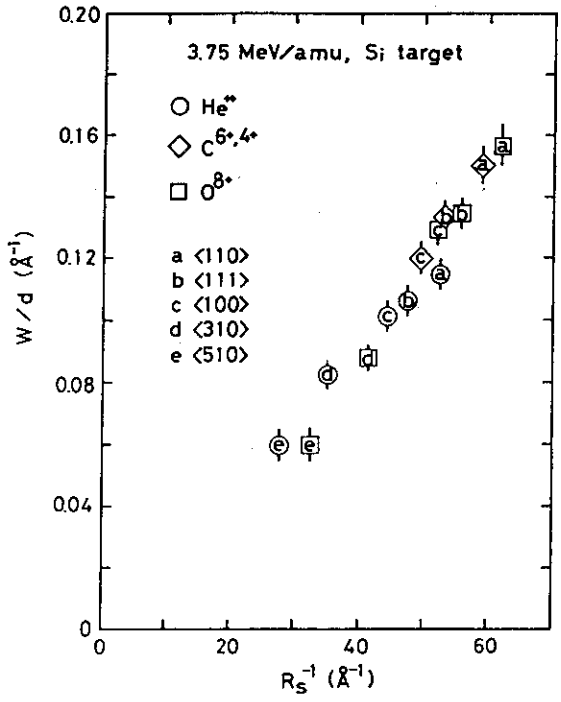

Fig. 4 Universal plot of W/d as a function of R_s^{-1}, for 3.75-MeV/amu ion.

all the data are distributed on a smooth curve within a deviation of about 5%, indicating an increase in the effective number of target atoms with decreasing the shadow cone radius. This plot strongly supports the interpretation of the experimental results in terms of the shadowing effect.

The analysis presented here includes an unknown parameter t. Thus, it should be necessary to estimate t for the present case . Figure 5 shows the calculated ionization probabilities for K, L_1,and $L_{2,3}$ shells of Si for the ⟨110⟩ incidence of 15-MeV He^{++} together with the 30-MeV case, which are normalized to those of the surface atom, respectively. The detail of the calculation has been published previously(7-9). In the treatment of electron emission induced by energetic particles, we may assume that the effective atomic size of Si is roughly the mean radius of L shells, though the valence electrons should appreciably contribute to increase this size. Since for 15-MeV He^{++} the ionization probabilities for L shells decrease to 50% at about 200 Å, as seen in Fig. 5, we obtain t≃450 Å for 15-MeV

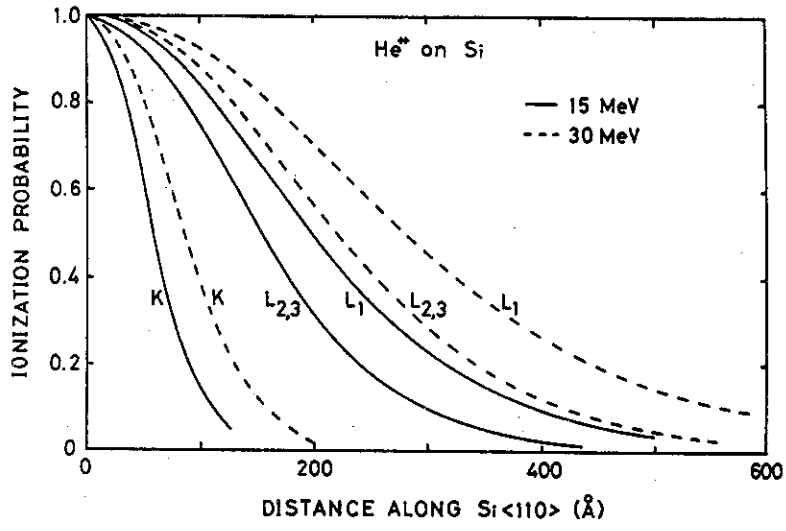

Fig. 5
Cauculated ionization probabilities for various Si shells under the <110> shadowing condition.

He^{++}(i.e., for 3.75-MeV/amu ions) from eq. [2] by using $N(R_s)d \simeq 200$ A and the observed value of W=0.44 . Similarly, we can estimate that $t \simeq 510$ A for 30-MeV He^{++}(i.e., for 7.5-MeV/amu ions) from the values of $N(R_s)d \simeq 280$ A and W=0.55.

Finally, we emphasize that the shadowing effect observed in the high-energy yield of secondary electrons is applicable to the characterization of thin epitaxially-grown crystals. Furthermore, this method should be sometimes advantageous over the conventional channeling (Rutherford backscattering) technique because the emission of those electrons is sensitive to the crystal structure near the surface.

(Acknowledgements)

We thank T. Uchino, O. Eryu, T. Gochou, and K. Takahashi for their assistance with the measurements. This work was supported in part by a Grant-in-Aid for Special-Research Project on Ion Beam Interactions with Solids from the Ministry of Education, Science, and Culture.

References

(1) G. D. Magnuson and C. E. Carlston: Phys. Rev. 129 (1963) 2409.
(2) N. Colombie, B. Fagot, and C. Fert: Radiat. Eff. 2 (1969) 31.
(3) B. A. Brushilovsky and V. A. Molchanov: Radiat. Eff. 23 (1974) 131.
(4) N. Benazeth: Nucl. Instru. Methods. 194 (1982) 405.

(5) D. S. Gemmell: Rev. Mod. Phys. 46 (1974) 129.
(6) J. R. MacDonald, L. C. Feldman, P. J. Silverman, J. A. Davies, K. Griffiths, T. E. Jackman, P. R. Norton, and W. N. Unertl: Nucl. Instru. & Methods 218 (1983) 765.
(7) H. Kudo, D. Schneider, E. P. Kanter, P. W. Arcuni, and E. A. Johnson: Phys. Rev. B30 (1984) 4899.
(8) H. Kudo, K. Murakami, K. Takita, K. Masuda, S. Seki, K. Shima, H. Itoh, and T. Ipposhi: Jpn. J. Appl. Phys. 24 (1985) 1440.
(9) H. Kudo, K. Shima, K. Takita, K. Masuda, K. Murakami, H. Itoh, T. Ipposhi, and S. Seki: Jpn. J. Appl. Phys. 25 (1986) 1751.
(10) L. C. Feldman: Nucl. Instru. & Methods 191 (1981) 211.
(11) L. C. Feldman, J. W. Mayer, and S. T. Picraux: Material Analysis by Ion Channeling (Academic Press, New York, 1982), p.13 and 223.
(12) J. M. Hansteen, O. M. Johnsen, and L. Kocbach: At. Data Nucl. Data Tables 15 (1975) 305.

I.5 GLANCING-ANGLE SCATTERING OF MeV LIGHT IONS AT THE CLEAN (001)SURFACE OF TIN TELLURIDE CRYSTAL

Michi-hiko MANNAMI, Kenji KIMURA, Masataka HESEGAWA
Department of Engineering Science, Kyoto University

1. Introduction

It is known that specular reflection occurs at glancing-angle incidence of fast ions upon the atomically smooth surface of a single crystal. Surface channelling occurs also when the direction of incident ions is aligned to a low index crystallographic axis parallel to the surface.(1,2) In both situations, the ion experiences a series of correlated small angle scattering with surface atoms, and cannot penetrate inside the crystal when the glancing-angle is small. Thus the physcial processes taking place during the scattering are expected to be different from those at transmission of ions through solid, and the interaction between the fast ion and the solid surface can be manifested in the ion scattering and related phenomena.

Here in this report, some of our recent experimental studies of glancing angle scattering of MeV light ions at a clean surface are introduced emphasizing on the energy loss of reflected ions and on the angular distribution of scattered ions.

2. Experimentals

The experimental setup was described elsewhere.(3,4) Only a brief outline is summarized. A single crystal of KCl with (001) cleavage surface was mounted on a 5-axes goniometer in a scattering chamber whose base pressure was 3×10^{-10} Torr. A single crystal of SnTe(001) was prepared by epitaxial growth in situ by vacuum evaporation on the KCl(001) surface. The crystal was kept at about 200°C during the experiment. The single crystal of SnTe(001) thus prepared has dislocations of densities less than 10^{9}cm/cm^{3} and the (001) surface is supposed to have bulk-exposed surface, because the surface showed sharp 1 x 1 RHEED pattern. A beam of ions from the 4MV Van de Graaff accelerator of Kyoto University was collimated by a

Most of the data in the present paper were published in references (3),(4),(5) and (6).

series of apertures to the divergence angles less than 0.5 mrad and to 0.1 x 0.1 mm on the specimen. Incident ions were 0.7 MeV protons and He^+ ions. The ions scattered at an angle θ_s in the plane which contains the incident beam and the normal to the surface were chosen by a movable aperture and counted with a solid state detector. The acceptance angle of the aperture was 0.9 mrad for scattered ions.

3. Experimental results

Fig. 1 shows an example of the observed energy spectra of scattered He^+ ions for various scattering angles when 0.7MeV He^+ ions were incident on SnTe(001) surface with a glancing angle 4.9 mrad. Each spectrum consists of a few well-defined peaks. The yield of ions has a maximum at the scattering angle about 10 mrad, which corresponds to the mirror reflection angle. The yield of ions forming the first peak (the peak with the highest energy) is about 70% of the total yield.

Similar set of energy spectra could be obtained when the incident beam is aligned to an axial channel parallel to the surface plane, however, the peaks in the energy spectrum were broader.

Here in this paper, we are interested only in the case of specular reflection, and the angular distribution of scattered ions and the energy loss of the scattered ions will be discussed.

Energy spectra

Fig.2 shows an example of the energy spectrum of scattered He^+ ions. The energy losses at each peak were determined by fitting the peaks with Gaussian distributions. The spacings between the 1st and the 2nd peak and those between the 2nd and the 3rd peak for scattered He^+ and He^{++} ions are shown for the glancing angle 2.9 mrad and the scattering angle 6.4 mrad in Fig. 3. The spacings are independent of the charge state of the scattered ions and increase gradually with increasing ion energy.

The simplest interpretation of the multi-peak feature of the energy spectrum is shown schematically in the inset of Fig. 2: The first peak is formed by ions reflected at the topmost atomic layer and the 2nd peak is due to ions scattered at the second atomic layer and so on. Thus the energy spacing must corresponds to the energy loss of ions during the oscillatory motion in planar channels. The energy loss of ions in one period of oscillation along (100) planar channel was measured by channelling/backscattering method. From the surface oscillation peaks in the backscattered He ions the energy loss was determined and is shown in

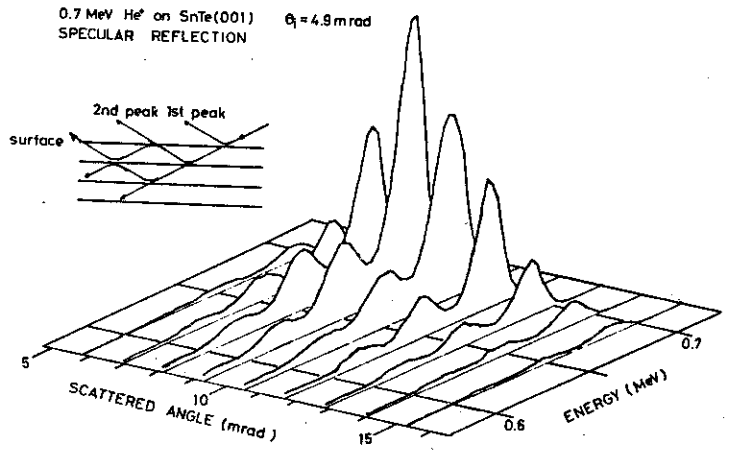

Fig.1 Energy spectrum vs. scattering angle

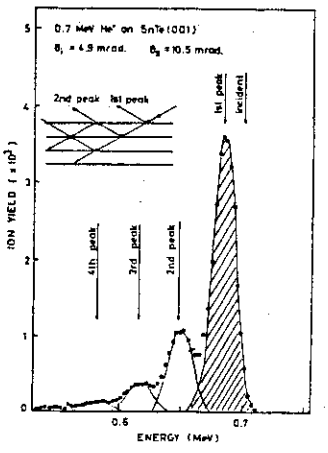

Fig. 2 Energy Spectrum of He

Fig. 3 for comparison of the peak separation values. From the concept of planar continuum potential in case of channelling, it is difficult to understand the penetration of ions through the topmost atomic layer to give 2nd, 3rd and 4th peak. This is supposed to be caused by thermal vibration of surface atoms and structural irregularities such as reconstruction of surface atoms or atomic height steps on the surface, however, we have not clarified the scattering process.

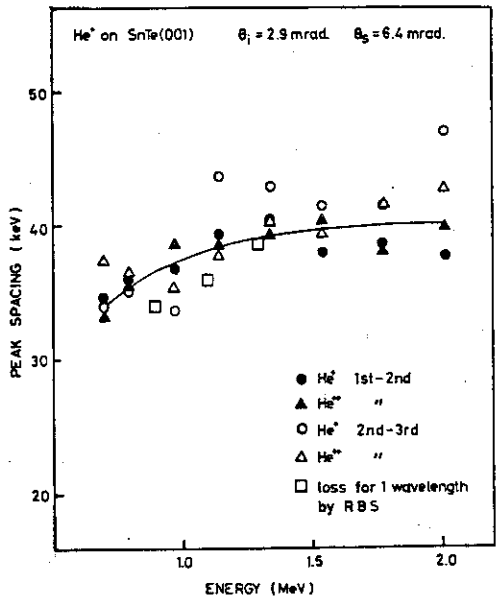

fig.3 Energy separation of peaks.

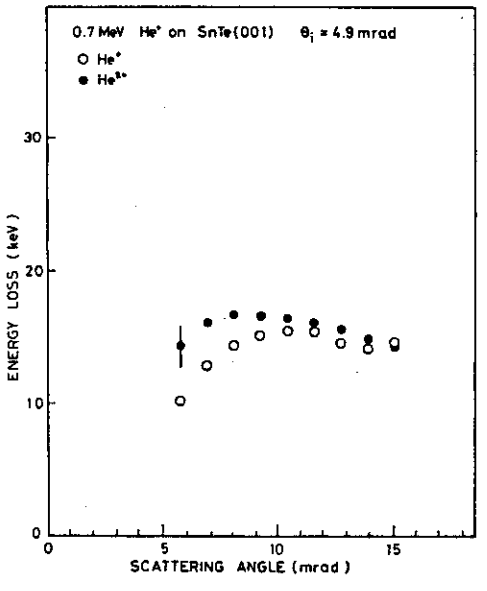

Fig.4 The most probable energy loss vs scattering angle

The feature of the observed energy spectra of the reflected protons at glancing angle incidence is different from that of He ions. The energy spectrum shows only one peak at the energy slightly smaller than the energy of incident ions. This is understood from the poor energy resolution of the solid state detector and it is expected that we could observed peaks in the energy spectrum if we have ion detector with better energy resolution.

Fig. 4 shows the most probable energy loss (peak energy) of the ions in the first peak as a function of the scattering angle when 0.7 MeV He^+ ions are incident on SnTe(001) surface with glancing angle 4.9 mrad. The most probable energy loss shows a broad peak at the scattering angle of specular reflection, and the energy loss of the scattered He^{++} ions is slightly larger than that of He^+ ions especially for smaller scattering angles.

Fig. 5 shows the dependence of the most probable energy loss of the specularly reflected He ions on the energy of incident ions when He ions are incident on the SnTe(001) surface with glancing angle 2.9 mrad. The energy loss is almost independent of ion energy.

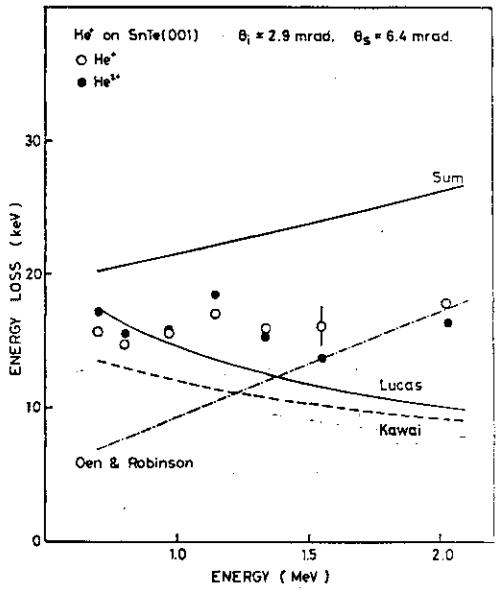

Fig.5 The most probable energy loss vs. ion energy.

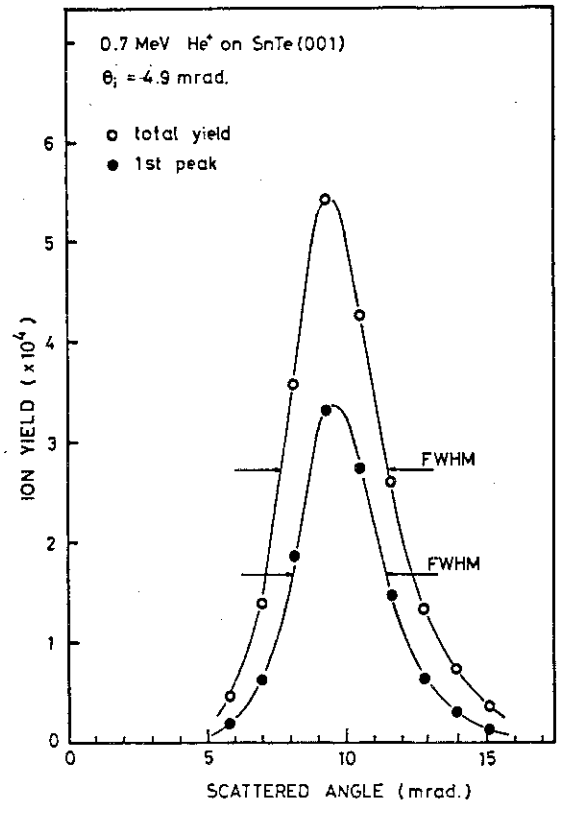

Fig.6 First peak yield and total yield against scattering angle.

Angular distribution of scattered ions

Angular distribution of scattered ions at glancing angle incidence of He and H ions are not sharp as expected from the picture of mirror reflection. Fig.6 shows the scattering angle dependence of the first peak yield in the energy spectrum and of the total yield when the glancing angle of incident He^+ is 4.9 mrad. The yields have maxima at the angle twice of the glancing angle. The angular width of the total yield is slightly wider than that of the first peak yield.

The full width at half maxima (FWHM) of the angular distribution of reflected ions depends slightly on the glancing angle as shown in Fig. 7. These data were obtained from the ions scattered at the topmost atomic layer, i.e. from the first peak in the energy spectrum. However, for proton data, the first peak in the energy spectrum cannot be resolved and those of total yield are shown. Thus the FWHM for protons may be slightly overestimated.

4. Discussion

Position dependent stopping power at (001) surface of SnTe(5,6)

If the stopping power of solid surface is determined by a position dependent function S(y), the most probable energy loss of reflected ions can be written as

$$\Delta E = \int S(y)dz, \qquad (1)$$

where the trajectory of ion lies on the yz-plane and the integration is along the ion trajectory. The trajectory of specularly reflected ion can be calculated with the use of the continuum model of planar channelling. The interaction between the ion and the surface atoms can be approximated to a planar continuum potential and the Moliere approximation to the Thomas Fermi screening function is employed to calculate the continuum potential. An analytical expression of ion trajectory can be obtained. Taking the zero of z-axis at the apex of the trajectory, and using only the third term in the Moliere potential, the trajectory is given as

$$y(z)=(a_{TF}/\beta_3)\ \ln\left[\cosh^2(\beta_3\Theta_i z/2a_{TF})2\pi n_p Z_1 Z_2 e^2 \alpha_3/E\Theta_i{}^2\beta_3\right] \qquad (2)$$

where a_{TF} is the Thomas-Fermi screening distance, n_p is the atomic density of the surface, Z_1 and Z_2 are the atomic numbers of projectile and crystal atom respectively, E is the ion energy, θ_i is the glancing angle and α_3 and β_3 are the constants in The Moliere potential. Substituting eq.(2) into eq.(1), the loss can be expressed as

$$\Delta E = 4a_{TF}/\beta_3\theta_i \int_{X_1}^{\infty} dX\ S(X/\theta_i)(X^2-X_i^2)^{-1/2} \qquad (3)$$

where $X = \theta_i \exp(\beta_3 x/2a_{TF})$, $X_1 = (2\pi n_p Z_1 Z_2 e^2 a_{TF}\alpha_3/E\beta_3)^{1/2}$. The observed energy loss is independent of θ_i as can be seen in the experimental data, the right hand side of eq.(3) must be constant and thus $S(X/O_i)$ must be proportional to θ_i/X . Using the relation, it is easy to derive the position dependent stopping power as

$$S(y) = A(E)\ \exp(-\beta_3 y/2a_{TF}) \qquad (4)$$

The integration in eq.(3) can be performed with the use of eq.(4) and the energy loss is obtained as

$$\Delta E = A(E)(2\pi a_{TF} E/\alpha_3\beta_3 n_p Z_1 Z_2 e^2)^{1/2} \qquad (5)$$

Since the observed energy loss is independent of the ion energy, A(E) must be proportional to $E^{-1/2}$. The position dependent stopping power is therefore expressed as

$$S(y) = C\ E^{-1/2}\ \exp(-\beta_3 y/2a_{TF}) \qquad (6)$$

where C is expressed $\Delta E(\alpha_3\beta_3 n_p Z_1 Z_2 e^2/2\pi a_{TF})^{1/2}$. The constant C is 7.7×10^3 $MeV^{3/2}cm^{-1}$ for He ions and is 2×10^3 $MeV^{3/2}cm^{-1}$ for protons. The stopping given by eq.(6) for 0.7 MeV He^+ is shown by a thick solid line in Fig. 7.

It is known that the energy loss of fast ions in solid is due to collective excitation of electron gas and to the single collision with core electrons. For the former, a few theoretical calculations have been published. (7,8) The result gave values smaller than our experimental results as shwon by broken line indiecated by "Kawai" in Fig. 8. This suggests that the loss due to single collisions has to be calculated. However the theories are not satisfactory to derive the

energy loss near the surface.

Oen and Robinson have given a formula of impact parameter dependent stopping power in ion-atom collision in their computer simulation of ion trajectories in solids. (9) Their formula is

$$Q(r) = (0.045\ K\ E^{1/2}/\pi a_{TF}^{2})\ \exp(-0.3r/a_{TF}). \qquad (7)$$

where K is a parameter. Theoretical basis of this formula is not clear and is supposed to be derived from an approximate electron density distribution near atom. In order to compare this formula with the present experimental results, the pre-exponential factor in eq.(7) is changed so that the stopping cross section calculated from eq.(7) coincides with the semi-emprical formula derived by Ziegler. (8) The resulting stopping formula is

$$S(y) = 0.09 n_p s y/\pi a_{TF}^{2}\ K_1(0.3y/a_{TF}), \qquad (8)$$

where s is the stopping cross section of the crystal atom and $K_1(z)$ is the modified Bessel function. The calculated results (indicated by Oen

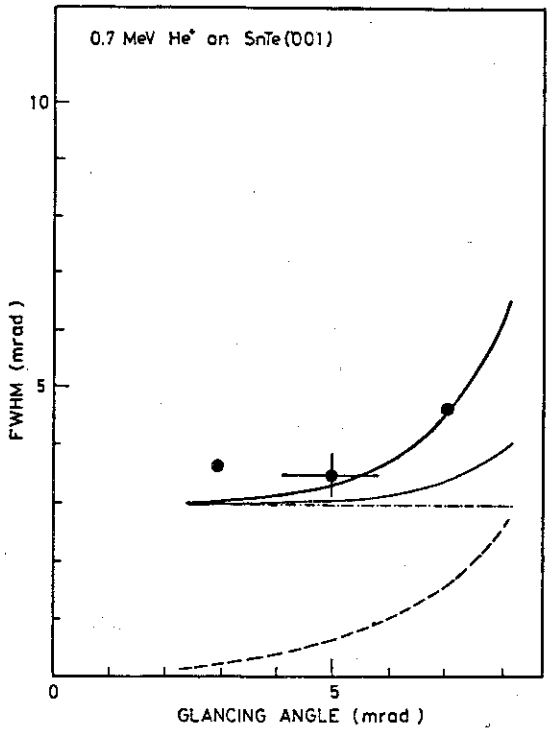

Fig.7 FWHM of the angular distribution of scattered ions.

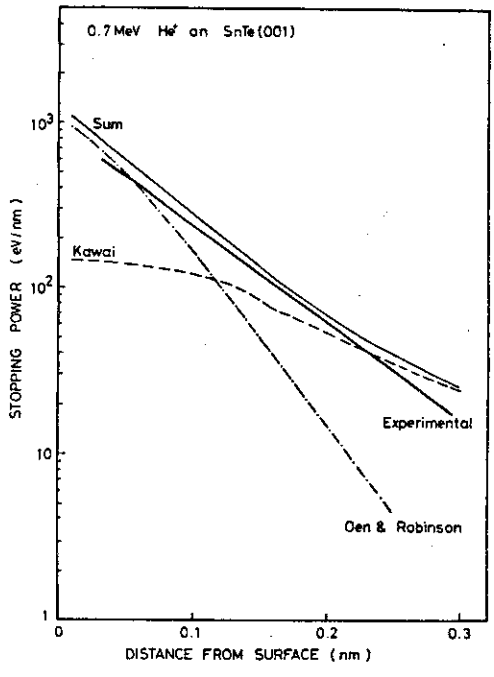

Fig.8 Position-dependent stopping power at the (001) surface of SnTe.

& Robinson) can be compared with the experimental results in Fig. 8, where the agreemnt is not so bad but the deviation beomes larger at larger y.

The sum of the stopping power derived by Kawai et al and that derived by Oen & Robinson is shown in Fig .8. The agreement between this sum and the experimental formula is good, however, the dependence of the stopping power on ion energy is different.

Scattering of planar channelling ions is similar to the surface specular reflection in various aapects and it is worth to compare the two cases. Energy loss of planar channelled ions transmitted through thin gold crystal has been studied by Robisnon.(10) He explained the experimental results by a emprical stopping power,

$$s(y) = s_o + s_1(\cosh(\beta_3 y/2a_{TF}) - 1) \qquad (9)$$

where y is the distance from the channel centre and s_o and s_1 are numerical constants. Assuming the present experimental stopping power formula to be valid for ions in planar channel, we derived the stopping power for ions travelling in planar channel as the superposition of two continuum planes; The stopping power is then

$$s(y) = s'\cosh(\beta_3 y/2a_{TF}) \qquad (10)$$

where s' is a constant. This is similar to the experimental stopping power except for the constant term $(s_o - s_1)$, which is supposed to be due to the electronic scattering with valence electrons. This may be the first experimental position dependent stopping power at a surface of solid.

Angular distribution of reflected ions (4)

When ions are reflected at a single crystal surface at glancing angle incidence, the ions experiences a series of correlated small angle scattering with surface atoms. To describe this scattering process, we first assume that the ions travel along the trajectories defined by the continuum surface planar potential. We then assume that the nuclear and electronic scattering give rise to the small angle deflection form these trajectories. Each scattering events are assumed to occur randomly along the ion trajectory. The multiple scattering can be formulated

with a stochastic theory. (11,12)

Let Θ be the deflection angle of ion from the trajectory defiend by the continuum potential, and $W(z,\Theta,\phi)d\phi$ be the probability that an ion, having a deflection angle Θ, is deflected $(\phi, \phi+d\phi)$ after travelling a unit distance at z. This probability depends on z, i.e. y(z), where the y-axis is parallel to the surface normal and the incident ion lies on the yz-plane. The stochastic equation for $f(z,\Theta)d\Theta$, the probability of finding an ion in $(\Theta,\Theta+d\Theta)$ at z, is expressed as

$$\partial f(z,\Theta)/\partial z = \int d\phi \left\{ W(z,\Theta,\phi)f(z,\Theta)+W(z,\Theta+\phi,-\phi)f(z,\Theta+\phi)\right\} \qquad (11)$$

where the energy loss of ion is neglected. If we assume that $W(z,\Theta,\phi)$ does not depend on Θ, $W(z,\Theta,\phi)$ reduces to $W(z,\phi)$. Thus the eq.(11) can be expanded into a series as

$$\partial f(z,\Theta)/\partial z = \sum_{n=1}^{\infty} (1/n!) \sum_{l=0}^{n} M^{x}{}_{l}(z) M^{y}{}_{n-1}(z) \partial^{n} f(z,\Theta)/\partial \Theta_x{}^{l} \partial \Theta_y{}^{n-l}, \qquad (12)$$

where

$$M^{i}{}_{l}(z) = \int W(z,\phi)\phi_i{}^{l} d\phi , \qquad (i = x,y) . \qquad (13)$$

When the terms with $n>2$ are neglected in eq.(12), a diffusion equation is derived;

$$\partial f(z,\Theta)/\partial z = K_z(z)\, \partial^2 f(z,\Theta)/\partial \Theta_x{}^2 + K_y(z)\partial^2 f(z,\Theta)/\partial \Theta_y{}^2, \qquad (14)$$

where

$$K_i(z) = (1/2) \int W(z,\phi)\phi_i{}^2 \, d\phi \qquad (i = x,y) . \qquad (15)$$

This can be solved with an initial condition that $f(-\infty,\Theta) = \delta(\Theta)$ as

$$f(z,\Theta) = 1/2\, \sigma_x \sigma_y \exp(-\Theta_x{}^2/2\sigma_x{}^2 - \Theta_y{}^2/2\sigma_y{}^2) , \qquad (16)$$

where

$$\sigma_i{}^2 = 2 \int dz K_i(z) , \qquad (i = x,y). \qquad (17)$$

The probability $W(z,\Theta,\phi)$ contains the nuclear and electronic scattering contributions. The nuclear scattering is due to ion-atom collision, mostly atoms displaced from their equilibrium positions by thermal vibration. For an atom displaced at r and an ion at y from the surface, the defelction angle due to their collision is approximately expressed as

$$\phi^2 = (\gamma \Phi(R)/\partial R)^2 r^2 \cos^2\alpha + \phi(R)^2 r^2 \sin^2\alpha / R^2 , \quad (18)$$

where R is the impact parameter of the collsion. The diffusion coefficent is then become

$$K_i(z) = 1/2 \int dr d\alpha di \, \Phi^2 (i/R)^2 \, n_p \, g(r,\alpha), \quad (i = x,y), \quad (19)$$

where $g(\alpha,r)$ is the distribution of the position of vibrating atoms. If $g(r,\alpha)$ is approximated to a gaussian distribution, the integration in eq.(18) can be performed and the numerical diffusion coefficients are obtained.

The deflection due to electronic scattering can be related to the energy loss of the ion.(13) If the impulse approximation is used, the scattering angle is related to the energy loss E, ion energy E, electron mass m and ion mass M by

$$\phi^2 = m \Delta E / ME \quad (20)$$

With the use of this relation ,the contribution of electronic scattering to σ_x and σ_y are calculated.

The calculated FWHM of the angular distributions of scattered ions are shown in Figs.7 and 9 at 0.7 MeV He and proton incidence. For the thermal vibration of atoms, Debye temperature θ_D = 155K is used. As the nuclear scattering has small contribution to the FWHM at smaller glancing angles, while the electronic scattering has almost constant contribution to the FWHM as shown in Figs 7 and 9. Total FWHM, i.e. the sume of nuclear and electronic contributions, is also shown by thin solid line.

The agreement between the experimental and calculated FWHM's is poor. This is improved by taking larger displacement of atoms due to thermal vibration. Good agreement can be obtained when the Debye temperature of surface atoms to be 72 ± 6 K. The modified total FWHM is shown by thick solid line in Fig. 9.

In the present experimental analysis, we could determine the thermal vibration of surface atoms. In comparison with the surface peak analysis in RBS/channelling method, present method is advantageous, because we can study only the ion scattering by surface atoms, while in the RBS/-channelling method it is difficult to eliminate the scattering at sub-surface atoms. The present analysis has the potentiality to study the thermal vibration of the second layer atoms by the analysis of second peak of the energy spectrum.

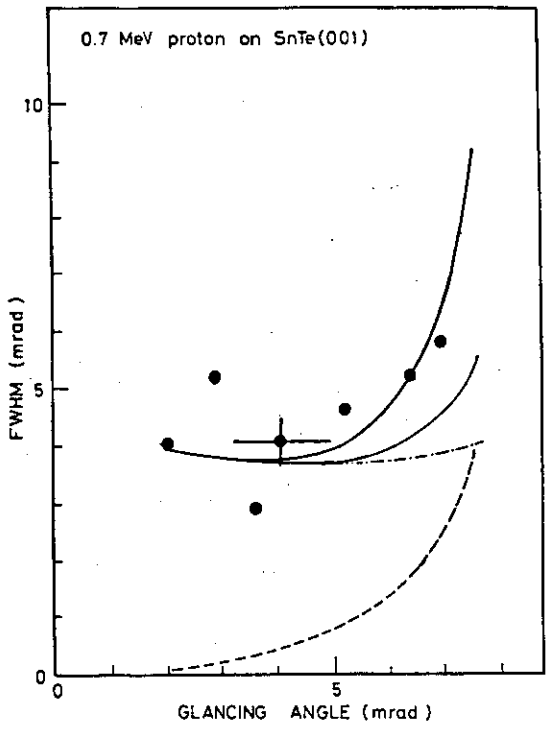

We are grateful to the members of Department of Nuclear Engineering of Kyoto University for the use of the 4MV Van de Graaff accelerator. This study was supported by the Special Grant-in-Aid for Scientific Research on Interaction of Ion Beam with Solids from the Ministry of Education, Sceince and Culture.

Fig.9 FWHM of the angular distribution of scattered protons.

References

(1) K.Morita: Radiat. Eff. 52 (1980) 235.
(2) M.Hou & C.Varelas: Appl.Phys. A33 (1984) 121.
(3) M.Mannami, K.Kimura, K.Nakanishi & A.Nsihimura: Nucl. Instrum & Methods Phys. Res. B13 (1986) 587.
(4) K.Kimura & M.Mannami: Nucl. Instrum. & Methods Phys. Res. in press.
(5) K.Kimura, M.Hasegawa & M.Mannami: Phys. Rev. in press.
(6) K.Kimura & M.Mannami: Surf. Sci. in press.
(7) A.A.Lucas: Phys. Rev. B20 (1979) 4990.
(8) R.Kawai, N.Itoh & Y.H.ohysuki: Surf. Sci. 114 (1982) 137.
(9) O.S.Oen & m.T.Robinson: Nucl. Instrum. & Methods 132 (1976) 647.
(10)M.T.Robinson: Phys. Rev. 179 (1969) 327.
(11)C.W.Gradiner. Handbook of Stochastic Methods for Physics, Chemistry, Natural Science (Springer Verlag, 1983) p42.
(12)T.Oshiyama & M.Mannami: Phys. Lett. A81 (1981) 43.
(13)J.Lindhard: K.Dans.Vidensk.Selsk. Mat-Fys. Medd. 34 (1965) no.14.

I.6 RADIATIVE ELECTRON CAPTURE IN HEAVY ION AND He COLLISIONS

Kiyoshi KAWATSURA, Akio OOTUKA*, Masao SATAKA, Ken-ichiro KOMAKI*, Yasuaki SUGIZAKI, Hiroshi NARAMOTO, Kunio OZAWA**, Yohta NAKAI and Fuminori FUJIMOTO*

Department of Physics, Japan Atomic Energy Research Institute, * College of Arts and Sciences, University of Tokyo, ** Energy Research Laboratory, Hitachi Ltd.

The X-ray spectra emitted during the radiative capture of target electrons into the projectile K shell have been measured under single collision conditions for a He gas target. The experiment was performed for 40 - 76 MeV F^{q+}(q=8,9) and 120 - 175 MeV Cl^{q+}(q=16,17) ions. The centroid energies of the radiative electron capture (REC) X-rays have been found to be in good agreement with the calculated ones. It is also confirmed that the widths of the REC X-ray distributions for Cl^{17+} ion impact are in good agreement with the simple model calculations.

Introduction

Radiative electron capture (REC) in fast ion-atom collisions was first observed by Schnopper et al.(1). Since then, many investigations of REC processes have been reported. Most of the experimental REC data has been accumulated by using either solid target or gas target cell with entrance window. The REC X-ray spectra consist of the emissions from the different charge states of the projectile ions during collisions. Therefore, the observed data should be corrected to obtain the real REC X-ray spectra. The experiments should be carried out under single collision conditions to compare directly experimental data with the theoretical calculations.

With regard to the He gas target, the REC X-ray spectra have been measured by Kienle et al.(2) (160 - 250 MeV N, 140 MeV Ne and 288 MeV Ar), Sohval et al.(3) (45 - 65 MeV O), Kawatsura et al.(4) and Tawara et al.(5) (15 - 40 MeV F^{8+} and F^{9+}), and Kambara et al.(6) (110 MeV Ne). All experiments are in poor agreement with each other. In the present work,

we extended our REC data under single collision conditions of F^{8+} and F^{9+} ions incident on a He gas target to higher energies (40 - 76 MeV) and to heavier projectile ions (120 - 175 MeV Cl^{16+} and Cl^{17+}).

Experiments

The present experiment was performed using the tandem accelerator at Japan Atomic Energy Research Institute (JAERI). Beams of highly ionized fluorine (F^{8+} and F^{9+}) and chlorine (Cl^{16+} and Cl^{17+}) were accelerated to energies ranging from 40 to 76 MeV, and 120 to 175 MeV , respectively. A collision chamber contained a single nozzle for target gas jet and was connected to the beam line through the differential pumping system of turbomolecular pumps. The base pressure of the beam line and collision region was less than 2×10^{-7} Torr. The relative pressure of target gas was monitored with a B-A gauge, which was from 0 to 6×10^{-4} Torr. A test for single collision conditions was performed by observing the characteristic K X-ray and REC X-ray intensities as a function of pressure at each energy and charge state of the incident projectiles. In the present experiment, the pressure in the collision chamber was about 5×10^{-4} Torr for all measurements.

The characteristic K X-rays and the broad REC X-rays were observed with a HORIBA Si(Li) X-ray detector which had a 220 Å Au electrical contact layer and a 0.2 μm Si dead layer in addition to a 15 μm Be window. The detector was placed at 90° to the beam direction. The X-rays were collimated with a graphite cap with a hole of 5 mm in diameter. An energy calibration was made by using standard sources of Mn Kα and Kβ X-rays and Cu Kα and Kβ X-rays. The energy resolution was about 170 eV (FWHM at 5.9 keV). The X-ray count rates were kept below 80 /sec to avoid spectral distortion due to pulse pile-up.

Results and discussion

In the previous work(4,5), one of us (Kawatsura) have measured the X-ray spectra from the REC process to projectile K shell under single collision conditions for F^{8+} and F^{9+} ions incident on a He gas target in the collision energy range of 15 to 40 MeV. Using the same projectile ion and target, we extended our measurements to higher energy range of 40 to 76 MeV. Fig. 1 shows the X-ray spectra from F^{8+} and F^{9+} ions incident

on a He gas target at 76 MeV (4 MeV/amu). Two overlapping peaks at about 0.8 keV and 1.0 keV correspond to the K X-ray lines which have energies expected for transitions in hydrogen-like ions (F^{8+} ions). The former peak (at 0.8 keV) was due to the 2p - 1s transition and the latter peak (at 1.0 keV) was a superposition of the lines from the np - 1s transitions ($n > 2$). For bare ion impact (F^{9+} ion), the hydrogen-like X-ray transitions were caused by the electron capture into excited states of the projectiles. For one-electron ion impact (F^{8+} ion), on the other hand, the hydrogen-like X-ray transitions were caused by the electron excitation of the projectile K shell. The helium-like X-ray transitions caused by the electron capture were not observed. The cross section for electron excitation is much larger than that for electron capture at high energy. The broad peak around 3 keV corresponds to the radiative capture of bound electrons from He atom into the K-shell of the bare or one-electron ions (REC X-rays). The photon energy of the REC process is given as (7)

$$\hbar\omega = \varepsilon_f - \varepsilon_i + (1/2)mv_0^2 + \vec{v}_0 \cdot \vec{P} = \varepsilon_f - \varepsilon_i + (m/M)E_0 + mv_0 v_{iz} \qquad (1)$$

where $\hbar\omega$ is the energy of the REC X-rays, ε_f the binding energy of the electron in its final state, ε_i the initial electron binding energy, m the electron mass, M the mass of the projectile, E_0 the energy of the projectile ion, $\vec{v}_0$ the projectile velocity, $(1/2)mv_0^2$ the kinetic energy of the target electron viewed in the frame of the projectile due to the motion of the projectile, $\vec{P}$ the momentum of the electron due to its presence in a target atomic orbital, and v_{iz} the velocity component parallel to the incident projectile direction of the electron to be captured. Radiative electron capture is the capture of target electrons into bound states of the projectiles. An analogous process is the capture into continuum state of the projectiles (Primary Bremsstrahlung, PB). This process is predominant when the photon energy is less than $T_0 = 1/2mv_0^2$. The cross section for PB decreases strongly when the X-ray energy exceeds T_0, which is about 2.2 keV for 76 MeV (4 MeV/amu) F ion impact. In this case, the K REC X-ray spectra is overlapped mainly with the PB X-ray spectra and partly with the L REC X-ray spectra as shown in Fig. 1. The similar results have been observed for high energy O ion impact(3) and Ne ion impact(6). In order to avoid overlapping between REC and PB, we extended our measurements of the REC X-ray spectra towards the heavier projectiles. Fig. 2 shows the X-ray spectra for Cl^{16+} and

Cl^{17+} ion incident on a He gas target at an energy of 140 MeV (4 MeV/amu), which is the same velocity as 76 MeV F^{8+} and F^{9+} ions. The REC X-rays (at about 6 keV) are found far from the PB X-rays which are overlapped by the Cl K X-ray spectra. The characteristic K X-ray spectra for Cl ion impact are also different from those for F ions. The velocity of Cl projectiles is lower than that of the 1s electron of the projectile Cl ions. The cross section for electron excitation is less than that for electron capture process. It is found for the Cl^{16+} ion impact that the X-ray emissions through the electron capture into excited states of projectile ions ($1s2p - 1s^2$, $1snp - 1s^2$) are predominant. The X-rays through the electron excitation of the projectile ions ($2p - 1s$, $np - 1s$) are also observed, but less intensive.

The centroid energy of the REC X-rays which changes with the projectile energy is given as

$$\hbar\omega = \varepsilon_f - \varepsilon_i + (1/2)mv_0^2 = \varepsilon_f - \varepsilon_i + (m/M)E_0. \qquad (2)$$

In the present measurements, ε_f and ε_i correspond to the binding energies of the 1s electrons of the projectile ions and He atoms (24.5 eV). The 1s binding energies for hydrogen-like F and Cl ions are 1.103 keV and 3.946 keV, and those for helium-like F and Cl ions are 0.954 keV and 3.659 keV, respectively. The experimental and calculated data for the REC centroid energy are shown in fig. 3 and 4 as a function of the projectile energy. The experimental results are, generally speaking, in good agreement with the calculated ones. Our previous data(4,5) seem to be confirmed by this experiments. In the case of the Cl ion impact, the experimental results for the REC centroid energy are systematically about 40 eV lower than the calculated ones. Kienle et al.(2) have also found that the observed centroid energies were lower than the calculated ones by 300 eV for 140 MeV Ne^{10+} on He and by 50 eV for Ar on He. They explained that these differences were probably due to screening effects. The energy shift for Ne ion impact seems to be too large. More accurate experiment and more reasonable explanation are necessary.

The full width at half maximum (FWHM) of the REC X-rays is given by Sohval et al. (3) as

$$\Gamma_{REC}(FWHM) = 2.04\ (T_0 T_i)^{1/2}. \qquad (3)$$

T_0 is $(1/2)mv_0^2$ and T_i the kinetic energy averaged of the target electron. In fig. 5 shown are the experimental results of FWHM of the REC X-rays for

Cl^{17+} ion impact on a He gas target as a function of the projectile energy. The results of the previous work and theoretical calculations are also shown in fig. 5. The present data are in better agreement with the calculated ones than those obtained by the previous experiments(3-6). They have used relatively light ion projectiles (O, F and Ne). The REC X-ray spectra were more complicated as shown in fig. 1 . It is , therefore, very difficult to deduce proper spectra of REC X-rays from the experimental data. Our present results are considered to be more precise. In addition to energy dependence of Γ_{REC}(FWHM) of the REC X-rays, charge state dependence was also measured. The results of Γ_{REC} for Cl^{16+} ion impact are about 5 % smaller than those for Cl^{17+} ion impact. These results are very similar to those of our previous work(4,5). Our recent experimental results of Γ_{REC} for different projectile ions (Si and S) at higher energies ($\geq$ 5.5 MeV/amu) deviate to smaller values from the calculated ones. The measurements of the REC X-ray spectra for Cl projectiles at higher energies are now in progress.

References

(1) H.W. Schnopper, H.D. Betz, J.P. Delvaille, K. Kalata, A.R. Sohval, K.W. Jones and H.E. Wegner: Phys. Rev. Lett. 29 (1972) 898.

(2) P. Kienle, M. Kleber, B. Povh, R.M. Diamond, F.S. Stephens, E. Grosse, M.R. Maier and D. Proetel: Phys. Rev. Lett. 31 (1973) 1099.

(3) A.R. Sohval, J.P. Delvaille, K. Kalata, K. Kirby-Docken and H.W. Schnopper: J. Phys. B9 (1976) L25.

(4) K. Kawatsura, H. Tawara and P. Richard: IEEE Trans. Nucl. Sci. NS-28 (1981) 1053.

(5) H. Tawara, P. Richard and K. Kawatsura: Phys. Rev. A26 (1982) 154.

(6) T. Kambara, Y. Awaya, A. Hitachi, M. Kase, I. Kohno and T. Tonuma: J. Phys. B15 (1982) 3759.

(7) M. Kleber and D.H. Jakubassa: Nucl. Phys. A252 (1975) 152.

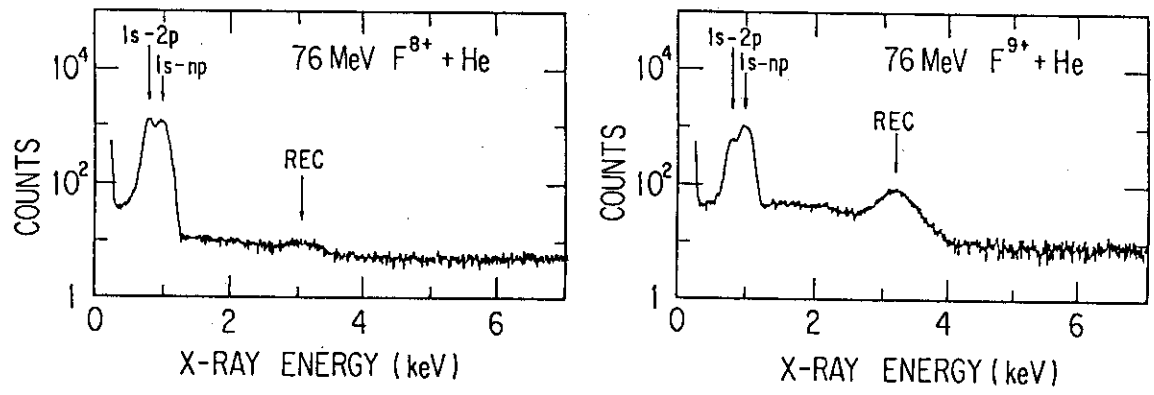

Fig. 1 The X-ray spectra obtained from 76 MeV F^{8+} and F^{9+} ions incident on a He gas target.

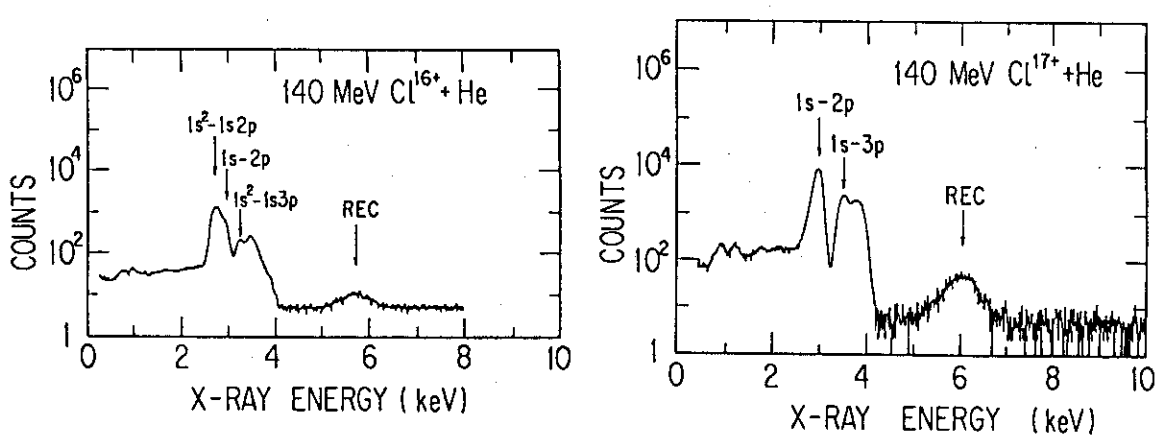

Fig. 2 The X-ray spectra obtained from 140 MeV Cl^{16+} and Cl^{17+} ions incident on a He gas target.

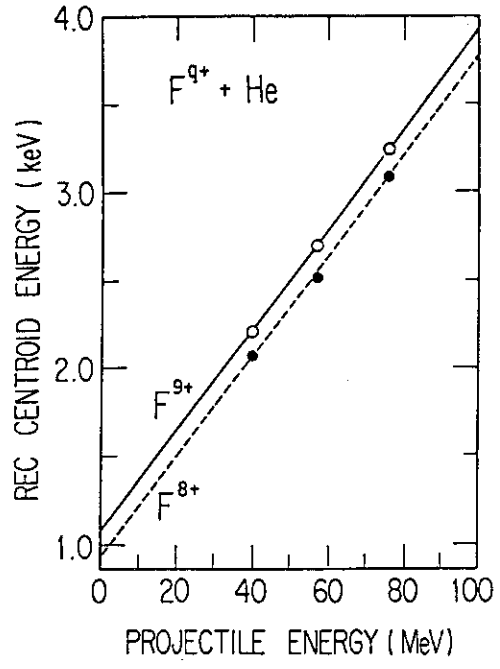

Fig. 3 Centroid energy of the observed REC X-rays from F^{8+} and F^{9+} ions incident on a He gas target as a function of the projectile energy. The solid and dashed lines are calculated ones from eq. (2).

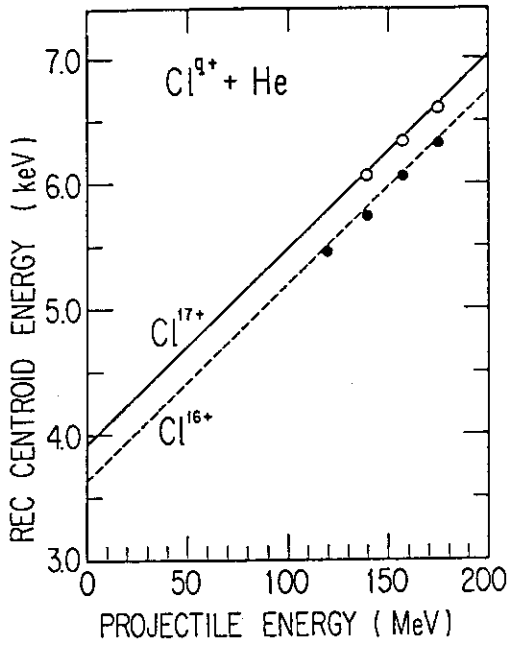

Fig. 4 Centroid energy of the observed REC X-rays from Cl^{16+} and Cl^{17+} ions incident on a He gas target as a function of the projectile energy. The solid and dashed lines are calculated ones from eq. (2).

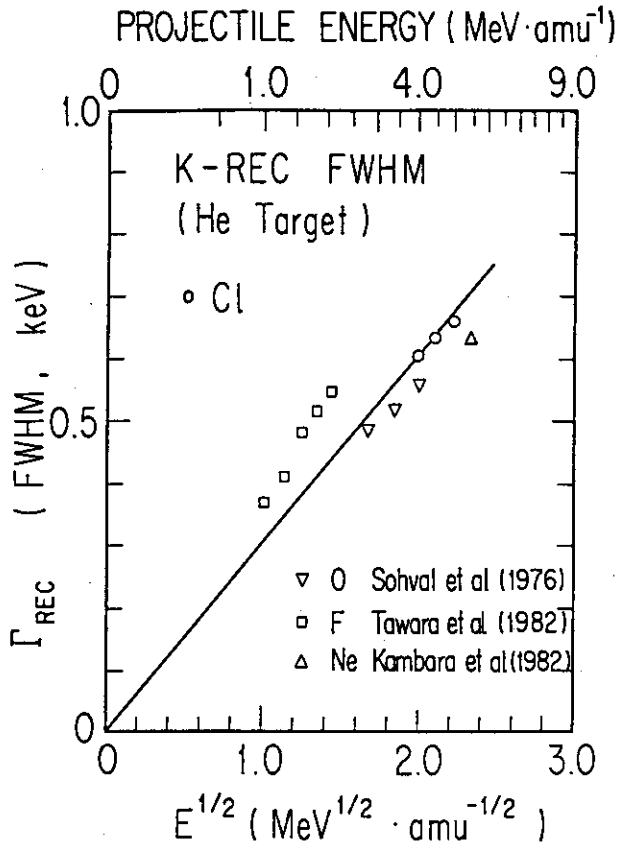

Fig. 5 Full width at half maximum (FWHM) of the REC X-rays from Cl^{17+} ions incident on a He gas target. The solid line is calculated one from eq. (3).

I.7 Z_T OSCILLATION OF ELECTRON CAPTURE CROSS SECTION

Fumio FUKUZAWA

Department of Nuclear Engineering, Kyoto University, Kyoto, 606 Japan

Equilibrium mean charges of H and ^{4}He ions emerging from solids were measured for many kinds of target materials, and were found to show oscillatory dependence on target atomic number. This oscillation was found to originate from the Z_t oscillation of electron capture cross section. Even for very fast $^3He^{2+}$ ions, Z_t oscillation of electron capture cross section was recognized.

1. Introduction

It was shown by Phillips [1] for the first time experimentally that the equilibrium charge ratio of hydrogen ions emerging from solids differ significantly for different materials. In his experiment, fresh material was evaporated on the exit side of a target foil just before measurement. The change of charge ratio with time after evaporation was shown to be due to the growth of the surface contaminating layer which may be carbon containing molecules or oxides. In order to see the target dependence of charge ratio of emerging ions, therefore, the surface of the target must be clean. The use of foils as the targets with fresh surfaces limits the kind of materials. Then, for many years after Phillip's experiment, there were only insufficient data to discuss about the material dependence of charge ratio of emerging ions.

In our laboratory, a simple method to measure charge ratio with thick targets was developed [2]. This method uses a combination of electric (or magnetic) deflection field and a position sensitive solid state detector, and can analyze the charge ratio of scattered ions with continuous energy distribution. The use of thick targets allows us to use all solid materials without difficulty and makes suface cleaning very easy. With this method, many data of charge ratio of emerging He ions were systematically accumulated in MeV energy region, and the target material dependence of

charge ratio was clarified over the wide range of target atomic number for the first time.

Similar target dependence of charge ratio of H ions with relatively low energy was also observed. In high energy region, the electron capture cross sections of $^3He^{2+}$ ions for various target materials have been measured to see the target dependence.

In the followings, the physical basis of the target dependence of charge ratio is considered, and experimental data are compared with simple theoretical calculations.

2. Theoretical target dependence of mean charge of fast ions

Equilibrium mean charge is determined by the electron capture and loss cross sections of ions passing through media. This is true for light ions such as H and He ions, because there are no significant contribution of excited states of these ions in determining charge ratios. Because there are no density effect for these ions, the data with gas targets and with solid targets can be treated indiscriminately. To see simply the origin and behavior of the target dependence, semiclassical models for the loss and capture processes are useful.

Target dependence of the electron loss cross section based on Bohr model[3] is given by the following relation,

$$\sigma_{loss} = C(E) Z_t^{2/3} \qquad (1)$$

where Z_t is target atomic number, and C(E) is a constant depending on collision energy E. The value of C(E) was determined by comparing with known experimental values of loss cross sections for gas and vapor targets ranging over the wide range of target atomic number.

In contrast to the monotonic target dependence of the electron loss cross section, the electron capture cross section is expected to show an interesting oscillatory behavior of target dependence, which can be seen obviously by using the Bohr-Lindhard model[4]. In this model, the electron capture process is divided into two processes; the release of an electron from the target atom by the Coulomb force of the incident ion, and the capture of this released electron by the incident ion. In order to release an electron from the target atom, the incident ion must approach to it within the release distance R_r determined by the following relation,

$$qe^2/R_r^2 = mu^2/a \quad , \qquad (2)$$

where q is the charge number of the incident ion, m is the electron mass

and, u and a are orbital velocity and orbital radius of an electron under consideration. The released electron is assumed to has no relative velocity with the target atom and, therefore, to move with the same velocity V of the incident ion relative to this incident ion. In order to capture this electron, the incident ion must be within the distance from the target atom less than the capture distance R_c determined by the following relation,

$$qe^2/R_c = mV^2/2 \quad . \tag{3}$$

In the case of $R_r < R_c$, the release process takes place under the condition that the incident ion can capture this electron. The capture cross section is given by the following formula,

$$\sigma_{cap} = \pi R_r^2 \quad . \tag{4}$$

While, in the case of $R_r > R_c$, the incident ion cannot capture the released electron at the distance of R_r, and the electron capture cross section becomes zero. In actual case, however, the above two processes are not instantaneous but gradual ones. By taking into consideration of these facts, the capture cross sections are given by the following modified formulae,

$$\sigma_I = \varepsilon \pi R_r^2 \qquad \text{for } R_r < R_c \ , \tag{5}$$

$$\sigma_{II} = \varepsilon \pi R_c^2 \beta [(R_c/V)/(a/u)] \qquad \text{for } R_r > R_c \ , \tag{6}$$

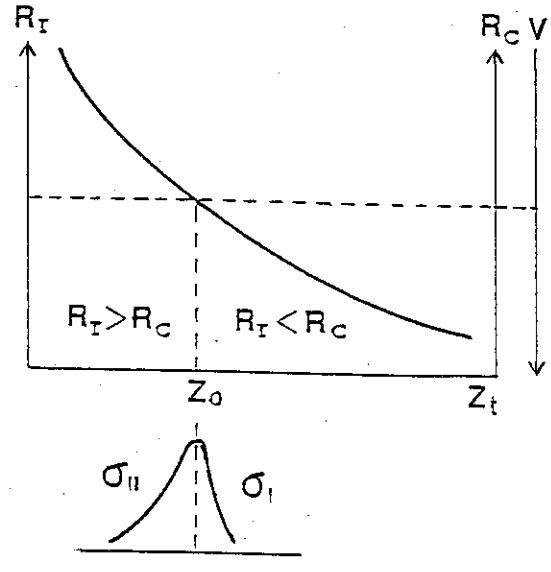

Fig. 1 The relations of the release radius R_r vs target atomic number Z_t and the capture radius R_c vs the velocity V of the incident ion. At the target number Z_o, where R_r is equal to R_c, the electron capture cross section is maximum.

where ε is the capture probability of the release electron and β is the timing factor corresponding to gradual loss and capture processes. Two constants ε and β are used for adjustable parameters in the comparison with experimental data [5]. Continuous distribuations of the values of u and a obtained by the Thomas-Fermi atomic model give only monotonic general trend of target dependence of th e capture cross section. If the discrete values of u and a are used,however, the capture cross section will show the target dependence with some structure other than monotonic dependence.

In fig. 1 is depicted schematic-

ally the relation of R_r vs Z_t for a given shell electron of the target atom. The value of R_c is independent of Z_t, and is determined by the charge number q and the velocity V of the incident ion. The values of R_r and R_c become equal for the target atom of atomic number Z_o. For the target with Z_t less than Z_o, R_r is larger than R_c. The capture cross sections for these targets are calculated by σ_{11}, which varies as Z_t^2 for the K shell electron. While, for the target with Z_t larger then Z_o, R_r is smaller than R_c. For these targets, the capture cross sections are calculated by σ_1, which varies as Zt^{-3} for the K shell electron. Therefore, the capture cross section for this shell electron becomes maximum for the target of atomic number Z_o. This phenomena correspond to the so-called "velocity matching".

There are many electron shells in the target atom. For given energy of the incident ion, "velocity matching" of each shell electron takes place at definite target atomic numbers. The Z_t oscillation of electron capture cross section will be observed as a result of these "velocity matching"s. In fig. 2, the release radius and the capture radius calculated by eqs. (2) and (3) for the incident He^{2+} ion are depicted for all target shell electrons. Orbital electron velocities were estimated from the binding energies [6], and orbital radii were determined as the positions of maxima of the electron probability densities [7]. For 1 MeV He^{2+} ion, for example, the capture cross section has peak values at the target numbers corresponding to the crossings of these curves and the horizontal line passing the energy scale of 1 MeV. For other incident ions with different charge number and velocity, the radius scale should be shifted by considering the relations, $R_r \propto q^{1/2}$ and $R_c \propto q/(T/A)$, where T/A is the incident energy per nucleon.

The equilibrium mean charge q of ions with only two charge states is expressed as a function of σ_{cap} and σ_{loss};

$$q = q_o + (\sigma_{cap}/\sigma_{loss} + 1)^{-1} , \qquad (7)$$

where q_o is the charge number of the lower charge state. Eq.(7) is applicable, in practice, to H and He ions with velocities larger than Bohr velocity. As the σ_{loss} changes only monotonically with Z_t, the equilibrium mean charge q of ions is expected to show the Z_t oscillation with just opposite phase to that of σ_{cap}.

3. Experimental observation of Z_t oscillation

3-1 Equilibrium mean charge of He ions

Equilibrium charge fractions of backscattered He ions from thick solid targets were measured for many kinds of material. The method of measurement is described in detail in the previous papers [2,8]. Surface cleaning was made by raising target temperature [9,11], and by evaporating fresh material continuously during measurement [10,11]. By combining these data and the mean charges calculated by eq.(7) with experimental cross sections σ_{cap} and σ_{loss} for gas and vapor targets, target dependence of the equilibrium mean charge of He ions was clarified. As a typical example, in fig. 3, the mean charges of 1.0 MeV He ions are plotted as a function of Z_t. A solid curve in this figure is theoretical mean charge calculated by eq. (7) with the cross sections σ_{cap} and σ_{loss} of eqs.(5), (6) and (1). The parameters ε and β were chosen so as to obtain good fit to the experimental data: ε = 0.5 and β = 4. Good reproduction of experimental oscillation means that the shell structure of the target atom plays an important role in the electron capture process as has been described in section 2. In the energy range of 0.6-2.5 MeV, similar results were obtained. Further, theoretical capture cross sections calculated by the OBK approximation [12] and by the two state atomic expansion method [13] were found to give similar Z_t oscillation.

3-2 Equilibrium mean charge of H ions [14]

For H ions with energies larger than several tens keV, dominant charge states are H^0 and H^+. In this case, measurement of charge fractions is rather simple; the energy spectra of scattered H ions from a thick target with and without magnetic field in the path of definite scattering direction are measured for the same amount of incident H beam. The former is due only to H^0 fraction and the latter contains all fractions of H^0 and H^+. From these two spectra, each fraction of H^0 and H^+ is obtained as a function of energy.

In fig. 4, as a typical example, are plotted the equilibrium mean charges of 50 keV H ions emerging from various targets. A solid curve in this figure is theoretical one calculated similarly as the case of He ions . For comparison, the theoretical mean charge with σ_{cap} calculated by OBK approximation is drawn as a dotted curve. The Z_t oscillation of target dependence is clearly seen, and the amplitude and the phase of this

oscillation are, as a whole, fairly in good agreement between experiment and theory. With increasing the energy of H ions, the amplitude of Z_t oscillation of the mean charge was found to decrease just as was expected.

3-3 Electron capture cross section of very fast $^3He^{2+}$ ion [15]

The $^3He^{2+}$ ion from the AVF cyclotron of RCNP was used for measurement of the electron capture and loss cross sections in collisions with different kinds of target foils. The energies of ^3He ions were 52, 62 and 72 MeV. Because the capture and loss cross sections are very small for such high energy, incident ^3He ions suffer only single collisions in thin target foils. The surface contaminating layer is not important in this case. Then, the growth curve method with various thicknesses of the target foils give the electron capture and loss cross secions.

Foils with different thicknesses were prepared by evaporating fresh materials of Cu, Ge, Ag, Sn, and Au on the carbon foils which were of same thickness. After passing through foil, $^3He^+$ ions were separated from $^3He^{2+}$ ions with a magnetic field and were counted for given amount of $^3He^{2+}$ beam . By applying least square fitting to the growth curve of the yield of $^3He^+$ ions, the electron capture and loss cross sections were determined.

As a typical example, in fig.5, the electron capture cross sections for 52 MeV $^3He^{2+}$ ions are plotted as a function of target atomic number. The dotted curves in this figure are the OBK calculation for different electron shells of target atoms, and the solid curve is the total of these cross sections. In order to obtain agreement of absolute values, experimental cross sections were multiplied by 4 in this figure. The Z_t oscillation is not conspicuous, but can be observed significantly just as expected by theoretical calculation.

4 Conclusions

Equilibrium mean charges of H and He ions were measured for many kinds of target materials, especially for solid targets with clean surfaces, and were found to change oscillatorily with target atomic number Z_t. This Z_t oscillation originates from the so-called "veloity matching" in the electron capture process, and reflects the electron shell structures of target atoms. This interpretation is supported by comparing the experimental target depencence with the theoretical calculation of mean charges taking

into account the atomic structure. Good agreements between theory and experiment were obtained over the wide range of incident energy; 50 keV/A ～ 24 MeV/A.

This work was supported in part by the Special Project Research on Interaction of Ion Beams with Solids from Ministry of Education, Science and Culture.

References

[1] J.A.Phillips, Phys. Rev. 97 (1955) 407
[2] F.Fukuzawa, Phys. Lett. 43A (1973) 147
[3] N.Bohr, K. Dansk. Vidensk. Selsk. Mat.-F;ys. Meddr. 8 (1948) 18
[4] N.Bohr and J.Lindhard, K. Dansk. Vidensk. Selsk. Mat.-Fys.Meddr.28 (1954) 7
[5] A.Itoh, Y.Haruyama, Y.Kanamori, T.Kido and F.Fukuzawa, Bull. Inst. Chem. Res., Kyoto Univ. 60 (1982) 289
[6] W.Lotz, J. Opt. Soc. Am. 60 (1970) 206
[7] J.P.Desclau, At. Data Nucl.Data Tables 12 (1973) 311
[8] Y.Kido, M,Asari, A.Nakata and F.Fukuzawa, Nucl. Instrum. Meth. 143 (1977) 601
[9] Y.Kido, Y.Kanamori and F.Fukuzawa, Nucl. Instrum. Meth. 164 (1979) 565
[10] Y.Haruyama, Y.Kanamori, T.Kido and F.Fukuzawa, J. Phys. B: At.Mol. Phys. 15 (1982) 779
[11] Y.Haruyama, Y.Kanamori, T.Kido, A.Itoh and F.Fukuzawa, J. Phys. B: At. Mol. Phys. 16 (1983) 1225
[12] I.S.Dmitriev, N.F.Vorobiev, V.P.Zaikov, V.S.Nikolaev and Ya.A. Teplova, J. Phys. B: At. Mol. Phys. 15 (1982) L351
[13] T.Kaneko and Y.Ohtsuki, Phys. Status Solidi (b) 111 (1982) 491
[14] F.Fukuzawa, M.Yanagawa, M.Kushida, T.Ohdaira, M.Imai, K.Sonoki and Yan-Chin Jiang, to be published
[15] I.Katayama, H.Ikegami,K.Sugai, A.Aoki, Y.Haruyama, H.Ogawa, K.Yoshida and F.Fukuzawa, to be published

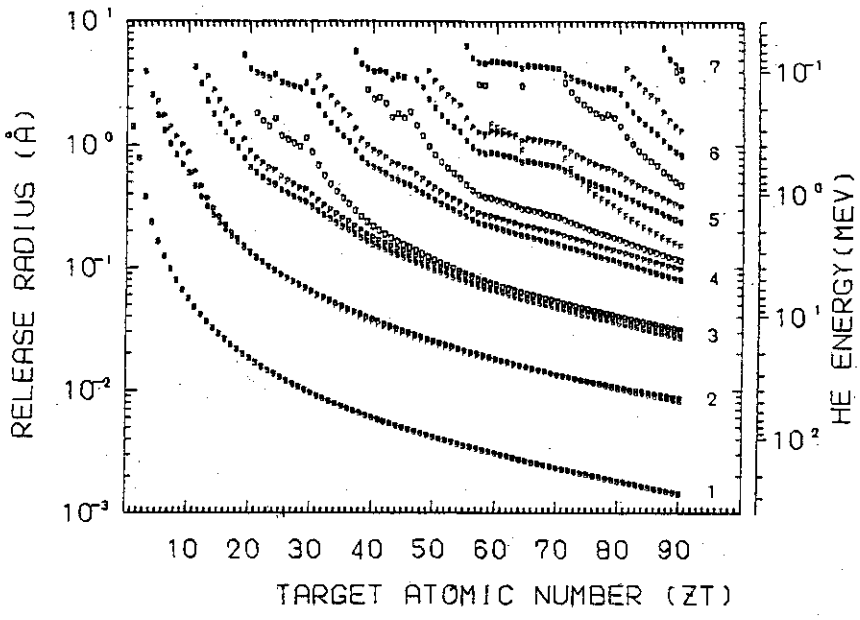

Fig. 2 Release radii for different target shell electrons for the incidence of He^{2+} ion. See text.

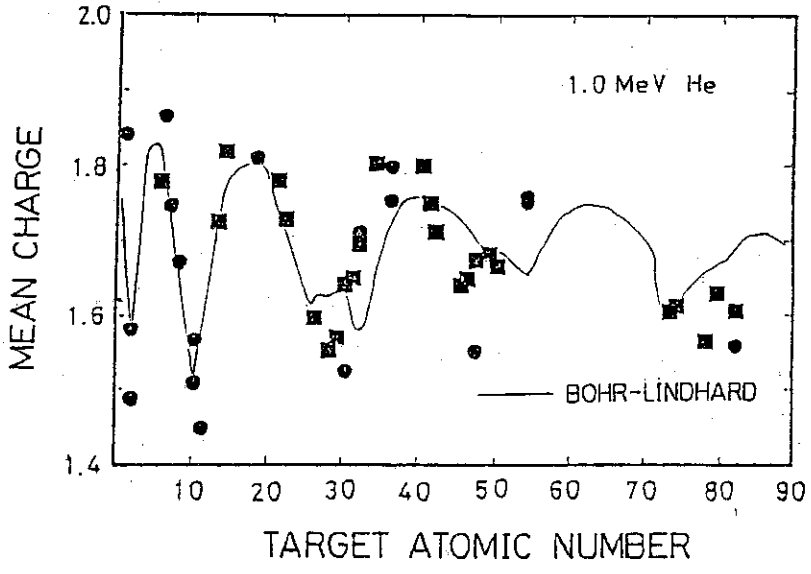

Fig. 3 Z_1 oscillation of mean charge of 1 MeV He ion. Circles are for gas or vapor targets, and squares are for solid targets.

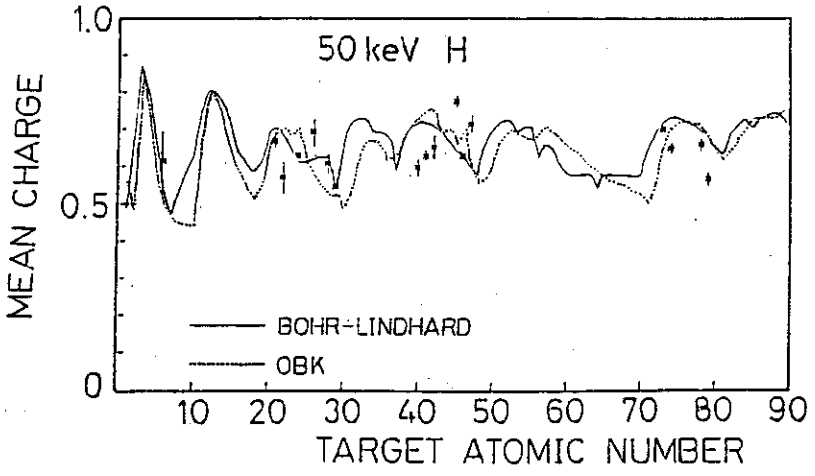

Fig. 4 Z₁ oscillation of mean charge of 50 keV H ion. A solid curve is theoretical one calculated by using Bohr-Lindhard capture cross section, and a dotted curve is that by using OBK approximation.

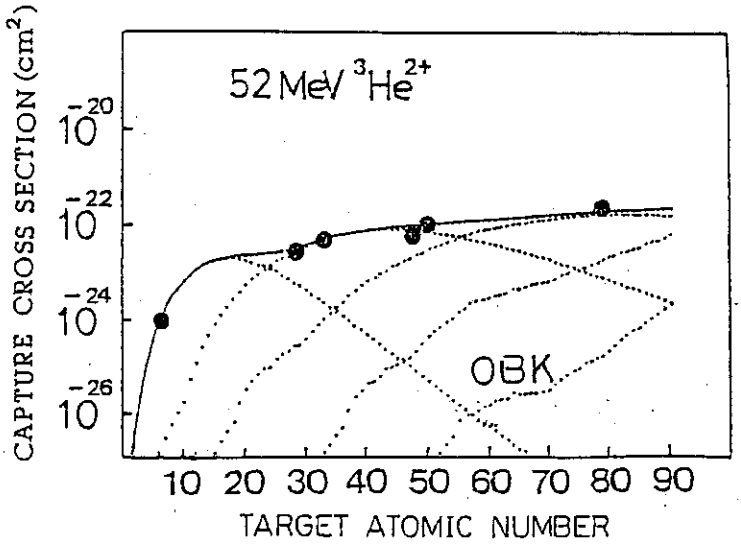

Fig. 5 Z₁ oscillation of the electron capture cross section of 52 MeV $^3He^{2+}$ ion. Dotted curves are calculated by OBK approximation for different electron shells of target atoms, and the solid curve is the total of these cross sections. Experimental points were multiplied by factor 4.

I.8 HIGH RESOLUTION EXPERIMENTS USING HIGHLY CHARGED RECOIL IONS PRODUCED BY TANDEM ACCELERATORS

Hiroyuki TAWARA

Institute of Plasma Physics, Nagoya University,
Nagoya 464

Abstract : Some of recent interesting experiments using highly charged recoil ions produced in energetic heavy ion collisions are described.

1 Introduction

Recently it has been confirmed that highly charged secondary recoil ions are copiously produced in energetic, heavy ion collisions with rare gas atoms or molecules. Their production mechanisms are also understood fairly well at least qualitatively. In such energetic heavy ion collisions, helium-like, hydrogen-like or even bare ions are observed with considerable intensities. For example, in 15.4 MeV/amu U^{75+} ion impact on Ar gas atoms, Ar^{18+} bare ions are produced. As shown in Fig.1, the high efficiencies of production of such highly charged recoil ions in ehavy ion impact are quite in contrast to those in electron or proton impact which are structureless.[1)]

These highly charged recoil ions have many features over highly charged ions with high velocities obtained from accelerators : low kinetic energy (usually less than a few eV, compared with a few MeV/amu ions provided directly from accelerato or a few MeV ions from recently developed sophisticated technique of Acceleration-Deceleration. This feature provides us many interesting and important consequences over high energy heavy ion beam which is commonly used in highly charged ion studies.

2 High precision measurements (ppm level) of transition energies --- comparison of recoil ion technique over beam foil technique or plasma source

The beam-foil spectroscopy (BFS) techniques are widely used in observing and investigating transitions of highly charged heavy ions where the emitted photons or electrons are observed at 90 degrees with respect to the beam direction. In BFS techniques, because of high velocities of ions (normally > 0.1 c), the Doppler broadening of the spectrum is the most serious limitation to the precision measurements of transition energies. In order to reduce the Doppler broadening, very narrow and long collimators are used which result in small yields in the observing transitions. See Fig.2(a)[2)] where an example of X-rays from $^3P_1$ and $^1P_1$ transitions of Ar^{16+} ions with the energy of 6 MeV/amu is shown. Note their statistics is not too good.

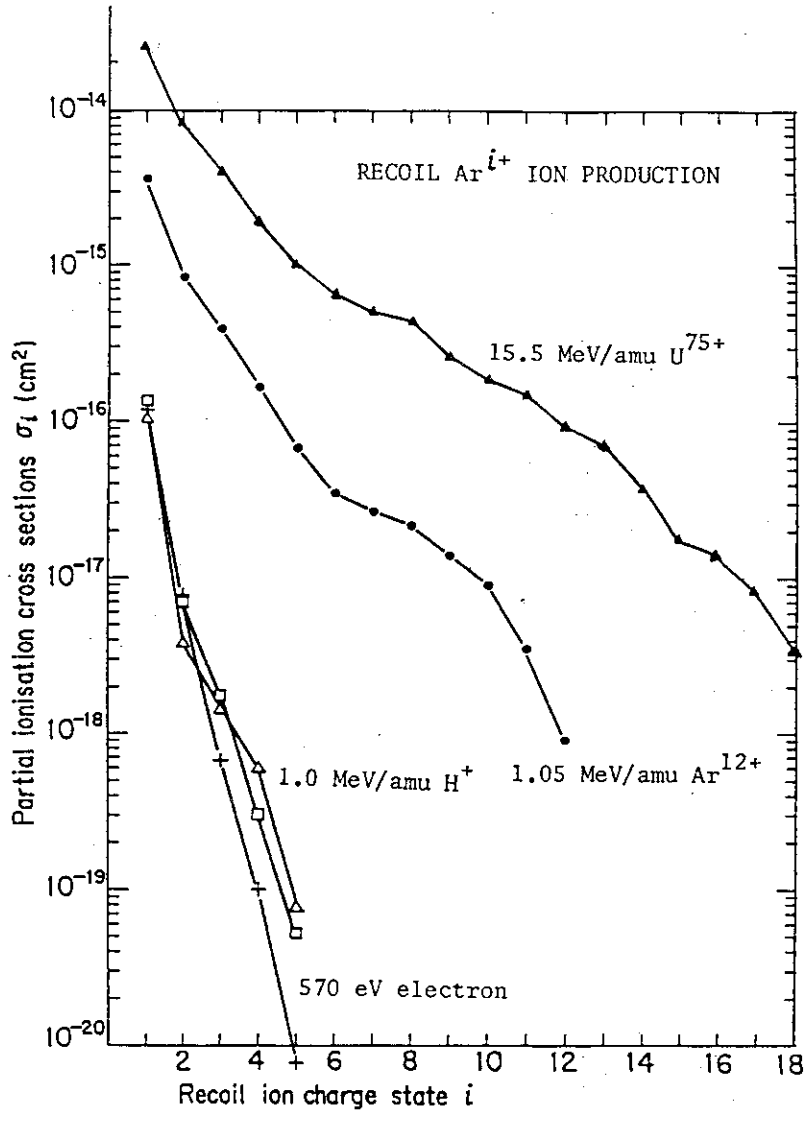

Fig. 1 Ar^{i+} recoil ion production cross sections for various projectiles as a function of the ion charge state.

As shown in the relationship

$$E_L = E_0(1 - \beta^2)^{\frac{1}{2}} / (1 - \beta\cos\theta)$$

where E_L and E_0 are the Doppler-shifted and unshifted transition energies, respectively, β is the ion velocity over the light velocity and θ is the observation angle with respect to the ion direction, further care should be exercised in order to reduce the uncertainties related with high velocities: i) precise setting of the observation angle θ (of the order of milli-degrees), ii) minimun ion energy straggling and iii) minimum ion beam divergence. Even with such cautions, serioud contribution, usually not easily controllable in many cases, can not be avoided from satellites due to the spectator electrons which depend upon the ion velocity and foil material. To minimize the satellite effects, some systematic observations should be made by varying the ion energy and the extrapolation to the zero energy is made. One of the

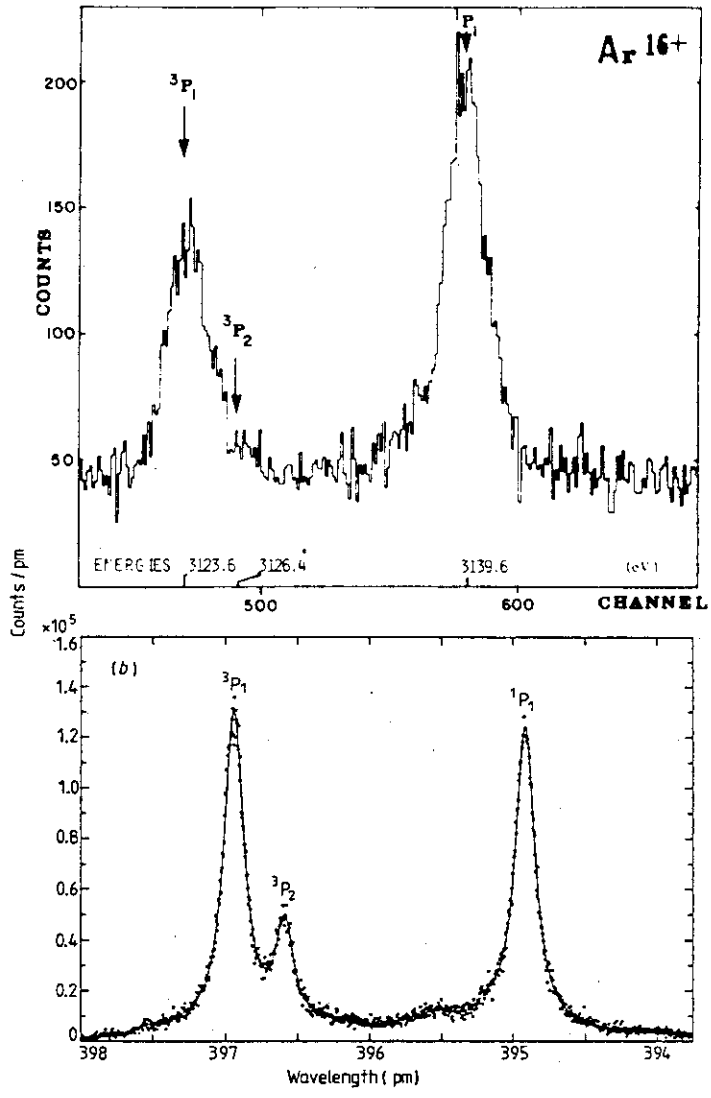

(a)

(b)

Fig. 2(a) (upper) and (b) 9lower) X-ray spectra from $^3P_1$ and $^1P_1$ to ground state transitions of Ar^{16+} ions. (a) is obtained from 6 MeV/amu and (b) from recoiled ions,respectively.

most precise measurements of X-ray energies observed in high energy BFS technique was recently reported by Richard et al.[3] who determined Lyman α_1 and α_2 line energies of $C\ell^{16+}$ ions with the accuracy of 34 ppm.

One of the straight-forward techniques to further reduce the Doppler broadening is the reduction of the ion kinetic energy by deceleration after stripping the electrons at optimum energies which has been recently developed at some laboratories. Deslattes et al.[4] first accelerated $C\ell^{9+ - 11+}$ up to 130 MeV, where the ions were stripped to $C\ell^{17+}$, and then decelerated them down to 23.5 - 67.1 MeV. Then they sent these ions into He gas targets to get $C\ell^{16+}$ where practically no satellite is observed because the double electron capture probabilities from He atoms are very small at these energies (at least two orders of the magnitude smaller than the single electron capture. Of

course atomic hydrogen targets are most preferable where no double electron capture occurs).

On the other hand, recent advancement of plasma confinement and heating techniques makes it possible to obtain high temperature plasmas which result in producing highly stripped impurity ions at or near the plasma center. In fact H-like or He-like impurity ions have been observed in many tokamaks. The energies of these ions is much smaller, compared with those from accelerators. For example, in Alcator C plasmas at MIT where plasma current of 500 kA, confinement time of 500 ms, electron temperature of 1.7 keV, ion temperature of 1.3 keV and electron density of 1-3 x 10^{14} /cm^3 were obtained, X-rays from Ar^{17+} ions were observed which originated from one electron capture into Ar^{18+} produced in the plasmas from atomic hydrogen. Because of high densities of these plasms, fairly serious satellite effects show up in the spectrum, resulting in asymmetric shapes of peaks. This satellite effect can not be controlled easily in large plasma machines. Assuming the known satellites included ,Marmar et al.[5] could determine Lyman α_1 and α_2 lines of Ar^{17+} ions with the accuracy of 11 ppm. Though this accuracy can be improved further down to a few ppm levels by careful arrangement and better equipment, the limitation could be the Doppler broadening due to the movement of bulk plasmas (convection).

The most important feature of highly charged recoil ions is the fact that their recoil energy transferred by heavy projectile ions is very much small, compared with all those mentioned above. Though the detailed distributions of their recoil energy depend upon the impact parameter of collisions, rough estimation can be made by the following formula :

$$E_r = 4 \times 10^{-4} q^2 i^2 / (M E_p b^2)$$

where E_r is the recoil energy in eV, q and i are the charge of projectile ion and recoil ion, respectively, M is the mass of the recoil ion, E_p is the projectile energy in MeV/amu and b is the impact parameter. It can be assumed that the maximum ionization can occur at the impact parameter of about 10 times the radius of the electron shell considered [6] ($b \simeq 10\, a_0/i$). For example, in 15 MeV/amu U^{75+} ion impact on Ar, the recoil energy of Ar^{18+} ions is estimated to be about 4 eV. A typical spectrum from Ar^{16+} ions recoiled by 5.9 MeV/amu U^{66+} ions are shown in Fig.2(b).[7] No Doppler broadening can be seen here. However, spectrum broadening due to satellites ($2\,n'\ell' \rightarrow 1sn''\ell''$) are cearly observed. Of course this broadening can be controlled somehow by changing the target gas pressure. A comparison of these spectra shows that the spectrum from recoil ions has much better statisitics and better symmetry of the peaks, compared with that from high energy ions.

In this particular case, total uncertainty is estimated to be 12 ppm with the most significant contribution in the known reference energy calibration source of 10 ppm (Cd $L\alpha_1$ line).
Furthermore, recent observation of Lyman α_1 and α_2 from recoil Ar^{17+} ions results in the accuracy of 5 ppm level (energy calibration:1.34 ppm, energy dispersion:0.80 ppm, detector position:1.60 ppm, satellite:4.55 ppm)[8].
By further careful measurements, for example, by changing the gas pressure to see the effect of the satellites, the ultimate accuracy could be about 2 ppm when the recoil ions are used.
A summary of the features and the best results obtained in various techniques mentioned above is given in Table 1.

Table 1 A summary of the features and results in various techniques

method	accuracy	feature
beam foil	34 ppm	relatively large Doppler effect less satellite effect
accel-decel with gas atom	10 ppm	less Doppler effect but still some less satellite effect due to double electron capture (no satellite effect should be expected for atomic hydrogen target
plasma	11 ppm	less Doppler effect satellite effect (uncontrollable ?)
recoil ion	5 ppm	no Doppler effect satellite effect due to double electron capture(controllable)

It should be pointed out that, with these accuracies achieved, we can now obtain information of contribution of quantum electrodynamics(QED) effect to the 1s states. For example, the observed 1s QED correction to Ar^{17+} ions is determined to be 1.145 ± 0.016 eV which can be compared with the theoretical value of 1.1413 ± 0.007 eV[8], though the experiments are still one order of magnitude worse than theory.

3 Life-time measurements using highly charged recoil ions
--- comparison with beam foil technique

Beam-foil technique is widely used in determining the life-times of excited metastable states of highly charged ions. However, the life-times of the forbidden transitions for higher Z ions are known to increase drastically.

They are of the order of > 200 ns for ions of Z > 20 for example。On the other hand, the minimum energies of hte ions with appropiate intensities should be > 10 MeV/amu (4.3×10^9 cm/s). This means that the distance to be covered in the life-time measurements of such high Z ions through beam-foil technique becomes as large as 10 m. Such observation over long distances poses us serious limitation on complete collection of the emitted electrons or photons due to the beam divergence.

Instead, we can use highly charged recoil ions produced in heavy ion collisions These recoil ions are, then , accelerated up to a few keV。The measuring distances of the life-time of 200 ns are only a few 10 cm。The emitted photons or electrons are observed immediately after acceleration, for example, by the position sentive detectors。A typical example of such measurements is shown in Fig。3(a) where the energetic heavy ions(IB) produced highly charged recoil ions of Ar^{16+} at the point G. Then these ions are accelerated and focused into a position sensitive detector (PD) of X-rays accompanied with soller slit (S) to dermine the positions of the ions at the instance of the photon emission。In Fig。3(b) is shown the variation of the intensities of

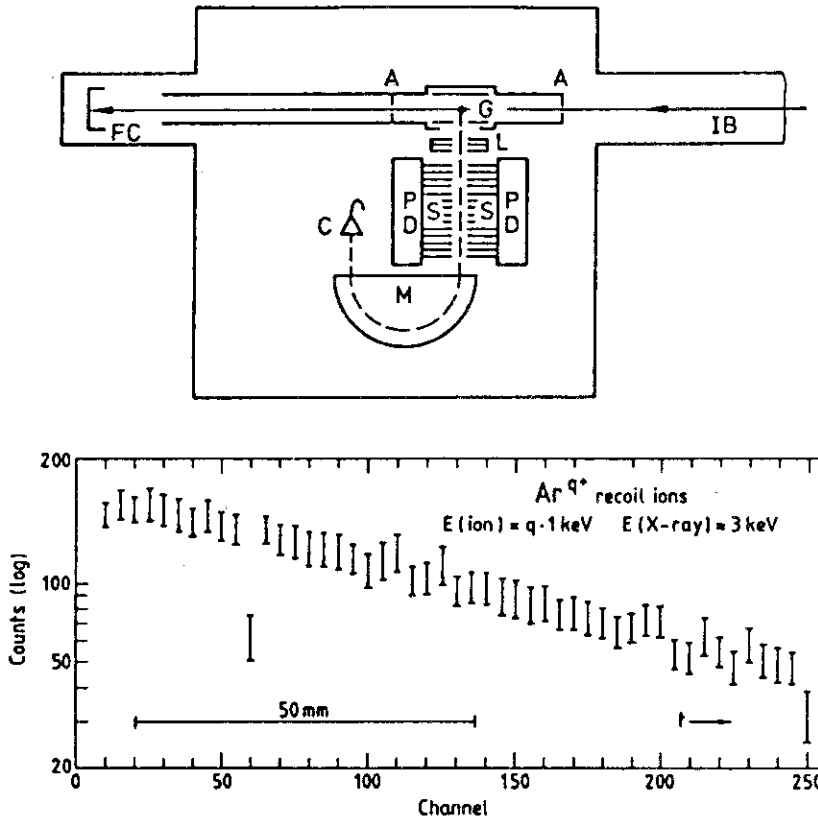

Fig。3 Life-time measuremnts of the metastable state of highly charged ions using recoil ions。(a) experimental set-up. (b) the variation of the intensities of K-xrays of Ar^{16+} ions accelerated up to 16 keV over the distance。

K X-rays emitted from Ar^{16+} ions in the transition from the metastable ($1s2s\ ^3S_1$) state to the ground state ($1s^2\ ^1S_0$) through M1 process as a function of the distance over only 10 cm after acceleration[9]. This variation of the intensities over the distance gives the life-time of 180 ± 40 ns, which can be compared with 170 ± 30 ns determined by Schmieder and Marrus[10] who used high energy beam-foil technique by observing the photon intensity variation over the distance of 2m. Note that the life-time associated with $Ar^{16+}(1s2p\ ^3P_2)$ state via M2 transition to the ground state is 1.7 ns. Thus they decay very quickly before entering the accelration region.

4 Trapping and cooling of highly charged recoil ions

The cooling of the ion beams is now becoming an important technique to study the collision processes and associated applications of these ions. However, serious loss of the ions in the process of the energy retardation can occur. In particular, highly charged ions, which are usually obtained at relatively high energies of a few MeV/amu, must be reduced their energies many orders of magnitude, resulting in prohibitive loss of the intensities. In contrast, as mentioned in the previous sections, the highly charged recoil ions should have a number of advantages over the high energy ion beams obtained directly from accelrators. In fact, the efficient trapping and cooling can be achieved by using such recoil ions because of their small recoil energy provided in the collisions. If these ions are properly trapped for a long period of time, we can obtain all the ions in the ground state because the

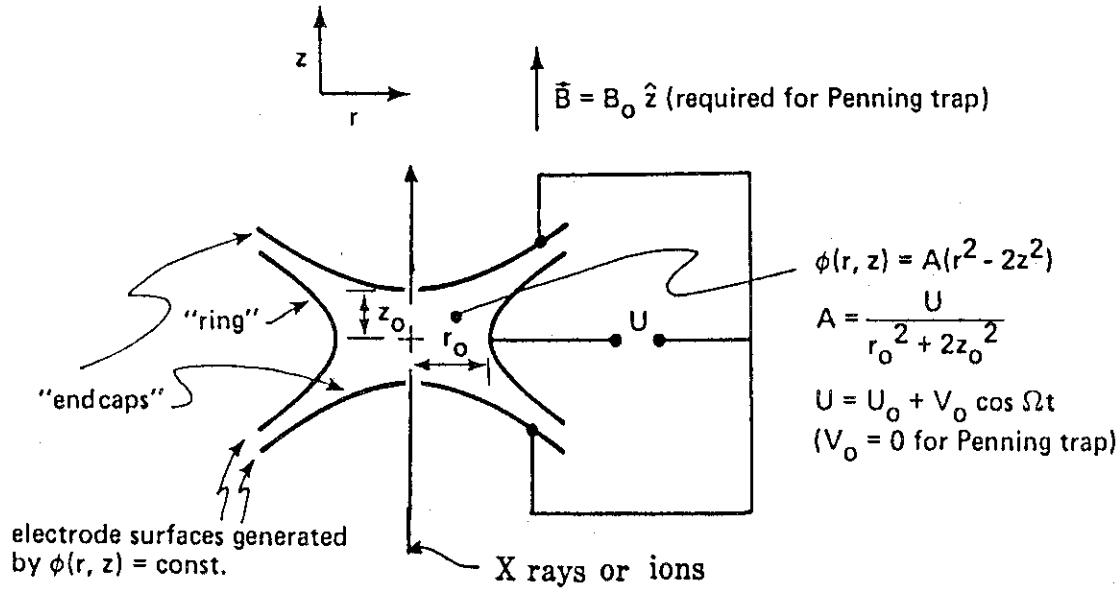

Fig. 4 Schematics of typical trapping apparatus of ions. The projectile heavy ions of photons pass through the trap from the bottom. The recoil ions produced are trapped by the properly arranged electrode configuration.

metastable state ions could decay during trapping.

To trap such highly charged ions efficiently, so-called Penning or Paul trapping systems, among many techniques, seem to be most useful (see Fig.5[11]). In this system the properly controlled electrodes in combination with magnetic field or high frequency field are used. And the projectile heavy ions from an accelerator are sent into the trap where the secondary recoil ions are produced and, without serious loss through energy retardation, can be trapped. During trapping, most of the ion losses are due to the electron capture in collisions withresidual gases which results in the change of the trapping condition, followed by escaping into the wall of the trap. Though no precise data are available for the electron capture at very low energies, we can estimate the survial times of highly charged trapped ions mainly due to the loss by electron capture. In Table 2 are shown the survival times to 1/2 of the primary intensities for Ar^{18+} ions at the chamber with the background pressure of 1×10^{-10} Torr as a function of the ion energy, assuming that the electron capture cross sections at such low energies are not different from those at 10 eV (2×10^{-14} cm^2).

Table 2 The estimated survival times of Ar^{18+} ions at various energies at the residual pressure of 1×10^{-10} Torr.

Energy (eV)	Temperature (K)	Velocity (cm/s)	Survival time to 1/2 (s)
10		7.0×10^5	15
2.6×10^{-2}	300	3.5×10^4	300
3.4×10^{-4}	4	4.1×10^3	2700
8.6×10^{-8}	1×10^{-3}	6.4×10	1.7×10^5 ($\simeq$ 2 days)

As seen in this Table, the direct recoil ions of Ar^{18+} can survive and are stored up to only 15 - 20 s even if the trapping system work perfectly. On the other hand, at the liquid helium temperature, the storage time becomes long ($\simeq$ 1 hr). Further if cooled down to milli-Kelvin (10^{-3} K), the ions can be stored for about 2 days, during which time a series of the observations can be made.

There are a number different methods of cooling ions and atoms from eV down to , say, 10^{-7} eV corresponding to the tenperature of 10^{-3} K :

i) stochastic cooling (probably efficient at relatively high energies around eV region)

ii) electron cooling

iii) laser cooling or radiation-pressure cooling(effective for very low energy region or for almost stationary ions).

Among these techniques of the cooling, the laser-cooling should be most efficient at the lowest energies. In fact this is widely used for cooling of atoms and singly charged ions。 However, if highly charged ions are involved, there are a lot of problems to be solved : As we go to heavier ions, the laser should have shorter wavelengths comparable to the energy of the transitions or the energy level spacings。 Possibly X-ray lasers should be most effective in such an application of heavy ion cooling。

As far as we are concerned with highly charged ion storage, secondary ions produced by photo-ionization processes are surely the best because their recoil energy is zero and in fact their energies are determined mainly by the temperature of the parent atoms prior to ionization。

There are a number of the applications of these cooled heavy ions. One of them , already in use, is the microwave frequency standards by using the laser cooled singly charged ions where their stabilities of the order of 10^{-15} has been achieved [12]。

Another example is that highly charged, heavy ions with such low energies as 10^{-7} eV/amu can be used to study higher order effects of the gravitation (non-Newtonian) and to find the "fifth" force which may play a role in developing the unified theory of interactions。 In particular, heavy ions of highly ionized states could be a good candidate in such investigations.

5 Concluding remarks

As discussed above, energetic, heavy ions accelerated through powerful accelerators up to 1 - 10 MeV/amu can provide us highly charged secondary (recoil) ions with fairly good efficiencies. These highly charged recoil ions get only small recoil energies of the order of less than a few eV. This advantage of small recoil energy provides us some oppotunities of pursuing a number of the interesting experiments :i) very high precision measurements of transition energies, ii) life-time measurements of metastable states of high Z ions and iii) trapping and storage of highly charged ions are a few to be listed among many probabilities.

These experiments, in particular trapping and cooling experiemnts of highly charged ions seem to be very attractive with a number of possible applications opened.

It should be pointed out that the recoil ions can be obtained through almost any ion beam available from accelerators without disturbing the on-going experiments : that is, simply the accelerated energetic heavy ions pass through a jet of gas atoms located above the ion path and the (secondary)

recoil highly charged ions are extracted from the beam path and sent into experimental apparatus. This kind of experiments can be continued, independent of whether other experiments are going on or not.

In particular, the tandem van de Graaff accelerators could be good system for such experiments mentioned above because of good beam quality, low energy spread and availabilities of highly charged projectile ions (see Fig.5).

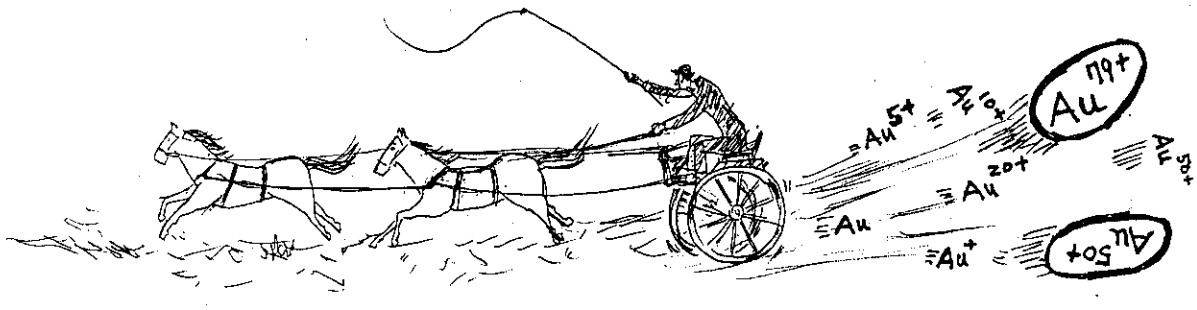

Fig. 5 A tandem (van de Graaff) can provide gold in various ionization states ?

References

1) T.Tonuma, H.Shibata, S.H.Be, H.Kumagai, M.Kase, T.Kambara, I.Kohno, A.Ohsaki and H.Tawara, Phys. Rev. A 33 (1986) 3047
2) J.P.Briand, J.P.Mosse, P.Indelicato, P.Chevallier, D.Girard-Vernhet, A.Chetioui, M.T.Ramos and J.P.Desclaux, Phys. Rev. A 28 (1983) 1413
3) P.Richard, M.Stockli, R.D.Deslattes, P.Cowan, R.E.LaVilla, B.Johnson, K.Jones, M.Meron, R.Mann and K.Schartner, Phys. Rev. A 29 (1984) 2939
4) R.D.Deslattes,R.Schuch and E.Justiniano, Phys. Rev. A 32 (1985) 1911
5) E.S.Marmar, J.E.Rice, E.Kalle, J.Kalle and R.E.LaVilla, Phys. Rev. A 33 (1986) 774
6) R.E.Olson, J.Phys. B 12 (1979) 1843
7) R.D.Deslattes, H.F.Beyer and F.Folkmann, J.Phys. B 17 (1984) L689
8) H.F.Beyer, R.D.Deslattes, F.Folkmann and R.E.LaVilla, J.Phys. B 18 (1985) 207
9) G.Hubricht, E.Trabert and H.M.Hellmann, Z.Phys. D 4 (1987) 209
10) R.W.Schmieder and R.Marrus, Phys. Rev. Letters 25 (1970) 1245
11) D.J.Wineland, W.M.Itano and R.S.van Dyck, Adv. Atom. Mol. Phys. 19(1983) 135
12) J.J.Bollinger, J.D.Prestage, W.M.Itano and D.J.Wineland, Phys. Rev. Letters 54 (1985) 1000

I.9 RECENT STUDIES ON ATOMIC PHYSICS AT RIKEN ACCELERATORS

Yohko AWAYA

The Institute of Physical and Chemical Research
(RIKEN)
Wako, Saitama 351-01

Experimental studies of heavy ion atom collisions at RIKEN have been made mainly by using RIKEN linear accelerators in these five years. The main subjects studied are 1) electron configurations of heavy ions passing through thin foils. 2) Auger electron spectroscopy of target atoms excited by heavy ion bombardments, 3) beam foil spectroscopy about highly ionized ions around Z of 13, which will be given by another talk in this symposium, 4) Impact parameter dependence of inner-shell ionization probability and that of charge state distribution of projectile ions, and 5) the dissociation of target molecules by heavy ion impact.

Recently, a Ring cyclotron was constructed and started to work so we expect to make heavy ion atom collision experiments in the energy range of about 22 MeV/u.

Among the subjects listed above, I will report about the 4), which concerns to the studies of impact parameter dependent phenomena.

I] Charge distribution of projectile heavy ions scattered at small angles

The studies of the impact parameter dependent charge state distribution of projectile heavy ions is just started. For this study the magnetic charge analyzer with a position sensitive parallel plate avalanche counter (PPAC) was prepared. By using this analyzer, we can analyse the charge state from q to 0.6q simultaneously and resolve the state with q and q+1 at $q \approx 20$. Specification of the magnet is as follows: radius=1.5 m, maximum field = 1.5 Wb/m^2, the angle of deflection= 25^0, the gap of pole pieces = 3 cm, total weight = 3 tons, the aperture of the vacuum chamber of the magnet is 10cm x 2.3 cm. The size of the entrance window of the PPAC is 10cm x 2 cm and the resolving power of the position is 1.1 mm FWHM. It is operated at around 6 Torr

in pressure.

In order to define the scattered angle, which corresponds to the impact parameter, a movable small aperture is prepared at the entrance of the analyzer.

As a test experiment, we measured the mean charge of some species of heavy ions and also the charge distribution of Cr ions scattered at 0.01deg. to 0.06 deg. by a 10 $\mu g/cm^2$ carbon foil. We are now preparing a differential pumping gas target system to study the charge state distribution of scattered projectile ions under single collision condition.

II] Measurement of Impact Parameter Dependent Probabilities and Total Cross Sections for Target K-Shell Ionization by He^+ Ions

We have measured the impact parameter dependent K-shell ionization probabilities, $P_K(b)$, of Ca. Cr and Cu from collisions with 1.01 MeV/u He^+ ions by scattered particle-K X ray coincidences. The He^+ ion beam was momentum analysed and collimated to 1mm x 1 mm with a divergence of 0.02 deg. The targets was prepared by evaporating Ca, Cr and Cu on 2.5 $\mu g/cm^2$ C foils. K X rays from the target atoms are detected by using a Si(Li) detector. In the forward direction of incident beams a parallel plate avalanche counter (PPAC) whose anode is divided to 16 rings was placed. By using this PPAC the scattered angle of 0.13^o to $1,4^o$, which corresponds to the region of b extended from well inside the Bohr radius a_K to far outside a_K. Coincidence between each ring of PPAC and K x rays was stored by event to event mode.

The total K-ionization cross section σ_K was obtained by measuring the scattered particles by the target by surface barrier detector and yield of K x rays. The cross section obtained from integrating $P_K(b)$ with thus measured total cross sections within the error of 30 %.

A comparison of the $P_K(b)$ and σ_K with SCA calculations of Trautmann et al using RHFS wavefunctions for united atom and separated atoms states is made.

Details of this work is reported in the reference 1).

Reference

1) R. Schuch, Y. Awaya, T. Kambara, T. Mizogawa, Y. Kanai and H. Shibata: Z. Phys. D - Atoms, Molecules and Clusters 4, 339 (1987).

I.10 LIFETIME MEASUREMENTS OF MULTI-CHARGED Cl ION

Masao SATAKA, Kiyoshi KAWATSURA, Hiroshi NARAMOTO, Yasuaki SUGIZAKI, Yohta NAKAI, Akio OOTUKA[*], Ken-ichiro KOMAKI[*], Fuminori FUJIMOTO[*], Kunio OZAWA[**], and Keishi ISHII[***]

Department of Physics, Japan Atomic Energy Research Institute, [*]College of Arts and Sciences, University of Tokyo, [**]Energy Research Laboratory, Hitachi Ltd., [***]Faculty of Engineering, Kyoto University

Beam-foil investigations of highly ionized chlorine have been performing in the wavelength region 80 - 470 Å at the JAERI tandem accelerator. The ion beam energy is varied from 80 to 150 MeV. The beam-foil studies of Cl ions at an energy as high as a several ten MeV have been reported thus far by two groups(1-3). As the ion beam energy in the present work is the highest among all, the spectrum mainly consists of lines with line multiplet belonging to higher charge states than Cl XIII. The line identification in the region of 170 - 260 Å has been reported in the reference(4). In the succeeding paper(5), the line identification in the region of 80 - 180 Å has been reported. In the present paper, we report lifetime measurements for $\Delta n=0$ transitions belonging to Cl XIV - Cl XV in the wavelength between 230 Å and 460 Å.

Experimental apparatus has been described in detail in reference(4). The radiation from foil-excited chlorine beam is measured by a 2.2 m grazing incidence spectrometer mounted at 90° to the ion beam direction. Intensity decay curve measurements are made in the usual manner. The carbon foil mounted on a wheel is translated relative to the viewing region of spectrometer. The foils whose thicknesses are about 15 $\mu g/cm^2$ can be positioned within the accuracy of 0.05 mm. The foil position is automatically scanned by stepping motor and each step corresponds to preset value of the integrated current measured by a Faraday cup behind the foil.

Strong lines in the spectrum between 230 Å and 420 Å were identified with the lines of $\Delta n=0$ transitions of the type $2s^2 2p^k - 2s2p^{k+1}$ and $2s2p^{k+1} - 2p^{k+2}$ belonging to Cl XIII - Cl XV and the lines of hydrogen-like transitions belonging to Cl XIV - Cl XVI. We have measured the intensity decay curves of lines attributed to $\Delta n=0$ transitions belonging to Cl XIV - Cl XV. We are analyzing these intensity decay curves by non-linear least square method(6).

In table 1 we list the some results of measured lifetimes with lifetimes measured by Ishii et al.(2) and Forester et al.(3). The wavelengths and transitions cited in table 1 are taken from the table in ref.(7). In figure 1 shown is the intensity decay curve for $2s2p\ ^1P_1$ level in the Cl XIV (237.7 Å) measured at 120 MeV. The decay curve is decomposed into two exponential functions. The early portion corresponds to the decay of $2s2p\ ^1P_1$ level. The derived lifetime is 0.14±0.02 nsec. The value is in good agreement with the result of Forester et al.(3) whose value was 0.15±0.03 nsec. It is considered that the late portion mainly contributed from transition of $2s2p\ ^1P_1 - 2p^2\ ^1D_2$ (458.4 Å). The resultant lifetime derived by late portion of decay curve is 0.60±0.06 nsec. The measured life time of $2p^2\ ^1D_2$ using 458.4 Å line is 0.63±0.02 nsec. The both values agree well within the experimental errors.

The decay curves except for 237.8 Å in the table 1 are composed in a one exponential function. The measured lifetimes for lines at 384.0 and 415.6 Å, belonging to the Cl XV resonance doublet, have been measured more precisely than previous measurement(4). The lifetime of $2p\ ^2P_{3/2}$ of Cl XV is 0.76±0.01 nsec. The lifetimes is in excellent agreement with the result of Forester et al.(3). But the measured lifetimes are slightly larger than the theoretical results of Martin and Wiese(8) (0.74 nsec), Armstrong et al.(9) (0.69 nsec) and Cheng et al.(10) (0.72 nsec). The measured lifetimes for $2p^2\ ^3P_2$ based on 286.3 Å and 276.1 Å should be essentially same and the resultant lifetimes are in good agreement each other.

References

(1) R. Hallin, J. Lindskog, A. Marelius, J. Pihl and R. Sjödin: Physica Scripta 8(1973)209.

(2) K. Ishii, E. Alvalez, R. Hallin, J. Lindskog, A. Marelius, J. Pihl, R. Sjödin, B. Denne, L. Engström, S. Huldt and I. Martinson: Physica Scripta 18(1978)57.

(3) J. P. Forester, D. J. Pegg, P. M. Griffin, G. D. Alton, S. B. Elston, H. C. Haydon, R. S. Vane and J. J. Wright: Phys. Rev. A18(1978)1476.

(4) M. Sataka, K. Ozawa, K. Kawatsura, H. Yamaguchi, T. Kitahara, K. Masai, A. Ootuka, K. Komaki, F. Fujimoto: JAERI-M 85-125 (1985)65.

(5) K. Ishii, M. Sataka, K. Kawatsura, Y. Nakai, K. Ozawa, K. Komaki and A. Ootuka: this issue.

(6) D. J. G. Irwin and A. E. Livingston: Computer Phys. Comm. 7(1974)95.

(7) R. L. Kelly: Atomic and Ionic Spectrum Lines below 2000 Angstroms, ORNL-5922(1982).

(8) G. A. Martin and W. L. Wiese: J. Phys. Chem. Ref. Data 5(1976)537; G. A. Martin and W. L. Wiese: Phys. Rev. A14(1976)699.

(9) L. Armstrong Jr. and W. R. Fielder: Phys. Rev. A14(1976)1114.

(10) K. T. Cheng, Y. -K. Kim and J. P. Desclaux: Atomic Data and Nuclear Data Tables 24(1979)111.

Table 1 Radiative lifetimes for Δn=0 transitions in Cl XIV - Cl XV.

ION	WAVELENGTH (Å)	TRANSITION	LIFETIME (nsec)		
			Present	Forester[a]	Ishii[b]
XIV	458.4	$2s2p\ ^1P_1 - 2p^2\ ^1D_2$	0.63	0.60	0.54
XV	415.5	$2s\ ^2S_{1/2} - 2p\ ^2P_{1/2}$	1.04	0.95	1.0
XV	384.0	$2s\ ^2S_{1/2} - 2p\ ^2P_{3/2}$	0.76	0.76	0.71
XIV	290.5	$2s2p\ ^3P_1 - 2p^2\ ^3P_0$	0.16		
XIV	286.3	$2s2p\ ^3P_2 - 2p^2\ ^3P_2$	0.16	0.16	
XIV	284.3	$2s2p\ ^3P_1 - 2p^2\ ^3P_1$	0.16		
XIV	276.1	$2s2p\ ^3P_1 - 2p^2\ ^3P_2$	0.16		
XIV	237.7	$2s^2\ ^1S_0 - 2s2p\ ^1P_1$	0.14	0.15	

a Forester et al. (3).

b Ishii et al. (2).

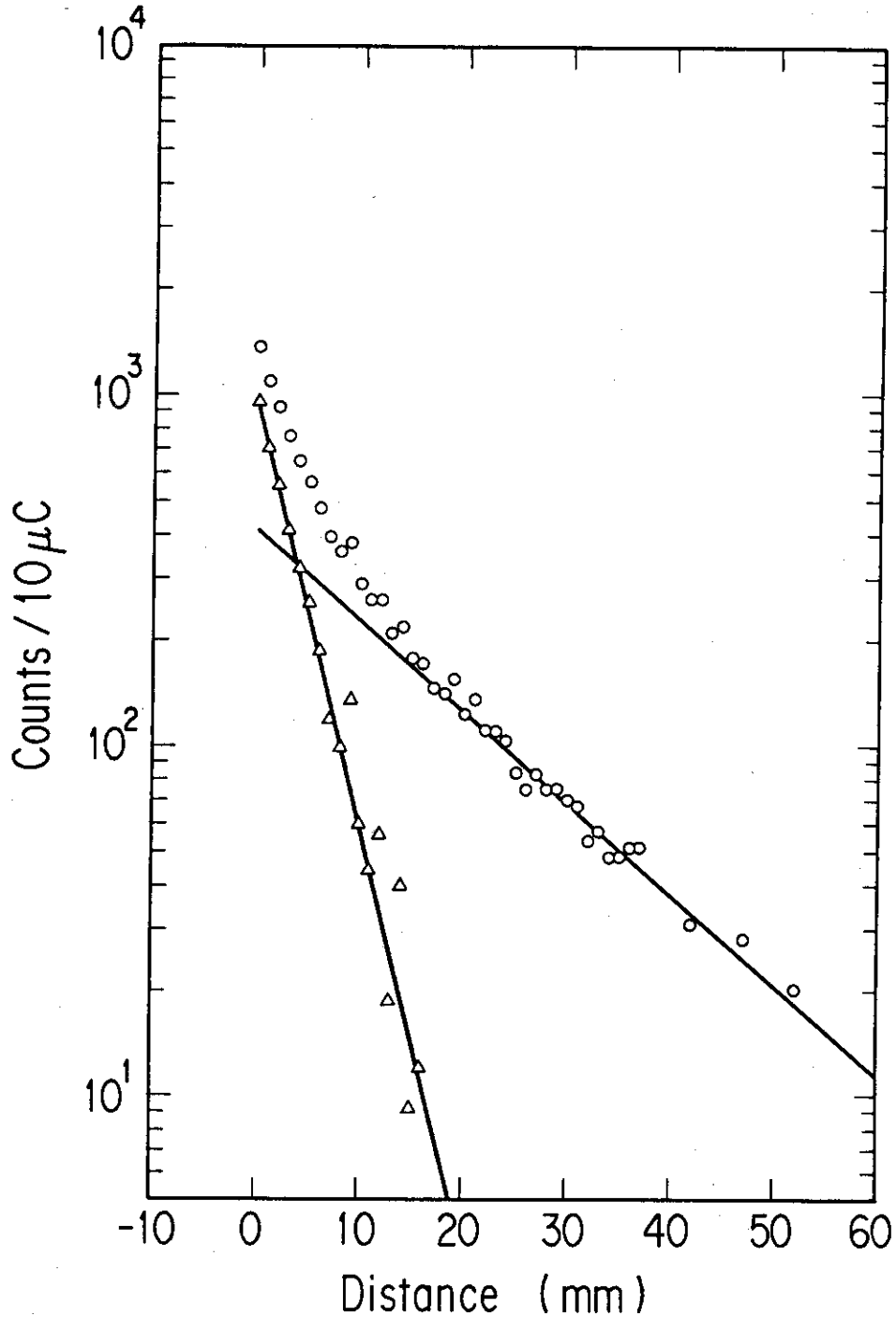

Fig.1 Intensity decay curve for $2s2p\ ^1P_1$ level in the Cl XIV (237.7 Å) measured at 120 MeV. The decay curve is decomposed into two exponential functions.

I.11 LINE IDENTIFICATION OF FOIL-EXCITED Cl ION

Keishi ISHII*, Masao SATAKA, Kiyoshi KAWATSURA,
Yohta NAKAI, Kunio OZAWA, Ken-ichiro KOMAKI**
and Akio OOTUKA**

Department of Physics, Japan Atomic Energy Research Institute , *Department of Engineering Science, Kyoto University, **College of Arts and Sciences, University of Tokyo

1. Introduction

The investigation of spectra and lifetimes in multiply charged ions is of importance in the fusion-oriented plasma physics. The measurements can also provide a severe test of atomic structure theory. In this report, we present the beam-foil work on Cl ions at an energy as high as a hundred MeV by use of the JAERI tandem accelerator. The Cl ion beam was passed through a thin carbon foil. Photon emission, following the beam-foil interaction, was observed in the vacuum ultraviolet region. In the previous paper(1), we have reported identification of the spectrum between 170 and 260 Å. Most of the lines were identified as 2s-2p transitions(2). Two lines were newly classified as n=4-5 transitions in Cl XIV and Cl XV.

Bashkin and Martinson observed many new lines originated from the hydrogenic transitions in the foil-excited Cl spectrum(3). Hallin *et al.* extended the ionization states to Cl XIV, using the ion beam energy up to 42 MeV(4), followed by Bashkin *et al.*(5) and Bhardwaj *et al.*(6). We have further extended the observation to the shorter wavelength region by use of a hundred MeV ion beams(1).

Similar hydrogenic transitions are also observed in the spectra of foil-excited ions for oxygen(7), for fluorine(8), for argon(9), for chromium(10), for iron and nickel(11,12) and for fluorine, silicon and copper(13).

In the present work, the hydrogenic transitions in Cl XIV, XV and XVI have been identified again in the vacuum ultraviolet region with the aid of theoretical calculations: the term energy calculation of the hydrogenic levels with polarization correction, and the calculation based on the atomic structure theory(14).

2. Experiment

The experimental set-up is the same as shown in the preceding paper of this proceedings. The Cl ion beam at energy of 80, 120 and 150 MeV was passed through a thin carbon foil ($\sim 15 \mu g/cm^2$). The photon emission was observed in the direction perpendicular to the beam velocity by a grazing incidence monochromator (McPherson 247) in the wavelength range between 75 and 175 Å. The observation location was fixed immediately downstream from the foil. The photoelectric signals were counted by a set of standard pulse counting NIM modules in conjunction with a microcomputer. The wavelength scanning was driven by a stepping motor. Approximate ionization stage of the lines were estimated by comparison of the recorded spectra of different beam energies. The spectra were calibrated against He-like and Li-like lines.

3. Results and Discussion

A typical spectrum observed at 120 MeV is shown in Fig.1. In the wavelength range between 75 and 175 Å, no Cl line has ever been observed, for ionization stage higher than Cl X, to our knowledge. Although the predicted values of the energy levels, consequently wavelengths, for the transitions in Cl XVII (H-like) are available(15,16), they are hardly seen in our spectrum. Reference lines used in the present spectrum thus are the calculated He-like 3-4, 4-5 and Li-like 3-4, 4-5 transitions. According to Edlén(17), the term value T can be expressed as:

$$T(n,\ell,Z) = T_H(n,\ell,Z) + \Delta_p(n,\ell,Z), \qquad (1)$$

where T_H is the hydrogenic term value with relativistic correction included. The polarization energy Δ_p can be expressed as:

$$\Delta_p(n,\ell,Z) = A(Z)P(n,\ell)[1+k(Z)q(n,\ell)]. \qquad (2)$$

Here the functions $P(n,\ell)$ and $q(n,\ell)$ are tabulated in Ref.16. The constants $A(Z)$ and $k(Z)$ involve dipole and quadrupole polarizabilities of core electrons. For He-like ions(18), the polarization constants are given as

$$A(Z) = (9/2)[(Z-1)/Z]^4, \qquad (3)$$

and

$$k(Z)=(10/3)[(Z-1)/Z]^2. \quad (4)$$

For Li-like ions(19), they are given by

$$A(Z)=9[(Z-2)/(Z-s)]^4, \quad (5)$$

with $s=0.3397+0.102(Z-0.4)^{-1}$ and

$$k(Z)[A(Z)]^{1/2}=0.2113Z+0.598-2.4Z^{-1}. \quad (6)$$

In Table I, are given the calculated wavelengths in Cl XV and Cl XVI with and without polarization corrections, which are lying in the region of 70 to 170 Å. The calculated weighted transition probabilities gA are included, too. The entries in "weighted average" are the weighted means of individual components and are the expected peaks, when each line is not resolved. It is well known that the transitions with $\Delta n=1$ are dominated among all possible hydrogenic transitions in the foil-excited spectra(3-13). The four lines with dagger mark given in Table I were used as reference in the calibration of the present spectrum: one line at 73.12 Å appeared as the second order at 146.24 Å, and the line at 83.20 Å appeared both in the first and second orders. A line at ∿91 Å with satellite peak on the longer wavelength side was classified as n=3-4 transition in Cl XIV (Be-like) with the aid of the atomic structure calculation(14). The dominant three transitions are given in Table II, where calculated and observed wavelenghts are also tabulated. The theoretically generated spectrum for this transition is shown in detail in Fig.2, where multiplet components are drawn individually with the height proportional to the weighted oscillator strength. The curve represent the sum of each component having instrumental width. The weak peak on the shorter wavelength side is missing in the observed spectrum. This suggest that the yrast level is favorably populated in n=4 complex. In the same way, a line at ∿133 Å is identified as n=4-6 transition in Cl XIV. This line is, however, too weak to be studied in its structure. All the peaks clearly observed in this region are identified. A few weak lines are still left unidentified, which are probably originated from the transitions between multiply excited states.

We are grateful to the staff of the JAERI accelerator laboratory for their support for the present experiment.

References

1) M.Sataka, K.Ozawa, K.Kawatsura, H.Yamaguchi, K.Ishii, T.Kitahara, K.Masai, A.Ootuka, K.Komaki, F.Fujimoto :JAERI-M 85-125(1985) p.65.
2) R.L.Kelly: Atomic and Ionic Spectrum Lines Below 2000 Angstroms, ORNL-5922(1982).
3) S.Bashkin and I.Martinson: J.Opt.Soc.Am. 61(1971)1686.
4) R.Hallin, J.Lindskog, A.Marelius, J.Pihl and R.Sjödin: Phys.Scripta 8(1973)209.
5) S.Bashkin, J.Bromander, J.A.Leavitt and I.Martinson: Phys.Scripta 9(1973)285.
6) S.N.Bhardwaj, H.G.Berry and T.Mossberg: Phys.Scripta 9(1974)331.
7) B.Denne, L.Engström, S.Huldt, J.O.Ekberg, L.J.Curtis, K.Ishii, E.Veje and I.Martinson: Phys.Scripta 21(1980)151..
8) L.Engström: Phys.Scripta 31(1985)379.
9) J.P.Buchet, M.C.Buchet-Poulizac, A.Denis, J.Desesquelles and G.DoCao: Phys.Scripta 9(1974)221.
10) J.P.Grandin, M.Huet, X.Husson, D.Lecler, D.Touvet, J.P.Buchet, M.C.Buchet-Poulizac, A.Denis, J.Desesquelles and M.Druetta: J.Physique 45(1984)1423.
11) W.N.Lennard, R.M.Sills and W.Whaling: Phys.Rev. A6(1972)884.
12) W.N.Lennard and C.L.Cocke: Nucl.Instrum & Methods 110(1973)137.
13) L.C.McIntyre, J.D.Silver and N.A.Jelly: in "Beam-Foil Spectroscopy" eds. I.A.Sellin and D.J.Pegg (Plenum, New York, 1976) Vol.1,p.331.
14) R.D.Cowan: "The theory of Atomic Structure and Spectra" (Univ. Calif. Press, Berkley, 1981).
15) J.D.Garcia and J.E.Macek: J.Opt.Soc.Am. 55(1965)654.
16) G.W.Erickson: J.Phys.Chem.Ref.Data 6(1977)831.
17) B.Edlén: Handbuch der Physik, ed. S.Flügge (Springer-Verlag, Berlin, 1964), Vol.27, p.80.
18) A.Dalgarno: Advances in Physics 11(1962)281.
19) B.Edlén: Phys.Scripta 19(1979)225.

Table I Calculated wavelengths for hydrogenic transitions in Cl XV (Li-like) and Cl XVI (He-like) used as reference lines. Units in Å.

Ion	Transition Δn		Δ_p correction none	Δ_p correction incl.	g_4 ($\times 10^{10} s^{-1}$)	Weighted Average	Remarks
Cl XV	1	3d-4f	83.274	83.242	560.	83.20†	Also second
		3p-4d	83.174	83.174*	215.		order
		3s-4p	82.850	82.850*	63.2		
Cl XV	2	4f-6g	116.619	116.616	696.	116.61†	
		4d-6f	116.576	116.543	52.2		
Cl XV	3	4f-7g	96.202	96.200	32.7	96.20	Blended
Cl XVI	1	3d-4f	73.185	73.167	725.	73.12†	Second
		3p-4d	73.085	73.085*	278.		order
		3s-4p	72.761	72.761*	81.9		
Cl XVI	1	4f-5g	158.153	158.150	279.	158.08†	
		4d-5f	158.067	158.024	136.		
		4p-5d	157.882	157.882*	58.8		
Cl XVI	2	4f-6g	102.494	102.492	90.1	102.47	Very weak
		4d-6f	102.451	102.432	67.6		
Cl XVI	3	4f-7g	84.550	84.549	42.4	84.55	Blended

*Polarization not corrected.

†Used as reference lines.

Table II Calculated and observed wavelengths for n=3-4 transition in Cl XIV (Be-like).

Transition	Wavelength(Å) Calc.	Obs.
$1s3p\ ^3P - 1s4d\ ^3D$	88.40	missing
$1s3d\ ^3D - 1s4f\ ^3F$	91.61	91.73 ± 0.23
$1s3d\ ^1D - 1s4f\ ^1F$	94.87	94.63 ± 0.23

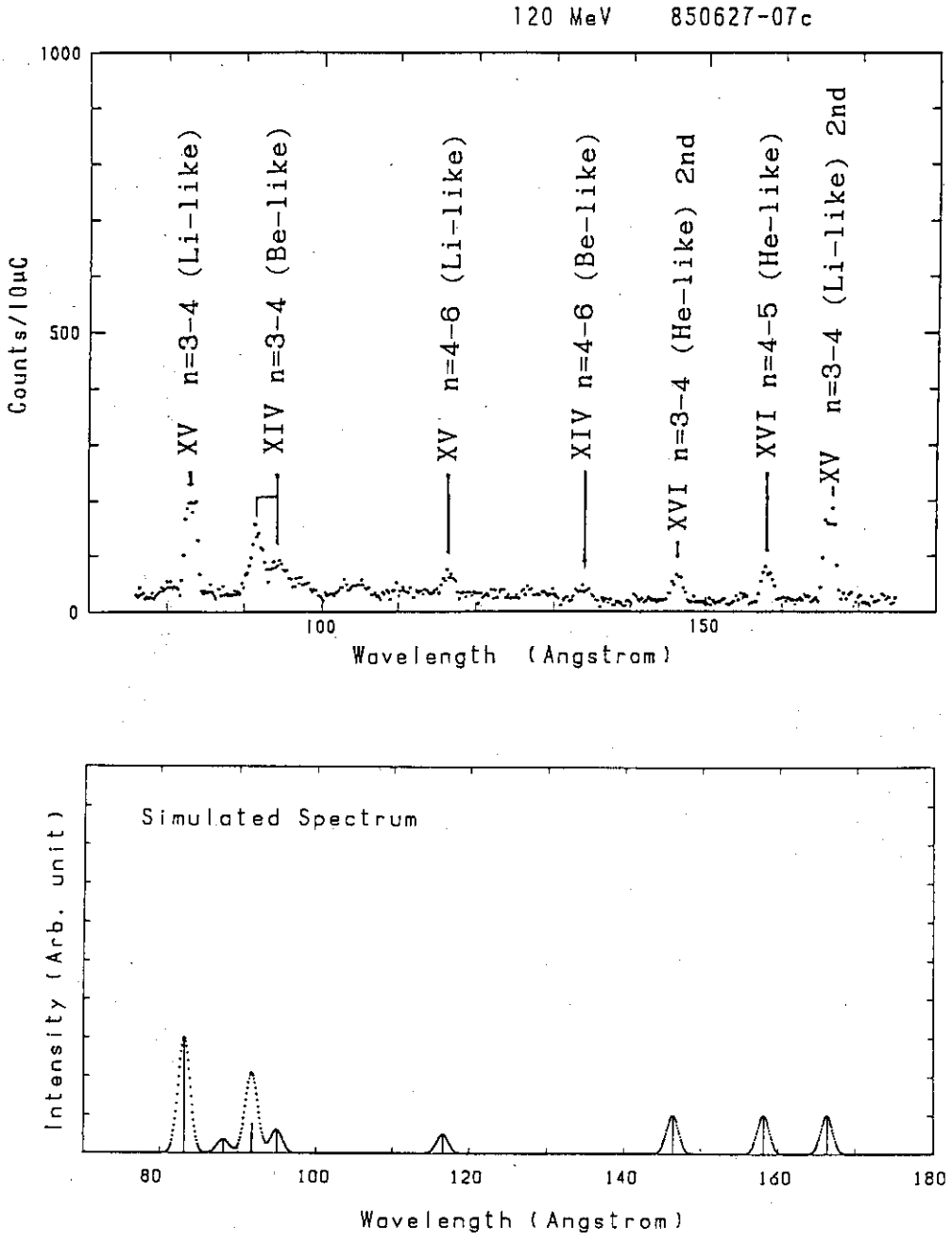

Fig.1 A portion of spectrum between 75 and 175 Å at 120 MeV (upper). Simulated spectrum is also shown, where an appropriate excitation model is assumed (lower).

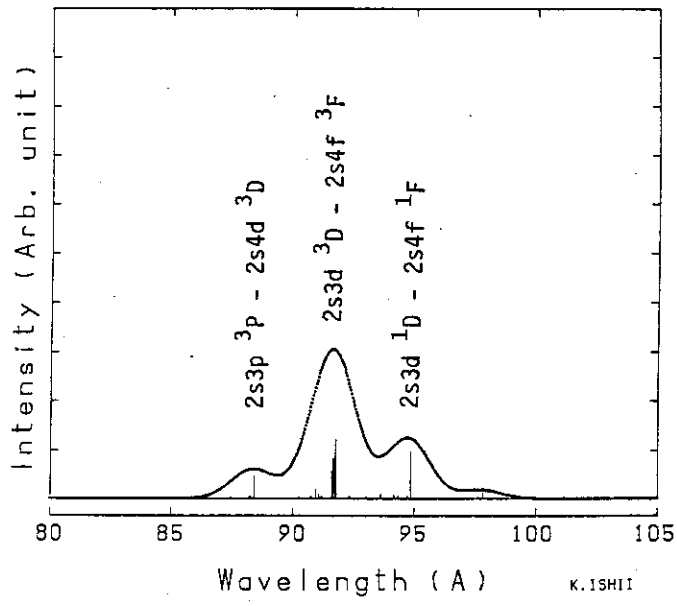

Fig.2 Detailed structure of n=3-4 transition in Cl XIV (Be-like). All the multiplet components are included (*e.g.* 1s3s-1s4p transition), but only the strongest ones are labelled.

I.12 SPECTRUM AND LIFETIME OF HIGHLY IONIZED ALUMINUM

Kozo ANDO, Yohko AWAYA, Susumu KOHMOTO, Hidekazu KUMAGAI, Tadao TONUMA and Seiji TSURUBUCHI*

Atomic Processes Laboratory, The Institute of Physical and Chemical Research (RIKEN), *Faculty of Technology, Tokyo University of Agriculture and Technology

1. Lifetime measurement of Al X 2s2p ^{1}P level

For determining a lifetime of a level, all cascade transitions must be measured and are took into account in analysis of lifetime. The level of 2s2p ^{1}P has four cascade transitions as shown in Figure 1, but a decay curve of a spectral line from 2s3p ^{1}S level was not measured because its wavelength was too short for the spectrometer. At first, decay curves were analyzed to become sum of multi-exponentials by DISCRETE program(1). A lifetime of 2s2p ^{1}P level was determined by the ANDC method with CANDY program(1) and got the value of lifetime of 0.0492±0.0005 nsec. This value is too short in comparison with other data. In these cascade transitions, a line 395.62 A of 2s2p $^1P_1$ - 2p^2 $^1S_0$ transition was mixed with a line 395.36 A of 2s2p $^3P_1$ - 2p^2 $^3P_2$, so that a cascade transition from 2p^2 ^{1}S was omitted in CANDY analysis.

The final value of lifetime of 2s2p ^{1}P level was 0.1923±0.015 nsec.

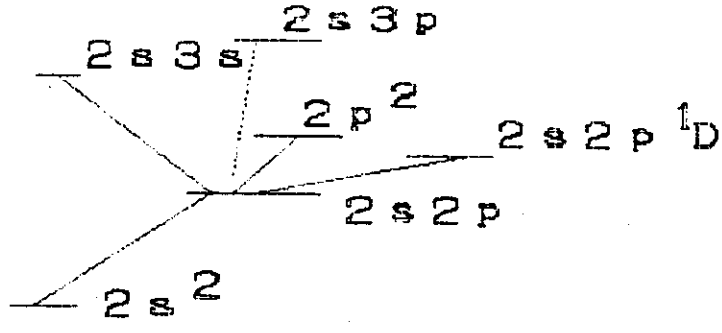

Fig. 1 Schematic diagram of primary transition 2s^2 - 2s2p ^{1}P with cascade transitions.

2. Identification of Al X 2p3d - 2p4f Transition Array

In beam-foil spectra, spectral lines arising from the f levels are so strongly observed that the transition from other unknown f levels would be expected to appear in the spectra. In a Be-like ion of aluminum, the transitions from displaced levels of 2p4f to those of 2p3d have not yet

been identified. A preliminary calculation of atomic energy levels using the Hartree-Fock approximation predicts that the transition array of 2p3d-2p4f will appear near strong lines of 2s3d ^{3}D - 2s4f ^{3}F and a theoretical pattern of the array calculated by Cowan's program(2,3) is also similar to the observed line group near 2s3d ^{3}D - 2s4f ^{3}F lines.

The strong lines in the transition array mainly come from transitions 2p4f ^{3}G to 2p3d ^{3}F levels, but the energy values for the lower levels 2p3d ^{3}F of this lines are unknown. Therefore, energies of the ^{3}F levels are estimated from an isoelectronic sequence.

Slater integrals for the upper levels of 2p4f configuration in the expressions of term energies are experimentally determined from the observed level energies by least-squares fit calculation. The strongest line in the theoretically calculated spectrum did not fit to the experimental one, so that the lower levels of the ^{3}F were shifted to lower values and procedure of least-squares fitting was repeated. As shown in Figure 2, the theoretically calculated transition array becomes to be very similar to the experimental spectrum.

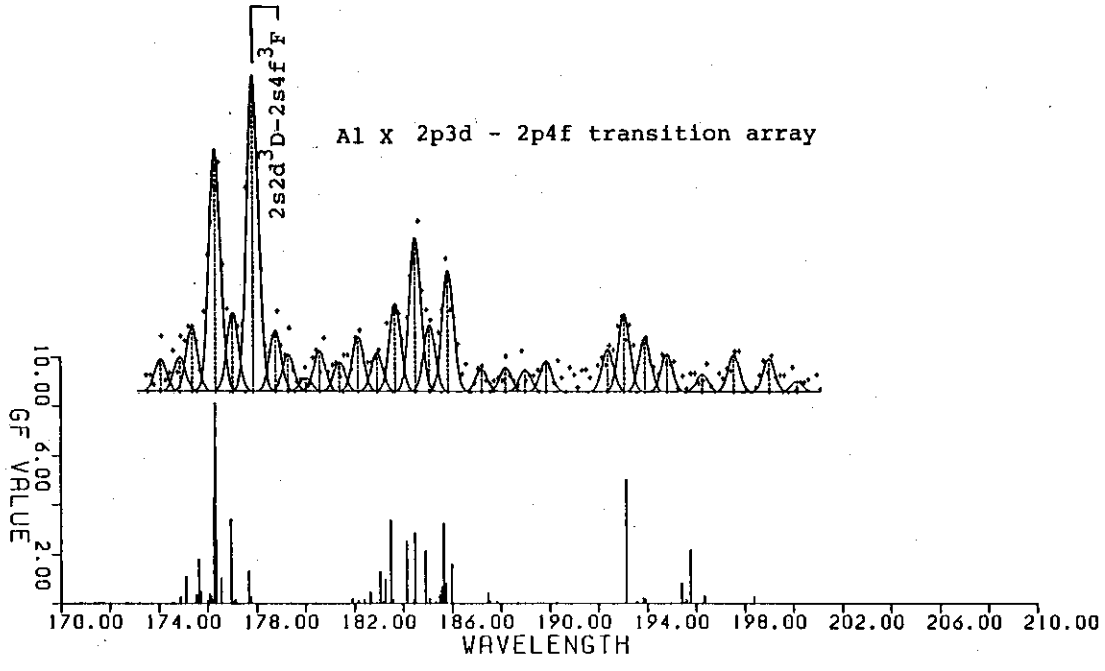

Fig. 2 Comparison between the spectrum obtained by the beam-foil experiment(upper) and the theoretically generated one of 2p3d-2p4f transition of Al X (lower).

References

(1) L. Engström: Nucl. Instrum. & Methods **202** (1982) 369.

(2) R. D. Cowan and D. C. Griffin: J. Opt. Soc. Am. **66** (1976) 1010.

(3) R. D. Cowan: The Theory of Atomic Structure and Atomic Spectra (Univ. of California Press, California, 1981).

I.13 FUNDAMENTAL PROBLEM IN THE RELATIVISTIC APPROACH TO ATOMIC STRUCTURE THEORY

Takashi KAGAWA
Department of Physics, Nara Women's University
Nara 630

1. Introduction

Interest in the relativistic calculation of structures for multiply ionized ions has increased in recent years in connection with the study on space and nuclear fusion plasmas. In high-temperature plasmas observed in solar corona or the Tokamak, most atoms including heavier ones are highly ionized.

In the theoretical calculation of energy levels and oscillator strengths of highly ionized atoms, various relativistic effects as well as the correlation effeccts must be included into the theory adequately because the relativistic effects become large as atomic number increases or as degree of ionization in an atom become high.

The relativistic formalism for many-electron systems was firstly developed by Breit[1,2] who obtained the relativistic Hamiltonian for two-electron systems as a sum of the Dirac one-electron Hamiltonian $H_D(i)$ and two electron operators V_{ee} due to the Coulomb and the Breit interactions, given by

$$H = \sum_{i}^{N} H_D(i) + V_{ee}. \qquad (1)$$

The Dirac one-electron Hamiltonian in atomic units is written as

$$H_D(i) = c\vec{\alpha}_i \cdot \vec{p}_i + c^2\beta_i + V(r_i), \qquad (2)$$

where $V(r_i)$ is the nuclear potential and c is the velocity of light. $\vec{\alpha}$ and β are the Dirac operators in the matrix

form.

The two-electron operators V_{ee} is written as

$$V_{ee} = \sum_{i<j}^{N} \sum \left\{ \frac{1}{r_{ij}} + H_B(i,j) \right\}, \tag{3}$$

where

$$H_B(i,j) = - \frac{\vec{\alpha}_i \cdot \vec{\alpha}_j}{r_{ij}} - \frac{1}{2} (\vec{\alpha}_i \cdot \vec{\nabla}_i)(\vec{\alpha}_j \cdot \vec{\nabla}_j)\, r_{ij}. \tag{4}$$

The relativistic self-consistent-field (RSCF) method has been used to calculate the wavefunctions and energy levels. Two schemes for the RSCF equation are developed: One is the relativistic Hartree-Fock or Dirac-Fock (DF) method[3] using numerical integration method and the other the relativistic Hartree-Fock-Roothaan (RHFR) one[4,5] using a finite basis set to describe orbitals.

The methods described above are based on a single configuration wavefunction in jj-coupling for the state considered. However, the magnitude of the relativistic effects in each electron is different, namely, inner-shell electrons move under the stronger nuclear potential than outer-shell electrons. This means that atomic electrons require different treatment for their coupling and relativistic effects. The multiconfiguration Dirac-Fock (MCDF) theory [6,7] has been developed to introduce wavefunctions in intermediate coupling into the theory. Using the finite basis set method, we have developed the multiconfiguration relativistic Hartree-Fock-Roothaan (MCRHFR) method.[8] Theoretical calculations with these methods have successfully been applied to the calculation of structures for multiply ionized ions.

However, it is known that the relativistic atomic structure theory contains a serious fundamental problem so called the Brown-Ravenhall (BR) problem[9] or variational collapse. This problem arises from the fact that the energy

spectrum of the relativistic Hamiltonian for many-electron systems is not bounded from below because the negative-energy solutions as well as the positive-energy ones are obtained from the relativistic equation.

In this report, two methods to avoide the BR problem in the relativistic calculation, that is, the projection operator method and the general variation method are briefly described.

2. Projection operator method

Firstly, the BR problem is mentioned for two-electron systems.

We start with the Hamiltonian in eq. (1) with N=2. If V_{ee}=0 in eq.(1), the wavefunction for the ground state, that is, the lowest positive-energy state, can be obtained as the product of the Dirac $1s_{1/2}$ orbitals, so that the ground state energy in this case is two times the ground state enenrgy for the hydrogen-like atom. This situation is illustrated in Fig. 1(a). However, if one constructs a wavefunction as a product of the Dirac orbitals belonging to a positive- and a negative-energy continuum states appropriately, he can obtain the same energy as the exact ground state energy given above. The latter case is shown in Fig. 1(b). Moeover, in the latter case, one can construct infinite number of wavefunctions belonging to the

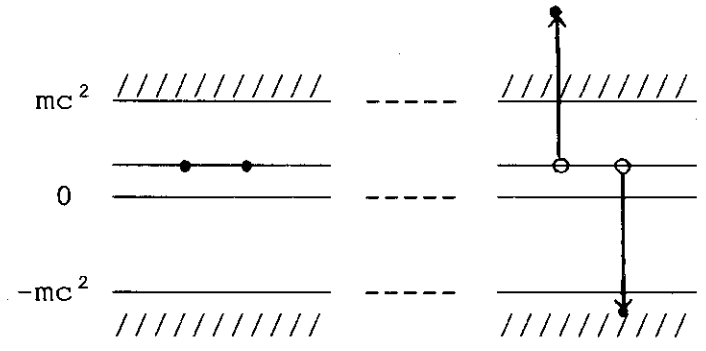

Fig. 1 The bound state (a) and continuum (b) states having the same energy for two-electron systems.

same energy.

When the V_{ee} is applied to the system, the bound state shown in Fig. 1(a) and the continuum one in Fig. 1(b) are mixed, so that the transition probability from the bound state to one of the continuum states having the same energy become non-zero. This situation leads to the autoionization process well known in the electron-atom or ion collision experiment. If so, no stable bound state for the system can exist, which contradicts the situation in actual systems. This is the BR problem which one now encounters in developing the relativistic atomic structure theory.

In order to remove the BR difficuty in the relativistic formalism for many-electron systems, Sucher[10] has proposed the use of a modified Hamiltonian containing a projection operator which projects the positive-energy solutions in the relativistic wave equation. Following Sucher, a modified Hamiltonian for many-electron systems is written as

$$H_+ = \sum_i^N H_D(i) + \Lambda_+ V_{ee} \Lambda_+, \tag{5}$$

where

$$\Lambda_+ = \Lambda_+(1)\Lambda_+(2)\cdots\cdots\Lambda_+(N), \tag{6}$$

$$\Lambda_+(i) = \sum_k |\psi_k^{(+)}(i)><\psi_k^{(+)}(i)|, \tag{7}$$

and $\psi_k^{(+)}(i)$ is an eigenfunction belonging to the positive-energy state for $H_D(i)$.

The problem in the use of the projection operator method is that the projection operator for the system cannot be determined uniquely. If the self-consistent-field (SCF) local potential V_{SCF} is given, eq. (5) can be rewritten as

$$H_+ = \sum_i^N H_D(i) + V_{SCF} + \Lambda'_+(V_{ee} - V_{SCF})\Lambda'_+, \tag{8}$$

where

$$\Lambda'_+ = \Lambda'_+(1)\Lambda'_+(2)\cdots\cdots\Lambda'_+(N) \tag{9}$$

and

$$\Lambda'_+(i) = \sum_k |\psi'^{(+)}_k(i) \quad \psi'^{(+)}_k(i)|. \tag{10}$$

In this case, $\psi'^{(+)}_k(i)$ is a SCF orbital belonging to the positive-energy state.

The expectation value for the second term of H_+ in eq. (8) with respect to the $\Psi_{SCF}(1,\cdots\cdots,N)$ becomes zero. This is the condition that the Hartree-Fock solution should satisfy. So it is said that relativistic HF solutions with a wavefunction expressed by the single Slater determinant yield an approximate ground state energy for atomic systems without the BR problem.

Recently, a numerical calculation[11] for the Dirac equation with the pure Coulomb potential to test accuracy of the projection operator method has been carried out and a comment on the work also appeared[12].

3. General variation method

In this section, the general variation (GV) method[13,14] is briefly described.

Suppose that $\tilde{\Phi}$ and W are the exact wavefunction and energy, respectively, for the system under consideration, we obtain in the following eigenvalue equation,

$$H\,\tilde{\Phi}_n = W_n\,\tilde{\Phi}_n, \tag{11}$$

where H is the Hamiltonian for the system. In relativistic cases, a variational wavefunction Ψ can be expanded in terms

of a complete set of the exact wavefunctions belonging to positive- $\tilde{\Phi}^{(+)}$ and negative- $\tilde{\Phi}^{(-)}$ energy states of the Hamiltonian as

$$\Psi = \sum_i a_i^{(+)} \tilde{\Phi}_i^{(+)} + \sum_i a_i^{(-)} \tilde{\Phi}_i^{(-)}, \tag{12}$$

where $a^{(+)}$ and $a^{(-)}$ are expansion coefficients for positive- and negative-energy states, respectively. As the GV method can be shown to be valid for any Hamiltonian including relativistic ones under consideration, we, for simplicity, omit indices of (±) for a_i and $\tilde{\Phi}_i$ in eq. (12), and write the equation in the following form,

$$\Psi = \sum_i a_i \tilde{\Phi}_i, \tag{13}$$

where

$$\sum_i |a_i|^2 = 1 \quad \text{for} \quad \langle \tilde{\Phi}_i | \tilde{\Phi}_j \rangle = \delta_{ij}. \tag{14}$$

Now we write expectation values of the Hamiltonian and its squared with Ψ as

$$E = \langle \Psi | H | \Psi \rangle \tag{15}$$

and

$$D = \langle \Psi | H^2 | \Psi \rangle. \tag{16}$$

We start with the following relation:

$$\Delta = \langle \Psi | (H - E)^2 | \Psi \rangle$$

$$= \langle \Psi | H^2 | \Psi \rangle - 2E \langle \Psi | H | \Psi \rangle + E^2$$

$$= D - E^2. \tag{17}$$

The key inequality for an exact energy W_n in the GV method is obtained by rewriting Δ in eq. (17) with the normalization condition for Ψ in eq. (14) as follows,

$$\Delta = \sum_i |a_i|^2 W_i^2 - 2E \sum_i |a_i|^2 W_i + E^2 \sum_i |a_i|^2$$

$$= \sum_i |a_i|^2 (W_i - E)^2$$

$$\geq (W_n - E)^2 \sum_i |a_i|^2$$

$$= (W_n - E)^2$$

$$\geq 0. \qquad (18)$$

From the inequality in eq. (18), upper and lower bounds for an exact energy W_n with a variational wavefunction Ψ are given by

$$E + \sqrt{\Delta} \geq W_n \geq E - \sqrt{\Delta} \ . \qquad (19)$$

This is the general variation (GV) method in which a variational wavefunction is varied so as to minimize the value of Δ. As mentioned above, it can be applied to any systems including relativistic ones whose Hamiltonian is not bounded from below.

Relativistic calculations for hydrogen-like systems by use of the general variation method have been carried out.[15] Extension of the method to many-electron systems is now, in progress.

References

(1) G. Breit: Phys. Rev. 34 (1929) 553; 36 (1930) 383; 39 (1932) 616.
(2) H. A. Bethe and E. E. Salpeter: Quantum Mechanics of One- and Two-Electron Atoms (Springer-Verlag, Berlin, Heidelberg and New York, 1957) p. 172.
(3) I. P. Grant: Adv. Phys. 19 (1970) 747.
(4) Y.-K. Kim: Phys. Rev. 154 (1967) 17; 159(E) (1967) 190.
(5) T. Kagawa: Phys. Rev. A12 (1975) 2245.

(6) I. P. Grant, B. J. McKenzie, P. H. Norrington, D. F. Mayers and N. C. Pyper: Comput. Phys. Commun. 21 (1980) 207.
(7) J. P. Desclaux, Comput. Phys. Commun. 9 (1975) 31.
(8) T. Kagawa: Phys. Rev. A22 (1980) 2340.
(9) G. E. Brown and D. G. Ravenhall: Proc. R. Soc. London Ser. A208 (1951) 552.
(10) J. Sucher: Phys. Rev. A22 (1980) 348.
(11) G. Hardekopf and J. Sucher: Phys. Rev. A30 (1984) 703.
(12) J-L Heully et. al.: Phys. Rev. A33 (1986) 4426.
(13) D. H. Weinstein, Proc. Natl. Acad. Sci. USA20 (1934) 592.
(14) J. K. L. MacDonald, Phys. Rev. 46 (1934) 828.
(15) T. Kagawa: Intern. J. Quant. Chem. 23 (1983) 973.

PART II

SOLID STATE PHYSICS AND MATERIAL SCIENCES

II.1 RADIATION DAMAGE OF INSULATORS BY ELECTRONIC EXCITATION

Noriaki ITOH

Department of Physics, Faculty of Science,

Nagoya University, Furocho, Chikusa, Nagoya 464, Japan

I. Introduction

Energetic heavy ions impinging into solids lose most of their kinetic energy by electronic excitation, which is known to influence the radiation damage or formation of lattice defects by radiation in insulators(1). The degree how the electronic excitation plays a role in forming radiation damage depends on materials. Some materials, such as alkali halides(2), are damaged by electronic excitation, while in many materials synergistic enhancements of radiation damage in the presence of elastic and inelastic encounters between incident particles and solids have been observed(3,4). Surfaces are also known to be damaged by electronic excitation, as demonstrated by measurements of laser-induced desorption and modification of surface structures(5).

The primary process of defect formation by electronic excitation is known to be self-trapping of excitons and subsequent transformation of the self-trapped exciton to defects originated from the adiabatic instability in the configuration of the self-trapped excitons at a certain excited states(1,2,6). Thus, in discussing the radiation damage induced by electronic excitation, it is convenient to divide the insulators into three categories: (I) insulators in which excitons are not self-trapped, (II) insulators in which excitons are self-trapped but no permanent defects are produced by electronic excitation and (III) insulators in which permanent defects are produced by electronic excitation.

The number of defects produced by electronic excitation in the solid of type (III) is usually proportional to the number of electronic excitation, namely to the fluence of incident particles. On the other hand the contribution of the electronic excitation to radiation damage in other materials is not necessarily a linear function of the number of excitation: for example, the desorption yield by a laser pulse is a super-linear function of the fluence of the laser pulse(7). Thus the

most crucial information needed to understand the contribution of electronic excitation on radiation damage is (i) to survey the types of materials in which excitons are self-trapped, (ii) to understand the origin of the super-linearity and (iii) to understand the mechanism of the interplay between the radiation damages induced by electronic and elastic encounters.

The purpose of the present paper is to review the experimental studies carried out currently in our group for the purpose of elucidating the contribution of electronic excitation to radiation damage in insulators.

II. Lattice relaxation associated with two interacting self-trapped excitons(8)

The alkali halides are the materials in which the mechanism of radiation damage induced by electronic excitation has been understood most satisfactorily(2). Thus they are most suited to be used in investigating the origin of the super-linearity, which may arise from interaction of excitons. We studied lattice relaxation caused by interaction of two excitons in alkali halides by measuring luminescence and F-center (vacancy) formation by irradiation with a laser pulse of a wide fluence range. RbI and KI are considered to be particularly suited to this type of studies since free excitons are mobile but self-trapped in a short time and hence interaction between free and self-trapped excitons is considered to take place at a reasonably high frequency.

Measurements have been carried out of the luminescence and optical absorption change in RbI induced by irradiation with a XeCl excimer laser pulse (308 nm). The intensity of the π-luminescence which is emitted in proportion to the density of excitation at a low fluence was found to saturate as the laser fluence increases and a new luminescence band starts to increase in proportion to the 4th power of the laser fluence (Fig. 1). Nearly at the fluence where the new luminescence band starts to increase, the F centers are found to be formed in proportion to nearly the 4th power of the laser fluence. Thus it is concluded that a free exciton interacted with a self-trapped exciton is relaxed into defects or into a new luminescence center which may be ascribed to a Cl_2^{2-} center.

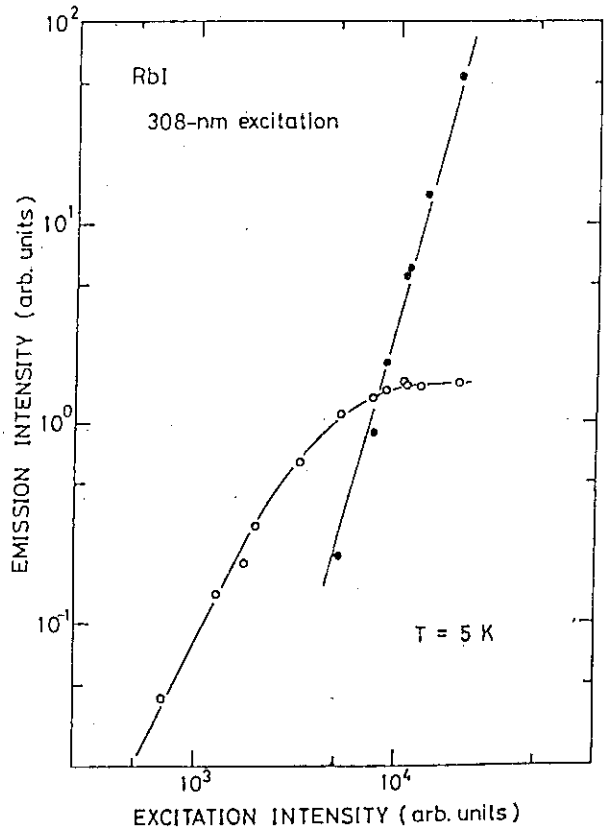

Fig. 1 The dependence on the intensity of the laser pulse of the intensities of π-luminescence (open circle) and of new luminescence (closed circles) induced at high excitation density in RbI at liquid helium temperature.

The result described above indicates clearly that the relaxation of an exciton in the proximity of another exciton is different from the relaxation of an isolated free exciton. The result can be regarded as evidence for lattice relaxation under high density electronic excitation being different from that under low density electronic excitation.

III. Self-trapped excitons in Al_2O_3 (9)

It has been well established that excitons in SiO_2 are self-trapped. We have undertaken experimentnal studies to decide whether excitons in Al_2O_3 are self-trapped. One way of proving self-trapping of excitons is to show that a strong transient lattice relaxation is induced upon electronic excitation. For SiO_2, a transient volume change, the decay time of which is the same as those of luminescence

and transient optical absorption change over a wide temperature range, has been shown to be induced upon electronic excitation. Thus it has been concluded that the self-trapped excitons emitting luminescence and exhibiting transient optical absorption are generated. The conclusion has been further substantiated by an ODMR study(10).

For Al_2O_3, a transient volume change has been found to be induced but no luminescence nor transient optical absorption change that has the same decay time as the volume change was found, as for SiO_2. The magnitude of the volume change, however, is found not to be influenced by doping of the crystal with Cr^{3+} at a concentration of nearly 1 %. Thus the volume change was concluded to be intrinsic possibly due to self-trapped excitons. The decay time of the volume change was found to be on the concentration of the Cr^{3+} impurity and the result was ascribed to the energy transfer from the self-trapped excitons to the Cr^{3+}.

The result described above gives strong evidence for existence of self-trapped excitons in Al_2O_3. Comparing with existing knowledge of self-trapping of excitons for oxides, we note that the excitons are not self-trapped in MgO but self-trapped in SiO_2 and Al_2O_3. The self-trapping is appeared to be related to the ionicity, which is somehow in accordance to the Toyozawa(11) and Rashba(12) criterions.

IV. Structural change of GaP surfaces induced by laser irradiation(13,14)

A few pieces of circumstantial evidence have been presented for desorption and modification of the surface layers induced by dense electronic excitation(5). The experimental studies so far have been carried out under a condition where a substantial number of surface layers are destroyed during measurements. We need to understand the way how the surface is modified within a mono-layer regime by electronic excitation and how the clean surface reacts to photons to cause modification.

We have investigated laser-induced change in the LEED patterns of GaP $(\bar{1}\bar{1}\bar{1})$ surfaces. In order to avoid the temperature rise of the surfaces, laser pulses near the indirect band-gap energy was used. The threshold laser fluence that causes the change from the recon-

structed (17x17) structure to the (1x1) structure for the indirect band-gap photons was found to be nearly the same as that for the direct band-gap photons. It follows that the surface modification by the indirect band-gap photons, at least, can not be ascribed to the temperature effect. Furthermore it is found that the wavelength dependence of the threshold fluence has a dip near the indirect band-gap energy (Fig. 2). Since the bulk optical absorption coefficient increases monotonously by a factor of 200 as the photon energy increases from the indirect band-gap energy to the direct band-gap energy, the

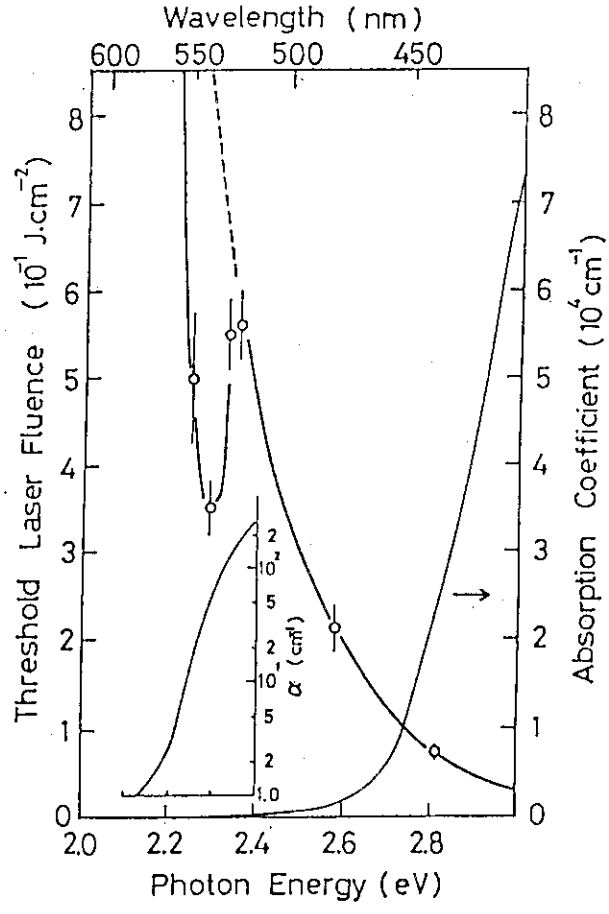

Fig. 2 The dependence of photon energy of the threshold laser fluence for laser-induced transformation from the reconstructed (17x17) structure to the (1x1) structure of GaP ($\bar{1}\bar{1}\bar{1}$) surface.

decrease in the threshold laser fluence near the indirect band-gap energy cannot be ascribed to the bulk electronic excitation. Thus it is concluded that electronic excitation at the surface causes surface modification. The effect of the repetition of the laser pulse on the threshold fluence was also measured and only a small dependence was found. The result has been interpreted in terms of the super-linear dependence of the laser induced effects.

The result described above shows that the electronic excitation at the surfaces modify the surface structure in GaP. No bulk damage by electronic excitation of GaP is known to be induced. Thus the process is entirely different from the damage production in the bulk. A few models have been presented so far but further experimental and theoretical investigation is needed to clarify the mechanism of this surface modification induced by dense electronic excitation at the surface.

References

(1) N. Itoh and K. Tanimura, Radiat. Eff. 98, 269 (1986).

(2) N. Itoh, Adv. Phys. 31, 491 (1982).

(3) G. Gotz, Radiat. Eff. 98, 189 (1986).

(4) R. G. Macaulay-Newcombe and D. A. Thompson, Nucl. Instrum. Methods, B1, 176 (1984).

(5) N. Itoh, Nucl. Instrum. and Methods, to be published.

(6) Y. Toyozawa, J. Phys. Soc. Jpn. 44, 482 (1978).

(7) M. Okigawa, K. Takayama, T. Nakayama and N. Itoh, Proceedings of Thirteenth International Conference on Defects in Semiconductors, eds. L. C. Kimerling and J. M. Parsey, Jr. (AIME, Warrendale, 1985) p.547

(8) K. Tanimura and N. Itoh, to be published.

(9) C. Itoh, K. Tanimura and N. Itoh, J. Phys. C. 19, 6887 (1986).

(10) W. Hayes, M. J. Kane, O. Salminer, R. L. Wood and S. P. Doherty, J. Phys. C 17, 2943 (1984).

(11) Y. Toyozawa, Physica, 116B, 7 (1983).

(12) E. I. Rashba, Excitons, eds. E. I. Rashba and M. D. Sturge North-Holland, Amsterdam, 1982, p. 543.

(13) Y. Kumazaki, Y. Nakai and N. Itoh, Surf. Sci. Lett. in print.

(14) Y. Kumazaki, Y. Nakai and N. Itoh, to be published.

II.2 LATTICE DEFECTS IN SiC

Yukio KAZUMATA, Hiroshi NARAMOTO,
Norio MASAKI and Akira KIKUCHI*

Department of Physics, Japan Atomic Energy Institute, *Faculty of Engineering, Ibaraki University

1. Introduction

Silicon carbide has been utilized in various fields such as the first wall material of a fusion reactor, a coating for nuclear fuel and semiconducting devices. In these many applications, the study of defects induced by irradiation is not only an essential but also a common problem to be tackled. A variety of defects has been reported by several researchers (1～8), particularly in a review article by Choyke(1).

As for paramagnetic defects, Balona and Loubser(2) have reported seven different esr spectra and they have proposed the models relevant to the spectra. Veigner et al (3) have found an isolated carbon vacancy in n-type SiC by quenching from high temperature. Besides these defects, nitrogen-vacancy and exchange-coupled vacancy pairs have been observed in n-type SiC irradiated by fast neutrons by Vainer and Il'in(4). Particularly, the relevance between nitrogen-vacancy pairs and luminescence centers (D_1 and D_2 centers) has been pointed out.

In heavily ion-implanted SiC, Raman spectra are found to be rich in resonant and localized modes (1). Molecular Si-H stretch modes to Si-H bonds formed at a carbon vacancy have been observed at 2221 and 2247 cm^{-1} in H^{+1} implanted crystals (5). In heavily H^+ implanted crystals, the 1435 cm^{-1} band observed has been attributed to a C=C bond due to two carbon atoms forming a split <100> interstitial at a Si vacancy site (6). The planar hexagonal ring network like graphite was also found at 1400－1600 cm^{-1} (7 - 8).

Amorphization by heavy bombardment and the influence of oxygen ions at the surface to amorphization have been examined

in polycrystalline α-SiC by McHargue et al with Rutherford backscattering and the nuclear reaction, $^{16}O(d,p)^{17}O^{*}$, technique (9 - 10).

In spite of these many studies, comprehencive understanding of lattice defects in SiC is far from satisfaction, and that no experiments have been done for the correlation between point defects and lattice disorder. The experiments for paramagnetic defects and also the change of Raman spectrum by ion bombardments are taken up in this paper. Lattice disorder is reflected in Raman scattering and point defects, particularly paramagnetic defects, are observed by esr. In the earlier works described above, esr experiments had been carried out in the crystal irradiated by neutrons and electrons, while ion implantations had been used for Raman scattering. To obtain the correlation, in this paper, ion bombardments were applied to study both esr and Raman scattering. Two paramagnetic centers were found in crystals irradiated by neutrons and ions, and plausible models corresponding to these centers were proposed. The change of Raman spectrum due to both acoustic and optical phonons were studied as a function of the fluence of bombarding ions. The Raman lines from the phonons at the center of the Brillouin zone were less sensitive to the amount of defects, but the lines from the phonons in the intermediate points in the zone significantly reduced their intensities even by low fluence of ion bombardments.

2. Experimental procedures

Four different samples were used in this experiment. These samples were named A, B, C and D sample. The A sample was a transparent single crystal colored in pale green, and the size was about 1.5x1.5 mm^2 in area and 0.2 mm in thickness. The B sample was also a single crystal in a large size of 20 mm in diameter and 30 mm in length. This sample was transparent but in somewhat dark green coloration. In the experiments, the sample was cut in the size of 4x10 mm^2 in area and 2 mm in thikness. The C sample was a single crystal as well but in opaqueness colored in dark brown. The crystal

structure of these three single crystals was confirmed to be in 6H SiC by x-ray diffraction. Finally, the D sample colored in green with thin yellow was a polycrystal containing α and β phases synthesized by chemical vapor deposition (CVD) by Toshiba Co.

These samples were bombarded by the variety of ions from a van de graaff and a tandem accelerator at nitrogen temperature (NT) in vacuum of 10^{-7} mmHg. After ion bombardments, temperature of the samples was warmed up to room temperature (RT) and the measurements by esr and Raman scattering were done. The fluence of a bombarding particle was monitored by an ORTEC Model 439 Digital Current Integrator and a Model 875 Counter.

Esr was measured at NT by a 9 GH_z conventional spectrometer made by Echo Co. The cavity of the spectrometer was operated in the TE_{011} mode with 100 kH_z modulation coils. For measurements at NT, a small quartz Dewar vessel was inserted into the cavity. Esr frequency and static magnetic field were measured with an HP-5246L frquency counter and a proton resonance spectrometer Echo EFM-30AD, respectively. Raman scattering was measured at RT by NR-1000 Raman spectrometer manufactured by Japan Spectroscopic Co., Ltd.

3. Results and Discussion

3-1. ESR experiment

The results of esr are shown in Fig.1 for the four samples before ion bombardment. In the A sample, three well-resolved lines are observed, which arise from nitrogen donors substituted for carbons in the host lattice. Even in the B sample, three lines are also observed but the intensity at the center of the lines is significantly stronger, as compared with the result of the A sample. The spectrum of the C sample, at the third in the figure, shows a very complicated feature, which is presumably due to the large amount of impurity ions. Finally, in the D sample a narrow line is observed despite polycrystalline nature.

These four samples were irradiated by neutrons and ions. Typical esr spectra are shown in Fig.2 for different

irradiation conditions. As shown in Fig.2(1), besides the strong line at the center (g=2.0030), fine structure is observed at NT in the A sample after the irradiation by neutrons at a liquid helium temperature. Similar spectrum is observed in the B sample irradiated by 100 MeV C^{+5} and N^{+5} ions. However, nothing but a strong line without any structure was yielded by the bombardments of low energy light ions and high energy heavy ions, for instance, such as 1.0 MeV D^{+} and 150 MeV Au^{7+} ions as shown in Fig.2(3).

An increase of the intensity of the central line was studied as an increase of the fluence of bombarding ions. As shown in Fig.3, any noticeable change is not observed at the fluence of 10^{15} P^{+}/cm^{2} by 1.0 MeV P^{+} ion bombardments. At the fluence of 10^{16} P^{+}/cm^{2}, the transparent A sample blackened to be opaque and the intensity of the line increased significantly. Further increase of the fluence up to 10^{17} P^{+}/cm^{2} caused an additional line in the line. For 140 MeV Cl^{8+} ion bombardment, as shown at the bottom of Fig.3, the additional line is seen as a small bump near the downward peak of the central line.

As described above, two different esr spectra were observed by ion bombardments. The spectrum with a fine structure was analyzed by the spin Hamiltonian,

$$H = g\beta S H + S D S \qquad (1)$$

where the first term on the right hand side means zeeman energy, and the second one is due to spin-spin interaction. From the angular dependence of the spectrum, the parameters, g and D, were derermined to be D=592.5 gauss, $g_{\parallel}$=2.002 and $g_{\perp}$ =2.0060. From these parameters, the model of V^{0}_{c} proposed by Balona and Loubser (2) is acceptable, where V^{0}_{c} stands for an uncharged carbon vacancy.

Another spectrum, the central line at g=2.0030, is hard to deduce the model. The intensity of this line changes from one sample to another sample even before irradiation. Further, as described above, the intensity of the line increased with an increase of the fluence. The results of esr

experiments with the samples quenched from high temperaturte(3) and of channeling experiments (11) have pointed out the presence of carbon vacancies in an unirradiated sample. All these experiments presume that the esr line is closely bounded up with a carbon vacancy.

3-2. Raman scattering

Raman spectra for the unirradiated samples are shown in Fig.4. Every Raman line in the A and B sample was assigned to the normal modes from the experiment by a polarized light beam and with the formula

$$I = C \nu_s^4 \left[(n_p + 1) / \nu_p \right] (e_\rho^i \alpha_{\rho\sigma} e_\sigma^s)^2 \quad , \quad (2)$$

and by consulting with the figures in the reference (12). In eq.(2), C is a constant, ν_s is the Stokes-shifted Raman frequency, ν_p is the vibrational frequency of the oscillator, n_p is the occupation number of the initial vibrational state, e_ρ^i is the ρth component of the unit polarization vector of the incident light, e_σ^s is the σth component of the scattered light, and $\alpha_{\rho\sigma}$ is the Raman tensor and given by Loudon (13). The lines with the wave number less than 600 cm^{-1} are associated with acoustic phonons while the lines between 700 and 1000 cm^{-1} are due to optical phonons. Two phonon mode is observed at 1515 cm^{-1} as a broad band. Much difference cannot be seen in comparison between the A and the B sample, but in the C sample the lines associated with the acoustic phonons are missing. Further, in the D sample the lines from the acoutic phonons disappear as well and some differences from the above three samples are seen even in the lines from the optical phonons.

The change of the Raman spectrum by irradiation is shown in Fig.5 for the A sample on the 1 Mev P^+ ion bombardments. No significant change is observed at the fluence of 1×10^{15} P^+/cm^2. An increase of the fluence to 1×10^{16} P^+/cm^2 remarkably decreases the intensity of the Raman lines from the acoustic phonons and the sample turned transparency into opaqueness. The results by 100 MeV C^{5+} ion bombartdments is

shown in Fig.5 in comparison with above figures. At the fluence of 10^{17} P^+/cm^2, the lines from optical phonons detoriorate remarkably and above this fluence samples will be turned into amorphous state.

The line at 969 cm^{-1} is from the phonons at the center of the Brilloun zone but the other lines are due to the pnonons away from the center. Consequently, from this experiment it will be concluded that the phonons at the center of the Brilloun zone receive less influence by ion bombardments in comparison with those at the intermediate and the boundary of the zone.

References

(1) W.J. Choyke: Radiation Effects in Semiconductors, 1976 (The Institute of Physics, Bristol and London. ed by N.B. Urli and J.W. Corbett) p58.

(2) L.A. de S.Balona and J.H.N. Loubser: J. Phys. C;solid st. Phys. 3 (1970) 2344.

(3) A.I. Veinger, V.A. II'in, Yu.M. Talrov and V.F. Tsvetkov: Sov. Phys. Semicond. 13 (1980) 1385.

(4) V.S. Vainer and V.A. II'in: Sov. Phys. Solid State 23 (1981) 2126, 33 (1982) 1432.

(5) D.M. Gruen, R. Varma and R.B. Wright: J. Chem. Phys. 64 (1976) 5000.

(6) L.A. Rahn, P.J. Colwell and W.J. Choyke: Proc. 3rd Int. Conf. on Light Scattering in Solids. ed by M. Balkanski, R.C.C. Leite and S.P.S. Porto (Paris: Flammarion) 1976, p607.

(7) S.A. Solin and R.J. Koblicka: Amorphous and Liquid Semiconductors. Vol.2 (ed by J.Stuke and W. Brenig (New York: wiley) 1974, p1251.

(8) R.B. Wright and D.M. Gruen: Radiation Effects 33 (1977) 133.

(9) C.J. McHargue, M.B. Lewis, J.M. Williams and B.R. Appleton: Material science and Engineering, 69 (1985) 391.

(10) C.J. McHargue, G.C. Farlow, C.W. White, J.M. Williams, B.R. Appleton and H. Naramoto: Materials Science and

Engineering 69 (1985) 12

(11) I. Nashiyama, s.Nishijima, N. Kobayashi, S. Yoshida and E. Sakuma: Denki gakkai shiryo (in Japanese) EMI-86-136

(12) D.W. Feldman, J.H. Parker,Jr., W.J. Choyke and L. Patrick: Phys. Rev. 170 (1968) 698.

(13) R. Loudon: Advan. Phys. 13 (1964) 423.

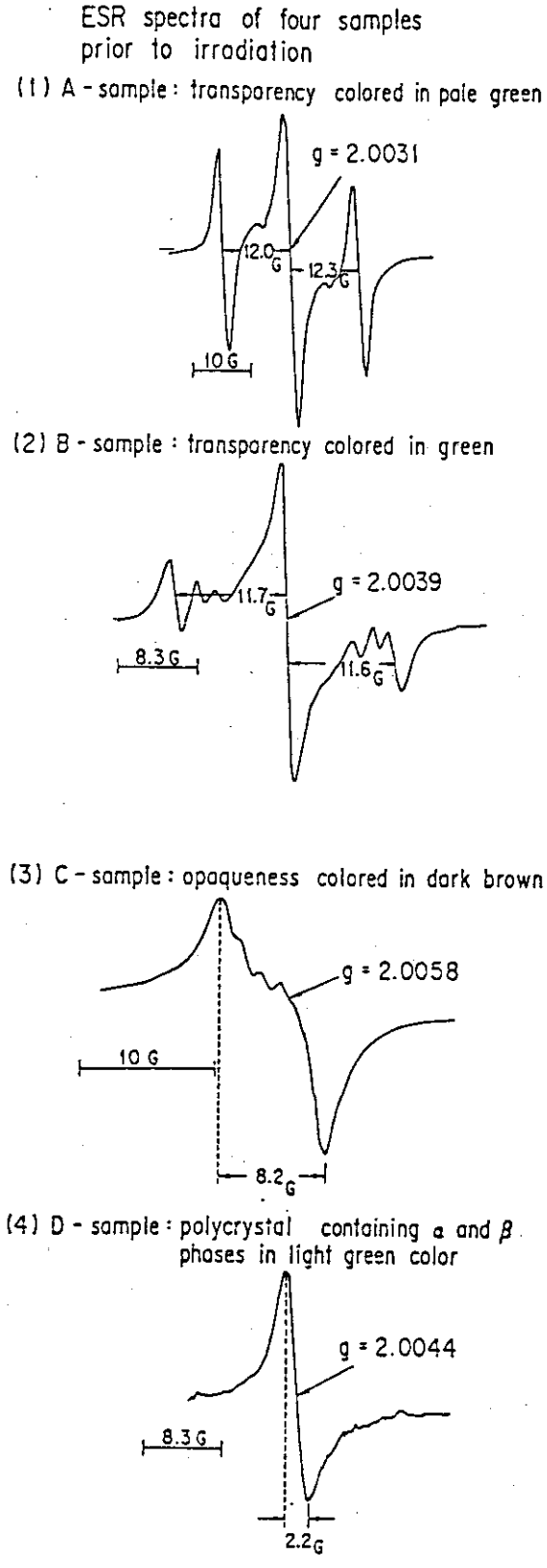

Fig.1 Esr spectra of four samples before ion bombardments, measured at NT.

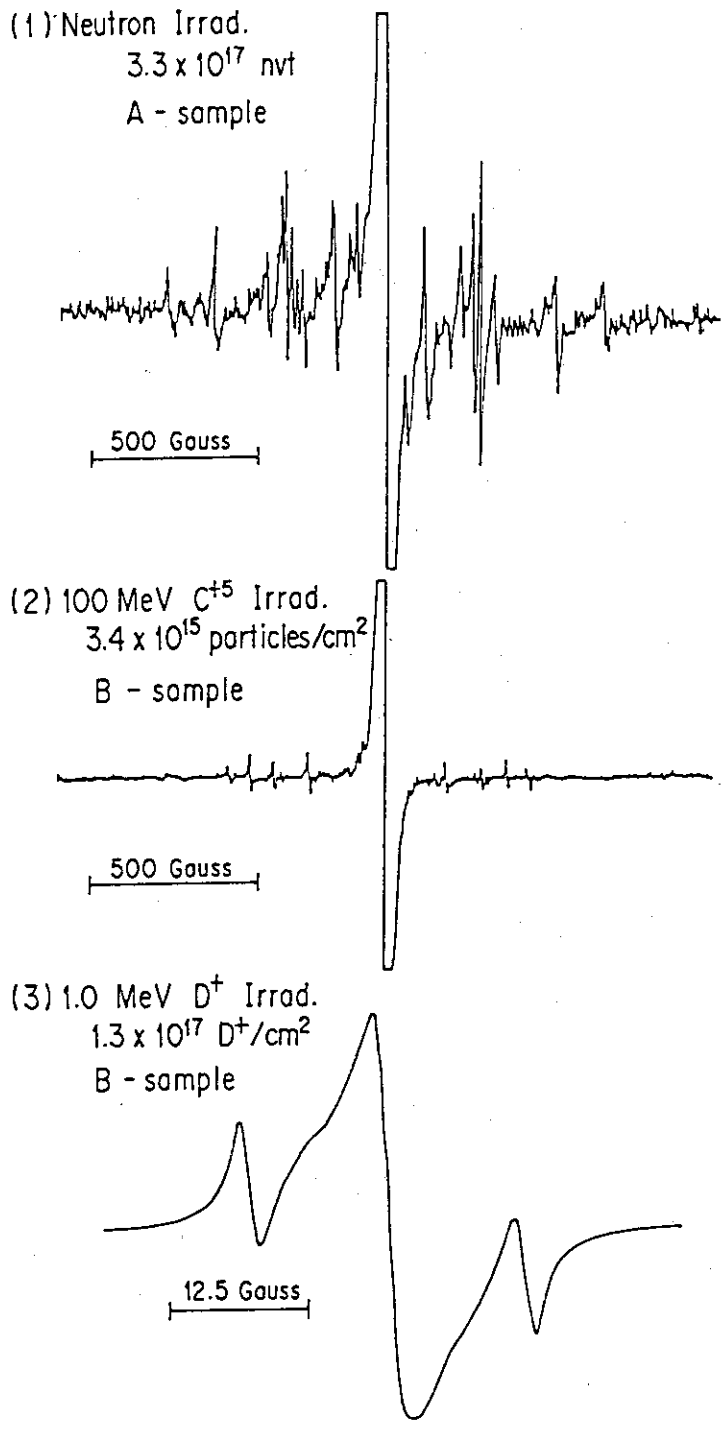

Fig.2 Esr spectra after irradiations.

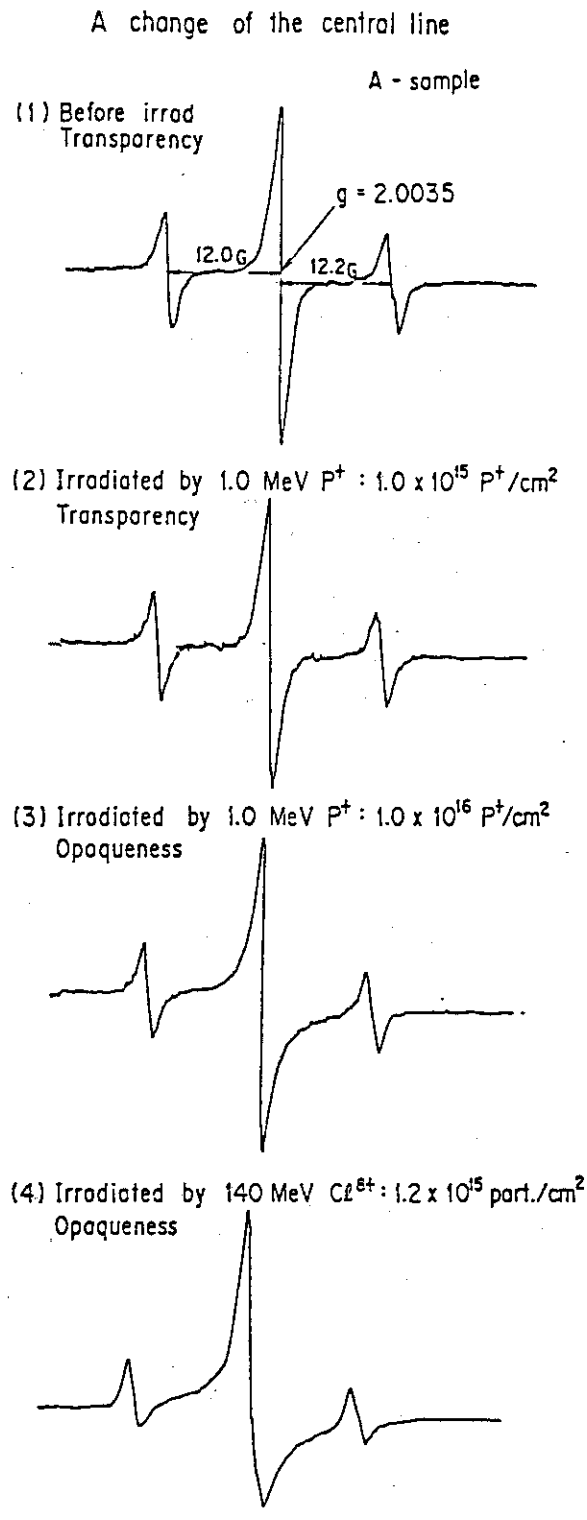

Fig.3 The change of the central line with an increase of the fluence for 1 Mev P^+ ion bombardment.

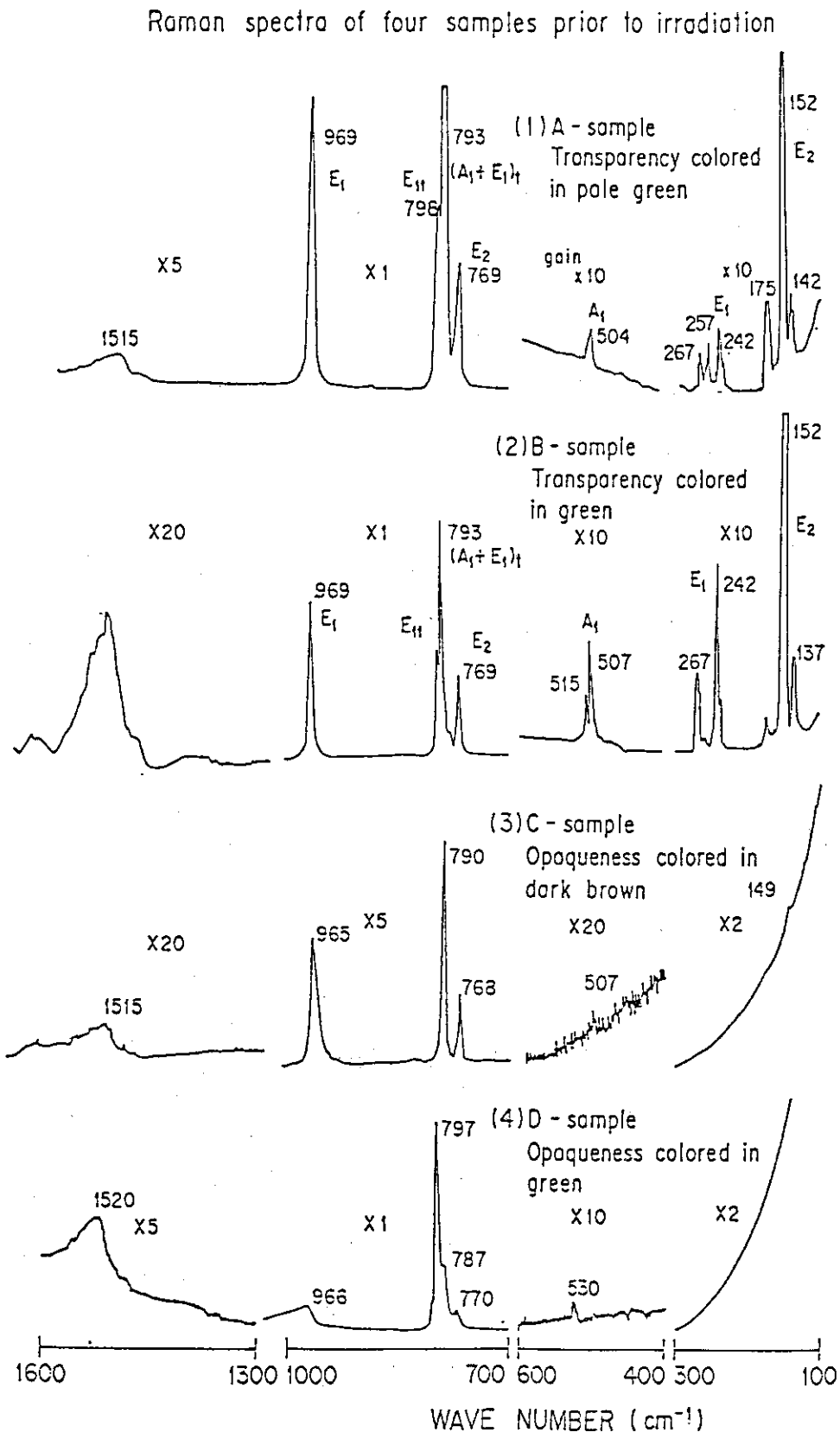

Fig.4 Raman spectra of four samples before ion bombardments, measured at RT.

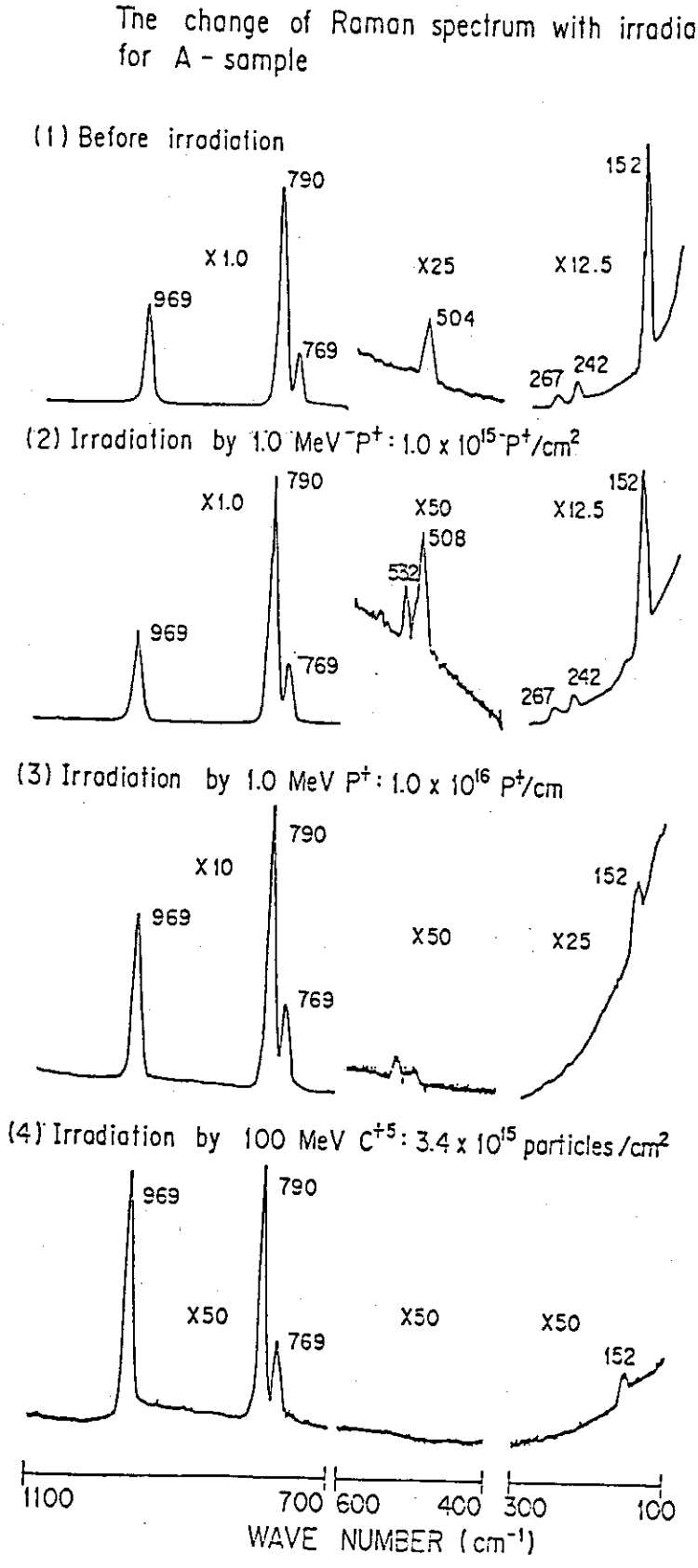

Fig.5 The change of Raman spectrum with an increase of the fluence for 1 MeV P^+ ion bombardment.

II.3 ELECTRON IRRADIATION-INDUCED PHENOMENA IN ALLOYS AND CERAMICS

Chiken KINOSHITA, Kiyomichi NAKAI and Sadakichi KITAJIMA

Department of Nuclear Engineering, Faculty of Engineering, Kyushu University

1. INTRODUCTION

The electron microscope, in particular the high voltage electron microscope (HVEM), provides many experimental advantages for investigating radiation effects. The most important advantage of the electron microscope is that it permits direct observation of phenomena during electron irradiation. Since the first use of electron microscopy for the *in situ* observation of the nucleation and growth process of dislocation loops [1], it has been used to investigate not only radiation damage itself, but also the kinetic process of point defects. Systematic experiments and their analysis have led to an understanding of the fundamental aspects of radiation damage in metallic, ionic and covalent crystals. The purpose of the present paper is to review the recent progress in the phenomena induced by electron irradiation in alloys and ceramics. Particular emphasis is placed on our results related to transformations, such as irradiation-induced defect aggregation, chemical disordering, precipitation, spinodal decomposition and amorphization. Most results have been published elsewhere.

2. KINETIC BEHAVIOR OF POINT DEFECTS AND DEFECT CLUSTERS

A systematic understanding of the kinetic behavior of point defects in alloys and ceramics has been tried through the observation of the nucleation and growth process of dislocation loops in a high voltage electron microscope. The solid solution of Fe-7.5at%Mo (A), Fe-14.0at%Mo (B), Cu-1.3at%Ti (C), Cu-4.9at%Ti (D) and Cu-47.0at%Ni (E) alloys and MgO were irradiated at temperatures from 300 to 1200 K. Dislocation loops of interstitial character are formed, and the loop nucleation stage is

complete early in the irradiation. The size of dislocation loops was followed as a function of time under irradiation at various temperatures. Loops grow with a relationship proportional to some power of the irradiation time, the power is ~ 1/3 below T_0 and approaches 1 above T_0 (T_0 ~ 560, 580, 400, 410, 370 and 900 K for A, B, C, D, E and MgO, respectively). The volume density C_L and size D of loops after the rapid nucleation can be expressed by $C_L \propto \varphi^{1/2} t^0$ and $D \propto t^{1/3}$ and by $D \propto \varphi^{1/2} t$ for the irradiation below and above T_0, respectively, where φ is the electron flux and t the irradiation time.

The kinetic behavior of interstitial loops should be directly related to the behavior of point defects. The kinetics of loop nucleation and growth may be classified in terms of the mobility of interstitials M_I and of vacancies M_V, nucleation sites of loops and so on. When di-interstitials form the nuclei of loops at temperatures where only interstitials are mobile, the density of interstitial loops saturates at the beginning of irradiation and the loops grow in proportion to the cube root of the irradiation time. This also happens in impure metals. The dependences of volume density C_L and size D of dislocation loops on t, φ and irradiation temperature T is [2]

$$C_L \propto \varphi^{1/2} M_I^{-1/2} t^0, \qquad D \propto t^{1/3} \tag{1}$$

Explicit expression for M_I is $M_I = \nu \exp(-E_M^I/kT)$, where E_M^I is the migration energy of interstitials. When vacancies are mobile, or when $M_I \gg M_V \geq 100 \sim 1000$ jump/s, interstitial dislocation loop may grow in proportion to the irradiation time [2], that is

$$D \propto \varphi^{1/2} M_V^{1/2} t. \tag{2}$$

The kinetic behavior of loops in A, B, C, D and E is in accordance with the nucleation-growth model, in which di-interstitials are stable nuclei of loops. The model characterizes T_0 as the temperature where the mobility of vacancies in the each alloy becomes effective. According to the model, the dependence of C_L and dD/dt on irradiation temperature below and above T_0 is respectively related to the migration energies of interstitials E_M^I and vacancies E_M^V. Experimental results are used for getting $E_M^I = (3.0 \pm 0.6) \times 10^{-20}$ J and $E_M^V = (1.6 \pm 0.1) \times 10^{-19}$ J

for A, E_M^I = (2.9 ± 0.6) × 10^{-20} J and E_M^V = (2.6 ± 0.3) × 10^{-19} J for B, E_M^I = (1.2 ± 0.4) × 10^{-20} J and E_M^V ≒ 1.3 × 10^{-19} J for C, E_M^V ≒ 1.3 × 10^{-19} J for D and E_M^I = (3.8 ± 0.7) × 10^{-21} J and E_M^V ≒ 1.2 × 10^{-19} J for E [3, 4, 5] .

For diatomic oxides such as MgO, it is seldom the case that displacement rates are identical for both anions and cations ; nor in general will defect mobilities for each ion be the same. Consequently, those features of diatomic oxides have to be taken into account for describing the nucleation and growth process of loops. Following the similar treatment to that for getting Eqs.(1) and (2), we adopted the pseudo-chemical rate theory for describing the nucleation and growth process of loops, and got equations analogous to those in metals, or Eq.(1) and Eq.(2) [6] .

The kinetic behavior of loops in MgO follows Eq.(1) and Eq.(2), below and above 900 K, respectively, and implies that the loops nucleate with one pair of Mg- and O-interstitials. At temperatures above ~ 900 K, the size of individual loops was traced and the temperature dependence of the growth rate of the loops is used for yielding the migration energy for the slower vacancies, presumably O-vacancies, as (3.1 ± 0.3) × 10^{19} J [7] .

3. IRRADIATION-INDUCED CHEMICAL DISORDERING

In atomic displacement processes, replacement collision sequences play an important role as a medium for transporting energy and mass through crystalline materials. Most of the displacement occur via the replacement collision sequences, leaving the vacancy at the beginning of the sequence and depositing the excess atom as an interstitial at the end of the sequence. When superlattice alloys such as FeAl and Ni_3Al are irradiated with high energy particles at low temperatures, where interstitials and vacancies are immobile, the displacement and/or replacement collisions are accompanied by chemical disordering. Two chemical disordering mechanisms involve : (1) replacement collisions along mixed atom rows ; and (2) the recombination of displaced atoms with vacancies on the "wrong" sublattice.

The HVEM has been used for measuring the change in long-range order parameter S of alloys during electron irradiation, and results have been discussed in terms of the chemical ordering and/or disordering mechanisms.

However, the superlattice intensity method has mostly been used for measuring S, which is the electron microscopy analog of the classical X-ray method. This method is very convenient to use, but dynamical electron diffraction effects produce serious ambiguities in experimental data. Kinoshita *et al.* [8], on the other hand, proposed a method of determining S from measurement of thickness fringes in electron micrographs. They applied it to clarifying the dominant mechanism for electron irradiation-induced chemical disordering of Fe-48.6at%Al which has B2-type superlattice and a high concentration of structure vacancies [9]. The extinction distance of the 100 superlattice reflection of Fe-48.6at%Al at the exact 200 Bragg position depends more strongly on S as the electron energy increases. The relative positions of the thickness fringes in 100 and 200 dark-field micrographs taken at the exact 200 Bragg condition were related to S by the many-beam dynamical theory with an appropriate choice of atomic scattering factors based on the experimental results. The variation under irradiation was measured for irradiation along directions near <100> and <110> with electrons of energy 0.25 - 1.25 MeV at room temperature. The values of S decrease with irradiation time t, and follow the equation

$$S = S_0 \exp(-K\varphi t), \tag{3}$$

where S_0 is the initial value of S, K the chemical disordering cross-section which can be expressed in units of barns and φ the electron flux. The values of K increase with increasing energy of electrons and are independent of irradiation directions. Equation (3) is also supported by theoretical predictions based on disordering mechanisms (1) and (2). With the use of the electron-atom collision theory the theoretical cross-section K based on mechanism (1) depends strongly on irradiation direction, which is not shown by the experimental results. The successful application of mechanism (2) to the results suggests that recombination of displaced atoms with vacancies on the "wrong" sublattice is the dominant process for disordering in Fe-48.6at%Al alloy, which contains a high concentration of structure vacancies.

4. IRRADIATION-INDUCED PRECIPITATION AND SPINODAL DECOMPOSITION

The effects of electron irradiation on phase stability have been more extensively studied in alloys, where displacements are solely due to direct displacement, not only because of scientific interest, but also for the assessment of nuclear materials. Two types of irradiation-induced precipitation have been found in many systems, and a number of mechanisms have been suggested to explain these phenomena. One is inhomogeneous precipitation around point defect sinks. This type of irradiation-induced precipitation has been successfully interpreted as resulting from the accumulation of solute atoms that have drifted toward defect sinks or the matrix. The other is homogeneous in the form of coherent or incoherent precipitates. A brief introduction to our new phenomena and possible mechanisms of homogeneous irradiation-induced phase transformation is given here [3, 4, 5, 10].

Electron irradiation induces γ and/or γ' phases in Cu-1.2at%Be alloy above the solvus temperature (> 573 K) where fcc single-phase is expected in the phase diagram. The irradiation-induced precipitation is observed at higher temperatures as the electron flux φ is increased. The nucleation of precipitates is completed within 100 s from the beginning of irradiation, and the density stays constant for incresing irradiation time t. The saturated density of precipitates C_P is proportional to $\varphi^{1/2}$, and the size of precipitates D_P reaches a plateau with t after linear growth in the early period, $t \leqq t_0$, of the irradiation. The value of t_0 increases with increasing φ and irradiation temperature T. In α Cu-Be alloys Be atoms may form mixed dumbbell interstitials (MDIs), and di-MDI may be stable. On the assumption that a di-MDI and/or a complex of an impurity and the di-MDI act as a nucleation site of the precipitate and the growth of precipitates is due to the flow of MDIs into them, the behavior of precipitates, which is analogous to the nucleation and growth process for interstitial loops in metals, may be understood [10].

Electron irradiation also induces a modulated structure in Fe-14at%Mo even at temperatures higher than the spinodal temperature ($\sim$ 680 K) of the alloy [3]. The modulated structure is along the <100> direction and accompanies satellite spots along the same direction on the corresponding diffraction pattern. The wavelength of the modulated structure λ remains constant for increasing irradiation time after rapid formation of the modulated structure. Such kinetic behavior, according the Cahn-Hilliard theory, suggests a modulated structure being induced by spinodal

decomposition. The Cahn-Hilliard theory gives the wave number of modulated structure β_m $(2\pi/\lambda)$ in terms of the spinodal temperature T_S as

$$\beta_m^2 \propto (T - T_S), \tag{4}$$

where T is the annealing temperature. If Eq.(4) holds for spinodal decomposition under irradiation, a plot of observed β_m^2 versus T, which is irradiation temperature in this case, should be linear and should intersect the T-axis at T_S. The plot shows a decrease in β_m^2 with increasing T and abrupt changes around 600 K. Below and above 600 K the kinetics of interstitial loops confirms, respectively, Eqs.(1) and (2), showing vacancies sufficiently mobile above $\sim$ 600 K. The irradiation-induced spinodal decomposition, therefore, is strongly related to the behavior of point defects, and is presumably due to the relaxation of the coherency strain in composition modulation with point defects [4, 5].

5. IRRADIATION-INDUCED CRYSTALLINE-AMORPHOUS TRANSFORMATION IN CERAMICS [11]

In order to provide valuable insights into the mechanism of irradiation-induced amorphization, single (S) and/or sintered (P) graphite (S, P), SiC (S, P), ZrC (P), TaC (P), WC (P), BN (P), Si_3N_4 (P), AlN (P) and ZrO (P) were irradiated at temperatures from 130 to 300 K in the HVEM with 1 MeV electrons up to 2×10^{26} electron/m^2. None of those crystals except graphite is amorphized at 300 K. At 130 K, however, SiC other than graphite is completely amorphized. The required fluence is approximately constant at temperatures below 230 K. At temperatures between 230 and 300 K, the required fluence increases very quickly with irradiation temperature. The required fluence was also determined at 130 K as a function of electron energy and electron flux ; it is independent of electron flux, but decreases with increasing electron energy. Thus, the cross-section for amorphization decreases with increasing electron energy, as that for elastic collisions does.

Approaches on the basis of bond type or homologous crystallization temperature were considered as an empirical guide to whether substances will amorphize on ion impact. The impact zone of a 1 MeV electron,

however, can not be regarded as a liquid zone which is indispensable for the homologous crystallization temperature criterion. Therefore, the production of cascades is not the necessary condition for the irradiation induced amorphization, and the bond type criterion seems to be the best. Accumulation of defect concentration $\geqq$ 10% may lead to amorphization. In the case of electron irradiation, the maximum defect concentration of $1/Z$, Z being the number of sites within a spontaneous recombination volume, is expected. However, the condition such as $Z \leqq 10$, which achieves the critical defect concentration, is not realistic. Structural topology, whose importance was originally pointed out for amorphization of SiO_2, may play an important role for stabilizing the critical defect concentration.

6. CONCLUSIONS

Energetic particles induce point defect clustering and chemical disordering. In some cases, they also induce phase transformations, such as precipitation, spinodal decomposition and amorphization. The electron microscope, in particular the HVEM, provides many experimental advantages for investigating radiation effects. Our recent progress in studies on irradiation-induced transformation in alloys and ceramics is reviewed.

REFERENCES

[1] M.J.Makin : *Phil. Mag.*, 18 (1968) 491.

[2] M.Kiritani and H.Takata : *J. Nucl. Mat.*, 69/70 (1978) 277.

[3] C.Kinoshita, K.Nakai and S.Kitajima : *J. Materials Science Forum*, 15-18 (1987) 949.

[4] K.Nakai, C.Kinoshita and and S.Kitajima : *Proc. of XIth Int. Cong. on Electron Microscopy*, Kyoto, Japan, (1986) p.1109.

[5] K.Nakai, C.Kinoshita and and S.Kitajima : *Proc. of XIth Int. Cong. on Electron Microscopy*, Kyoto, Japan, (1986) p.1111.

[6] C.Kinoshita, K.Hayashi and S.Kitajima : *Nucl. Inst. Meth.*, B1 (1984) 209.

[7] C.Kinoshita, K.Hayashi and T.E.Mitchell : *Adv. Ceram.*, 12 (1984) 490.

[8] C.Kinoshita, T.Mukai and S.Kitajima : *Acta Cryst.*, A33 (1977) 605.

[9] T.Mukai, C.Kinoshita and S.Kitajima : *Phil. Mag.*, A47 (1983) 255.

[10] K.Nakai, C.Kinoshita, S.Kitajima and T.E.Mitchell : *J. nucl. Mat.*, 133/134 (1985) 694.

[11] C.Kinoshita, K.Miyata, N.Nishi, K.Nakai and S.Kitajima : *Proc. of XIth Int. Cong. on Electron Microscopy*, Kyoto, Japan, (1986) p.1097.

II.4 IRRADIATION EFFECT ON ION CONDUCTIVITY OF LITHIUM OXIDE

Kenji NODA, Yoshinobu ISHII, Hisayuki MATSUI*,
Satoshi SUZUKI*, Mikio HORIKI* and Hitoshi WATANABE

Department of Fuels and Materials Research, Japan Atomic Energy Research Institute, *Faculty of Engineering, Nagoya University

1. Introduction

Lithium oxide (Li_2O) is a very attractive candidate of a solid tritium breeder material of D-T fusion reactors, because of its high tritium breeding potential. Li_2O will be irradiated by neutrons with energies up to 14 MeV during operation of the fusion reactor, and a huge number of irradiation defects will be introduced in Li_2O by the high energetic neutrons themselves, triton (2.7 MeV) and helium ions (2.1 MeV) produced from $^6Li(n,\alpha)^3H$ reactions. These defects will induce swelling and cracking of Li_2O (1,2), and furthermore they may have a large influence on migration of tritium and helium as well as of lithium and oxygen atoms composing Li_2O.

Ion conductivity of Li_2O depends on impurities and lattice defects including the irradiation defects, and also reflects migration behavior (diffusion) of ions composing Li_2O. Recently, the ion conductivity of non-irradiated Li_2O was investigated in the temperature range from 570 to 1420 K to evaluate the self diffusion coefficients of lithium ions (3,4). In such studies it was found that there was a close relationship between diffusivity of lithium ions and that of tritium. So, the irradiation effect on the migration behavior of tritium as well as lithium ions can be studied by measuring the ion conductivity change due to the irradiation.

In the present study, the ion conductivity of a Li_2O single crystal specimen irradiated with oxygen ions was measured and the correlation between the ion conductivity and the irradiation defects or correlation between diffusivities of tritium as well as lithium ions and the irradiation defects were discussed.

2. Experimental

The specimen used was a thin plate of Li_2O single crystal (about 7 mm

in length, 8 mm in width and 0.3 mm in thickness). The specimen was annealed at 1270 K for 10 h in vacuum better than $1x10^{-3}$ Pa to eliminate OH^- ions or LiOH in/on the specimen. After the annealing, the specimen was mounted on the specimen holder as quickly as possible, and then the holder was set to the stage for the ion conductivity measurement in an irradiation vacuum chamber which was attached to the Tandem accelerator at JAERI.

The specimen was irradiated using the Tandem accelerator by oxygen ions with energy of 120 MeV. In the irradiation, the oxygen ion beam was projected to the specimen in the direction of thickness, and the projected range (penetration depth) of the oxygen ions irradiated for Li_2O is about 0.1 mm. So, a third part of the specimen in the direction of thickness was irradiated. Measurements of the ion conductivity along the direction perpendicular to the direction of the thickness were conducted "in-situ" in the irradiation chamber with the two-terminal ac method using YHP Model 4192 A or 4194 A impedance analyzer after interrupting sometimes the successive irradiation. The conductivity was determined by measuring the complex impedance in the range from 0.5 to 200 kHz. The total oxygen ion fluence of $3.5x10^{19}$ ions/m^2 was attained.

After the irradiation, the recovery behavior of the ion conductivity was investigated by isochronal annealing experiments. The specimen irradiated was heated for 90 min. at each annealing temperature from 520 to 570 K.

3. Results and discussion

Prior to the irradiation, the conductivity of specimen was measured in the temperature range from 411 to 519 K in the vacuum irradiation chamber. Fig. 1 shows typical examples of the complex impedance plots of the Li_2O specimen at various temperatures in the frequency range from 0.5 to 200 kHz. The bulk resistances are shown as the intersecting points of semicirculars with real axis (abscissa of Fig. 1). The relationships between the conductivity before the irradiation and reciprocal temperatures are shown with those extrapolated from the data of as-received and well-annealed Li_2O single crystal specimens measured by Ohno et al. in Fig. 2. The measurements were done two times (the first run and the second run). Both data are almost identical and slightly smaller than those of well-annealed specimen by Ohno et al. It was shown in the studies by Ohno et al. that the ion conductivity of Li_2O is very sensitive to the content of OH^- ions included in

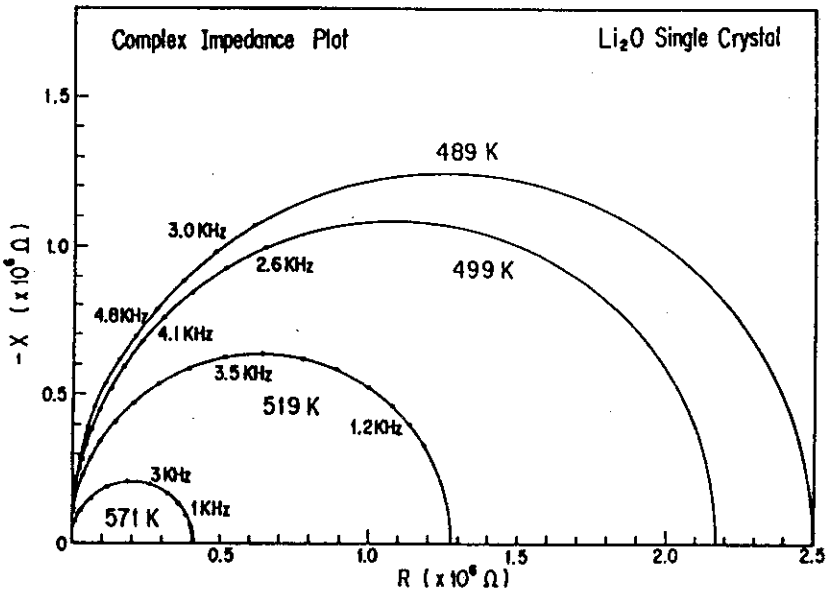

Fig. 1 Complex impedance plots for Li_2O at various temperatures in the frequency range from 0.5 to 200 kHz.

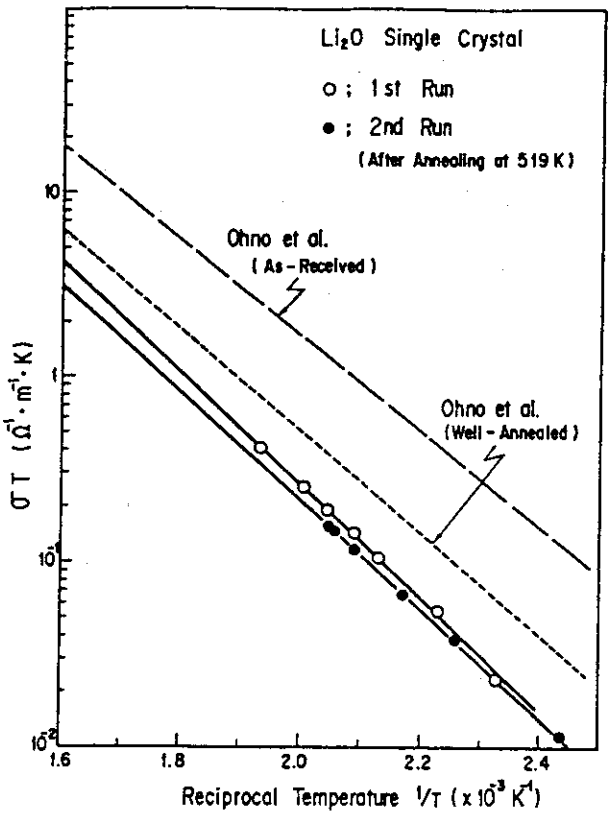

Fig. 2 Relationships between the ion conductivity before the irradiation and reciprocal temperatures.

the specimen and that the OH^- ions raise the conductivity (3). In view of this, the content of OH^- ions of the specimen in the present study was found to be smaller than that of well-annealed specimen in the study of Ohno et al.

Fig. 3 shows the ion conductivity at 489 K as a function of measurement time for each measurement at various fluence (7.1×10^{18}, 2.5×10^{19} and 3.5×10^{19} ions/m^2) together with that before the irradiation. Each measurement was started when the specimen temperature of 489 K was attained. The conductivities at each fluence and before the irradiation decreased with the measurement time and then the constant values of conductivities were attained after 10^4 s. This decrease of conductivity with measurement time was assumed to be due to desorption of water or OH^- ions near the surface of specimen, which arose from adsorption of water vapor in vacuum at temperatures lower than the measuring temperature (489 K) before the irradiation or during the irradiation. Such adsorption-desorption behavior of water near the surface of Li_2O in vacuum was confirmed by an experiment in which behavior of water or hydrogen near the surface of Li_2O single crystal specimen in vacuum at various temperatures was studied with elastic recoil detection method using 2.0 MeV helium ions (5). Consequently, the constant values for each measurement can be regarded as the ion conductivity of the specimen.

In Fig. 4 the ion conductivity of the Li_2O single crystal specimen at 489 K is shown versus the oxygen ion fluence. The conductivity decreased with the fluence in the examined fluence range (up to 3.5×10^{19} ions/m^2). This suggests that diffusivity of lithium ions is decreased by the irradiation. If the diffusion of lithium ions is closely related to that of tritium, it can be said that the diffusivity of tritium is decreased by the irradiation, i.e., introduction of irradiation defects.

Recently, the diffusion coefficients of tritium in Li_2O single crystals were measured in the temperature range from 550 to 950 K (6). In the study, the values of diffusion coefficient below 570 K deviated to the slightly low values from the line of Arrhenius' plot which was fitted for the data above 570 K. This result is qualitatively in good agreement with the data obtained in the present study.

The recovery behavior of the ion conductivity was observed by measuring at 489 K after each annealing, and it is shown in Fig. 5. The decrease of conductivity due to the irradiation was completely recovered in the temperature range from 520 to 570 K. This recovery temperature range is similar to

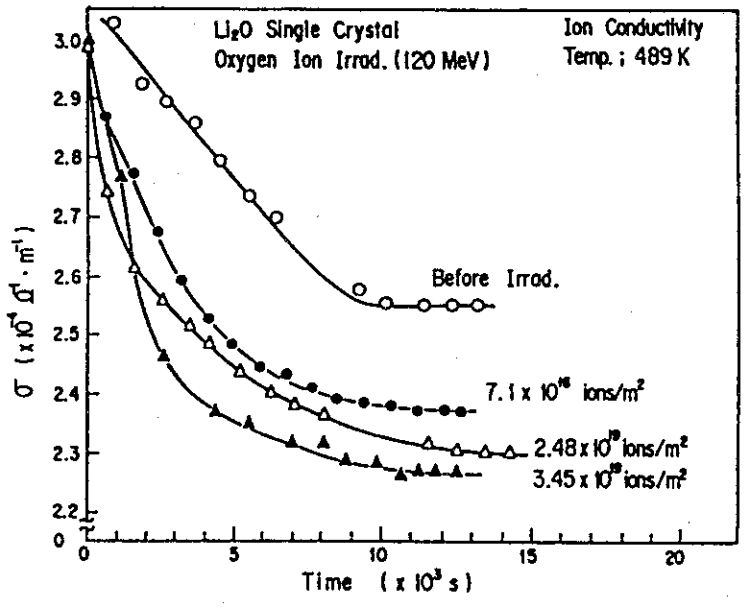

Fig. 3 The ion conductivity of Li_2O at 489 K versus measurement time for each measurement at various fluences and those before the irradiation.

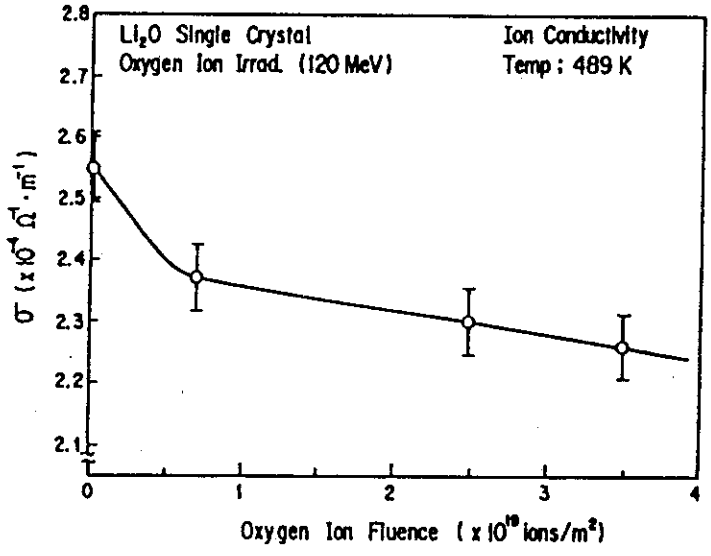

Fig. 4 The ion conductivity of Li_2O at 489 K versus the oxygen ion fluence.

that of the F^+ centers which are predominant irradiation defects in Li_2O (7-9).

The ion conductivity of Li_2O reflects migration behavior of lithium ions(i.e., mobility and concentration of lithium ions), since the diffusivity of lithium ions is much larger than that of oxygen ions. So, the conductivity can be expressed by

$$\sigma = Ne\,\eta_{V_{Li}}\,\mu_{V_{Li}} \qquad (1)$$

where N is the number of lithium ions, $\eta_{V_{Li}}$ mol fraction of lithium ion vacancies, $\mu_{V_{Li}}$ mobility of lithium ion vacancies. The lithium ion vacancies have negative charge, while the F^+ centers have positive charge. Therefore, the lithium ion vacancies are electrostatically attracted by the F^+ centers. The F^+ centers are immobile below their recovery temperature. Consequently, the decrease of ion conductivity (the decrease of diffusivity of lithium ion) can be attributed to the decrease of mobility of lithium ion vacancies due to retardation by the F^+ centers or the decrease of the number of mobile lithium ion vacancies due to trapping by the F^+ centers. However, the above-mentioned result is preliminary, and further investigations are required to clarify the irradiation effect on diffusivity of lithium ions or tritium and the mechanism of the irradiation effect.

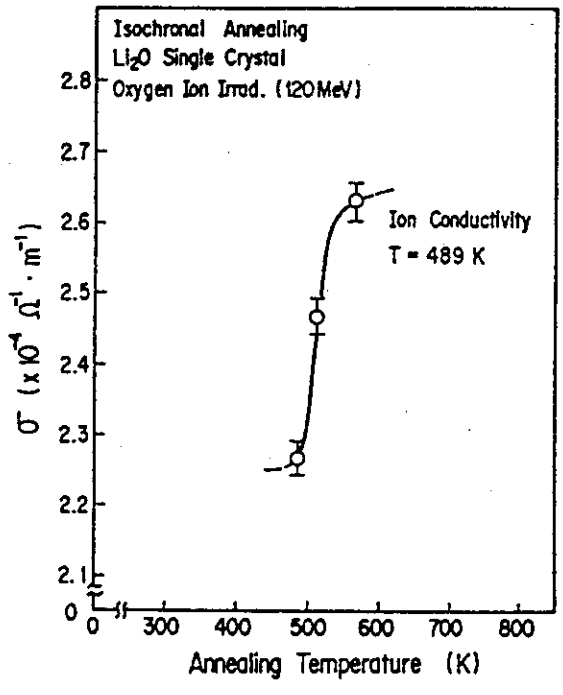

Fig. 5 The recovery behavior of the ion conductivity of Li_2O irradiated with oxygen ions.

Acknowledgment

The authors wish to express their thanks to Dr. T. Kondo, Dr. K. Shiba

and Dr. N. Shikazono for their interest in this work.

References

(1) G. W. Hollenberg: J. Nucl. Mater. 122-123 (1984) 896.
(2) G. W. Hollenberg and D. L. Baldwin: J. Nucl. Mater. 133-134 (1985) 242.
(3) H. Ohno, S. Konishi, K. Noda, H. Takeshita, H. Yoshida and H. Watanabe: J. Nucl. Mater. 118 (1983) 242.
(4) H. Ohno, S. Konishi, T. Nagasaki, T. Kurasawa, H. Katsuta and H. Watanabe: J. Nucl. Mater. 133-134 (1985) 181.
(5) L. M. Howe, J. A. Sawicki, K. Noda and M. H. Rainville: private communication.
(6) T. Tanifuji, K. Noda, T. Takahashi and H. Watanabe: J. Nucl. Mater. in press.
(7) K. Noda, K. Uchida, T. Tanifuji and S. Nasu: J. Nucl. Mater. 91 (1980) 234.
(8) K. Noda, K. Uchida, T. Tanifuji and S. Nasu: Phys. Rev. B 24 (1981) 3736.
(9) K. Noda, Y. Ishii, H. Matsui and H. Watanabe: Radiat. Eff. 97 (1986) 297.

II.5 DETERMINATION OF THE PHYSICAL STATE OF IMPLANTED HYDROGEN IN Si BY RBS COMBINED WITH ERD USING ^{4}HE IONS

Sadae YAMAGUCHI, Akio SAGARA*, Khoji KAMADA*, Yutaka FUJINO**

Institute for Materials Research Tohoku Univ., *Institute of Plasma Physics Nagoya Univ., **Department of Nuclear Engineering Tohoku Univ.

Rutherford backscattering spectrometry (RBS) combined with elastic recoil detection (ERD) is applied to the characterization of hydrogen implanted into Si and He implanted Si. By monitoring the hydrogen concentration in the target with ERD, backscattering measurements of ^{4}He ion provide the information of the energy loss in the implanted hydrogen atoms. The results indicate that there are some difference in energy loss between gaseous and solid state.

1. Introduction

In the past few years, the behavior of hydrogen atoms implanted into materials has become a target of research from the technological interest in the field of fusion research. In plasma machines, high fluxes of hydrogen isotopes are implanted into the first walls surrounding the plasma. The retention in the surface layer, the diffusion into bulk material, and the release of the hydrogen are of importance for the plasma composition, the mechanical properties of the wall and the tritium inventory in future devices.

For non-implanted systems, the behavior of hydrogen in metals has been described in numerous papers and reviews(1). In the defect-free metal, hydrogen atoms are dissolved interstitially and hence are highly mobile even arround room temperature. For ion-implanted systems, however, the formation of gas bubble or hydride precipitates near the surface is favoured compared to the diffusion into the bulk, due to the large local concentration achievable by ion implantation. The knowledge of physical state (gas, liquid or solid) and chemical binding of the implanted ions is important to understand blistering and hydrogen embrittlement of the first wall.

In this paper, we report the determination of the depth distribution of

15-keV protons implanted into Si and He implanted Si at room temperature by both Rutherford backscattering and elastic recoil detection using ^{4}He ions, and suggest the possibility to study the physical state of the implanted ions through the change of stopping power for fast charged particles in medium.

2. Experimental

The high energy ion beam analyses were carried out in a vacuum chamber which was connected to a 2.5 MV Van de Graaff accelerator for analysis and a 200 kV Cockcroft-Walton accelerator for implantation (Fig. 1). A system pressure of less than 1×10^{-8} Torr was maintained during the analysis and implantation. The hydrogen concentration was measured by elastic recoil detection as well as Rutherford backscattering. Two surface barrier detectors were used in the experiments. One of them was installed at a scattering angle of 20° and equipped with a Mylar absorber of 9 μm thickness in order to suppress elastically scattered ^{4}He ions. This detector provided recoil proton spectra. The second detector measured the back scattered ^{4}He ions at 150° scattering angle.

3. Results and discussion

Two types of targets have been used in this investigation: (1) silicon single crystal [abbreviated as Si]; (2) silicon single crystal preimplanted with 20-keV ^{4}He at fluence of 1×10^{17} He/cm^2 [He implanted Si].

Figure 2 and 3 shows a backscattered energy distribution of 1.5 MeV He for Si targets before and after the implantation of 20-keV helium ions at a fluence of 1×10^{17} He/cm^2 at 293K in a ramdom direction, respectively.

From the comparison between Fig. 2 and Fig. 3, it will be

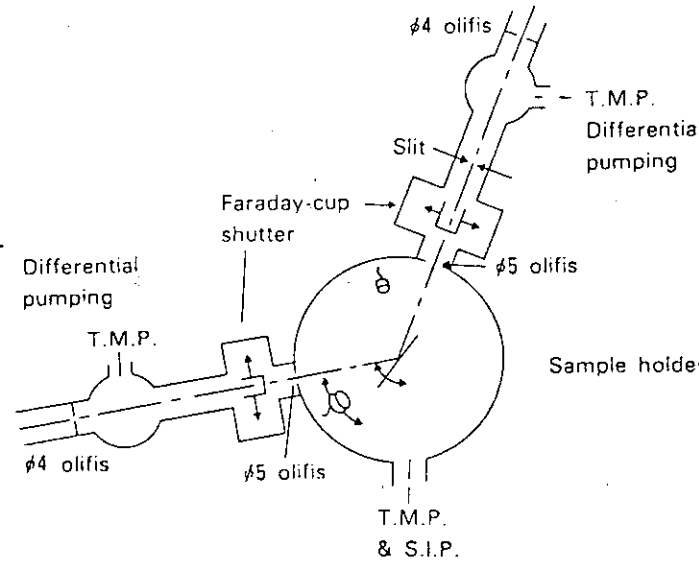

Fig. 1 Experimental setup

seen that the implantation of light ions lead to a decrease of the electronic stopping power at the depth corresponding to the projected range for the implanted ions(2).

The implantation of 20-keV protons has been carried out to a fluence of 6×10^{17} H/cm^2 succeeding the RBS measurements described above. Rutherford backscattering spectra as well as the recoil proton spectra have been taken

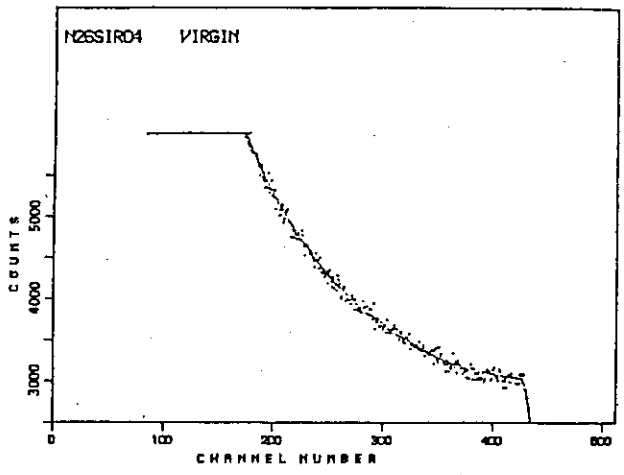

Fig. 2 Backscattered energy distribution from Si target before He implantation.

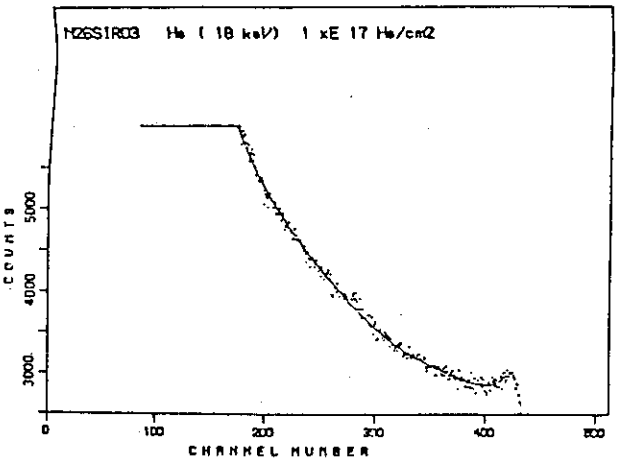

Fig. 3 Backscattered energy distribution from Si target after He implantation.

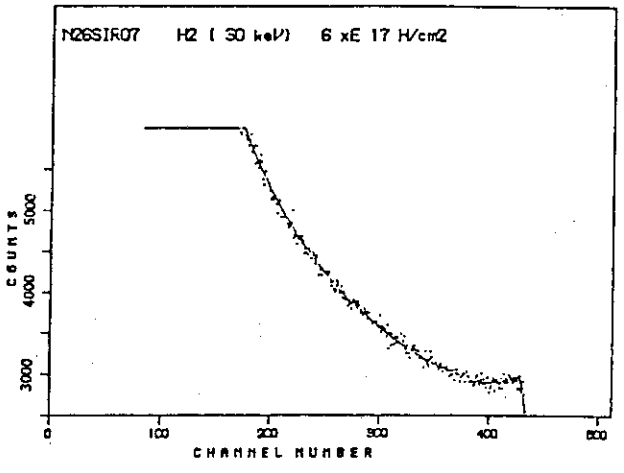

Fig. 4 Backscattered energy distribution from Si target after H implantation.

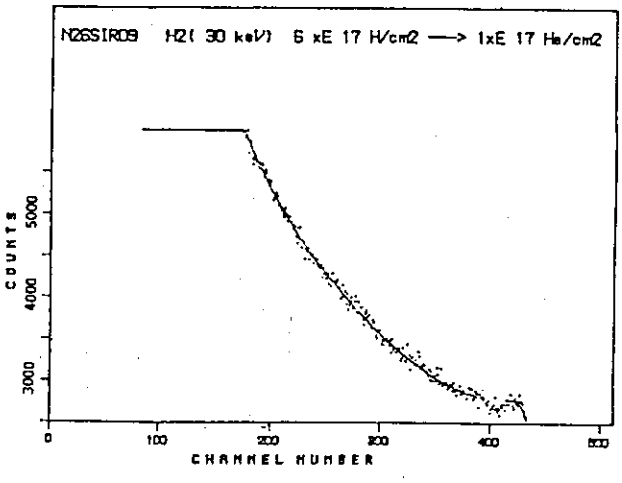

Fig. 5 Backscattered energy distribution from He implanted Si after H implantation.

simultaneously after the proton implantation. The same angle of incidence and deflection have been used for all measurements.

Figure 4 and 5 shows a backscattering spectrum from Si and He implanted Si after the implantation with 20 keV proton to a fluence of 6×10^{17} H/cm^2, respectively. The backscattering yields from the H implanted specimens are clealy lower than those before the H implantation. If one assume the Bragg's rule to stopping power for the H implanted Si, the experimental ratio between the signal height in the energy spectrum is related to the H concentration as follows,

$$\frac{H(E_i)_{Virgin} - H(E_i)_{Imp.}}{H(E_i)_{Imp.}} = \frac{N_H}{N_{Si}} \cdot \frac{[\varepsilon]_H}{[\varepsilon]_{Si}}$$

where N_H/N_{Si} is the concentration ratio of hydrogen and silicon. The quantities $[\varepsilon]_{Si}$ and $[\varepsilon]_H$ are the backscattering cross section factors for the probe ions at E_i on Si and H, respectively.

Target	Virgin	Implanted
ERD	2.4	3.2
RBS(Gas)	2.05	3.0
RBS(Solid)	2.5	3.6

Table 1 H concentration

Figure 6 shows the concentration distribution of the implanted hydrogen evaluated from the backscattering spectra, here we adopt the stopping power for gas state hydrogen as given by Ziegler. From the ERD measurements, we determined independently the hydrogen concentration at the same time. The results are listed in Table 1, together with the results obtained from the RBS measurements using both the stopping power for solid state and that for gas state. It will be seen from this table that the hydrogen atoms in the He implanted samples may be in gas state, whereas the hydrogen in the Si samples without the He implantation are in solid state. The value of stopping power for hydrogen in the solid polymar of hydrocarbon is smaller than that in the corresponding monoatomic gas as well as those of Ziegler.

It is well established that the implanted He precipitate as gas bubble. The hydrogen atoms implanted into He implanted samples may be trapped in the He bubble as the gas state.

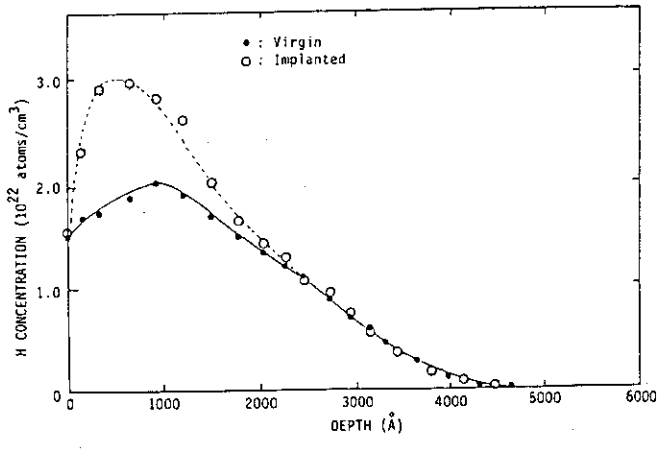

Fig. 6 H distribution for Si and He implanted Si determined by RBS.

References
(1) "Hydrogen in Metals" ed. G. Alefeld and J. Volkel, (Springer, 1978)
(2) J. Roth et al., Appl. Phys. Lett. 25 (1974) 643.

II.6 ANALYSIS OF Nb-Mo ALLOY WITH ENERGETIC HEAVY IONS

Hiroshi NARAMOTO, Kiyoshi KAWATSURA, Masao SATAKA, Yasuaki SUGIZAKI, Yohta NAKAI, Kunio OZAWA*, Sadae YAMAGUCHI**, Yutaka FUJINO** and Matto AOKI***

Department of Physics, Japan Atomic Energy Research Institute,*Energy Research Laboratory, Hitachi Ltd., *Faculty of Engineering, Tohoku University, ***The Institute for Solid State Physics, The University of Tokyo

1.Introduction

High eneregy heavy ions interact with atoms in solids in the various manners like high density excitation of electrons, elastic scattering and nuclear excitations depending on the projectile energy and the projectile-target combination. In the crystalline solids, incident ions feel the axial potential arising from the atomic strings, and these are anomalously transmitted along the crystallographic direction, which is called channeling. The above processes can be utilised to analyse the behavior of specific atoms in crystalline solids, which will become more effective than the standard ion beam analysis(1).

The location of hydrogen isotopes is inevitable information to understand the diffusional properties in the energy devise materials(2). Much interest has been devoted to look at the atomic behavior of hydrogen isotopes in the transition metals(3). However, the details of site preference in crystal lattice has not been clarified satisfactorily. The addition of substitutional solute atoms expands the solubility limit of hydrogen in Nb, which suggests the strong interaction of hydrogens with the solute atoms(4).

In order to investigate this situation more microscopically, are employed two complementary methods, IBA(ion beam analysis) with high energy heavy ions and PAC(perturbed angular correlation of γ-rays). The present report describes the results of IBA on $(Nb_{0.8}Mo_{0.2})D_{0.075}$ alloy specimen using high energy ^{35}Cl ions. RBS(Rutherford Backscattering Spectroscopy), PIXE (Parti-cle Induced X ray Emission) and NRA(Nuclear Reaction Analysis) are utilised to distinguish the information from the constituents, and in addition, are also shown the preliminary results of PAC experiment using 100-Pd/100-Rh nuclei introduced through the nuclear fusion reactions of ^{12}C ions with ^{93}Nb in a target.

2.Experimental procedure

Nb-Mo alloy with 20 % Mo contents was grown by an electron beam zone melting technique under the ultra high vacuum, and the solute content of Mo was determined to be about 20 % in atomic fraction through the PIXE process. Three kinds of ion beams were used to detect the three kinds of elements distinguishably in $(Nb_{0.8}Mo_{0.2})D_{0.075}$ alloy. In this alloy system, a conventional RBS analysis is not effective, and 80 MeV ^{35}Cl ions from a JAERI tandem accelerator were bombarded to specimens to induce the characteristic x-rays from Nb and Mo atoms. Deuterium atoms dissolved thermally into specimens were analysed using the nuclear reactions of D with 750 keV ^{3}He ions, $D(^{3}He,\alpha)H$. Protons were also supplementarily used to compare the PIXE results with those by ^{35}Cl ion bombardment. The details of experimental arrangement were already described elsewhere(5). The separation of two adjacent peaks of Kα x-rays from Mo and Nb atoms was performed using a Si(Li) x-ray detector with the resolution of 163 eV for Mn Kα x-rays(5.9 keV).

For the PAC experiment, thin foil targets of Nb with 10 um thickness were prepared and were irradiated with 100 MeV ^{12}C ions to introduce the 100-Pd/100-Rh nuclei through the fusion reactions of ^{12}C with ^{93}Nb. In the introduction of PAC probes, the target temperature is the critical factor to control the induced defects and to incorporate hydrogen isotopes into a specimen by diffusion within a vacuum chamber for the ion beam analysis. The two dimensional temperature distribution of a foil specimen was measured under the inbeam condition of ^{12}C ions detecting the photons in the infrared region. A specially designed detecting system(6T61) with a HgCdTe detctor was prepared for two dimensional scanning by Nihondenki Sanei Co. For the PAC measurement, a new γ-ray detectingsystem was developed to collect the angular correlation information with four γ-ray detectors which are placed perpendicularily with each other. Fig. 1 illustrates the block diagrams of this system. In this system, Both of 6 angular correlation and 4 energy data are obtained simultaneously.

3.Results and discussion

Fig. 2 shows x-ray spectra from $Nb_{0.8}Mo_{0.2}$ alloy specimen induced by 80 MeV ^{35}Cl bombardments. The yield in the lower energy region was reduced to avoid the influence of pile-up in the spectra using Al filter with 51 μm thickness. In this figure, it is clearly seen that the x-ray yield decreases drastically with changing the incident beam direction from random

to <100> crystallographic axis, and that the K x-ray peaks from Nb and Mo are well separated. These results suggest the channeling analysis using the PIXE process is effective even in Nb-Mo alloy crystal. As a result of multiple ionization by ^{35}Cl ion bombardment, some shift of about 100 eV is observed toward the higher energy side for the peak energies of Nb and Mo characteristic x-rays. The Mo content was determined to be about 20 %.

Fig. 3 shows the angular scans around the <100> axis for Kα x-rays from Nb and Mo atoms in alloy and pure Nb crystals when bombarded with 80 MeV ^{35}Cl ions. In this figure, it is observed that the full widths at the half maximum in the channeling dip curves are the same within the experimental error for Nb and Mo, and these are much smaller than that in pure Nb crystal shown with the data guided by a solid line. This decrease may be attributed to the lattice distortion introduced by the addition of solute elements

In the energy region mentioned above, the cross-section of Rutherford scattering is decreased to about 2 % of that for 2 MeV He ions, and the analysis of backscattered ^{35}Cl ions is not effective. In order to make sure the above results, the RBS analysis was made using 1.6 MeV protons. Fig. 4 shows the yield change of backscattered protons when scanned around the <100> axis of pure Nb((a)) and of $Nb_{0.8}Mo_{0.2}$ alloy((b)). The incident 1.6 MeV protons can not distinguish Nb and Mo atoms because of the elastic scattering kinematics, but it is confirmed also in the RBS analysis that the addition of Mo solutes makes the dip width of channeling decreased from 1.29° to 1.15°.

After the above measurements, deuterium atoms were introduced thermally to the content of about 7.5 %. In this specimen, the channeling experiment combined with PIXE process was also made around the <100> axis using 80 MeV ^{35}Cl ions. Fig. 5 shows the results of these angular scans. Data points with open and solid circles correspond to the x-ray yields from Nb matrix and the solute Mo atoms, respectively. The data points with triangles are from bremsstrahlung, but this result is not discussed anymore. In this figure, it is observed that the widths of the channeling dip curves are widened up almost to that of pure Nb, and that some noticeable difference is induced between the dip curves for Nb and Mo. The above result probably reflects that the introduction of deuterium atoms can relieve the internal strain around the under-sized Mo atoms. This interpretation is consistent with the dramatic increase of the terminal solubility of hydrogens in Nb-Mo alloy system(4).

The result of the previous figure also suggests the existence of strong interaction of Mo with deuterium, which will influence the site preference. To make clear this problem, the channeling experiment was made around the <100> axis, the (110) and (100) plane in $(Nb_{0.8}Mo_{0.2})D_{0.075}$alloy specimen for the incident 0.75 MeV ^{3}He ions. Fig. 6 shows the planar= scanned curves around the (110) and (100) plane. The yield of backscattered He ions forms a dip as shown with a solid line. However,the reaction yield from deuterium atoms forms a peak just around the (110)plane, and on the contrary, the yield around the (100) plane shows the dip charactor. These results with the peaking of deuterium around the <100> axis indicates the octahedral occupation of deuterium atoms.

In order to investigate this site-preference from the microscopic point of view, we have started the PAC study with a rather preliminary experiment. Fig. 7 illustrates the temperature distribution of Nb foil specimen under the in-beam condition of ^{12}C ions. The position of beam spot (5 mmϕ) is denoted by a "+" mark, and the specimen size(10 $\times$ 10 mm^2) is illustrated with a square. This figure is printed with the color originally, and it is hard to recognise the distribution of temperature quantitatively. However, the side views of the temperature distribution along the x and y axis can be seen. The maximum temperature at the beam center was below 80 ℃ when the beam current was adjusted to about 15 pnA. With increasing the beam current, the temperature changes nonlinearly, and it is necessary to measure the distribution in each experiment. To avoid the effect of ion irradiation, rather higher beam current was used when the introduction of probe nuclei is made.

Fig. 8 shows the induced γ-ray spectrum through the nuclear fusion reaction of ^{12}C projectile with ^{93}Nb in a target foil. The spectrum feature is rather simple and most of the remaining peaks are associated with the 100-Pd/100-Rh transition as suggested by Sielemann et al. (6). The cascade transition of 100-Rh in the lower energy region(74.6 and 83.9 keV) was used for the PAC experiment.

Fig. 9 shows the time differential PAC(TDPAC) spectrum of Nb foil obtained using the above nuclear transition. The probe nuclei were introduced directly by ^{12}C ion irradiation with high intensity(50 pnA). The half life of the intermediate state in the probe nucleus is rather long (214 ns), and it is easy to do the the TDPAC measurements. The coincidence counting rate was detected by semiconductor detectors placed perpendicularily and paralelly with each other. For the two field directions, the

perturbation is expected to have a phase shift of 180°, and the asymmetry ratio R(t)=(N(180°,t)-N(90°,t))/(N(180°,t)-N(90°,t)) was calculated to eliminate the component of the exponential decay. In this figure, R(t) holds almost the zero level in the entire delay time region, which denies the existence of the electric field gradient coming from the irradiation-induced defects. ^{12}C ion irradiation with high intensity probably contributes to the defect recovery. From the preliminary experiment of PAC, it has become clear that the carbon ion irradiation with high intensity promotes the incorporation of the probes into the substitutional sites in niobium lattice without crystal defects. On the contrary,under the above irradiation-condition, it is very difficult to introduce hydrogens by diffusion within a chamber. Further trials will be made to solve the above difficulty.

References

(1) for example: J. W. Mayer and E. Rimini ed. : Ion Beam Handbook for Material Analysis(Academic Press, Inc., New York, San Francisco, London, 1977).

(2) S. Yamaguchi, K. Ozawa, O. Yoshinari, M. Koiwa and M. Hirabayashi: Nuclear Instr. and Meth., 168(1980)301.

(3) Y. Fukai and H. Sugimoto: Advances in Physics 34(1985)263.

(4) T. Matsumoto, Y. Sasaki and M. Hihara: J. Phys. Chem. Sol. 36(1975) 215.

(5) H. Naramoto, K. Ozawa, K. Kawatsura, M. Sataka, S. Yamaguchi and K. Masai: JAERI-M 85-104(1985)p.29.

(6) R. Sielemann, H. Metzner, R. Butt, S. Klaumünzer, H. Haas and G. Vogl: Phys. Rev. B25(1982)5555.

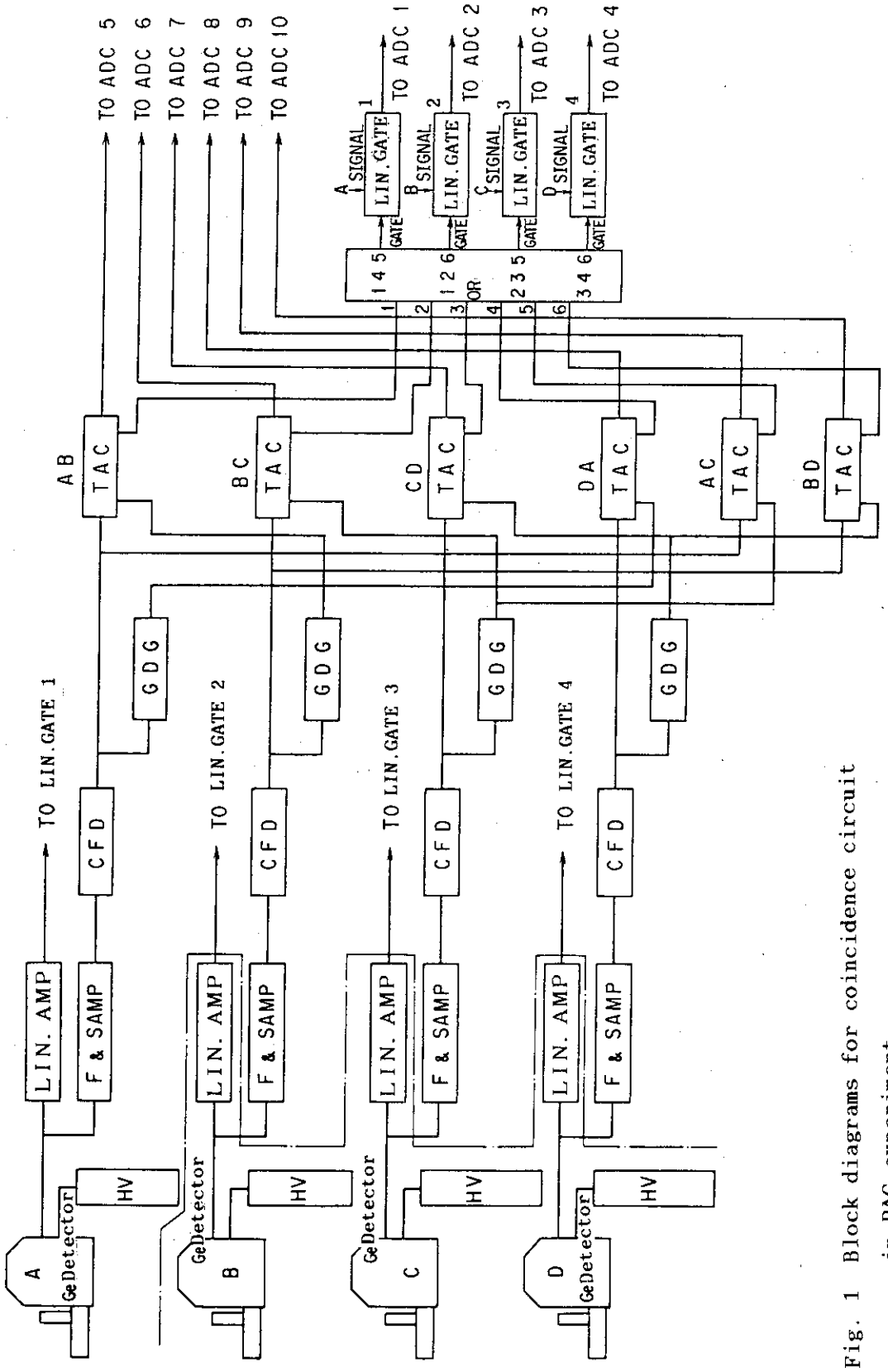

Fig. 1 Block diagrams for coincidence circuit in PAC experiment.

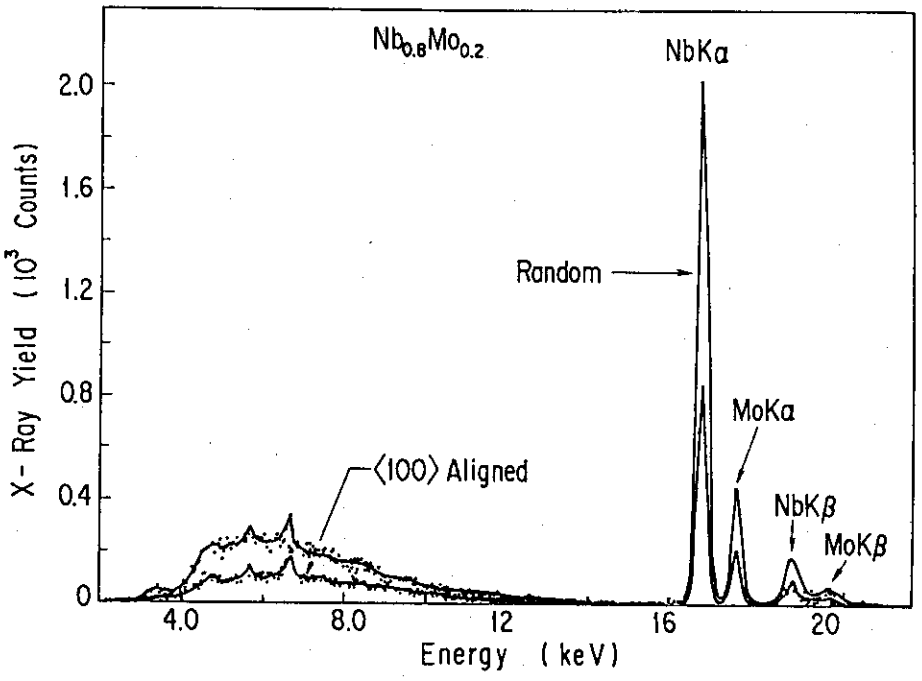

Fig. 2 Induced x-ray spectra from Nb-Mo alloy specimen bombarded with 80 MeV $^{35}Cl^{7+}$ ions. Spectrum with lower yield is ibtaibed in the <100> channeling condition.

Fig. 3 Angular scans of K x-ray yields around the <100> axis in Nb-Mo alloy and pure Nb crystal.

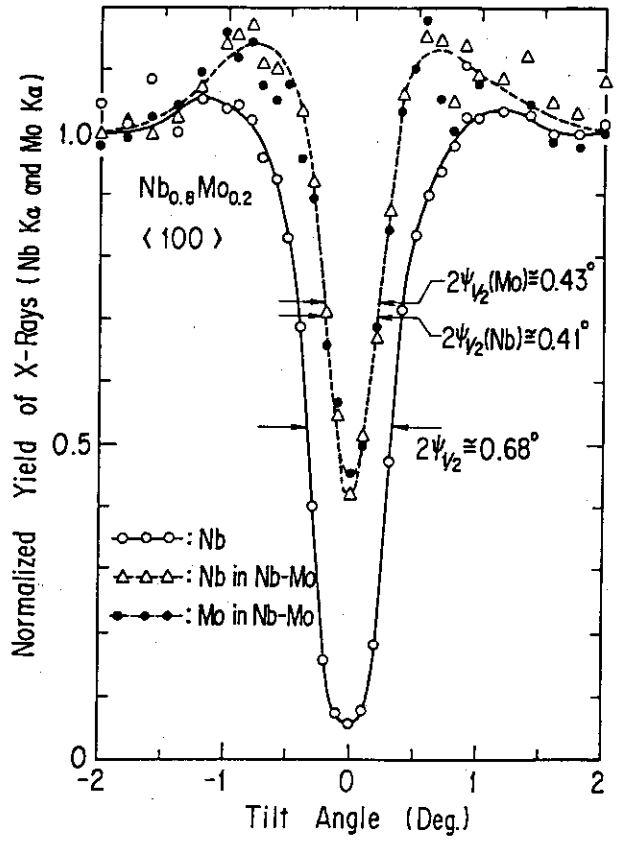

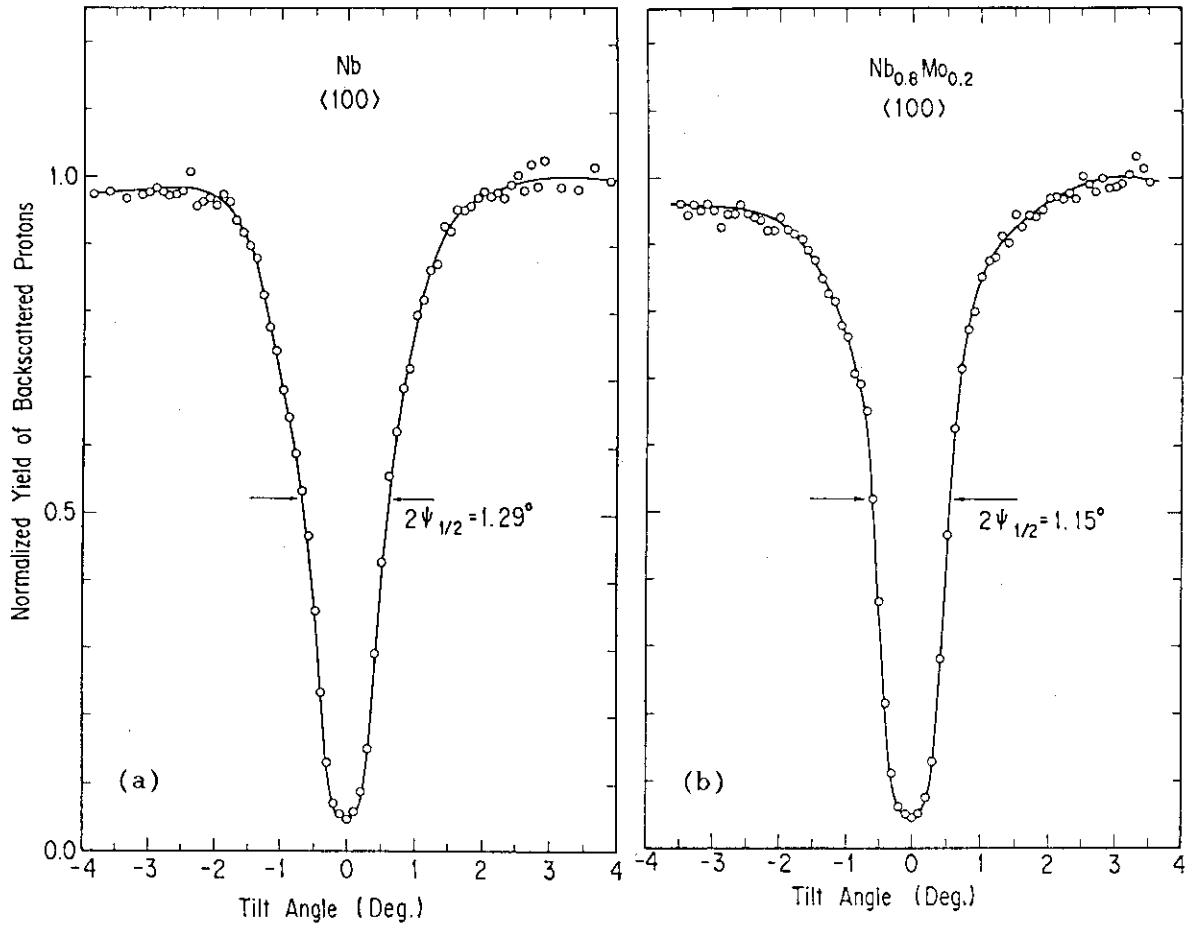

Fig. 4 Angular scans of back-scattered protons around the <100> axis. (a) and (b) for Nb and $Nb_{0.8}Mo_{0.2}$, respectively.

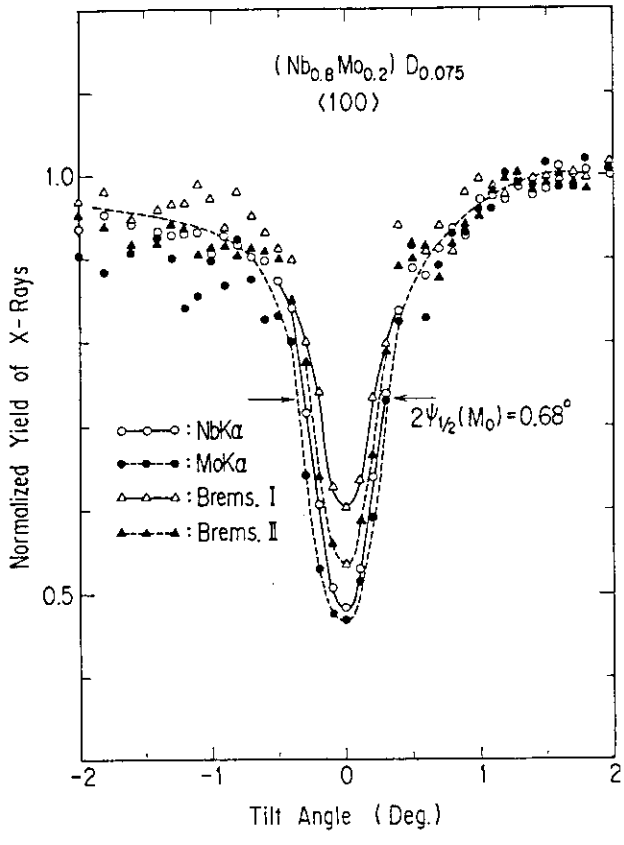

Fig. 5 Angular scans of K x-ray yields around the <100> axis in $(Nb_{0.8}Mo_{0.2})D_{0.075}$.

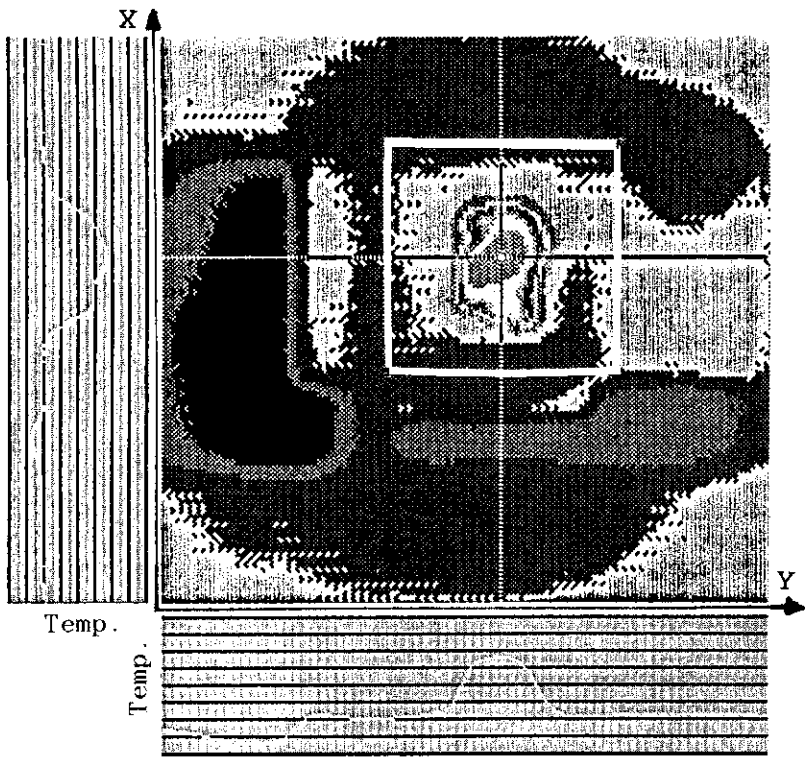

Fig. 6 Two-dimensional temperature distribution under 100 MeV ^{12}C ion irradiation. The maximum temparature is~80°C at the center.

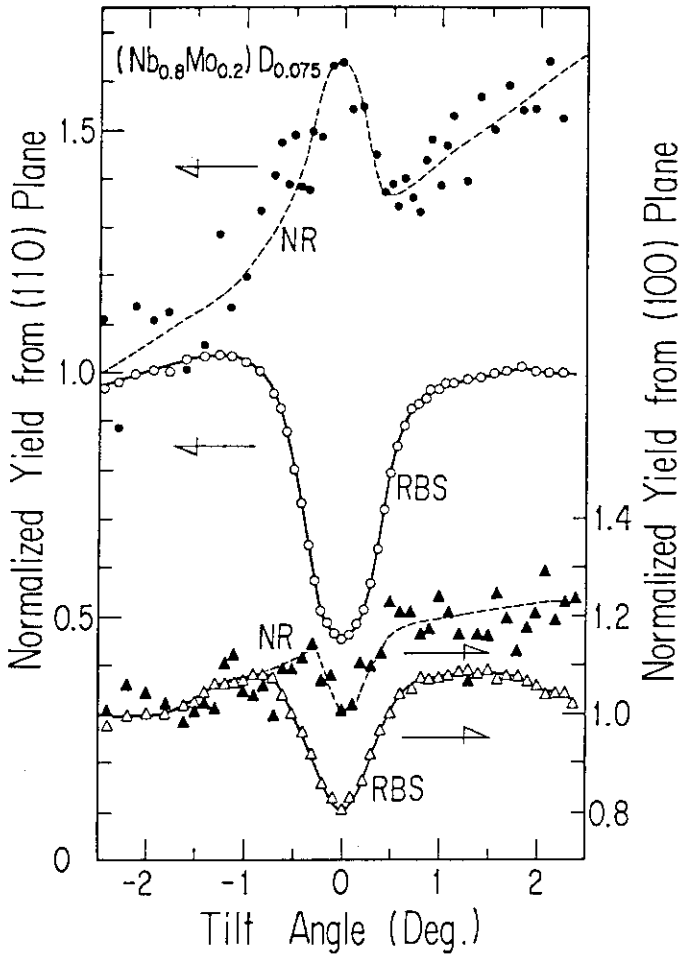

Fig. 7 Angular scans around the (110) and (100) axis of backscattered yield(solid line) and D(^{3}He, α)H nuclear reaction yield(dotted line) in $(Nb_{0.8}Mo_{0.2})D_{0.075}$.

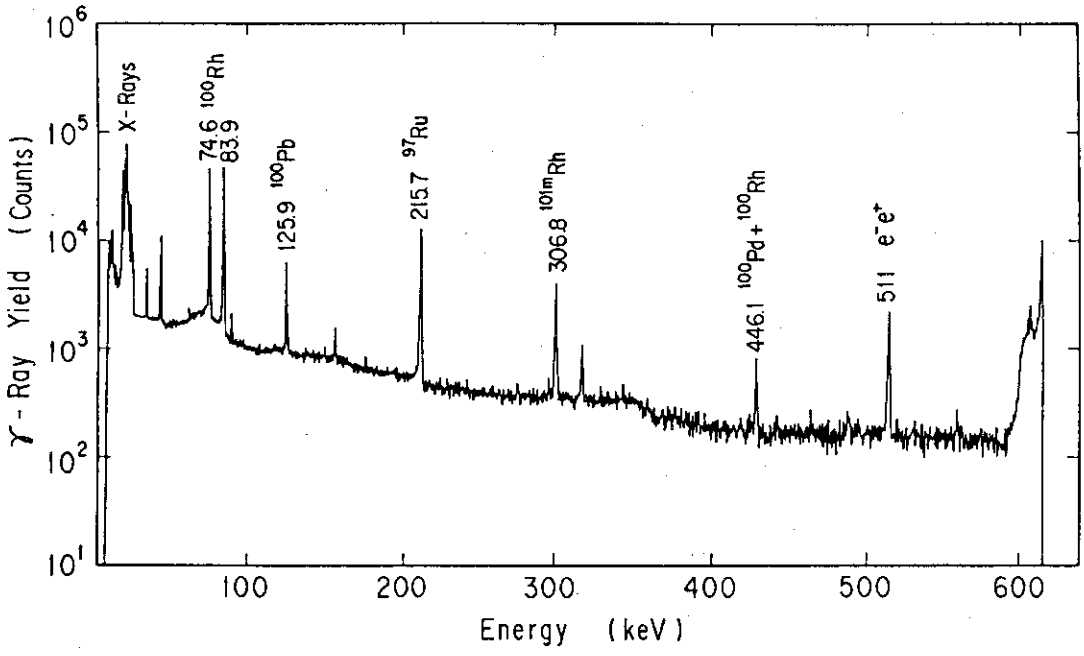

Fig. 8 Induced γ-ray spectrum in the low energy region from Nb target foil when bombarded with 100 MeV ^{12}C ions.

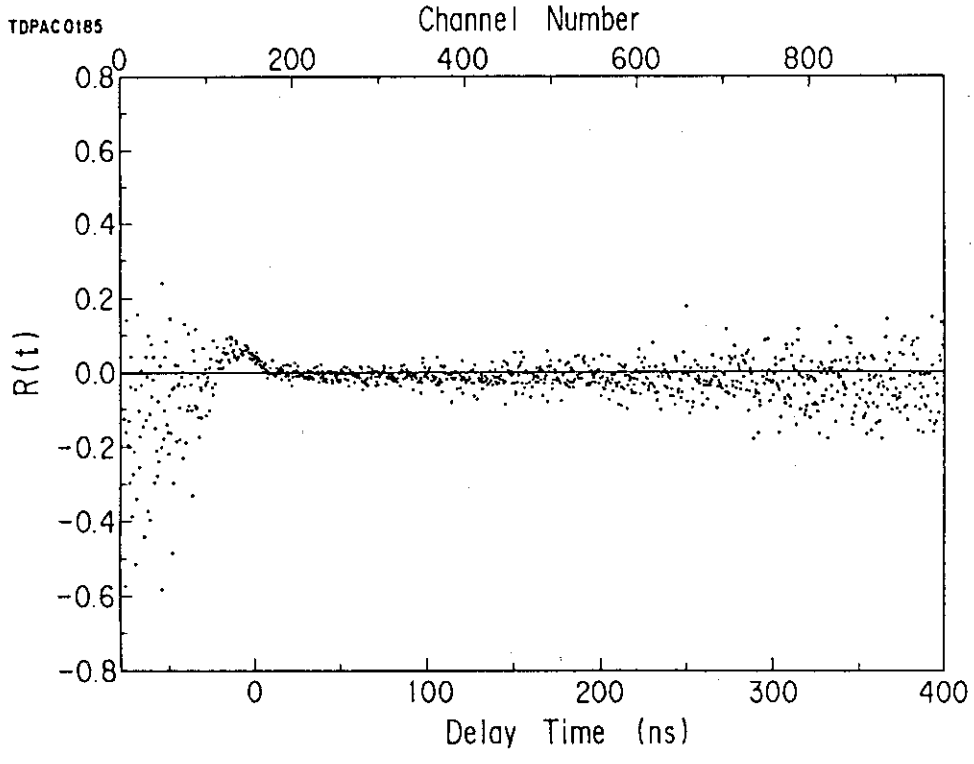

Fig. 9 R(t) spectrum in as-irradiated Nb when bombarded by 100 MeV ^{12}C ions. Measurement at RT.

II.7 MOSSBAUER (CEMS) STUDY OF ION IRRADIATION EFFECTS IN ALLOYS

Isao SAKAMOTO and Nobuyuki HAYASHI

Electrotechnical Laboratory

1. Introduction

Recently, it has been reported a large number of studies that has investigated the ion irradiation effects not only in the field of nuclear energy engineering but also in the fields of semiconductor technology and new materials innovation. In the former field the irradiation effects are sometimes useless and harmful for material's life. On the other hand, the irradiation effects in the latter fields are thought as useful one in improving metallurgical and electrical properties. In both cases, what matter is how to estimate the ion irradiation effects. The range of ions in solids is short and irradiation effects are restricted near the surface regions in solids. Many techniques have been used to detect ion irradiation effects, i.e., ion beam analysises such as Rutherford backscattering (RBS), x-ray diffraction, transmission electron diffraction (TEM) and so on.

To authors' knowledge we are the first who have investigated phase changes due to ion irradiation effects in alloys by means of internal conversion electron Mossbauer spectroscopy (CEMS). CEMS gives us selectively informations near the surface in solids, because the range of electron in solids is short. In the present work, we report the results of the ion irradiation effect in amorphous $Fe_{80}B_{20}$ (a-$Fe_{80}B_{20}$), boron film on Fe and type 304 stainless steel.

2. Experimental

A-$Fe_{80}B_{20}$ and SUS 304 were obtained from Allied Chemical Corp. and Good Fellow, respectively. The preparation of boron films on Fe samples were done by electron beam deposition. Their thickness were 1000 Å and 2000 Å. He^+ and Xe^+ ions were used to irradiate the alloys. These ions were accelerated by ETL 200 keV and 400 keV ion implantors. The temperature of samples did not rise above 140 ℃ for Xe^+ and 200 ℃ for

40 keV He^+ ion irradiation.

CEM spectra were measured at room temperature for all samples. A conventional Mossbauer spectrometer was used together with a source of approximately 50 mCi ^{57}Co in rhodium. The backscattered K conversion electrons (7.3 keV) and subsequent L Auger electrons (5.6 keV) emitted from ^{57}Fe were detected in a simple flow type gas proportional counter using He + 10 % CH_4 mixture. The electrons after struggling in solid outcome from the specimen surface. Therefore, the energy loss of outcoming electrons is roughly proportional to the depth where electrons are generated. This means that depth profiling of CEMS can be done by selecting the electrons energy with depth ranges such as 0 - 200 Å, 200 - 600 Å and $\geq$600 Å(1). The energy spectrum of outcoming electrons is shown in Fig.1. It should be noted that the electrons' range is comparable to ion ranges in solids and that CEMS is a very effective means to detect irradiation effect.

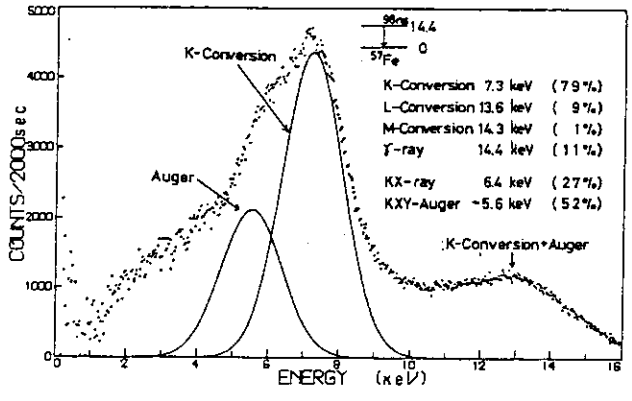

Fig.1 Pulse height spectrum of electrons emitted from 290 Å ^{57}Fe film.

3. Results and Discussion

3.1 Irradiation effect in a-$Fe_{80}B_{20}$

Amorphous materials are originally lack of long range orders and might be resistant to ion irradiation damage. We have investigated the ion irradiation effect in a-$Fe_{80}B_{20}$(2). The shiny side of a-$Fe_{80}B_{20}$ samples was irradiated with 40 keV He^+ ions to a dose range from 10^{17} to 10^{18} ions/cm^2. CEM spectrum of the as-received samples is shown in Fig.2 a). The spectrum, which is composed of well-defined but broadened lines, is commonly observed in amorphous magnetic solids. After 40 keV He^+ ion irradiations, the spectra have changed as shown in Fig.2 c) - e) depending

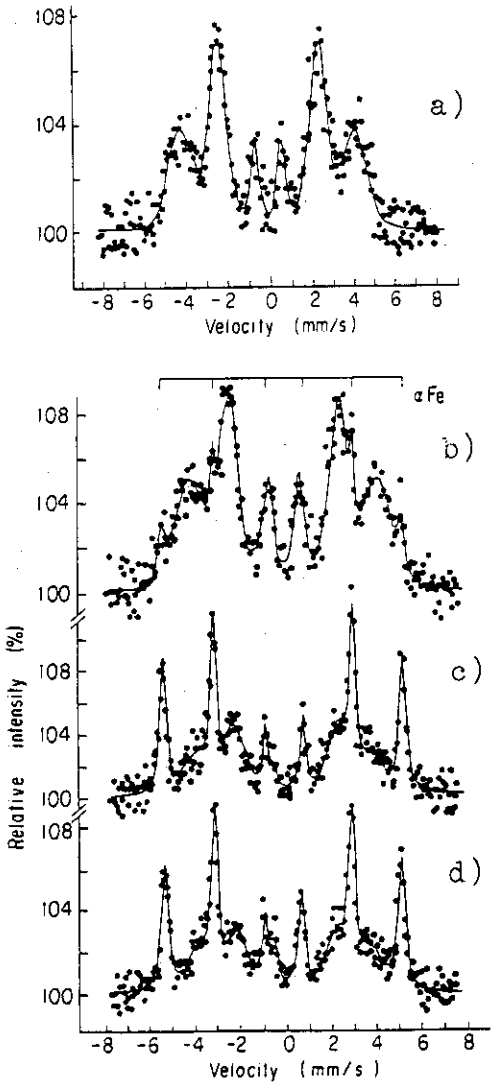

Fig.2 CEM spectra of 40 keV He^+ irradiated a-$Fe_{80}B_{20}$ alloy:
(a) as-received
(b) 5 x 10^{17} ions/cm^2
(c) 1 x 10^{18} ions/cm^2
(d) 3 x 10^{18} ions/cm^2.

Table 1 Hyperfine fields

Sample Preparation	Hyperfine field(kOe)
as-received	264.5±4.2
1 x 10^{18}	
a-Fe_xB_{1-x}	252.3±8.9
alpha Fe	330.9±0.4

on the dose of He^+ ion irradiation. It has been clearly shown that the formation of alpha-Fe has occurred and the amorphous state is still remained. The saturation of the alpha Fe formation has been observed at the higher doses. The spectra were analysed by a least-squares fitting of Lorentzian profiles with the assumption that internal field distribution is gaussian in amorphous state. The average hyperfine fields (h.p.f) H_0 calculated from Fig.2 are given in Table 1. While the h.p.f for induced alpha Fe is in agreement with that observed in crystalline Fe, H_0 values in the remaining amorphous state shows a decrease from H_0 in as-received sample. It is considered that the decrease indicates boron enrichment in the amorphous state. The amount of induced alpha Fe relative to amorphous state (I_α/I_a) is calculated as 0.8 for Fig. 2(c) spectrum. Postulating that the irradiation effect can be expressed as a-$Fe_{80}B_{20}$ $\rightarrow$ $I_\alpha/(I_\alpha+I_a)$ (α Fe) + $I_a/(I_\alpha+I_a)$ (a-Fe_xB_{1-x}), we can obtain as x=0.7 from the I_α/I_a value.

The obtained value is reasonable in comparison with the work of Chien et al(3).

It is well known that thermal treatment of a-$Fe_{80}B_{20}$ leads to the alpha Fe precipitation as a consequence of primary crystallization. However, it is remarkable that ion irradiation induces such a large amount of crystalline alpha Fe with the amorphous phase still remained. There is a difference in structural relaxation between ion irradiation and thermal treatment. It seems that irradiation may enhance diffusion of Fe atoms in the alloy and nucleation of the crystalline alpha Fe.

3.2 Irradiation effect in boron film on Fe

Boron-Fe system is one of the typical amorphous materials with practical use. The amorphous Fe_xB_{1-x} (a-Fe_xB_{1-x}) alloys is usually prepared by liquid-quenching. However, it is expected that amorphous alloy can be prepared by atomic mixing of boron film on Fe. The atomic mixing is a non-equilibrium process and has an advantage of forming amorphous alloys without compositional restriction.

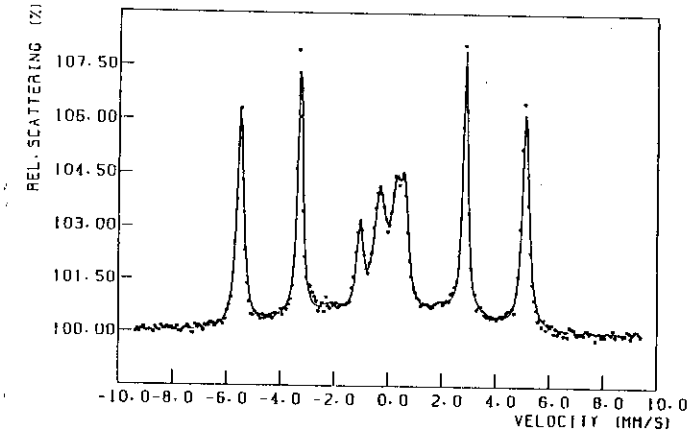

Fig.3 CEM spectrum of boron film on Fe irradiated with 400 keV Xe^+ to a dose of 1 x 10^{17} ions/cm^2.

Fig.3 shows CEMS after 2000 Å boron-Fe has been irradiated with 400 keV Xe^+ ions to a dose of 1 x 10^{17} ions/cm^2. The spectrum indicates the appearance of an irradiation-induced paramagnetic phase (quadrupole doublet) due to the atomic mixing, while magnetic peak (alpha Fe peak) comes from the substrate. The hyperfine parameters of the phase agree with the results of sputtered amorphous Fe_xB_{1-x} films by Blum et al(4). It has been confirmed by X-ray diffraction pattern that the phase has shown a broad diffraction band characteristic of an amorphous materials. Therefore, it is quite safe to conclude that the atomic mixing layer is the amorphous Fe_xB_{1-x}.

The magnetic property of the irradiation-induced a-Fe_xB_{1-x} is very sensitive to boron concentration as indicated in section 3.1. In the case of 1000 Å boron-Fe we have found that 400 keV Xe^+ ion irradiation induces the ferromagnetic phase of a-Fe_xB_{1-x} instead of the paramagnetic doublet in Fig.3. The doublet peak in CEM spectrum in Fig.3 suggest the magnetic transition temperature (T_c) lower than room temperature. It is likely that atomic mixing of 1000 Å boron-Fe results in amorphous alloy with low boron content and that T_c in the alloy is higher than room temperature; according to Chien and Unruh(5), Fe_xB_{1-x} with $x \leq 0.45$ is paramagnetic at room temperature. These results indicate that a-Fe_xB_{1-x} alloys with high boron concentration can be easily prepared by ion irradiation and that the boron concentration can be controlled by the film thickness.

3.3 Irradiation effect in type 304 stainless steel

Stainless steels are one of the candidates for structure materials of nuclear fusion reactors. Therefore, the irradiation effect of stainless steels has been extensively investigated, by means of a wide variety of methods. Since microscopic information seems to be still lacking, we have investigated the irradiation effect in SUS 304 by CEMS. As the crystalline phase (gammma phase) of 304 austenitic stainless steel is metastable at room temperature, it is expected that we can detect a noticeable irradiation effect in the same way as a-$Fe_{80}B_{20}$.

CEM spectrum of the as-received sample in Fig.4 a) shows a single peak from paramagnetic gammma phase. CEM spectra from the sample irradiated with 40 keV He^+ ions are shown in Fig.4 b) - d). The figure makes clear that a ferromagnetic phase is induced by the ion irradiation. The amount of the ferromagnetic alpha phase has increased depending on the increase of a irradiation dose. The irradiation effect has saturated at the higher dose. It is well known that implanted He atoms aggregate and form bubbles in solids, and that the internal pressure of He bubbles is very high. It is considered that the high pressure due to He bubbles induces a stress effect around He bubbles. It is likely that the observed gamma-alpha phase transformation is martensitic transformation drived by stress effect of He bubbles. Martensitic transformation is diffusionless and occurs through a shearing of discrete volumes of solids. We have confirmed by the combined method of CEMS and TEM(6) that gamma-alpha transformation in 17/7 steel, which has simpler composition to SUS 304,

has a martensitic nature with N-W orientation relationship in the fcc and bcc lattice.

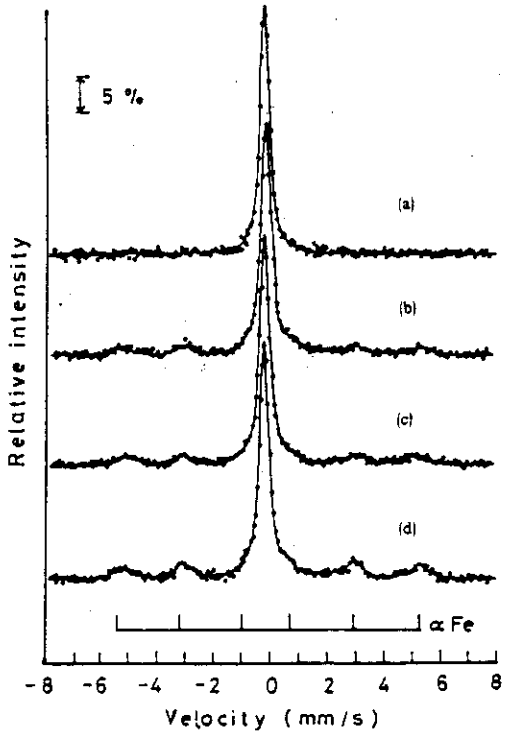

Fig.4 CEM spectra of 40 keV He^+ ion-irradiated SUS 304:
(a) as-received
(b) 8 x 10^{17} ions/cm^2
(c) 1 x 10^{18} ions/cm^2
(d) 1.6 x 10^{18} ions/cm^2.

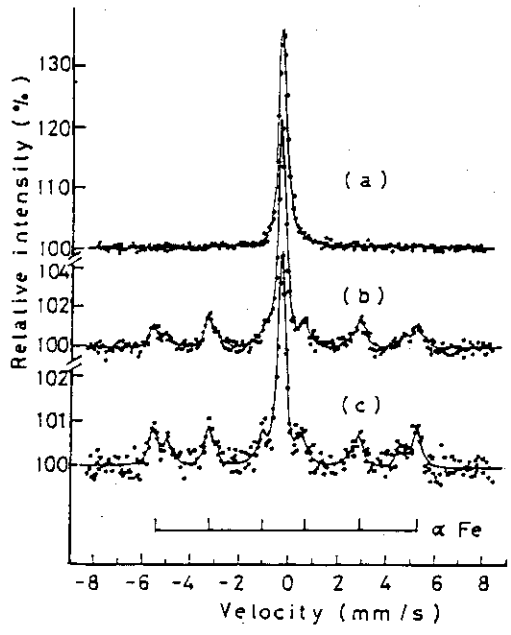

Fig.5 CEM spectra of SUS 304:
(a) as-received and irradiated to 3 x 10^{18} ions/cm^2
(b) is measured with high energy electrons
(c) with low energy electrons.

Depth profiling of CEM spectra are shown in Fig.5. SUS 304 foil was irradiated with 40 keV He^+ ions to a dose of 3 x 10^{18} ions/cm^2. Fig.5 b) is CEM spectrum taken with high energy electrons generated at the surface, while Fig.5 c) spectrum with low energy electrons generated at deeper region. The irradiation-induced ferromagnetic phase appears in both cases. The amount of the ferromagnetic phase relative to the austenitic phase is larger at the deeper region than at the surface region. It is worth noting that the depth dependency of the phase transformation is not inconsistent with the range distribution of He^+ ions, because the mean range is 1500 Å in SUS.

4. Summary

It has been demonstrated that CEMS, which is a non-destructive method by nature, is useful to determine the phase condition in the near surface region of ion-irradiated alloys. Depth profiling of CEMS, furthermore, is expected to give us more detailed information on the irradiation effect.

It has been shown that 40 keV He^+ ion irradiation induce a partial crystallization of alpha Fe in amorphous $Fe_{80}B_{20}$ alloys. The result is consistent with those from atomic mixing of boron film on Fe substrate where amorphous Fe_xB_{1-x} layers has been formed at the interfacial region. The result suggests that amorphous Fe_xB_{1-x} phase with enough boron content may be resistant to radiation damage. Gamma-alpha phase transformation has been found to be induced in SUS 304 irradiated with 40 keV He^+ ions. It is concluded that the transformation has martensitic nature.

References

(1) N. Hayashi et al : to be published.
(2) N. Hayashi and I. Sakamoto : Phys. Lett. A 88 (1982) 299.
(3) C. L. Chien, D. Musser, E. M. Gyorgy, R. C. Sherwood, H. S. Chen, F. E. Luborsky and J. L. Walter : Phys. Rev. B 20 (1979) 283.
(4) N. A. Blum, K. Moorjani, T. O. Poehler and F. G. Satkiewicz : J. Appl. Phys. 52 (1981) 1808.
(5) C. L. Chien and K. M. Unruh : Phys. Rev. B 25 (1982) 5790.
(6) N. Hayashi, E. Johnson, A. Johansen, L. Sarholt-Kristensen and I. Sakamoto : Proceedings of The International Conference on Martensitic Transformations (Nara,1986) pp.539.

II.8 H.I.T. FACILITY OF THE UNIVERSITYOF TOKYO AND CAVITY MICROSTRUCTURAL EVOLUTION IN DUAL-ION IRRADIATED Fe-Ni-Cr ALLOY

Akira KOHYAMA, Yutaka KOHNO and Kyoichi ASANO

Department of Materials Science, The University of Tokyo

Introduction

The concurrent production of displacement damage and deposition of helium in materials can be expected to have a significant influence on the evolution of the microstructure when compared to a material with only displacement damage. Since no operating fusion reactors or intense fusion-spectrum neutron sources exist at present, studies of helium effects rely upon dual-ion beam irradiation with helium and heavy ions as a simulation of fusion reactor environment [1-8]. For the purpose of this simulation irradiation, in Japan, the High-fluence Irradiation Test (H.I.T.) Facility of The University of Tokyo has been constructed since 1983, and was completed in 1985 with the accomplishment of the target station assembly for dual-ion irradiation. Fe-Ni-Cr ternary alloy has been investigated as the most probable candidate material, and many characteristic features of microstructural evolution under irradiation have been reported [9-12]. In this report, an outline of the H.I.T. facility is firstly introduced, and then, the experimental results on the cavity microstructural evolution of Fe-20Ni-15Cr sample mainly induced by nickel and helium dual-ion irradiation are presented and discussed in some detail.

Outline of H.I.T. Facility [13,14]

A major part of the H.I.T. facility is composed of two accelerators, i.e., a Van de Graaff accelerator for light ions and a Tandem accelerator (Tandetron) for relatively heavy ions. The Tandetron accelerator with the terminal voltage of 1 MV is equipped with a sputtering ion source, and provides energetic charged ions for producing displacement damage in a dual-ion irradiation experiment. The 3.75-MV Van de Graaff (VdG) accelerator for light ions can produce up to 300 micro-ampere of proton or helium ion beam with the maximum energy of 3.75 MeV. Configuration of accelerators and beam lines is described in Ref 13 in detail.

Figure 1 shows the view of dual-ion irradiation target chamber assembly. This is composed of the target chamber, pumping system, target stage with specimen holders, multi-channel beam profile monitors, target stage driving unit, energy degrader for light ions, beam masking attachment. Figure 2 shows the target stage after removal from the target chamber. The target stage can be equipped with two types of multi-channel beam profile monitor (BPM). The stage can be loaded with three sets of specimen holders, and each specimen holder can contain twenty, 3-mm diameter, TEM disk specimens. This target stage can move quickly in a direction normal to the heavy-ion beam axis.

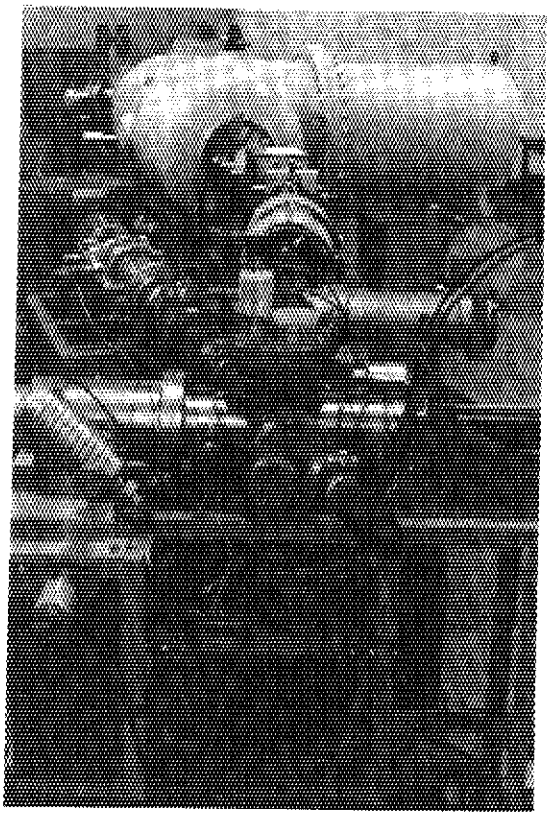

Fig.1 The target station assembly for dual-ion irradiation.

The beam profile monitors are made up of 20 or 37 pieces of 1-mm diameter Micro-Faraday Cups (MFC) with secondary electron suppressor. One of BPM is used for the heavy-ion profile measurement, and the other is used for light-ion. Beam profile monitoring by means of this types of BPM is advantageous for the simultaneous measurement of two dimensional distribution of absolute beam intensity as well as the shape of the beam profile. Figure 3 shows the schematic circuit diagram of the BPM operation. Thirty-seven detecting Micro-Faraday Cups (MFC) with 1-mm di-

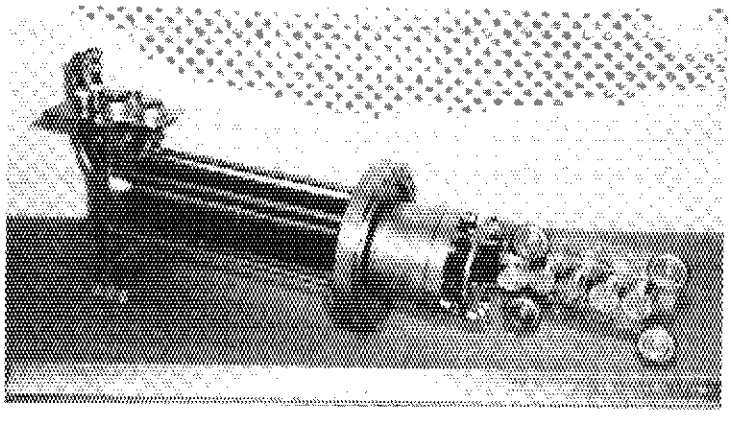

Fig.2 Target stage taken down from target chamber. At the right hand part, specimen holders and BPMs are attached.

ameter aperture and secondary electron suppressor are arranged at intervals of 2 mm in a circle of 14-mm diameter. Figure 4 shows an example of the oscilloscope display for the Ni beam profile monitored by this BPM. Figure 4-(1) indicates the initial beam profile which is centered on the target holder. Figures 4-(2) and 4-(3) show the results of a scanned beam with two scanning intensity levels. In Fig.4-(3), the effect of beam rastering on the uniformity of the beam intensity is clearly indicated.

Specimen heating and temperature control during dual-ion irradiation are accomplished by using a small-size electron beam heating (EBH) system.

Each target holder has a filament, a grid and a thermalizer block made of tungsten. The absolute temperature, which can be increased to about 800C, is measured by a pair of thermocouples contained in the thermalizer block.

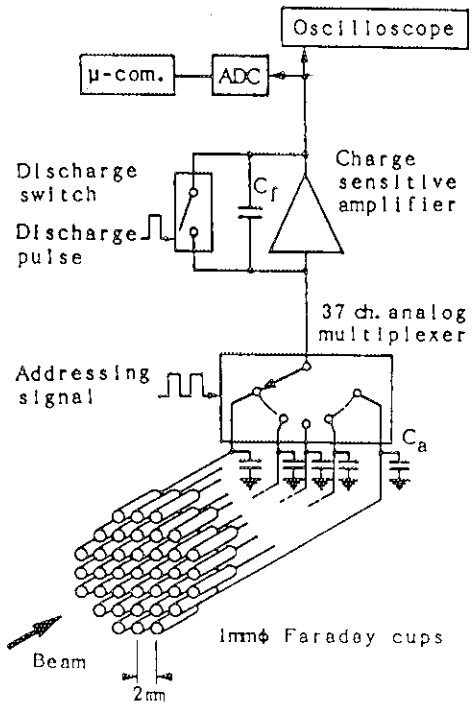

Fig.3 Schematic diagram of the electrical circuit for the multi channel beam profile monitor.

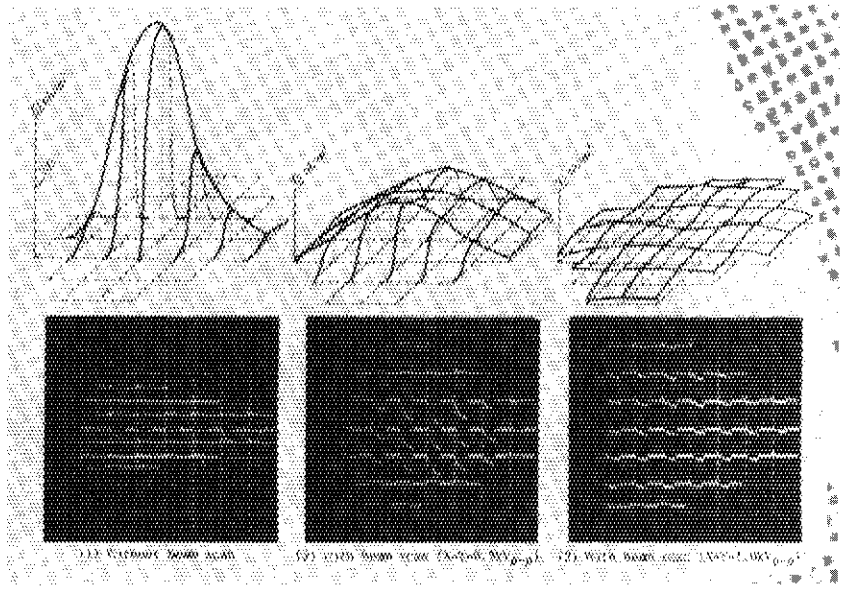

Fig.4 An example of the oscilloscope display for the Ni^{3+} beam. (1): initial profile without beam rastering, (2,3): results of rastered beam.

Cavity Microstructural Evolution in Dual-Ion Irradiated Fe-20Ni-15Cr Alloy

1. Experimental Procedure

For this experiment, Fe-20at.%Ni-15at.%Cr(Fe-20Ni-15Cr) alloy was used. The specimen was prepared from high purity materials, and was annealed at 1050C in an argon atmosphere.Nickel ion irradiation (3.0-MeV Ni^+) was used for displacement damage production, and helium injection was performed with degraded 0.83 MeV He^+. The energy of the injected helium ions was degraded to give a distribution of helium deposition in the specimen that similar to the damage depth distribution for the Ni^+ ions. The damage rate was 3 X 10^{-3} dpa/sec at the nominal sectioned depth of 450 nm in the specimens. Three different helium injection schedules, i.e., 15 appmHe/dpa, 50 appmHe/dpa, and 15 appm He injected at 25C prior to Ni^+ ion irradiation, were utilized in this experiment. The specimens were irradiated at about 700C in a vacuum of 10^{-8} torr. The irradiated specimens were prepared for TEM observations by jet-thinning method. Photomicrographs of dislocations and cavities in the specimen section extending from the 450-nm to the 650-nm depth were obtained with either the JEM-200CX or the JEM-1250.

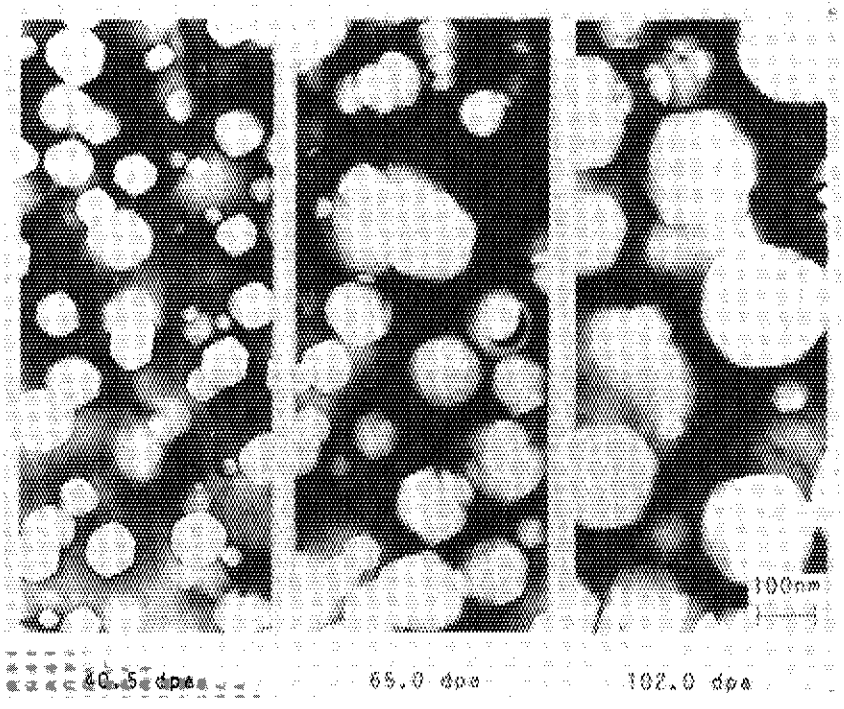

Fig.5 Cavity microstructural evolution in Fe-20Ni-15Cr alloy, 15 appmHe/dpa dual-ion irradiated at about 700C.

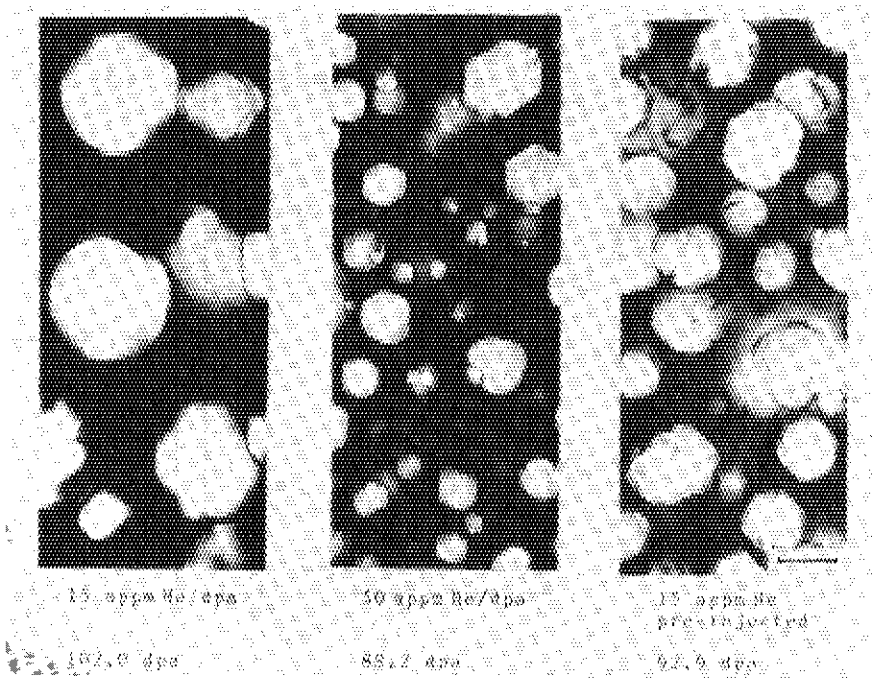

Fig.6 Effects of helium injection schedule on cavity microstructure of Fe-20Ni-15Cr alloy irradiated at about 700C. (Scale mark indicates 200 nm)

2. Experimental Results

Typical cavity microstructures for dual-ion irradiated Fe-20Ni-15Cr alloy with 15 appmHe/dpa at nominal damage levels of 40, 65, and 100 dpa are presented in Fig.5. At every damage level, the cavity size distribution is bi-modal with large cavities, greater than 4 nm, dominant. Also, the effect of the helium injection schedule on cavity microstructures at a nominal damage level of 100 dpa is presented in Fig.6. In the case of helium pre-injected specimens, there was little indication for the saturation of the swelling with increasing damage level. The dependence of the average cavity radius, cavity number density, and swelling on displacement damage that was dual- or single-ion

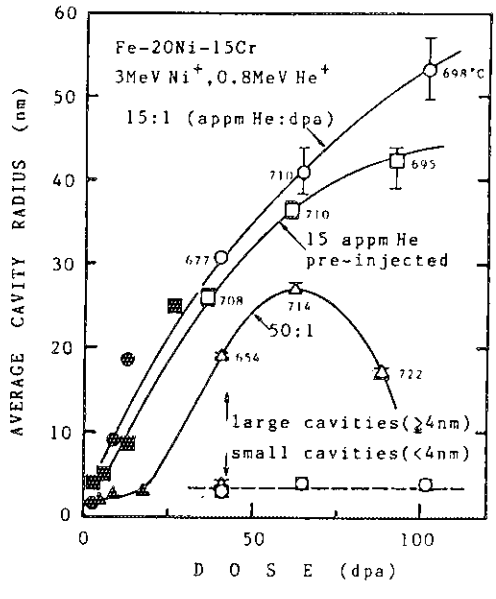

Fig.7 Dose dependence of cavity size in Fe-20Ni-15Cr.(Filled marks: after Agarwal et al [5] at 700C.

irradiated at 700C is shown in Figs. 7, 8, and 9, respectively.

The average cavity diameter of large cavities in the dual-ion irradiated specimens decreases with an increase of the He/dpa ratio. The average cavity size approaches a limiting value for damage levels higher than about 70 dpa. The pre-injection of helium (15 appm) causes cavities to be formed with an average diameter that is intermediate to the diameter in specimens with 15:1 and 50:1 helium injection rates. The bi-modal cavity size distribution that was determined for the 50 appmHe/dpa dual-ion irradiated samples at 40 dpa changed to a uni-modal cavity size distribution at 65 and 100 dpa. But, in the case of helium pre-injected samples, the cavity size distribution was uni-modal throughout the irradiation conditions.

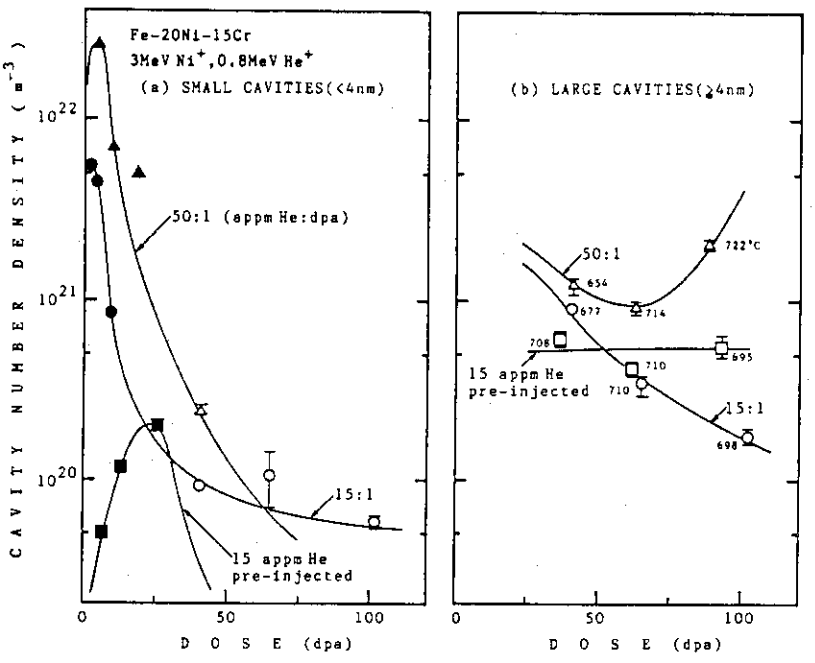

Fig.8 Dose dependence of cavity number density in Fe-20Ni-15Cr. (Filled marks: after Agarwal et al [5] at 700C.)

The cavity number density in helium pre-injected samples was initially $10^{20}/m^3$ but increased with increasing damage to a limiting value of 5 X $10^{20}/m^3$ at 90 dpa. In contrast, the cavity number density in dual-ion irradiated specimens was initially high with the majority of small

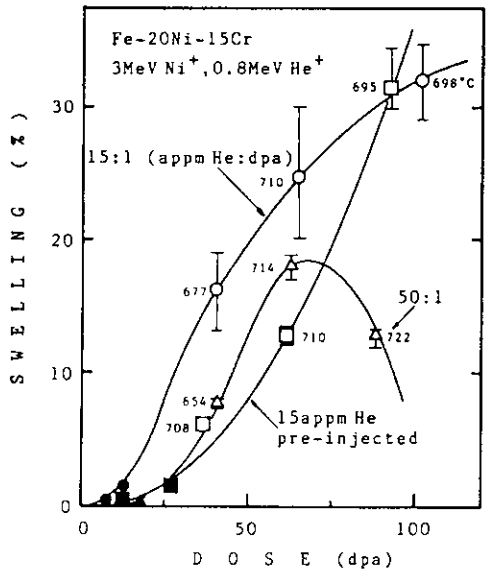

Fig.9 Dose dependence of swelling in Fe-20Ni-15Cr. (Filled marks: after Agarwal et al [5] at 700C.)

cavities of $10^{22}/m^3$ at 5 dpa and then decreased and approached a limiting value with increasing displacement damage. Figure 8 also indicates that the bi-modal cavity size distribution observed in dual-ion irradiated specimens tends to become a uni-modal cavity size distribution at a high damage region.

The specimens, regardless of helium injection rate or helium pre-injection, undergo a transition regime of displacement damage that produces only small swelling (less than 1%) before the onset of a constant, high swelling rate. An increase of the helium deposition rate resulted in a delay of the start of a constant swelling rate [5]. For the dual-ion irradiated specimens, there was a trend toward saturation of the swelling with increasing damage level that was closely related to the saturation and subsequent decrease of the number density of small cavities. For the helium pre-injected specimens, there was little indication for the saturation of the swelling with increasing damage level. In Fig.9, for the specimen that received 15:1 or 50:1 (He/dpa) helium injection rates, a constant rate of swelling, that is, 0.5%/dpa, between 25 and 65 dpa. It can be observed that the data point for the highest damage in the 50 appmHe/dpa specimen shows significant deviation from the line for constant swelling rate.

3. Discussion

3-1 Comparison with Other Fe-20Ni-15Cr Results

Agarwal et al [5], Loomis et al [6] and Johnston et al [7,8] irradiated Fe-20Ni-15Cr with Ni^+ ions after 15 appm He pre-injection. The former two researchers used the same facilities and microscopy, while Johnston et al used step-height for all swelling levels of larger than 10%. As shown in Fig.10, the data of Agarwal et al and present results are co-linear as expected, and exhibit the same eventual swelling rate as seen by Johnston et al. The shift in transient relative to Johnston's curve is

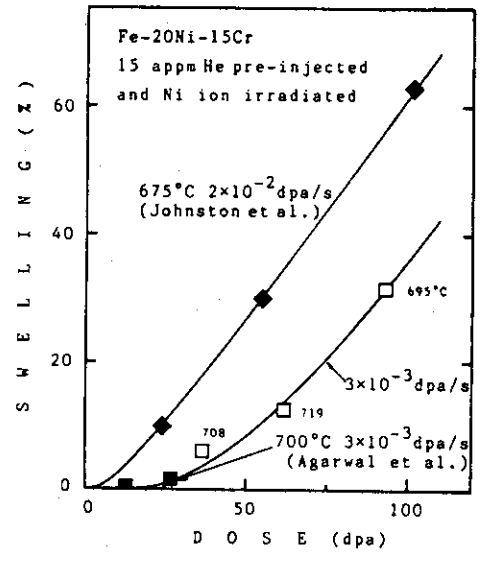

Fig.10 Comparison of swelling measured in Fe-20Ni-15Cr. (Filled marks: after Johnston et al [7,8] and Agarwal et al [5])

probably due to the large difference in displacement rate, as shown in Ref 19. The shift may also arise partially from the fact that Johnston's experiment was at 675C, while the other was at 695C to 710C. Garner has shown that the effect of increasing temperature lies in extending the transient [15-17].

It has also been shown that the swelling rate for ions is a function of depth, varying from a maximum of 1%/dpa at the front surface to about 0.2%/dpa at peak damage region [15]. Step-height data leads to an average value and present data is taken between 450 and 650 nm. Thus, the agreement at 0.5 to 0.6%/dpa may be fortuitous. Neutron irradiation experiments are not influenced by the surface, dpa gradient or injected interstitials, and swell at 1%/dpa in this alloy [15-17].

Agarwal showed that at 700C the transient regime is first shortened by helium co-injection and then lengthened as the helium injection rate is increased. A minimum is reached near 5 appmHe/dpa, increasing slightly at 16 appmHe/dpa, and increasing substantially at 55 appmHe/dpa [5]. The present results at 15 appmHe/dpa suggests that this trend was maintained in this experiment.

3-2 Saturation of Swelling

The present results imply that the swelling reaches saturation at high dpa and in one case there even appears the reduction in swelling. Johnston et al used step-heights to probe swelling levels in excess of 60%, and found no saturation. On the contrary, saturation during ion irradiation has been observed in Type 316 by Kumar and Garner [18] and by Packan and Farrell [19]. The transient regime of swelling for ternary alloys is known to be very sensitive to temperature and at higher temperature there is a sudden increase in the transient regime that can be quite large for only 10 to 20C [17]. However, there is another plausible cause of the apparent saturation or decrease in swelling obtained in this experiment. As the void diameter becomes a large fraction of the range, many, but not all, of the ions will penetrate the large voids without energy loss and deposit their energy at deeper depth. This factor alone will cause a decrease in swelling rate (unless the dpa rate is corrected) and would give the appearance of the onset of saturation. In addition, however, the swelling at shallower depths continues to increase; as the thin foil was taken at a fixed depth from the surface of the specimen, we probed a shallower mass-depth and, therefore, a lower displacement level than anticipated, giving

an apparent decline in the swelling rate. This problem will be accentuated if the swelling rate per dpa near the surface is greater than that near the peak. Garner et al, Johnston et al and Chickering et al have shown this to be the case [15].

3-3 Effect of Helium Injection Schedule

In a previous paper [12], we discussed the helium effect at the initial stage of cavity formation in Type 316. That is, pre-injection produces a relatively small number of vacancies and thus we would initially expect a large number of helium atoms per vacancy in pre-injected samples than in dual-ion samples. This could produce a high number density of essentially immobile defects in pre-injected samples that would tend to retard both dislocation microstructure development and void swelling. Even at high displacement damage levels up to 100 dpa, microstructure development is very similar with that observed in dual-ion irradiated samples with the total dose less than 25 dpa [5], indicating that without simultaneous helium injection microstructure development is retarded. In the linear swelling stage, cavity growth is predominantly bias-driven and injected helium is removed from matrix, thus cavity microstructure development may become similar to the single-ion irradiation or electron irradiation. The gradual increase of dislocations and cavities in pre-injected samples suggests that the linear swelling stage is still occurring at 100 dpa [20]. On the contrary, the dual-ion irradiated samples showed a saturation tendency in swelling and cavity number density. This could be related to the slow decrease in dislocation densities observed, although the difference is the factor of two [20]. For Fe-20Ni-15Cr alloys, the cavity size distribution was bi-modal with the small cavities dominant at low displacement damage and, with increasing He/dpa ratio, the number densities of small cavities and large cavities increased. This would reduce the growth rate of both types of cavities and thus reduces swelling.

References

(1) Proceedings, Workshop on Correlation of Neutron and Charged Particle Damage, ERDA CONF-760673, US-ERDA, 1976.

(2) Proceedings, Workshop on Solute Segregation and Phase Stability During Irradiation, J. Nucl. Mater. 83(1979).

(3) G.R. Odette, J. Spitznagel, A. Turner and W. Jesser: DAFS Report, DOE/ER-0046/8, Vol.1, A-3, US-DOE, 1982.

(4) A. Kohyama, G. Ayrault, A. Turner and N. Igata: J. Nucl. Mater. 122&123(1984)224.

(5) S.C. Agarwal, G. Ayrault, D.I. Potter, A. Taylor and F.V. Nolfi, Jr.: J. Nucl. Mater. 85&86(1979)653.

(6) B.A. Loomis, G. Ayrault, S. Gerber and Z. Wang: DAFS Report, DOE/ER-0046/8, US-DOE, 1983.

(7) W.G. Johnston: J. Nucl. Mater. 54(1974)24.

(8) J.F. Bates and W.G. Johnston: Proceedings, AIME Conference on Radiation Effects in Breeder Reactor Structural Materials, June 1977, Scottsdale, AZ, p.625.

(9) H.R. Brager and F.A. Garner: J. Nucl. Mater. 117(1983)159.

(10) G. Ayrault, H.A. Hoff, F.V. Nolfi, Jr. and A. Turner: J. Nucl. Mater. 103&104(1981)1035.

(11) A. Kohyama, G. Ayrault and A. Turner: J. Nucl. Mater. 117(1983)151.

(12) A. Kohyama, G. Ayrault, A. Turner and N. Igata: J. Nucl. Mater. 117 (1983)143.

(13) Y. Kohno, K. Asano, A. Kohyama, K. Hasegawa and N. Igata: J. Nucl. Mater. 141-143(1986)794.

(14) K. Asano, Y. Hosono, Y. Kohno and A. Kohyama: Nucl. Instrum. & Methods B17(1986)186.

(15) F.A. Garner: J. Nucl. Mater. 117(1983)177.

(16) F.A. Garner: J. Nucl. Mater. 122&123(1984)459.

(17) F.A. Garner and H.R. Brager: DAFS Report, DOE/ER-0046/16, US-DOE,1983.

(18) A. Kumar and F.A. Garner: J. Nucl. Mater. 117(1983)234.

(19) N.H. Packan and K. Farrell: Effects of Radiation on Materials, 11th International Symposium, ASTM STP-782, ASTM, 1982, p.885.

(20) A. Kohyama, B.A. Loomis, G. Ayrault and N. Igata: Effects of Radiation on Materials, 12th International Symposium, ASTM STP-870, ASTM, 1985, p.277.

II.9 LIGHT-ION IRRADIATION EXPERIMENTS IN NATIONAL RESEARCH INSTITUTE FOR METALS

Naoki KISHIMOTO, Johsei NAGAKAWA and Haruki SHIRAISHI

Nuclear Materials Division, Tsukuba Laboratories
National Research Institute for Metals

Introduction

Ion irradiation techniques have been extensively applied for simulating damage effects of fusion neutrons on the firstwall materials. In comparison with in-pile experiments using fast breeder reactors, the ion irradiation methods have advantages not only in their inexpensive cost but also in keeping well-defined experimental parameters (temperature, dose, stress etc) and varying them readily in the laboratory. The systematic analyses, for example, by changing He appm/dpa ratio(1-3) have contributed to obtaining understandings of elementary damage processes of mutually-interactive phenomena, such as defect aglomeration, void swelling, helium bubble formation, radiation-induced segregation and so on.

The basic goal of the simulative research on fusion reactor materials is to find out correlation rules between ion- and neutron-irradiation damages concerning not only those microstructural evolutions but also mechanical properties. Mechanical testing under ion bombardment provides important information in this context and would be an effective tool for the material development. However, the ion bombardment techniques have been less commonly applied to the mechanical testings, perhaps because of a few difficulties inevitable in the charged particles such as a small irradiation volume of uniform damage distribution and the beam heating .

Up to date, creep experiments using accelerators have been carried out in several institutes(4-13) in the world and the irradiation creep data have been utilized mainly to examine validity of the theoretical creep models. However, the creep mechanisms are not established as yet and there have been few attempts to correlate them to the results of neutron irradiation. Consequently more experimental data should be accumulated to clarify the mechanisms and to contribute to the establishment of the neutron-ion correlation rule. Thus, National Research Institute for Metals (NRIM) has primarily focused on the mechanical testings under ion bombardment(creep, fatigue, fracture toughness being planned) and has begun

the irradiation creep experiment since spring in 1986. In this report, we will outline the basic idea of our simulation research and the irradiation creep facility, including a few experimental data obtained at present.

Materials Testing Under Ion Bombardment

Requirements of the ion beam for the materials testing would essentially be to simulate the damage natures induced by fusion neutrons and to attain a relatively large irradiation volume of uniform damage distribution. The former requirement is attained by taking account of the atomic displacement effect and the helium generation effect through nuclear transmutation of the alloying elements (Fig.1). The latter is concerned with both selection of the beam energy and 2-dimensional beam-operation over the specimen area.

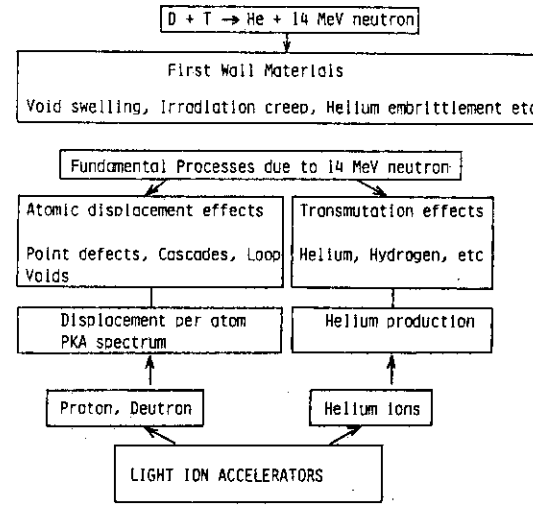

Fig.1 Radiation-damage features induced by fusion neutrons and an application of a cyclotron to simulation experiments.

As for the atomic displacement effect, the PKA (primary-knock-on atoms) energy spectrum should be simulated to determine the damage structure concerning cascade damaging effects etc. It is concluded from theoretical analyses(14,15) that proton of a similar energy gives rise to a close PKA spectrum to that of fusion neutron(Fig.2). It is practically supposed that proton and deuteron of 10-20 MeV are allowable in this viewpoint. The selection of the energy values may be, in a sense, a trade-off between damage rate and uniformity of the dpa depth profile. The high damage rate is forced to be sacrificed to some extent to perform the mechanical testing of a given specimen thickness.

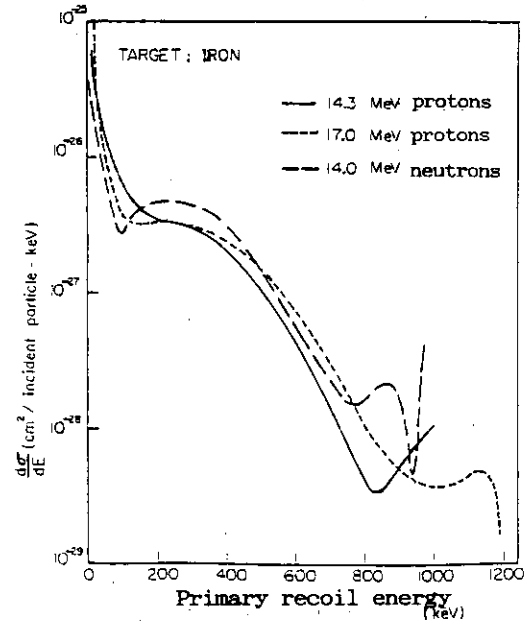

Fig.2 Primary recoil energy spectra for fusion neutrons of 14.0 MeV, protons 14.3 MeV and 17.0 MeV, in iron(15).

As for the helium generation, high energy proton beam can produce a fair

amount of helium for Ni-containing alloys, as shown in Fig.3(16,17), and helium ion injection is also an efficient method to simulate the helium generation effect. For these purposes a light ion cyclotron is one of the most suitable accelerators in the viewpoint of total performance , and the NRIM has purchased an AVF-type cyclotron (BC1710 by Japan Steel Works) with some modifications accommodating to the materials irradiation testing. Characteristics of the NRIM cyclotron are listed in Table 1. These energy

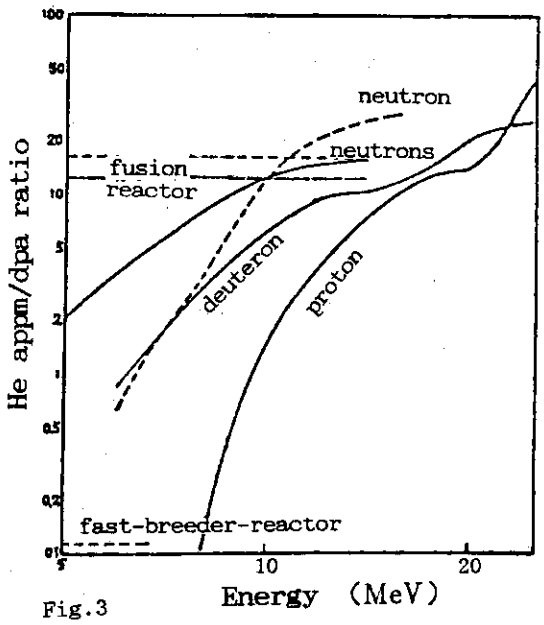

Fig.3 Ratio of He appm/dpa for fusion- and FBR-neutrons, neutron data, proton and deuteron in 316 SS(10).

Table 1 Characteristics of particles produced by the NRIM cyclotron.

Ion species	Energy	Max.Current	Dose rate at 10μA/cm^2	Dose
Proton	17 MeV	50 μA	2.5×10^{-7}dpa/s	0.1 dpa(100hr)
Deuteron	10 MeV	50 μA	1.7×10^{-6}dpa/s	0.6 dpa(100hr)
Helium-4	20 MeV	20 μA	4×10^{-6}appm/s	1300appm(10hr)
Helium-3	26 MeV	20 μA	same as above	

values of proton and deuteron would attain fairly good simulative conditions of the dpa structure and uniform damage distribution along the specimen depth, though the allowed thickness is limited approximately less than 0.1 mm. Also, helium atoms can be injected along the above thickness, by using those helium ion beams. Thus, the NRIM light-ion-cyclotron properly simulates fusion irradiation environments.

Table 2 Technical requirements of the ion beam, the beam transport and the target apparatus for the materials testing.

Needs of beam	Concerns	Transport	Target
1. Stability	Thermal shock Transient effects Long period(creep)	Computer control	Fast T-control Low drift device
2. Uniformity	T-distribution Damage gradient	Scanning Homogenizing	T-distr. control
3. High intensity	Damage rate	Transp. efficiency	High cooling rate

For the materials testing, each ion beam is required to be stable and uniform over the specimen area keeping the beam intensity as much as possible. These practical requirements for the materials testing are summarized in Table 2. They should be satisfied as the total system, that is, not only by the accelerator but also by the transport and the target apparatus. For example, the NRIM cyclotron system has successfully employed a computer-control for the beam operation and homogenizing devices such as electric-field scanning at 5 KHz (Fig. 4) and off-center magnetic-field lens (multipole-doublet: in progress).

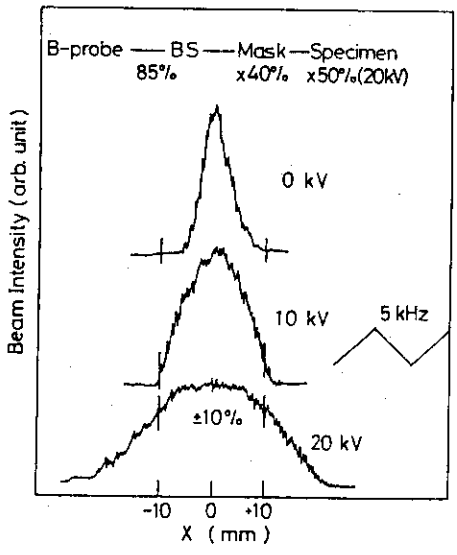

Fig.4 Electric-field scanning of the ion beam with triangular waveform at 5 KHz.

Radiation Damage Regime

Up to now, preliminary irradiation creep tests have been carried out by using 17 MeV proton and 10 MeV deuteron beam. Fig.5 shows a damage profile of 10 MeV deuteron, which is calculated by using the so-called TRIM code(18). The deuteron beam emitted from the cyclotron passes through a thin aluminum membrane (30 μmt for vacuum/helium sealing at the target window) and loses a fraction (~0.4 MeV) of the initial energy by inelastic collisions, which results in the beam heating of the specimen. As seen in Fig.5, the damage profile along the specimen depth is regarded fairly uniform for this thickness of the specimen. In this case, the fraction of displaced atoms produced in collision cascades is about 70 % as much as the total ones.

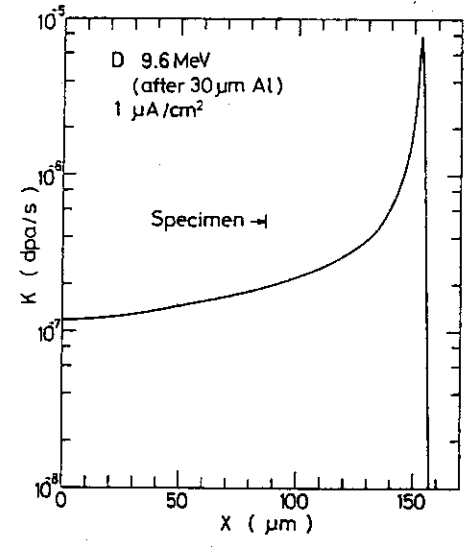

Fig.5 Damage profile induced by 9.6 MeV deuteron along depth of the specimen. The marked depth denotes the specimen thickness.

The present irradiation conditions are listed in Table 3. The beam current at the specimen position is about 4 $\mu A/cm^2$ and amounts to 5×10^{-7} dpa/s for

Table 3 Irradiation conditions for the typical cases.

	Deuteron	Proton	Unit
Beam Energy	10	17	MeV
Beam Current	4	10	$\mu A/cm^2$
Damage Rate	5×10^{-7}	2.5×10^{-7}	dpa/s
Dose	0.1(50 hr)	0.03(30 hr)	dpa
Temperature	400	300	°C

the deuteron irradiation. It takes about 10 hours for each period of the creep measurement and the total atomic displacement for a specimen reaches about the order of 0.1 dpa at the most. The total damage level is still less than the onset level where macroscopic changes like void swelling, irradiation segregation etc take place.

Irradiation Creep Apparatus

An important and difficult point for the irradiation creep measurement is the temperature control of the specimen under the fluctuating beam heating. Especially for the tensile creep measurement, the superimposed thermal dilatation, without sufficient temperature control, wrecks the creep strain measurement. The difficulty in this kind of temperature control arises from both the large beam heating and the small thermal mass-capacity of the specimen. The specimen temperature must be precisely controlled in the critical balance between the big thermal input and the heat removal by rapid cooling.

For this purpose, we have employed helium forced convection for the cooling and the DC heating to compensate the thermal fluctuation, by monitoring the specimen resistance for the temperature control. The high helium velocity is desired not only for effective cooling but also for temperature uniformity along the specimen length. Fig.6 shows the schematic situations of the temperature distribution arising from various heat-dissipation paths, and the

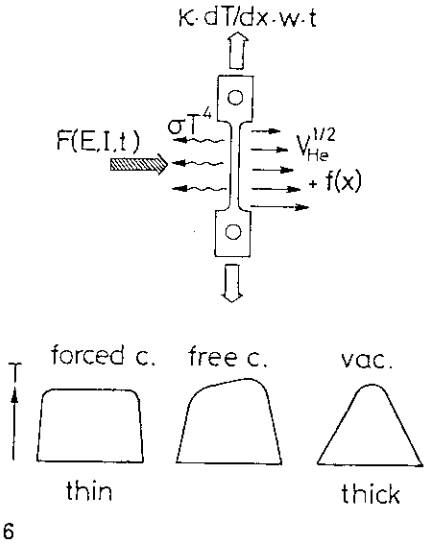

Fig.6 Schematic thermal situation of the specimen. Input: DC heating and beam heating (F). Output: black-body radiation($\sim T^4$), conduction to grips ($\sim dT/dx$) and helium flow($\sim V_{He}^{1/2}$).

typical examples actually observed are given in Fig.7. A laminar flow of high velocity attains homogeneous cooling rate per area along the gauge length, and minimizes temperature-gradient effects, such as gravitational distribution due to free convection, thermal conduction to the specimen grips through the specimen cross section. The total cooling rate at V_{He}=100 m/sec is about 50 Watt and a fairly uniform temperature distribution is obtained.

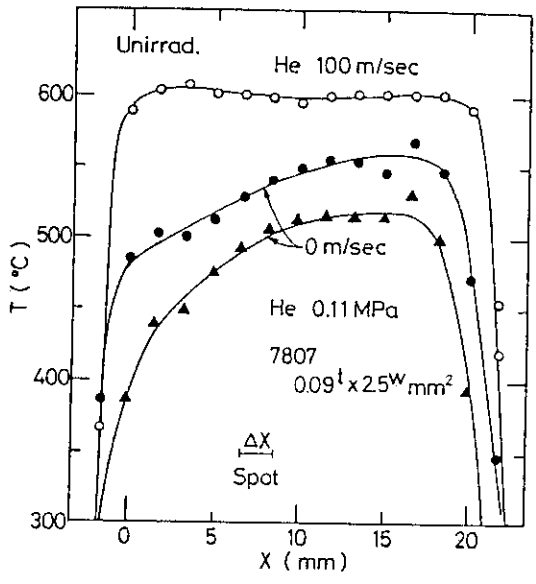

Fig.7 Temperature profiles along specimen length for helium free convection(0 m/s) and forced convection(100 m/s).

As seen in Fig. 8, the foil specimen gives a fast thermal response in the helium gas flow. In such a critical condition, it is important to set an appropriate response for the temperature cotroller. The necessary response of the controller must be much faster than that of the specimen, while too fast response tends to cause instabilities like overshooting or oscillation etc. After those experimental analyses of the thermal behavior, the response of the controller has been appropriately determined to be 6 msec. To prevent the long-term temperature drift, the environmental temperature around the apparatus is accurately controlled by using water coolant (± 0.1 K) etc and also low-thermal-expansion materials (quartz, Invar) are adopted for the core parts of the strain measuring device. Thus, the temperature stability of about ± 0.2 K has been achieved enough to distinguish the typical creep strain from the thermal dilatation.

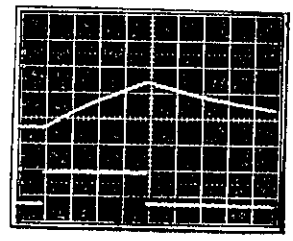

V_{He}=0 m/sec, τ =540msec

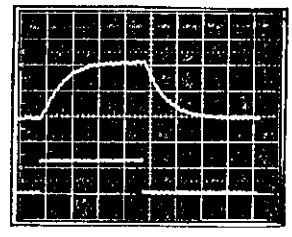

V_{He}=~100m/sec, τ =160msec

Fig.8 Thermal response of the specimen to input heat of 800 msec step-function for free and forced convection.

On the other hand, we have also developed another creep apparatus of torsion method. By using an electromagnetic force of a coil in the permanent magnetic field, torque stress is applied to a wire specimen and

the rotational displacement due to the creep deformation is optically measured. Since 3-dimensional thermal dilatation, in principle, does not directly affect the rotational deformation, this method is free from such a severe requirement for the temperature control. The control level of ± 1 K is enough accurate for the torsion method to measure the creep strain, and the resolution is still by two orders of magnitude superior to that of the tensile method. The detailed description of the torsion creep apparatus is obtained elsewhere(13).

Fig. 9 shows a schematic comparison of instrumental characteristics between the torsion and the tensile creep apparatus. The advantage for the torsion method is very high strain resolution to about 10^{-7} and, therefore, suitable for the data acquisition over wide stress and temperature ranges. It is also pointed out that this method enables us to change stress easily and conveniently to examine creep-fatigue interactive effects. For the tensile method, the resolution is not so very high but has other advantages of simple uniaxial stress mode and availability of microstructural observation. Consequently, both methods are supposed to be complementary to each other and contribute to obtaining understandings of the creep phenomena.

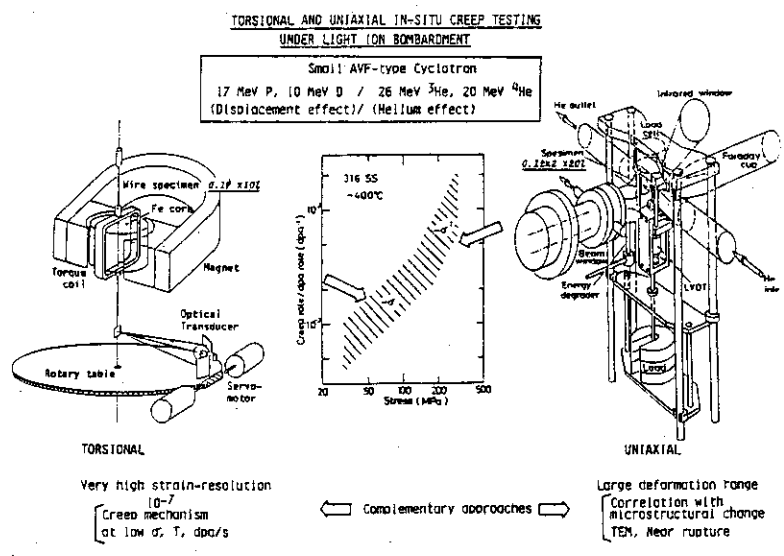

Fig.9 Torsion and tensile creep rigs and their instrumental characteristics depicted schematically.

Specimens

In our laboratory, experimental alloy series of Fe-Ni-Cr-MC, 316SS and PCA(Prime Candidate Alloy) have been investigated concerning mechanisms of the phase stability(19) and the post-helium-implantation creep(20) etc. Recently, our major interests are shifting towards more innovatory materials such as low-induced-radioactivity materials(Fe-(9-12)Cr-W,V,

30Mn-steels), alloys of single crystal(TMS-12), oxide-dispersive steels(MA754, MA956) and so on. Some works on these alloys are making progress, mainly about characterization and phase stability after helium injection .

For the irradiation creep work, the experimental alloys, Fe-25Ni-15Cr and 316SS have firstly been examined as reference materials. Chemical compositions for those alloys are listed in Table 4.

Table 4 Chemical compositions of alloys used.

Code	C	Ni	Cr	Ti	Si	Mn	Mo	B	Fe	Annealing
7807	0.07	25.7	15.7						Bal.	950 °C x 30 min
7811	0.02	25.2	14.8	0.95					Bal.	1000 °C x 30 min
316SS	0.04	13.9	16.1		0.44	1.42	2.5	0.0006	Bal.	950 °C x 10 min

For the alloys of 7807 and 7811, the ingots are rolled down to about 110 μmt, being intermittently annealled. By the recrystallization annealing at the given temperatures (Table 4), the grain size is adjusted to be about 20 μm for the both alloys. The annealled plates are cold-worked by 20 % and machined into platelet specimens whose gauge part is 0.087 x 2.5 x 20 mm^3. The 316 SS is used for wire-shaped specimens of torsion creep measurement. Wire of 0.8 mm in diameter is made by swaging and the above recrystallization annealing gives grain size of 10 μm. After the 20 % cold-work by drawing, the wire specimens (gauge 0.1 mm ϕ x 8 mm) are fabricated by electropolishing(13).

Experimental Results and Discussion

Figure 10 shows examples of recording traces for the tensile creep, at 400 °C. In order to equilibrate the thermal creep state, the specimen is crept under unirradiated conditions for more than 24 hours at given temperature and stress. At this temperature and stress, the steady-state thermal-creep rate is less than 1/10 of the irradiation creep rate and almost negligible within the present strain resolution. After the onset of deuteron irradiation, the creep curves consist of transient build-up and the following steady state where the creep rate remains constant. The transient period seems to be a few hours and not to depend on the stress greatly. Since this specimen is cold worked, the most plausible explanation would be anelastic deformation as first reported by Hudson et al(7). However, many other possibilities under irradiation would have to

be taken account, such as point defect evolution, relaxation of dislocation and solute/precipitate evolution etc. As an informative example in Fig. 10, dips are interestingly seen in the strain curves. Although they just come from the instable changes in the beam intensity, they may convey information of transient creep feabtures. Since the changes show exponential decays after a spike-like beam increase, they would be associated with transient relaxation after an instantaneous change like point-defect population-change. More well-defined experiments are necessary to clarify this kind of transient creep.

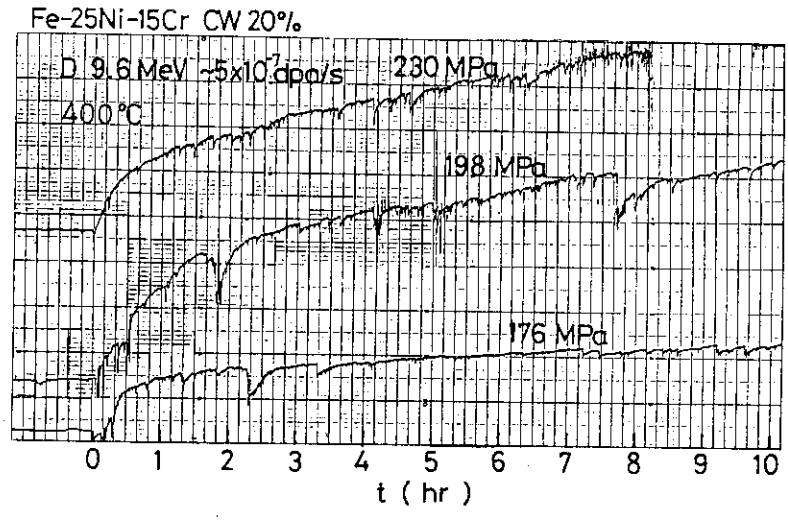

Fig.10 Irradiation creep curves of Fe-25Ni-15Cr at various stresses under 9.6 MeV deuteron bombardment.

Steady-state creep rate after those primary transients are plotted as a function of stress in Fig. 11. For comparison, the creep data of HPS and 316SS by KFA Jülich(17,21) are given in the same figure, where HPS(High Purity Stainless steel) denotes a FeNiCrMo alloy of 316SS's composition without minor elements (Si, Mn, C etc). Since the experimental conditions, especially of temperature, may be different between our data (full circle) and those KFA's data(open symbols), the detailed comparison would be difficult, but a few tendencies can be stated taking account of the weak temperature dependence of the irradiation creep(7). The magnitude of creep rate for 7807 is rather close to that of HPS and it indicates that the

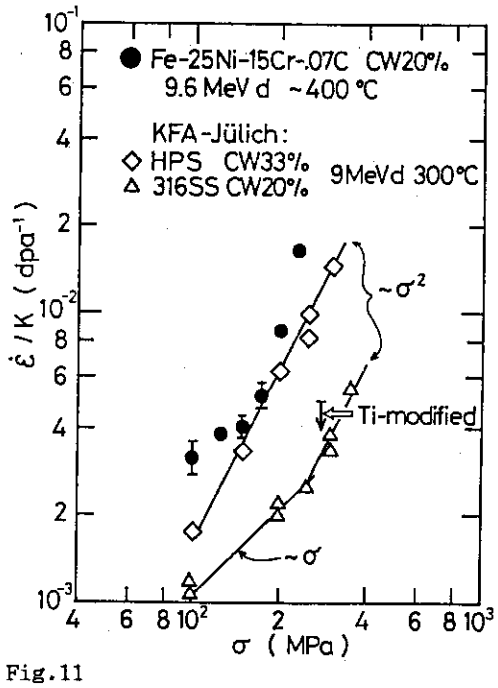

Fig.11 Steady-state creep rate of Fe-25Ni-15Cr during irradiation in comparison with the data of KFA Jülich(17,21).

increase in Ni content from 15% to 25 % does not make an improvement of the irradiation creep resistance. It may not be surprising from the former result(19) that the Ni-increase to such extent is not much enough to suppress void swelling. Also it may be suggested that sole addition of 0.07% carbon to the FeNiCr alloy (without another carbide former (?)) does not suppress the creep, though carbon has been said one of the candidate elements to decrease the creep deformation. On the other hand, Ti addition seems to improve the creep resistance even if the carbon level is very low.

As for the stress exponent of the creep rate, a transition from linear (n=1) to quadratic (n=2 or n≳2) dependence is seen below and above about 150 MPa. This tendency of stress dependence is qualitatively explained in terms of SIPA (stress induced preferred absorption) (22,23) and PAG (preferred absorption glide) (24) models. The both models are based on elastic interaction between point defects and dislocations. External stress field causes anisotropy of defect capture efficiency of the dislocations, and their climb motion takes place. For the higher stress region, glide motion of dislocation plays an important role to give the creep as well as the climb motion.

In spite of the qualitative agreement between those theories and the experimental results, the calculated magnitudes of creep rate do not agree with the experimental values, as seen in Fig.12(24). For the higher stress region , the theoretical values from PAG model for 7807 are much smaller than the observed values. The discrepancy becomes larger for 7807 and HPS than for 316SS. Since reliable data for the point defect parameters of Fe-Ni-Cr alloys are not sufficient, more data should be taken before judging the validity of those models. However, it seems to us that elastic properties would not greatly differ between 7807 and 316SS and that the existing PAG model could not explain such a large creep rate, even if considerable allowances be made for a variety of these parameters reported until now. Another mechanism to give more creep rate

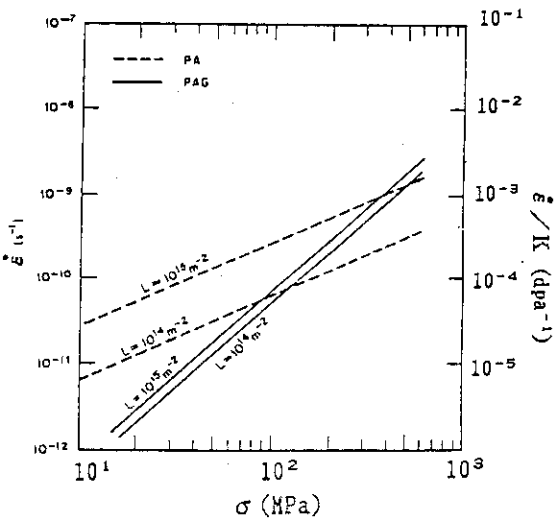

Fig.12 Theoretical creep rates from PA(SIPA)- and PAG mechanisms as a function of stress(24).

would be desired like some kinds of preferred glide (25).

As discribed at first, the torsion creep method has much superior strain resolution than the tensile one and, therefore, time dependence of creep rate can be investigated in details with this method. Fig. 13 shows the rotational displacement for 316SS under 17 MeV proton bombardment, as a function of time elapsed. The dots in the magnified scale show the scattering of data. Note that, by this method, the creep rate at such low temperature and low stress can be detected within a small error. The strain measurement was carried out over 30 hours, which duration is considerably long as compared to this kind of the former experiments. The derivative of this creep curve is plotted as a function of time, in Fig. 14. As seen in this figure, the creep rate decreases rapidly just after the beginning of irradiation and tends to saturate to a constant value with increasing time elapsed. At 300°C and 50 MPa, it takes more than 1500 min (0.025 dpa) for the creep rate to reach the constant value ie. the steady-state creep. It is important to properly evaluate such saturation tendency, and otherwise we might overestimate the creep rate than the true steady-state one.

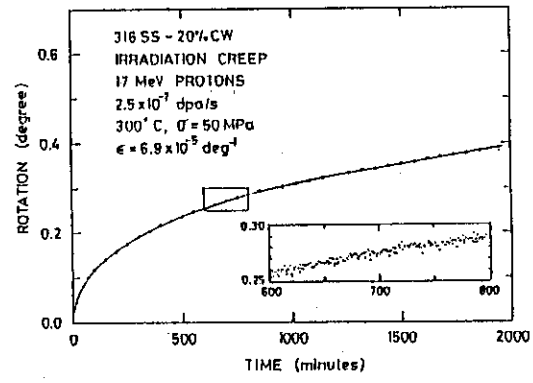

Fig.13 Irradiation creep curve of 316SS under 17 MeV proton bombardment by the torsion creep method.

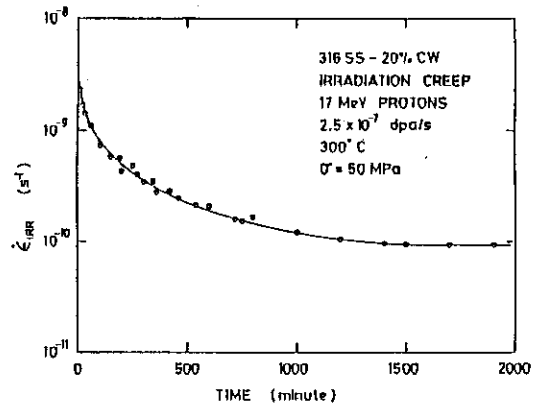

Fig.14 Time dependence of creep rate (derivative of the creep curve) of 316SS.

As for the quantitative discussion, the steady-state value is fairly close (within a factor of 2) to both the creep rate for in-pile experiments(26,27) and the calculated values with the SIPA model. However, there remains unsolved questions, that is, whether or not "the agreement" within such a factor is satisfactory to validate the SIPA model, and

whether or not the transient period is determined only by the accumulated dose. Comparing to the previous result (13) where 316SS gave 20 time creep rates as much as the present value, it is stressed that the "steady-state" creep rate is sensitive to the damage rate. Consequently, the damage-rate dependence would have to be systematically examined to clarify the combined effects of radiation damage and thermal process on the varying creep rate.

Summary

The light-ion cyclotron facility of the NRIM has started its operation since spring in 1986 and is dedicated to the mechanical testings under ion bombardment, simulating irradiation emvironments in the fusion reactors. Among several types of the testings planned (creep, creep-fatigue, fracture toughness etc), irradiation creep has been focussed on for the first step and the tensile and torsion creep rigs have been equiped in connection with the cyclotron system.

From the preliminary experimental results for Fe-25Ni-15Cr, it may be suggested:

1. the Ni-content of 25% does not improve the creep resistance,
2. minor elements like Ti play an important role in suppressing the creep, but the sole addition of carbon is not so effective,
3. the SIPA and PAG models qualitatively explain the stress dependence of creep rate but not quantitatively,

   and for 316SS,
4. it takes 0.025 dpa to reach the steady-state creep, at 2.5 x 10^{-7} dpa/s, 300 ℃ and 50 MPa, and
5. the evolution of irradiation creep is sensitive to the damage rate especially in the low dpa range.

More data are going to be accumulated to draw conlusive discussion on these statements.

Acknowledgements

The authors are indebted to Dr. A. Hasegawa for his computer calculation of the damage profile by using the TRIM code. They are also grateful to Mr. N. Yamamoto and our colleagues for cooperative operation of the cyclotron facility.

References

(1) M. R. Hayns, M. H. Wood and R. Bullough: J. Nucl. Mater. 75 (1978) 241.
(2) S. C. Agarwal, G. Ayrault, D. I. Potter, A. Taylor and F. V. Nolfi, Jr.: J. Nucl. Mater. 85-86 (1979) 653.
(3) K. Farrel, N. H. Packan and J. T. Houston: Rad. Eff. 62 (1982) 39.
(4) S. D. Harkness, F. L. Yaggee and F. V. Nolfi, Jr.: ANL-7883 (1972).
(5) P. L. Hendrick, A. L. Bement, Jr. and O. K. Harling: Nucl. Instr. Meth. 124 (1975) 389.
(6) P. L. Hendrick, D. J. Michel, A. G. Pieper, R. E. Surratt and A. L. Bement, Jr.: J. Nucl. Mater. 59 (1976) 229.
(7) J. A. Hudson, R. S. Nelson and R. J. McElroy: J. Nucl. Mater. 65 (1977) 279.
(8) E. K. Opperman, J. L. Straalsund, G. L. Wire and R. H. Howell: Nucl. Tech. 42 (1979) 71.
(9) T. C. Reily, R. L. Auble and R. H. Shannon: J. Nucl. Mater. 90 (1980) 271.
(10) P. Jung, J. Vieweg and C. Schwaiger: Nucl. Instr. and Meth. 154 (1978) 207.
(11) C. H. Henager, J. L. Brimhall and E. P. Simonen: J. Nucl. Mater. 90 (1980) 290.
(12) J. Nagakawa: J. Nucl. Mater. 116 (1983) 10.
(13) J. Nagakawa: J. Nucl. Mater. 136 (1985) 238.
(14) C. M. Logan, J. D. Anderson and A. K. Mukhergee: J. Nucl. Mater. 48 (1973) 223.
(15) D. A. Thompson, J. E. Robinson, R. S. Walker, A. M. Omar and A. B. Campbell: Proc. Int. Conf. on Radiation Effects and Tritium Technology for Fusion Reactors, Gatlinburg (1975) p. I-382.
(16) J. L. Straalsund: Radiation Effects in Breeder Reactor Structural Materials, Scottsdale (1977) p.191.
(17) P. Jung, C. Schwaiger and H. Ullmaier: J. Nucl. Mater. 85-86 (1979) 867.
(18) J. P. Biersack and L. G. Haggmark: Nucl. Instr. Meth. 174 (1980) 257.
(19) T. Kimoto, H. Shiraishi and R. Watanabe: J. Nucl. Sci. Tech. 19 (1982) 202.
(20) N. Yamamoto, H. Shiraishi and H. Kamitsubo: J. Nucl. Mater. 133-134 (1985) 493.
(21) C. Schwaiger, P. Jung and H. Ullmaier: J. Nucl. Mater. 90 (1980) 268.

(22) P. T. Heald and M. V. Speight: Phil. Mag. 29 (1974) 1075.
(23) W. G. Wolfer and M. Ashkin: J. Appl. Phys. 46 (1975) 547.
(24) L. K. Mansur: Phil. Mag. A39 (1979) 497.
(25) C. H. Henager, Jr. and E. P. Simonen: Proc. 12th Int. Conf. on Effects of Radiation on Materials, Williamsburg, (1984).
(26) G. W. Lewthwaite and D. Mosedale: J. Nucl. Mater. 90 (1980) 205.
(27) J. Lehmann, J. M. Dupouy, R. Broudeur, J. L. Boutard and A. Maillard: Proc. Int. Conf. on Irradiation Behavior of Metallic Materials for Fast Reactor Core Components, Ajaccio, France (1979), p.409.

II.10 MECHANICAL PROPERTY CHANGE IN METALS BOMBARDED WITH LIGHT-IONS

Katsunori ABE

Institute for Materials Research, Tohoku University

1. Introduction

High energy light ions are utilized to simulate the irradiation damage in wall materials of fusion reactors. The information about irradiation hardening behavior is required to know the mechanism in mechanical property changes such as ductility, toughness, creep and fatigue. Irradiation hardening is caused by interaction between dislocations and irradiation-induced defects which have been formed during bombarding through lattice displacements with and without implanted ions. The variations of ion concentration and of displacement-per-atom (dpa) with depth from the specimen surface are calculated by means of Monte Carlo program such as TRIM85 code (1). The number of dpa increases with depth and has a maximum near the peak of ion concentration i.e. projected range. The amount of irradiation hardening is supposed to be inhomogeneous within the specimen that is bombarded with such ions. The abrupt change in irradiation hardening is expected arround the projected range, and it can be detected directly by microhardness technique. On the other hand, relatively smooth change in irradiation hardening is expected in the region between the surface and the projected range, and the average hardening in the region can be measured by miniature-tensile-specimen technique (2). In this report, application of microhardness technique to molybdenum irradiated with He-ions is summarized briefly.

2. Irradiation and hardness measurement

High energy light ions, such as 16MeV proton, 16MeV deuteron, 10-50MeV He-ions, were bombarded into molybdenum metals using AVF Cyclotron at Tohoku University. Typical specimens were sheets of 0.5mm arranged parallel to the ion beam (3). Sheet type specimens normal to the ion beam were also used. A water-cooled and liquid-nitrogen-cooled copper holder with indium solder in a vacuum

chamber was used to keep the temperature at 148-573K. Beam heating with controlled thermal contact was used to get higher temperatures. Irradiation was performed with and without beam scanning. When a focused beam was used without scanning, the fluence distribution on the specimens was estimated by measuring the induced activity. Vanadium metal was used as a dosimetry material because of the appropriate activation yield and half life (4). Micro Knoop hardness was measured on the side surface with a position accuracy of about 1μm in the case of a 2gf weight (3).

3. Hardening by He-ions

Typical examples of microhardness changes around the projected range were shown in Fig. 1 in the case of electron-beam-zone-melted(EBZM) molybdenum single crystals bomberded with 10, 20, 50MeV He-ions, where hardness profiles at the same fluence level were normalized with the projected range (5). As ion energy increases, the peak height decreases and the peak width increases, which may correspond to the increase of straggling. The hardness depth profile is not symmetrical around the projected range, which shows not only the contribution of implanted helium but also that of dpa.

Figure 2 shows the change of hardness profile by post-irradiation-annealing in the case of EBZM-molybdenum bombarded with 50MeV He-ions (5). The hardness profile is not symmetrical in as-irradiated condtion; hardness in the region in front of the peak is larger than that in the region over the peak. The hardness profile become symmetrical and peak width as well as peak height decreased after annealing at 1473K. Since the annealing temperature was enough high for irradiation defects such as loops and voids to disappear, only cavities stabilized by helium gas atoms might survive after annealing. It is reasonable that residual hardening is caused by He-stabilized cavities.

Cavities were not observed in EBZM-molybenum as-irradiated at 148K, but cavities were grown into enough size to be observed after annealing. In that case, the degree of irradiation hardening and the distribution of cavities at each depth can be correlated with each other. Figure 3 shows the variation of cavity parameters and hardness with depth (5). The hardness depth profile is well represented by the cavity parameter. The degree of hardening by cavities is proportional to the square root of the product of size and density.

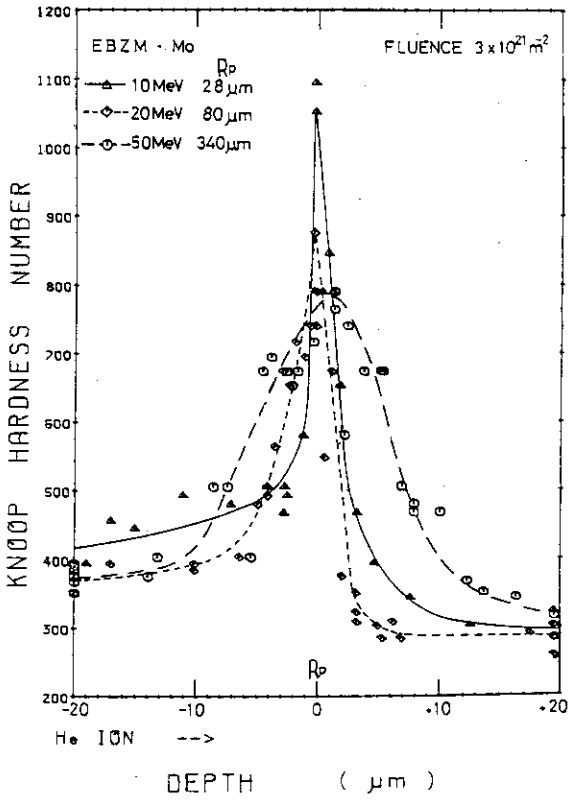

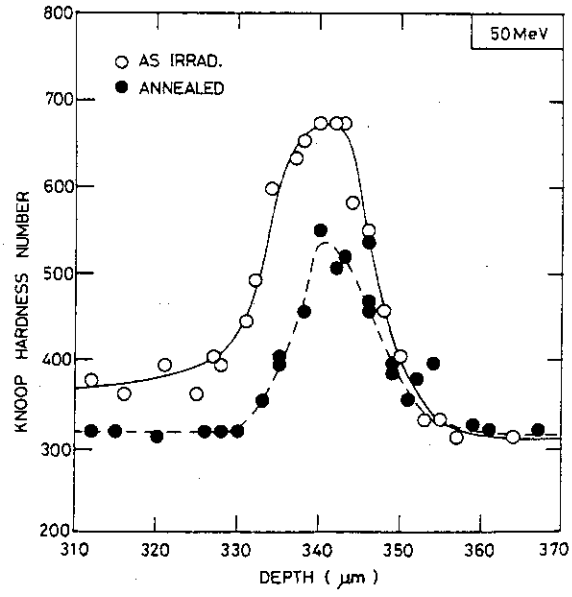

Fig. 2 The change of hardness profile by post-irradiation-annealing in Mo irradiated with 50 MeV He-ions at 373K and annealed at 1473K.

Fig. 1 Microhardness profile around projected ranges in Mo irradiated with 10, 20, 50MeV He-inos.

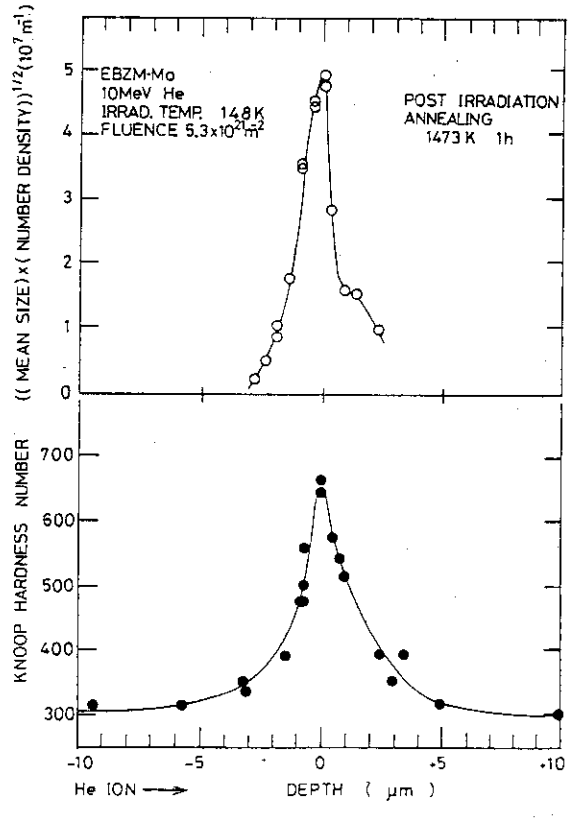

Fig. 3 The relation between cavity parameter and hardness number in Mo.

4. Summary

When the microhardness technique is combined with local dosimetry and TEM observation to study ion irradiation hardening, there are sevral advantages:

1) Information about local hardening can be obtained within 1μm scale.
2) It is applicable to areas where dpa, dpa/s, He and He/dpa continuously change.
3) The correlation between hardness profile and microstructure profile can be studied.
4) Inhomogeneous beam profile is utilized to determine fluence dependence of hardening.
5) Multiple specimens are examined in a irradiation experiment.
6) Post-irradiation annealing behavior in a small region is studied.

This technique, however, contains other subjects to be studied further (6):

7) Hardness values depend on indentation load, especially in small load range.
8) Hardness values depend on indentation direction in anisotropic materials such as bcc and hcp metals.

References

(1) J.F.Ziegler, J.P.Biersack and U.Littmark: The stopping and Range of Ions in Solids (Pergamon Press, New York, Oxford, Toronto, Sydney, Frankfurt, Tokyo, 1985) pp.232-255.
(2) K.Abe, F.Nagase, S.Morozumi: unpublished.
(3) K.Abe, A.Hasegawa, M.Kikuchi and S.Morozumi: J.Nucl.Mat. 103/104(1981)1169.
(4) K.Abe, A.Iizuka, A.Hasegawa and S.Morozumi: J.Nucl.Mat. 122/123(1984)972.
(5) K.Abe, A, Hasegawa, S.Morozumi: Radiation Effects, 101(1986)237.
(6) A.Hasegawa, K.Abe and S.Morozumi : J.Nucl.Mat. 133/134(1985)657.

II.11 LOW-ENEREGY ION-BEAM SURFACE CRYSTALLOGRAPHY

Masakazu AONO

RIKEN, Hirosawa 2-1, Wako, Saitama 351, Japan

Low-energy ion scattering spectroscopy (ISS) was initiated by Smith [1] in 1967 for the purpose of composition analysis of solid surfaces. However, it has been found that ISS is unsuitable for analyzing the surface composition quantitatively because noble gas ions, which are used in usual ISS experiments, are neutralized with a probability that depends on the chemical condition of surfaces in a complicated manner. At the same time, it has been found that ISS is rather useful for analyzing surface atomic arrangements [2]. However, ISS can analyze surface atomic arrangements only qualitatively because of the ambiguity of the neutralization probability of ions mentioned above.

In 1981, the present author and co-workers [3] demonstrated that surface atomic arrangements could be analyzed quantitatively without influence of the ambiguity of the neutralization probability of ions, if the experimental scattering angle was taken close to 180°. This special mode of ISS is called impact-collision ion scattering spectroscopy (ICISS). Lately, Niehus and Comsa [4] showed the advantage of using alkali ions in ICISS and called this method alkali impact-collision ion scattering spectroscopy (ALICISS).

Recently, Williams et al.[5] have developed a computer code which can simulate ion scattering in the ICISS mode in a short time using a personal computer. This makes it possible to analyze surface atomic arrangements with high reliability and accuracy using ICISS or ALICISS.

The present author and co-workers [6] have recently designed and constructed a novel low-energy ion scattering spectrometer in which an ion source and an ion energy analyzer are arranged coaxially (see Fig.1). This apparatus is called coaxial impact-collision ion scattering spectrometer (CAICISS) since it makes it possible to do experiments of ICISS at an ideal scattering angle of 180o. An interesting feature of CAICISS is that in contrast to usual ISS, CAICISS can 'see' not only surface atomic layers but also deeper layers. CAICISS is also suitable for in situ observations of various surface processes by virtue of its geometrical simplicity.

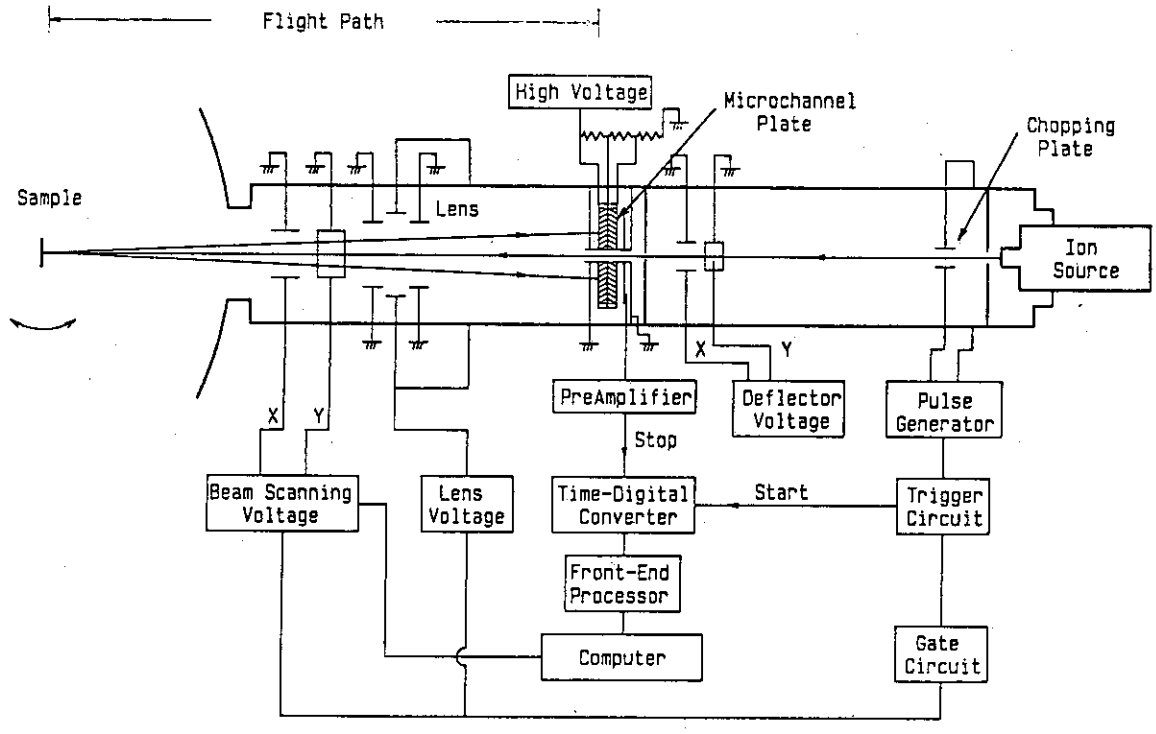

Fig.1 Coaxial impact-collision ion scattering spectrometer (CAICISS)

References

[1] D. P. Smith: Appl. Phys. 38 (1967) 349; R. F. Goff and D. P. Smith: J. Vac. Sci. Technol. 7 (1970) 72; D. P. Smith: Surf. Sci. 25 (1971) 171.

[2] See, for example, E. Taglauer and W. Heiland: Appl. Phys. 9 (1976) 261; T. M. Buck: Methods of Surface Analysis ed. A. W. Czanderna (Elsevier, Amsterdam, 1975).

[3] M. Aono, C. Oshima, S. Zaima, S. Otani, and Y. Ishizawa: Jpn. J. Appl. Phys. 20 (1981) L829; M. Aono and R. Souda: Jpn. J. Appl. Phys. 24 (1985) 1249.

[4] H. Niehus: Nucl. Instr. Meth. 218 (1983); H. Niehus and G. Comsa, Surf. Sci. 140 (1984) 18.

[5] R. S. Williams et al: to be published.

[6] M. Katayama, E. Nomura, N. Kanekama, H. Soejima, and M. Aono: to be published.

II.12 X-RAY TOPOGRAPHIC STUDY OF Si SINGLE CRYSTALS IRRADIATED WITH ENERGETIC HEAVY IONS

Hiroshi TOMIMITSU

Department of Physics, JAERI

1. Introduction

The lattice imperfection induced by ion-bombardments has been studied by X-ray diffraction topography(XDT). Schwuttke et al[1] showed that when Si single crystals were bombarded by 2 MeV N^+, B^+ and P^+ ions with doses more than 10^{15}ions/cm^2, disorders concentrated in the very thin layers corresponding to the range stragglings of projectiles, and the upper- and lower-parts of the specimen crystal separated by the disordered thin layer remained perfect. Further study by Bonse, Hart and Schwuttke[2] found the interference fringes arising from the two perfect regions separated by the very thin disordered layer.

The present author[3] has also reported the following results by the conventional XDT-observation in Si single crystals irradiated with 150 MeV Ni^{9+} and Cl^{9+} ions; 1) the specimens were deformed as a whole, 2) they sustained heavy strains which concentrated at the irradiation boundaries, and 3) systematic fringes were observed in the irradiated areas. The present author subsequently reported[4,5], from the XDT-observation of the Si wafers irradiated with 58 MeV B^{3+}, 70 MeV B^{4+}, 100 MeV C^{5+}, 120 MeV O^{7+}, 150 MeV Si^{9+} and 169 MeV Au^{13+} ions, that (1) only faint black-and-white contrasts were found at the irradiation boundaries by the irradiation of light ions like B and C; (2) on the other hand, besides these black-and-white contrasts, both the systematic fringes within the irradiated area and the macroscopic crystal deformation appear in the case of the irradiation with heavier ions (Cl^{9+}, Ni^{9+} and Au^{13+}).

In order to confirm the results mentioned above, further measurements were made on the specimens irradiated with the variety of energetic ions, and with several different irradiation conditions. The present article summarizes the results of the XDT-observation on those heavy-ion-irradiated Si single crystals.

2. Experimental Procedures

2.1 Specimen Crystal

Three types of Si wafers*) were used in this experiment as listed in Table 1, where the growth methods, Cz. and Fz., in the second column, the surface indices in the third, and the final treatment of the specimen crystal is described in the last column.

It should be remarked here, however, that almost all results by the present conventional XDT-observation are independent of the crystal types.

Table 1 Comparison of Specimen Wafers

Spec.-Type	Grow.-Method	Surface	Final Treatment
I	Cz.	(001)	Mirror Polished (Both Side)
II	Fz.	(001)	Polished/Etched (One Side)
III	Fz.	(111)	Both Side Chemical.-Etched

2.2 Ion Irradiations

Every irradiation was carried out with the maximum terminal voltage of the tandem accelerator of this institute, and maximum ion current for several hrs., during the irradiation period the specimen being kept at the LNT. Each irradiation condition, together with ion species, energies and dose, is listed in the left half of the Table 2.

2.3 XDT-Observation

XDT-observation was carried out with the conventional Lang's method, with a fine focus X-ray generator. Several reflections such as 004, 008; 111, 333; 220, 440; parallel, vertical and slanting to the specimen surface, were used, mainly by Mo-Kα1 radiation.

---

*) The author is much indebted to Drs.Abe and Masui of Sinetsu-Handotai Co. for their kind offering him all the Si Wafers used in these experiment.

3. Experimental Results

3.1 Dependence of Irradiation Effects on Projectile Masses

As already described in section 1, two of irradiation-effects have been revealed[3,4,5] through XDT-observation. The very faint, black-and-white contrasts, indicating the lattice strains, were observed at the irradiation boundaries in the case of the irradiation with light ions. Besides this characteristic contrasts, the systematic fringes in the irradiated area and the macroscopic deformation of the specimen crystal were found on the bombardment with heavy ions. On the basis of these results, some Si wafers under various specified irradiations were examined to ascertain how the types of irradiation effects are conditioned.

The results together with the irradiation conditions are summarized in Table 2. The effects of the projectile mass are clearly seen in the Table.

3.2 Effect of Beam Scanning on the Fringe Patterns in XDT

As for the origin of the interference fringe, Bonse, Hart and Schwuttke have attributed it to the inhomogeneity of the cross-sectional distribution of the projectile ions. In order to confirm this assumption, we investigated the specimen crystals irradiated with homogeneous- and inhomogeneous beam distribution.

The homogeneous irradiation was realized by the beam-scanning in the horizontal direction with application of the alternative electric field with the saw-toothed shape of several kV, after the cross-section of the beam was shaped into a vertically elongated form with homogeneous distribu tion.

The results are summarized in Table 3 together with the experimental conditions. The interference fringe could not be observed in the case of homogeneous irradiation, and consequently the assumption mentioned above was apparently proved.

Table 2 Summary of XDT-Observation for Each Irradiation Conditions (Without Beam-Scanning)

Ions	Energy (MeV)	Dose (ions/cm^2)	Results* Margin.Strain	Deform.	Fringe
$^{10}B^{4+}$	58	0.3×10^{13}	No	No	No
$^{10}B^{4+}$	66	6	Yes	No	No
$^{11}B^{3+}$	70	1	Yes	No	No
$^{12}C^{5+}$	100	5	Yes	No	No
$^{12}C^{5+}$	100	43	Yes	No	No
$^{16}O^{7+}$	120	7	Yes	No	No
$^{19}F^{6+}$	60	2	Yes	No	No
$^{28}Si^{8+}$	150	1	Yes	No	No
$^{28}Si^{9+}$	165	1	Yes	Yes	No
$^{32}S^{7+}$	50	0.1	Yes	Yes	Yes
$^{32}S^{8+}$	100	1	Yes	Yes	Yes
$^{32}S^{10+}$	165	1	Yes	Yes	Yes
$^{35}Cl^{9+}$	150	6	Yes	Yes	Yes
$^{35}Cl^{10+}$	150	4, 8	Yes	Yes	Yes
$^{58}Ni^{9+}$	165	0.5	Yes	Yes	Yes
$^{80}Br^{6+}$	90	10	Yes	Yes	Yes
$^{197}Au^{13+}$	169	1	Yes	Yes	Yes

* The visibility was compared on the topographs taken with 333, 004 and 220 reflections.

Table 3 Effect of Beam Scanning on the Fringe Pattern

Ions	Energy (MeV)	Dose ions/cm^2	Scanning Yes/ No	Fringe*
$^{32}S^{9+}$	150	29×10^{14}	Yes	No
$^{32}S^{10+}$	165	1	No	Yes
$^{35}Cl^{8+}$	120	52	Yes	No
$^{35}Cl^{8+}$	140	1	Yes	No
$^{35}Cl^{9+}$	150	6	No	Yes
$^{35}Cl^{10+}$	150	4, 8	No	Yes
$^{58}Ni^{9+}$	165	0.5	No	Yes
$^{58}Ni^{11+}$	192	3	Yes	No
$^{80}Br^{6+}$	90	10	No	Yes
$^{80}Br^{10+}$	120	3	Yes	No
$^{197}Au^{13+}$	169	1	No	Yes
$^{197}Au^{13+}$	210	1	Yes	No

* The visibility was compared on the topographs taken by 333 reflection.

3.3 Effect of Ion Energy on the Fringe Pattern in XDT

The observation of the interference fringe may depend on the length of the range of the projectile ions to the specimen crystal. We saw how the visibility changed with the ion energy, i.e. the range value, in the case of $^{19}F^{n+}$, $^{28}Si^{n+}$ and $^{32}S^{n+}$ ions with several energies.

The experimental conditions and the results are summarized in Table 4 together with the range values, and, as expected, the interference fringe seems to be affected by the ion energy, i.e. the range length. Further investigation is now in progress.

Table 4 Effect of Ion Energy on the Fringe Pattern

Ions	Energy (MeV)	Dose (ions/cm^2)	Range* (μm)	Fringe**
$^{19}F^{6+}$	60	2×10^{14}	37	Yes
$^{19}F^{7+}$	120	3	93	No
$^{28}Si^{8+}$	100	4	35	Yes
$^{28}Si^{9+}$	150	1	58	Yes
$^{32}S^{7+}$	50	2	15	Yes
$^{32}S^{8+}$	100	18	29	Yes
$^{32}S^{10+}$	165	1	52	Yes

* The values were interpolated from the table in Ref.6.

** The visibility was compared on the topographs taken by 333 reflection.

4. Conclusion

It was confirmed that the irradiation effects with heavy ions can be summarized as following;

1) The heavy lattice strains concentrated at the boundaries of the irradiated- and non-irradiated regions separated by the mask material.

2) The specimen crystals were often deformed macroscopically as a whole.

3) Characteristic and systematic fringes were observed within the irradiated area not only in the topographs taken with the reflecting planes perpendicular to the specimen surface but also in them slanting to the specimen surface.

Only the effect 1) mentioned above could, on the other hand, be observed in the case of the irradiation with lighter ions.

It was confirmed that the interference fringes could not observed on the specimens irradiated under the condition of homogeneous ion-distribution by beam-scanning, in good agreement with the assumption by previous authors[2].

As the ion energies or the range-values are seemed to affect on the interference fringes, the present author is trying to progress the observation.

References

1) G.H.Schwuttke, K.Brack, E.E.Gardner and H.M.DeAngelis: Proc. Santa Fe Conf.Radiation Effects in Semiconductors, ed. F.Vook,(Plenum Press,N.Y., 1968) pp.406.

2) U.Bonse, M.Hart and G.H.Schwuttke: Phys.Stat.Solidi 33 (1969) 361.

3) H.Tomimitsu: Jpn.J.Appl.Phys. 22 (1983) L674.

4) H.Tomimitsu: JAERI-M 84-129 (1984) pp.47.

5) H.Tomimitsu, Y.Kazumata and E.Sakai: JAERI-M 85-104 (1985) pp.93.

6) U.Littmark and J.F.Ziegler: Handbook of Range Distributions for Energetic Ions in All Elements (Pergamon Press, N.Y., 1980).

II.13 TRANSMISSION SPUTTERING OF COPPER AND SILVER BY HIGH-ENERGY IONS

Teikichi A. SASAKI and Yuji BABA

Department of Chemistry, Japan Atomic Energy Research Institute

1. Introduction

Transimission-sputtering experiments of heavy ions have been performed to investigate depth distribution of the energy deposition(1,2) and to elucidate the mechanisms responsible for very small yields for far beyond the range predicted(3-5). Although the sputtering yield provides information about sequences of nuclear collision cascades which are directly related to the energy-deposition distribution, the experiments have not been popular because of difficulty in preparation of a thin target appropriate for the ion bombardment. In the case of incident ion with an energy of ∿100 MeV, it has been revealed that the sputtering occurs only at the depth of the projected range of the ion(2). Furthermore, it has been pointed out that depth profiles of the sputtered atoms trapped in a catcher foil should be examined for the quantitative evaluation of the sputtering yield.

This communication presents an expression in semi-quantitative analysis of the transmission-sputtering yield which is more general than that previously reported(6). Auger electron spectroscopy (AES) was employed to obtain information about the depth profile of the sputtered particles and sputtering yield for C^{5+} (84.6 MeV)→Ag/Nb, F^{7+} (114 MeV)→Cu/Nb and F^{7+} (114 MeV)→Ag/Nb systems.

2. Experimental

Target materials were stack-foils of pure Cu and Ag metals (99.9 % up) from Furuuchi Chemicals and Goodfellow Metals, respectively. The thickness was determined by means of a

gravimetric method within an accuracy of ±0.2 μm. Nb foils with a thickness of ∿120 μm were used as catcher foils of the sputtered particles and were mechanically polished with diamond paste of 1/4 μm to make a mirrorlike plane. The stack-foils were set in a target holder made of copper together with the catcher foils. In some cases, 8 keV Ar^+ ion-etching was employed prior to the bombardment for the reduction of carbon and/or oxygen containing adsorbates.

Bombardments were carried out by means of heavy-ion accelerator at JAERI. The C^{5+} ions (84.6 MeV) of ∿175 nA or the F^{7+} ions (114 MeV) of ∿250 nA from the accelerator impinged the target at normal incidence under a pressure of ∿7 x 10^{-7} Pa. The other details on the bombardments were described elsewhere(2).

Information about the transmission sputtering was obtained with the AES technique by use of 5 keV electrons. The sputtering yields were estimated from the signal intensities of the Cu (LMM, 920 eV), Ag (MNN, 358 eV) and Nb (MNN, 167 eV) Auger lines. Ion etching for the depth profile of the sputtered particles deposited on the catcher surface was carried out with 8 keV Ar^+ ions from a PIG gun. The beam current during the etching was 0.3-1 μA/cm^2, determined by use of a small Faraday cup in an analyzer chamber of a VG ESCALAB-5 electron spectrometer.

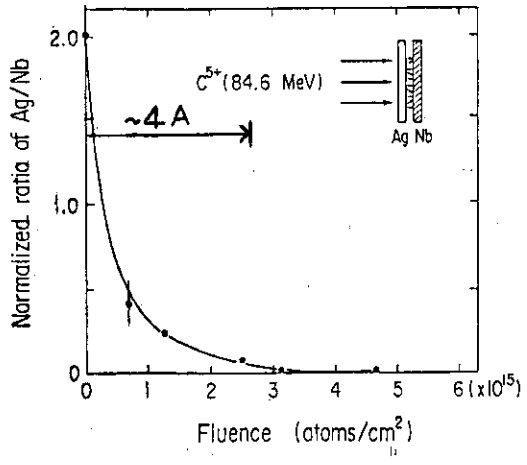

Fig. 1 Etching profile of the sputtered Ag particles deposited on near surface of the Nb catcher foil

3. Results and discussion

Figs. 1-3 show etching profiles of the particles sputtered on the Nb foils. Since etching rate in the present experiment was 0.2 nm per an Ar^+ fluence of 1 x 10^{15} ions/cm^2, the deposition of the sputtered atom is estimated to be within 3 atomic layers of the target surface. A

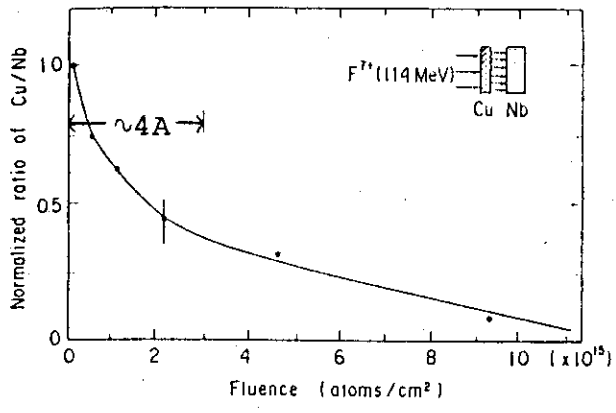

Fig. 2 Etching profile of the sputtered Cu particles deposited on near surface of the Nb catcher foil.

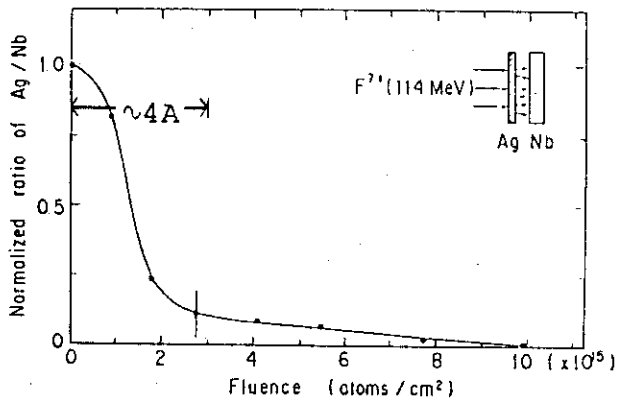

Fig. 3 Etching profile of the sputtered Ag particles deposited on near surface of the Nb catcher foil.

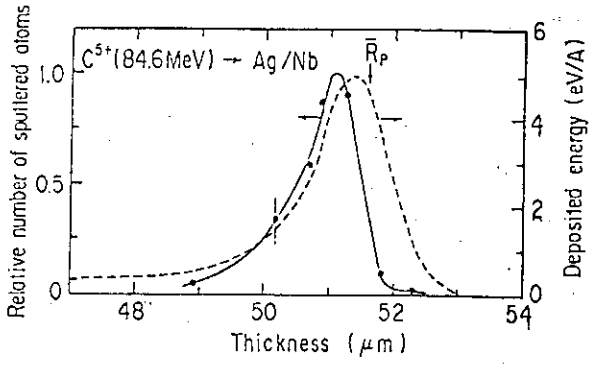

Fig. 4 Relative number of sputtered Ag atoms as a function of the target thickness. Total fluence was 3.5 x 10^{15} ions/cm^2. ———: experimental, - - - - -: energy-deposition distribution by the EDEP-1 code

tailing of the etching profile to the higher fluence in Fig. 2 is due to the surface roughness of the Nb foil which impeded uniformal Ar^+-ion etching. Detailed examination of Nb (MNN) and Ag (MNN) Auger spectra gave an evidence that the Ag particles sputtered are trapped in the oxide overlayer of the catcher foil, Nb_2O_5, and that their chemical state is not oxide but metallic one. Similar result was obtained for the Cu particles sputtered on the Nb catcher foil.

Relative numbers of the sputtered atoms are represented as a function of target thickness in Figs. 4-6. The peak

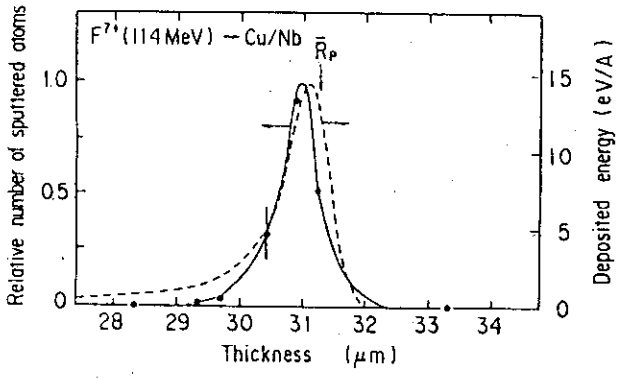

Fig. 5 Relative number of sputtered Cu atoms as a function of the target thickness. Total fluence was 1.7 x 10^{15} ions/cm^2. ———— : experimental, - - - - - : energy-deposition distribution by the EDEP-1 code.

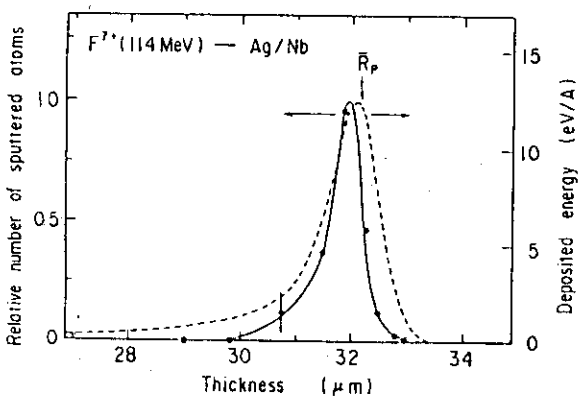

Fig. 6 Relative number of sputtered Ag atoms as a function of the target thickness. Total fluence was 4.0 x 10^{15} ions/cm^2. ———— : experimental, - - - - - : energy-deposition distribution by the EDEP-1 code.

positions of the experimental curves obtained locate by ∿1 % shallower than that of the nuclear energy-deposition distribution by the EDEP-1 code(7) modified for high-energy ions. Furthermore, the sputtering scarcely occurs in the region where the target thickness is less by 2.5 μm than the mean projected range, though considerable amount of the incident energy is dissipated in a form of the nuclear stopping.

The absolute yield for the transmission sputtering at target thickness t is estimated as,

$$Y(t) = N_s/N_f \qquad (1)$$

where N_s and N_f are the numbers of the sputtered atoms and incident ions per cm^2, respectively. On the other hand, the Auger peak ratio h_t/h_c is approximately correlated with x, the thickness of the sputtered atoms,

$$h_t/h_c = S_t(1-e^{-\mu_1 x})/S_c e^{-\mu_2 x} \qquad (2)$$

where S is the elemental sensitivity factor of the Auger spectra, μ_1 and μ_2 the ab-

sorption coefficients of the respective Auger electrons. The subscripts t and c denote the target and catcher foils, respectively. Eq.(2) is an expression fairly improved for the higher h_t/h_c ratio($\geq$1) which was not taken into account in the previous work(6). The absorption coefficients of the present Auger electrons are estimated to be 2 x 10^7/cm from the mean free paths of low energy electrons(8). Then the values of N_s can be estimated from the density of sputtered atoms and the value of x which is determined in eq.(2).

Since the N_s values obtained at the peak positions of the experimental curves are 6.3 x 10^{15} atoms/cm^2 in Fig. 4, 3.9 x 10^{15} atoms/cm^2 in Fig. 5 and 1.4 x 10^{16} atoms/cm^2 in Fig. 6, the maximum values of the sputtering yield are estimated to be 1.8 for the C^{5+} (84.6 MeV)→Ag/Nb system, 2.3 for the F^{7+} (114 MeV)→Cu/Nb system and 3.5 for the F^{7+} (114 MeV)→Ag/Nb system, respectively. Nuclear stopping calculations by the EDEP-1 code with the surface binding energy(9) of 3.5 eV for the Cu target and 2.9 eV for the Ag target provide the sputtering yields of 1.4, 2.0 and 3.1, respectively. The experimental data are in reasonable agreement with these calculated values.

References

(1) A. D. Marwick: Nucl. Instrum. Methods 132 (1976) 313.
(2) T. A. Sasaki, Y. Baba, K. Hojou and T. Aruga: J. Nucl. Mater. 132 (1985) 95.
(3) H. L. Bay, H. H. Anderson, W. O. Hofer and O. Nielsen: Appl. Phys. 11 (1976) 313.
(4) K. H. Ecker and K. L. Merkle: Phys. Rev. B 18 (1978) 1020.
(5) H. L. Bay, H. H. Anderson and W. O. Hofer: Rad. Effects 28 (1976) 87.
(6) T. A. Sasaki, Y. Baba and K. Hojou: "JAERI TANDEM, LINAC & V.D.G. Annual Report", JAERI-M 85-104 (1985) 37.
(7) I. Manning and G. P. Mueller: Computer Phys. Commun.

7 (1974) 85.
(8) C. R. Brundle: J. Vac. Sci. Technol. 11 (1974) 212.
(9) R. Hultgren, P. D. Desai, D. T. Hawkins, M. Gleiser, K. K. Kelley, D. D. Wagman: Selected Values of the Thermodynamic Properties of the Elements (American Society for Metals, Metals Park, Ohio, 1973).

II.14 Heavy Ion Microfilter of Polyvinylidene Fluoride

Yoshihide KOMAKI, Hitoshi OHTSU, *Norio MORISHITA and *Naohiro HAYAKAWA.
Department of Chemistry and *Takasaki Radiation Research Establishment, Japan Atomic Energy Research Institute.

Introduction

It is well known that charged particles with high energies give the straight trails of defects along the passages when travelling through a dielectric material and that the trails perforated through the material form characteristic etched holes by chemical treatments such as the alkaline etching. Making use of such phenomena, various microfilters of polymers (polycarbonate, cellulose esters, and polyesters)which are expected to be used for various purposes have been made by the irradiation of heavy ions and subsequent alkaline etching.

Recently, our attention has been paid to the study on the microfilter of polyvinylidene fluoride(PVDF) film, $(-C_2F_2H_2-)_n$, having the properties of chemical attack resistivity, excellent mechanical strength, and hydrophobic surface. It has been found therefrom that the number of holes occurring in the film is proportional to the number of incident particles passed through the film and the diameters of holes also depend on the etching conditions such as the time of etching.

The purpose of the present investigation is to examine the effect of incident energies of $^{35}Cl^{10+}$(150 MeV) and $^{64}Cu^{11+}$(180 MeV) ions on the enlargement of diameters of holes in the PVDF film.

Experimental

The equipments used consist of Raman Chamber and two Low Temperature Irradiation Chambers.

9.4 μm thick biaxially stretched PVDF films stacked severally were irradiated with scanning the beams of heavy ions. A sheet of film is 13 mm in diameter and 8 mm for the effective irradiation diameter, and has the hole density of $10^8/cm^2$. The specimens irradiated were etched in a closed vessel of all-Tefron containning a 10N NaOH solution with constant stirring at $85^oC \pm 0.1^oC$. After washed enough in a stream of water and dried in air, the films etched were measured the rate of transmittance of Ar through

the holes. The diameters of holes were estimated by the Knudsen's formula. The Knudsen's formula gives the true diameter only when the holes are perfect circular cylinder with the smooth wall and the flow is molecular through the holes. In this study, the diameter of hole should be called the effective hole diameter.

The surface of membrane was observed by a scanning electron microscope (JSM-35C), after depositing Au-Pd(5:5) alloy in vacuum on the film. The thickness of deposition is about 10 nm. The specimen was fixed with Ag-paste upon the holder of brass.

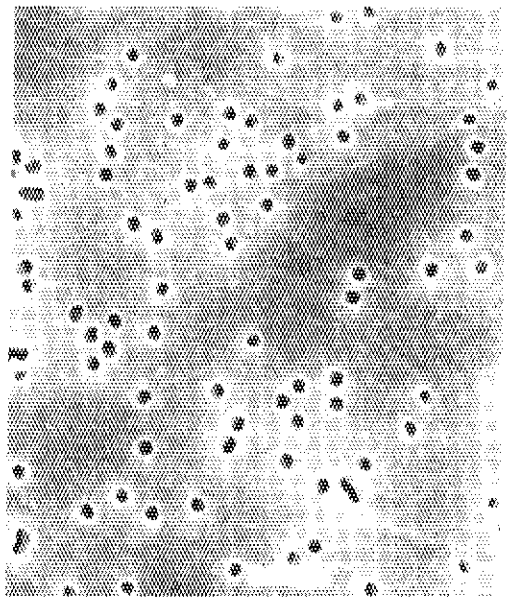

Fig. 1 SEM micrograph of the etched holes in the PVDF film irradiated by the Cu ions.

Results and Discussion

The etching for 9.4 μm thick PVDF film irradiated with the Cl, Ni, and In ions excluding the O ions has revealed the perforated holes. This shows that PVDF is rather insensitive polymer as a heavy ion track detector in comparison with polycarbonate and cellulose esters.

Figure 1 is a SEM of the surface of 9.4 μm thick PVDF film irradiated with the $^{64}Cu^{11+}$ ions(180 MeV) and etched in the 10N NaOH solution at 85°C for 50 hrs. The observed number of holes is $2\times10^{8}/cm^{2}$ on an average, and same between the inside surface and the outside. The number calculated is $3\times10^{8}/cm^{2}$ from measuring the ionic current of beams with Faraday electrode. The mean diameter estimated is 140 nm.

Figure 2 shows the results of the irradiation with the Cl, Ni, and Cu ions, in which the effective hole diameters obtained by measuring the rate of gaseous transmittance through

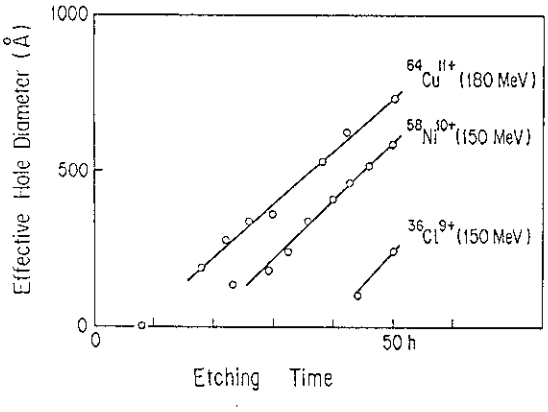

Fig. 2 Growth of effective hole diameter and the etching time.

The 9.4 μm thick PVDF film exposed to the Cl,Ni, and In ions and etched in the 10N NaOH solution at 85°C.

the holes after etching for the arbitrary time and dring are plotted against the etching time. From the figure, we see that (1), at the same period of etching, the effect of the heavy ions on the effective hole diameters is in order of Cu>Ni>Cl, and (2), at the same energy, the diameter for the Ni ion is larger than that for the Cl ion.

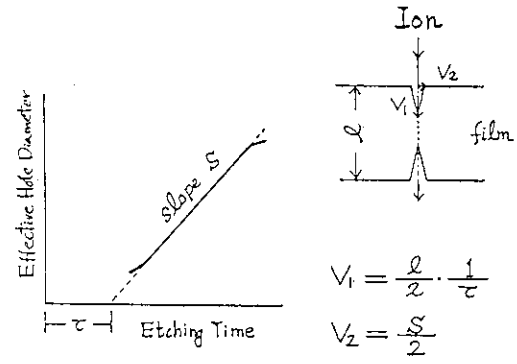

Fig. 3 Diagram for enlargement of the perforated holes. Definition of two etching rates, V_1 and V_2.

The enlargement of the perforated holes may be explained as follows. Each curve in Fig. 2 indicates that the effective hole diameter begins to enlarge proportionally with the time after a constant period of etching. During the period, any holes are not detected. The period means the time that the etchant attacks deeper along the trajectories of heavy ions from both surfaces of the film and connects at the center of the film.

Figure 3 shows a diagram for the enlargement of perforated hole by etching. The axial etching rate V_1 and the lateral etching rate V_2 are approximately given by the following relations,

$$V_1 = (\ell/2)(1/\tau),$$

and

$$V_2 = (S/2),$$

where ℓ denotes the thickness of the film , τ the induction time and S the slope of the curve. Using these equations, we can obtain the values of V_1, V_2, and V_1/V_2. These are listed in Table 1.

On the other hand, the ratio of V_1/V_2 is related to an angle of the taper in the perforated holes. When θ is defined as the angle of taper, θ is obtained as follows,

Table 1 The etching rate along the track(V_1), the lateral rate(V_2) and the ratio of V_1/V_2 for PVDF films etched in the 10N NaOH solution at 85°C.

	Ion	MeV/amu	V_1 (μm/h)	V_2	V_1/V_2
Cl-36	Cl 1	4.3	118	1.1	110
	Cl 2	3.6	140		130
	Cl 3	2.8	280		270
	Cl 4	1.9	380		360
Ni-58		2.6	230	1.0	230
Cu-64		2.8	600	0.9	680

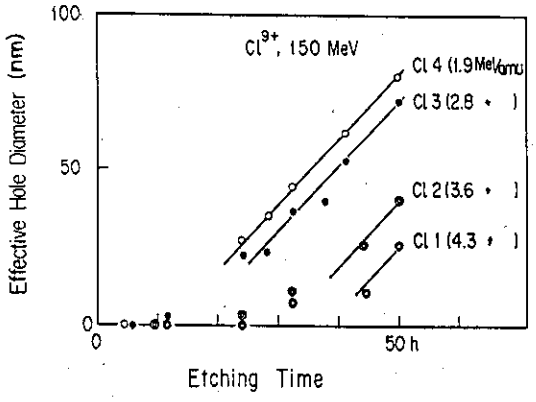

Fig. 4 The effect of incident energies of the Cl ions on growth of effective hole diameter.

The numbers in parenthesis indicate the calculated incident nergies on each film in stack, except of 4.3 MeV/amu.

Schilling's equation and converted to the incident energies on each surface of the films stacked. These values are indicated on the curves in Fig. 4. At the same period of etching, the diameters of the holes become large as the incident energy of the Cl ions decrease. Such a trend is same as in the case of V_1 in Table 1. As the slopes of the curves are almost same, the lateral etching rates may be so.

Figure 5 shows the incident energy (the Cl ion) dependency of two kinds of hole diameters. The diameters of holes on the surface were measured by SEM.

Except for Cl-1, the incident energies were calculated for Cl-2 to Cl-5. The symbols of Cl-1 to Cl-5 indicate the order of the incident ions into the films.

$\tan\theta = V_2/V_1$ or $\theta = \tan^{-1}(V_2/V_1)$.

It is reasonable that the larger the ratio of V_1/V_2, the smaller the angle, which corresponds to a cylinder.

Table shows that the track etching rate V_1 is far larger than the lateral rate V_2. The V_1 is larger as the energy is smaller. The values of V_1/V_2 are larger similarly. These facts mean that, though the resistivity for the chemical attack is large in the unirradiated PVDF, radiation damage makes the film easy to dissolve.

Figure 4 shows the relation between the etching time and the enlargement of holes by the irradiation of the 9.4 μm PVDF film with the $^{35}Cl^{10+}$ions. The ranges of the $^{35}Cl^{10+}$ions(150 MeV) in PVDF were calculated by the Northcliffe-

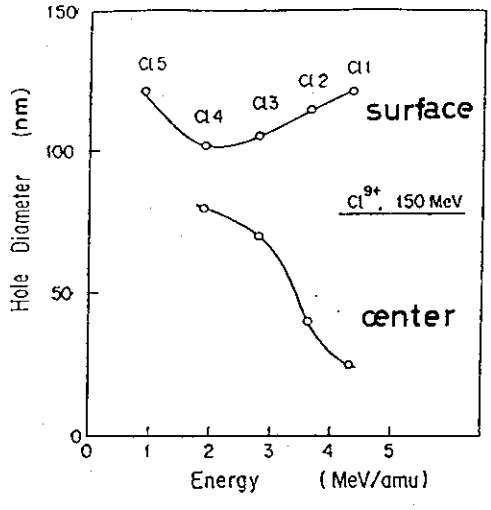

Fig. 5 Two kinds of diameters and the incident energies of the Cl ions.

The upper curve in the figure expresses the diameters of holes on the surface from measurement by SEM and the lower one the effective hole diameters determined from the gaseous transmittance through holes. The diameter was not obtained for Cl-5 in the lower case, where no incident ions penetrated through the thickness of the film.

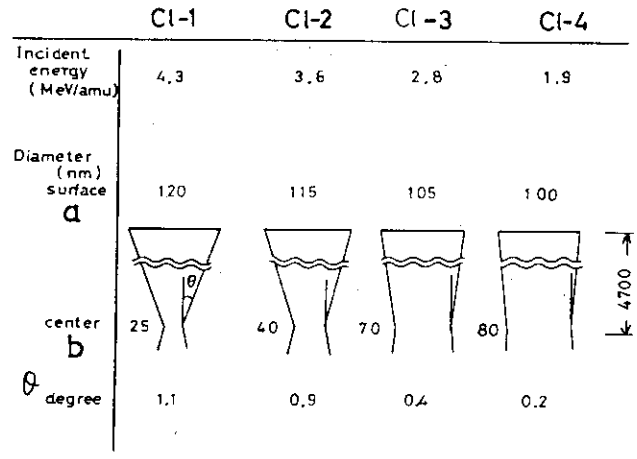

Fig. 6 The shapes of perforated holes estimated from the ratio of V_1/V_2.

Knudsen pointed out that the most slim diameter dominates the flow of gas in the long tube with the taper. Therefore, it is no doubt that the effective hole diameter indicates the smallest diameter along the length of tubes, that is, the central portion in the entire length.

It is found from the figure that the surface diameters of the holes(a) do not change considerably with the incident energies, but the effective hole diameters(b) increase at the lower energy. The difference between the effective hole diameter and the surface diameter is illustrated in Fig. 6.

From the ratio of V_1/V_2, the taper angles of each perforated hole show to be almost as small as one degree, which means that the shape of holes is almost cylindrical.

References

1. L.C. Northcliffe, R.F. Schilling, Nuclear Data Tables. A7, 233 (1970).
2. Y. Komaki,S. Ohno, H. Ohtsu, I. Ito,T. Seguchi,and M. Iwasaki.,Nucl. Tracks Radiat.Meas. 11, 99 (1986).
3. S. Dushman.,Scientific Foundations of Vacuum Technique, Chap. 11, John Wiley, New York.(1949).

II.15 IRRADIATION EFFECTS OF 16MeV PROTONS ON Fe-Cr ALLOYS

Yoshikazu HAMAGUCHI and Hisasi KUWANO

Department of Metallurgical Engineering
Muroran Institute of Technology

Introduction

The advantage of energetic proton irradiation experiments is that the penetration depth or range and straggling of proton in steels are fairly large, which are suitable for producing the damaged specimen of bulk size by using the ion irradiation technique. Since the positions of maximum damage and stopping of proton are almost identical, it is possible to examine the superposed effect of radiation damage and implanted protons by using the sample whose thickness is larger than the penetration range of protons. The disadvantage is that the energetic proton can produce the radioactive isotopes from the alloying elements, which need the care and make limitation of handling and measurements of irradiated specimens. The 14MeV neutrons produced by the fusion reaction in the fusion reactor core irradiate the first wall, vacuum vessel and blanket materials, and introduce the heavy damage and transmuted hydrogen and helium atoms into them. As the simulation experiment of 14MeV neutron irradiation effects on the ferritic steels, the changes of hardness, X-ray diffraction line width and internal magnetic field by the irradiation of 11MeV protons have been measured on the HT-9 and SUS410L ferritic steels(1,2). The significant result of proton irradiation on the SUS410L steel is the increasing of internal magnetic field in the specimen located around the maximum damage position. The main composition of the SUS410L steel is Fe-12%Cr alloy. There is a linear relation between the internal magnetic field and concentration of chromium in the Fe-Cr solid solution alloy system (3). The increasing of internal field in the SUS410L steel means the decreasing of Cr content in the matrix by the irradiation of protons. There are many evidences of irradiation-induced precipitation and radiation-induced segregation in the undersaturated and supersaturated solid solutions by the irradiation of proton and electron (4). In the usual sense, the decreasing of solute element in the matrix means the segregation of it at the sink site. However, since chromium is an oversize element in the iron matrix, it seems to be difficult to explain the segregation of Cr at the sink site by the mechanism of interstitial-solute interaction or inverse Kirkendall effect.

The purpose of this paper is to elucidate the relation between the degree of super- and/or under-saturation of Cr in the solid solution and the proton induced degradation of Cr content.

Experimental Procedure

The Fe-Cr alloy specimens of 4.7(5Cr), 10.4(10Cr), 16.9(16Cr) and 28.5(29Cr) mass % Cr were prepared for the proton irradiation. After all specimens were formed in the thin plate by the hot and cold rolling and solution annealed, they were cut out in the form of disk with 12 mm dia. and 30 μm thick. The 36 disks of the same kind of alloy were stacked and set into the irradiation chamber installed in the "Baby Cyclotron". The proton energy and current for the irradiation were 16 MeV and 10 μA/8mmϕ for 1 hour at the surface of stacked disks. The temperature of specimen during the irradiation was measured by the thermocouple contacting to the side of stacked disks, which showed between 160K to 250K, but real temperature of the specimen at the maximum damaged region should be about 200K higher than that shown by the thermocouple.

After the irradiation, the specimens were kept at room temperature. Ten pieces of specimen located on the incidental side were abandoned for the high induced activity and the remainder were used for the measurements. The hardness were measured by the micro-Vickers hardness of 50g loading and the average value of 10 measuring points were adopted for the measured value. X-ray diffraction line width was measured at the 211 diffraction line of Cu-K_α. A 30 mCi ^{57}Co-Rh source was used for the Mössbauer spectroscopy.

Experimental results

The depth profile of micro-Vickers hardness after the irradiation are shown in Fig. 1. The maximum hardness are at about 500 μm in depth, half width of the profile of hardness increase are about 140 μm and the maximum increasing of hardness are about 20 VHN in all samples. The dependence of Cr concentration is not observed in the hardness increasing.

The broadening of X-ray diffraction line width is observed on the high Cr alloy as shown in Fig. 2, but not observed on pure iron.

The depth profile of average internal magnetic field obtained from the Mössbauer spectrum after the irradiation are shown in Fig. 3. No remarkable increase of internal magnetic field has been observed in 5Cr alloy, but the alloys containing more than 10% Cr show the significant increase of

internal field after the irradiation. By using the linear relation between the internal magnetic field and concentration of Cr, the change of Cr at the mother matrix can be estimated, which is shown in Fig. 4. The decreasing of Cr in the matrix means that the segregation or precipitation of Cr-rich cluster is enhanced by the low temperature irradiation of protons, even though no indication of paramagnetic peak in the Mössbauer spectrum. To confirm this conclusion the successive aging of one hour from 100°C with the interval of 100°C was made on three specimens of 29Cr alloy irradiated at the different depth position. No significant increase of internal field has been observed in specimen B (only slightly damaged by protons) and specimen Y (affected no damage and implantation of proton) up to 400°C aging treatment as shown in Fig. 5. On a specimen I (located at the peak damage position) slight increase of internal field is observed at 300°C aging, which should suggest the enhancement of phase separation by the proton irradiation.

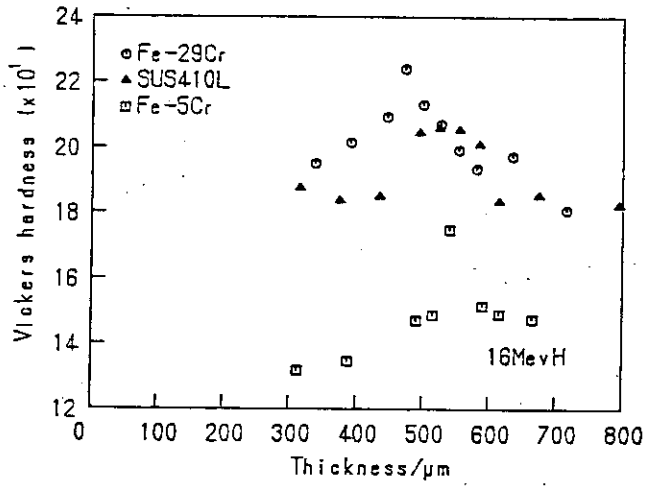

Fig. 1 Depth profile of micro-Vickers hardness after the irradiation

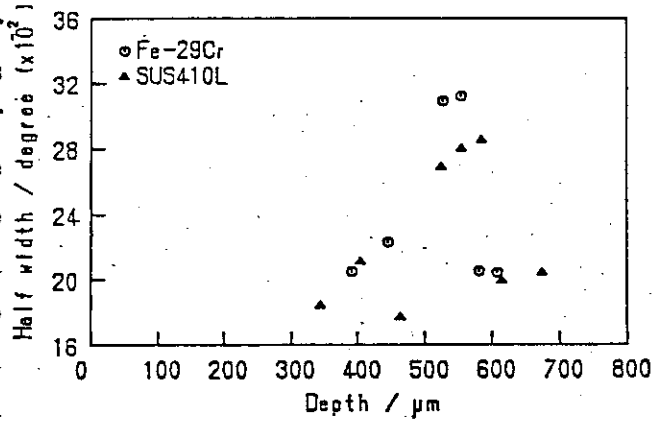

Fig. 2 Depth profile of X-ray diffraction line width after the irradiation

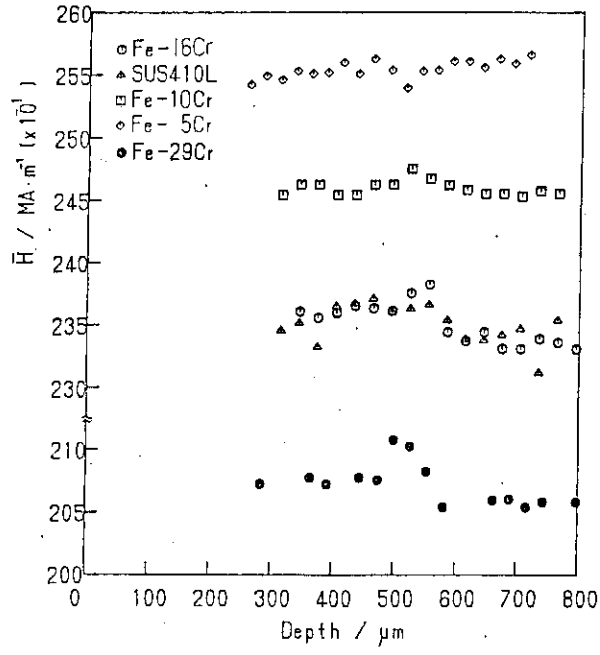

Fig. 3 Depth profile of internal magnetic field after the irradiation

Discussions

Experimental results show that the increasing of internal magnetic field is observed in the alloys containing more than 10 % Cr and is

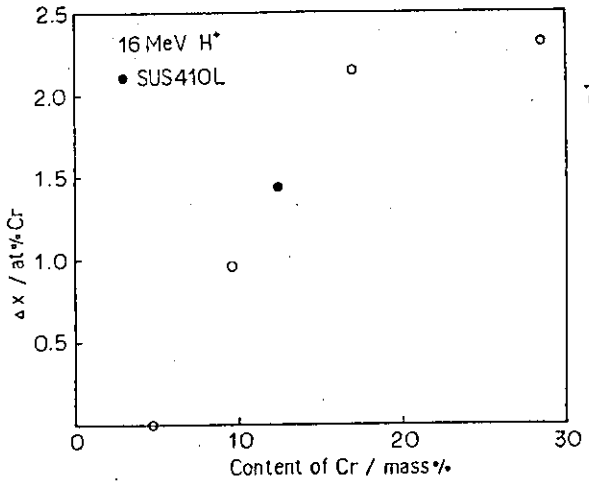

Fig. 4 Relation between Cr depletion after the irradiation and content of Cr in alloys

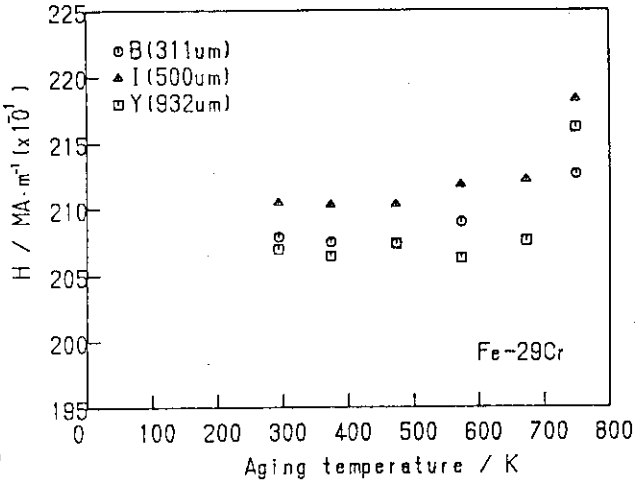

Fig. 5 Aging behavior of internal magnetic field in 29Cr after the irradiation at different position

not observed in the 5 % Cr alloy by the proton irradiation. To clear the mechanism of the enhancement of Cr segregation by the proton irradiation, additional experiments are desired: these are obtaining the data of internal field increase on alloys of Cr content between 5 and 10 %, the experimental results of irradiation by the energetic particle other than proton, and another experimental confirmation of the segregation of Cr, such as the observation and analysis by using the analytical electron microscope. Recently, Man et al.(5) reported the enhanced segregation of Cr under the high energy electron irradiation in hydrogen implanted Fe-10%Cr alloy, which seems to be one of the confirmation to our conclusion.

References

(1) Y. Hamaguchi, H. Kuwano, H.Kamide, R. Miura and T. Yamada: J. Nucl. Mater. 133&134 (1985) 636.

(2) Y. Hamaguchi, H. Kuwano, T. Misawa R. Miura and T. Yamada: J. Nucl. Mater. 141&143 (1986) 781.

(3) H. Kuwano and Y. Morooka: J. Jpn. Inst. Metals 44 (1980) 202.

(4) G. Martin, R. Cauvin and A. Barbu: Phase Transformations under irradiation, ed. F. V. Nolfi, Applied Science Pub. (1983) p.47.

(5) Man Hatusei, R. Nagasaki, H. Takahashi and S. Ohnuki: Abstract of The Japan Institute of Metals, spring meeting (1987) p.65

II.16 "TUNNEL STRUCTURE" FORMED IN AL ON HYDROGEN IMPLANTATION

Kohji Kamada, Akio Sagara, Hirotsugu Kinoshita* and Heishichiro Takahashi*

Institute of Plasma Physics, Nagoya University, Japan, *Faculty of Engineering, Hokkaido University, Japan

Change in microstructure of ion implanted surface has a great consequence in hydrogen isotope recycling and surface modification at first wall of fusion devices. Though we have a great deal of accumulations of reports and data on microstructural changes such as bubble formation and blistering after helium implantation into materials[1], works on effects of hydrogen implantation are rather rare, except a few works done on Cu[2-4] observing bubbles after bombardments with hydrogen isotopes at 120 K, works on the implanted hydrogen isotope traps by various kinds of lattice defects including bubbles in several metals,[5,6] and works on blistering on hydrogen isotope implantation in metals.[8-11] On the other hand, simulation studies on the recycling process, including diffusion, retention and surface recombination, have been pursuing with hydrogen isotope implantations. Therefore, the studies on microstructural change on the implantation is requisite for better understanding of recycling and surface modifications expected on the first wall. This paper concerns the report of the "Tunnel Structure" found with TEM observations in Al implanted with 25 keV H_2^+ at room temeprature to fluences exceeding 3×10^{17} H^+/cm^2.

Aluminium specimens were implanted at room temperature to fluences 4×10^{17} H^+/cm^2 to 2×10^{18} H^+/cm^2, and were probed with elastic reocil detection method (ERD)[12] using 1.5 MeV He^+ during the implantation, to obtain depth

distributions of the hydrogen. Following the implantation and profiling, samples were elctropolished using backthinning technique to protect the front implanted surface, and tested with TEM.

When hydrogen ions are implanted into Al at room temeprature, they are trapped by lattice defects created by themselves during the implantation rather than to stay around their projected range. This was clearly demonstrated in a previous paper[13], in which the depth profile measusred with ERD coincided well with the damage profile predicted by numerical simulation, provided the hydrogen fluence is less than 3×10^{17} H^+/cm^2 for 25 keV H_2^+ implantation. On increase of the flunece over this critical value, however, we observed a drastic collapse in the profile from a nearly Gaussian type to rather widely spread, double peaked or nearly double peaked profile, similar to the change observed before on He^+ implantation into Cu by Terreault et al..[14]

On TEM observations, the implantation produces a numerous number of bubbles ranging from 50 Å to 1000 Å in diameter, with a sharp peak at about 120 Å irrespective of the ion fluence. However, when the ion fluence exceeded the critical fluence of the profile collapse, widely spread bright contrast region appears in the electronmicrograph as seen in Fig. 1. The complimentary dark contrast region has the same contrast with that observed in a specimen implanted less than the critical fluence. This bright contrast does not depend on diffraction condition giving very similar contrast on either on-Bragg or off-Bragg condition. From stereomicroscopic observatons, which revealed the cross-sectional view of the bubble distribution, we observed that the bubbles are evacuated from the layer corresponding to this bright contrast area. These observations suggest that the matrix atoms are evacuated from this region, consequently becoming more tranparent locally to the electron beam. We named this microscopic structure in the subsurface layer "Tunnel Structure". Areal fracton of the "Tunnel Structure" per unit area of the implanted surface increased with the ion

fluence from about 60 % at 1×10^{18} H^+/cm^2 to more than 80 % at 2×10^{18} H^+/cm^2.

The collapse of the hydrogen profile is associated with the formation of this "Tunnel Structure". Before its formation, the observed profile corresponds almost exactly to the bubble distribution obtained by stereoscopic electron microscopy in both width and depth of the distribution. On the other hand, every specimen in which the profile collapse has been observed during the hydrogen implantation, reveals the "Tunnel Structure" on electron microscopy. The critical fluence is about 6×10^{17} H^+/cm^2 for 25 keV H_2^+ injection. The profile after the collapse is similar to the case of helium implantation into Cu[14], and assumes a double peaked profile, or nearly double peak profile, and becomes widely spread than before the collapse.

From sequential observations of bubble structures in different specimens on increasing hydrogen fluence, the laterally arranged bubbles which have been present before the formation of the "Tunnel Structure" disappear rather rapidly, eventually contributing to the formation of the structure. After the appearance of the "Tunnel Structure", bubbles due to further implantation are formed closer to a surface than the structure. And the volume of the "Tunnel Structure", about 3×10^{-6} cm^3/cm^2, is about an order of magnitude larger than the total bubble volume which has contributed to the formation of the structure. Further, in coincidence with the appearance of the structure the specimen surface roughens producing the undulation of the surface typically with bout 5000 Å in wave length and about 500 Å in depth, which was observable by stereoscopic electron microscopy with specimen surface decorated by gold evaporation.

These things altogether indicate the enormous amount of mass flow from the depth of "Tunnel Structure" toward the free surface. The mechanism of the mass flow is not very clear at present. However, in so-far proposed mechanisms to explain the formation of large cavities, the emission of interstitial type dislocation loops from bubbles might be

acceptable than other mechanisms such as inter-bubble fracture, bubble coalescence and bubble migration, since these are difficult to explain the enormous amount of volume increase of an order of magnitude and the concomitant flow of matrix atoms toward surface. In case of the loop emission mechanism, the volume increase of such amount might be not impossible if the bubbles are highly pressurized. For a typical bubble with 120 Å in diameter, it is necessary roughly 100 interstitial loops to be emitted to increase the volume 10 times, assuming $\pi r^2 b$ for the volume increase of a bubble of radius r for every emission of a dislocation loop with Burgers vector b. The emitted interstitials may deposit on a free surface giving the surface roughening.

Large area overview of the microstructure injected to a fluence of 2×10^{18} H^+/cm^2 is shown in Fig. 2. This micrograph shows a blister in addition to the bubbles and "Tunnel Structure". The blister can be recognized from its bend contour arising from bulge-out of its cover as reported previously[15]. In this micrograph we have a very interesting observation. Fig. 3 is an enlargement of the blistered area, and shows obviously the coarsening of the "Tunnel Structure" there, namely the disappearance of the dark contrast region observable in surrounding area. It is likely that the "Tunnel Structure" is a precursor for blister formation. Another point which we should emphasize is that the "Tunnel Structure" is presumed to be pressurized so as to be capable to bulge out the blister cover. Therefore, the "Tunnel Structure" is not connected to free surface, being different from "channels" observed on Mo by Jäger and Roth[16], otherwise such high internal pressure can not be maintained.

We have described a new microstructure revealed on hydrogen implantation into Al, which causes the collapse of hydrogen depth profile. The structure is not isolated but laterally connected throughout the injected area at a depth around the energy deposition peak of the implanted particle. From this structure matrix atoms are evacuated and eventually deposit on a free surface contributing to so

called swelling of material. Further investigation on the mechanisms of large mass flow toward surface is required.

Reference

(1) S.E. Donnelly: Rad. Eff. 90 1 (1985).
(2) P.B. Johnson, and D.J. Mazey, J. Nucl. Mater. 91 (1980) 41.
(3) P.B. Johnson, and D.J. Mazey, J. Nucl. Mater. 111/112 (1982) 681.
(4) P.B. Johnson, and D.J. Mazey, J. Nucl. Mater. 93/94 (1980) 721.
(5) W.R. Wampler, and S.M. Myers, Nucl. Inst. Meth in Phys. Res. B7/8 (1985) 76.
(6) S.M. Myers, W.R. Wampler F. Besenbacher, et al., Mater. Sci. Eng. 69 (1985) 397.
(7) L.H. Milacek, R.D. Daniels, and J.A. Cooley, J. Appl. Phys. 39 (1968) 2803.
(8) L.H. Milacek, and R.D. Daniels, J. Appl. Phys. 39 (1968) 5714.
(9) W. Möllor, T. Pfeiffer, and D. Kamke, in Ion Beam Surface Layer Analysis, eds. O. Mayer, G. Linker and F. Käppeler (Plenum Press, New York, 1976) II. p.841.
(10) G. Verbeek, and W. Eckstein, in Application of Ion Beams to Metals, eds. S.T. Picraux, E.P. EerNisse and F.L. Vook, (Plenum Press, New York, 1974), p.597.
(11) T.R. Armstrong, J. Nucl. Mater. 84 (1979) 118.
(12) S. Nagata, S. Yamaguchi, Y. Fujino, Y. Hori, N. Sugiyama, and K. Kamada, Nucl. Inst. Meth. B6 533 (1985)
(13) D. Kamada, A. Sagara, N. Sugiyama, and S. Yamaguchi, J. Nucl. Mater. 128/129 664 (1984).
(14) B. Terreault, G. Ross, R.G. St.-Jacques, and G. Veilleux, J. Appl. Phys. 51(3) 1491 (1980).
(15) J.H. Evans, Nature 256 299 (1975).
(16) W. Jäger, and J. Roth, J. Nucl. Mater. 93/94 756 (1980).

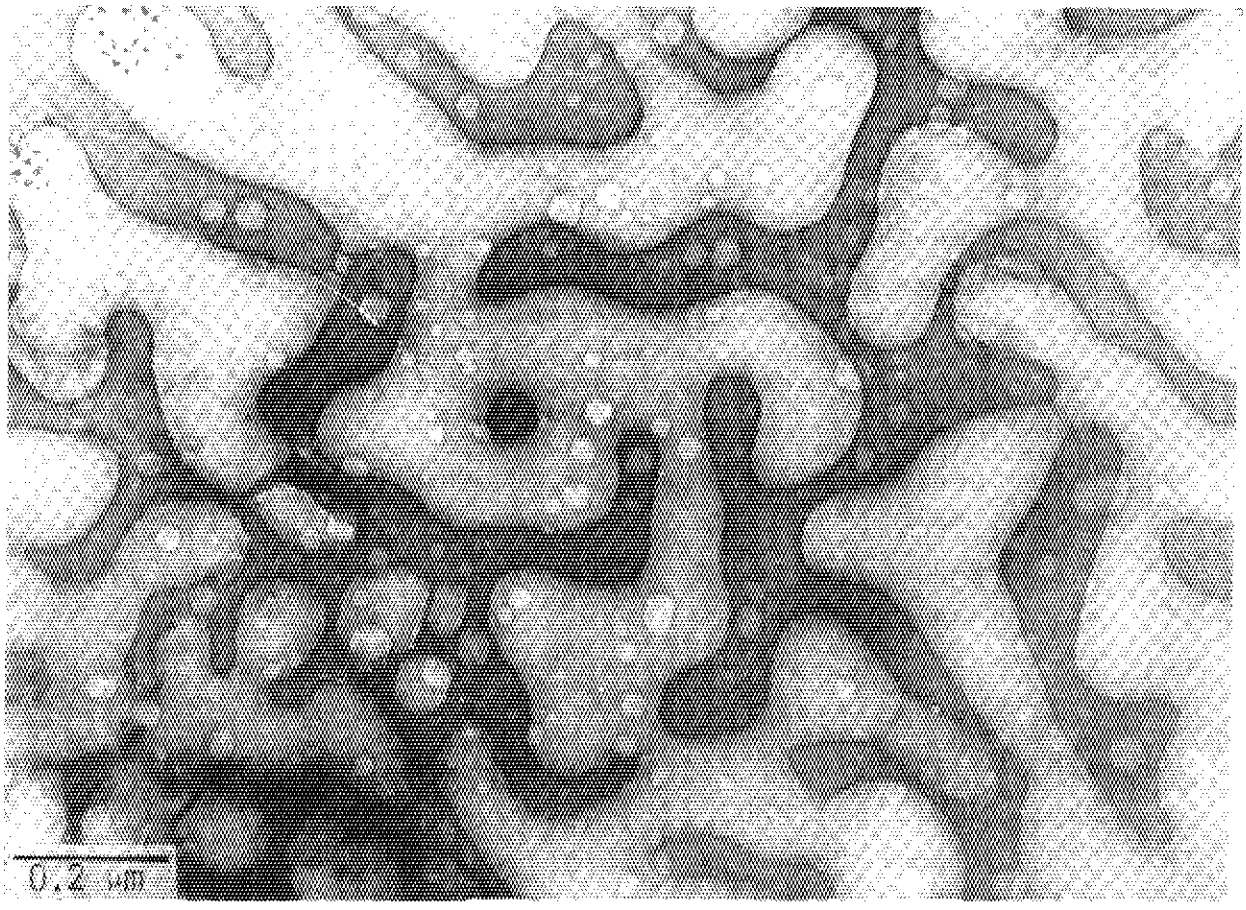

Fig. 1 175 keV electron micrograph of "Tunnel structure", together with bubbles, in Al implanted with 25 keV H_2^+ to a fluence of 2×10^{17} H^+/cm^2.

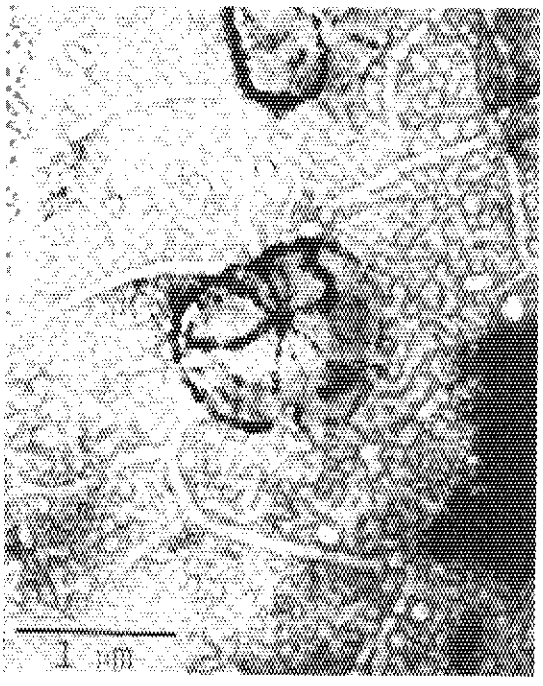

Fig. 2 Large area overview of the subsurface layer of Al implanted to a fluence of 1.1×10^{18} H^+/cm^2, showing bubbles, "Tunnel structure" and blisters.

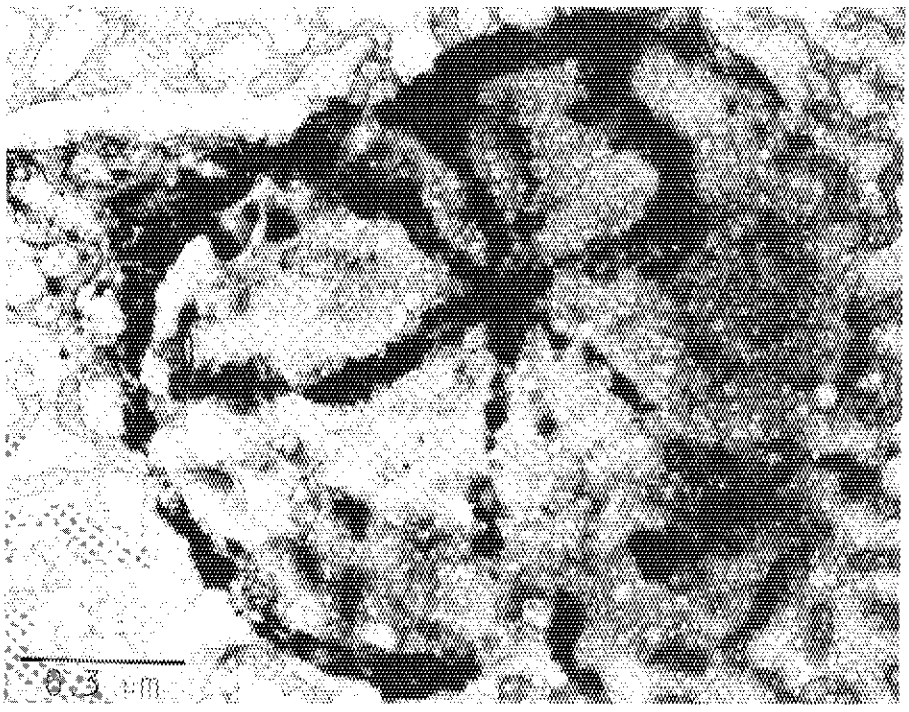

Fig. 3 An enlarged view of the blistered area, indicating the coarsening of the "Tunnel structure" under the blister cover.

II.17 POSITRON ANNIHILATION LIFETIME MEASUREMENTS OF IRON, IRON ALLOYS AND MOLYBDENUM IRRADIATED BY A TANDEM ACCELERATOR

Eiichi KURAMOTO, Noboru TSUKUDA, Minoru TAKENAKA, Yosoko TAKANO*, Naoki KIKUCHI**, Minoru NISHIZAKI***, Shiro MITARAI**** and Tokihiro KUROYANAGI****

Research Institute for Applied Mechanics, Kyushu University, *Atomic Energy Research Center, Toshiba, **Kobe Steel Company, ***Interdisciplinary Graduate School of Engineering Science, Kyushu University, ****Faculty of Science, Kyushu University

High energy Ni ions (90 - 100 MeV) were irradiated to various specimens (Fe, JFMS(Fe-10Cr-2Mo- - -) and Mo) at room temperature to final doses 0.01 - 0.1 dpa in range average. After irradiation specimens were investigated through isochronal annealing where a positron annihilation lifetime was measured. Three component analyses of lifetime spectra showed that during annealing interstitial clusters and microvoids were recovered stepwise and disappeared completely at high temperatures.

Introduction

Last several years various accelerators have been used for the investigation of radiation damage in metals and alloys in order to develop the radiation resistant materials. It is a great advantage of using accelerators producing heavy ion beams that high damage rate ($10^{-4} \sim 10^{-3}$ dpa/sec) is easily obtained compared with the irradiation of materials in nuclear reactors ($\sim 10^{-6}$ dpa/sec). The range of incident particles is, however, usually small (less than a few tens of micrometers) and the damage produced by incident particles is heterogeneously distributed over the range. On the other hand, positrons emitted from the source, for instance, ^{22}Na penetrate into specimens to the depth of about 100 micrometer. Hence the informations brought by positrons are range average of the radiation induced defects. Positron annihilation technique has become a very powerful non-destructive tool for the investigation of defects, i.e., vacancies, dislocations and voids. In this report results of positron annihilation studies of defects in Fe, JFMS and Mo irradiated by 100 MeV Ni ions accelerated by Tandem in Kyushu University will be denoted.

Experimentals

High-purity Fe ($RRR_H \sim 3500$), Mo (RRR $\sim$ 175000) and JFMS (Japanese Ferritic/Martensitic Stainless Steel, Fe-9.85%Cr-2.31%Mo-0.94%Ni-0.58%Mn-0.67%Si-0.12%V-0.06%Nb-0.05%C) were irradiated by 100 MeV Ni ions accelerated by 10 MV Tandem accelerator in Kyushu University. The irradiation temperature was room temperature and the total amount of irradiation dose was 0.01 $\sim$ 0.2 dpa in the average over the whole projected range of damage produced. In Fig. 1 the damage and injected ion distribution calculated by TRIM code[1] is shown in the case of Fe irradiated by 100 MeV Ni ions.

Positron lifetime measurement was performed for these irradiated specimens at room temperature using a conventional fast-slow coincidence circuit composed of ORTEC modules with plastic scintillators and Na^{22} positron source. The resolution time is 235 psec in FWHM. The isochronal annealing experiments were performed above room temperature to study the recovery behaviour of radiation-induced defects. The annihilation lifetime spectrum was decomposed into three components.[2,3]

Results and Discussion

In Figs. 2 and 3 the positron annihilation lifetime spectrum and the results of isochronal annealing experiments are shown for pure Fe irradiated by 100 MeV Ni ions to a total dose of 1.25×10^{14} Ni^{10+}/cm^2 ($\sim$0.02 dpa in range average). From the shape of lifetime spectrum it is obvious that the irradiation introduced longer lifetime component. Corresponding to this fact it is seen that in Fig. 3 the third component (longest lifetime component) exists, which indicates that vacancies have already migrated and formed microvoids at room temperature. Hence it must be considered that the second component corresponds to mainly interstitial clusters. During isochronal annealing both second and third component were recovered, but the third component disappeared earlier, about 300°C. Strictly speaking microvoid component became smaller than the observable limit by positron technique at this temperature. The second, interstitial cluster component was considered to be recovered by mainly by absorption of vacancies emitted from microvoids. The reason why the third component is smaller than the second component in spite of the equality of the total number between vacancies and interstitials comes from the difference of trapping rate of positrons between microvoids and interstitial loops. Positrons emitted from a source penetrate into the specimen to the depth of about 100 micrometer which is much longer than the

range where the radiation-induced damage is distributed (about 7 micrometer from the front surface as shown in Fig. 1). Hence in the result obtained in Fig. 3 the mattrix component is overestimated because some part of positrons were annihilated in the region beyond the damage region. But the fraction of positrons which was actually annihilated in the damage region must be much higher than that obtained from the simple consideration of the ratio between the damage range and the positron penetration range, because of trapping effect of positrons in the former region. This is a very important advantage in the usage of positron annihilation technique for the study of specimens irradiated by high energy ions.

In Figs. 4 and 5 the results of high-purity Mo are shown. Vacancies in Mo are not mobile at room temperature which corresponds to the absence of the third component in as-irradiated state. Above 200°C vacancies begin to migrate and form microvoids, namely, the third component appears. During isochronal annealing both the second and the third component gradually decrease, but until 600°C recovery have not been accomplished, then further annealing experiments are definitely required. In this irradiation experiment the total dose was 3.12×10^{13} Ni^{10+}/cm^2 ($\sim$0.01 dpa in range average). This is smaller than that in the case of Fe, but the total amount of the second and the third component is higher in Mo than that in Fe in as-irradiated state. This comes from difference of trapping efficiency of positrons between single vacancies plus interstitial clusters (in Mo) and microvoids plus interstitial clusters (in Fe).

In Figs. 6 and 7 the results of JFMS are shown, where the total dose was 1.25×10^{14} Ni^{10+}/cm^2 ($\sim$0.02 dpa in range average). Single vacancies start to move above 200°C and no microvoid formation was observed probably because of high absorption efficiency of vacancies to grown-in dislocations and grain boundaries. Vacancy migration temperature (around 250°C) obtained here is higher than that obtained in the electron irradiated JFMS (around 150°C). The difference comes from the trapping of vacancies probably by carbon atoms resolved from carbides which exist in cascade region. But more detailed experiments are required to clarify this radiation-induced resolution effect of carbides or other precipitates.

Acknowledgements

The authors wish to express their cordial thanks to Dr. H-J Kaufmann in Akademie der Wissenschaften der DDR for supplying ultra high purity Mo specimens.

References

1) J. P. Biersack and L. G. Haggmark, Nucl. Inst. Meth. 174 (1980) 257.
2) E. Kuramoto, N. Tsukuda, Y. Aono, M. Takenaka, Y. Takano, H. Yoshida and K. Shiraishi, J. Nucl. Mat. 133 & 134 (1985) 561.
3) E. Kuramoto, Y. Takano, N. Kikuchi and M. Takenaka, J. Nucl. Mat. 141 - 143 (1986) 829.

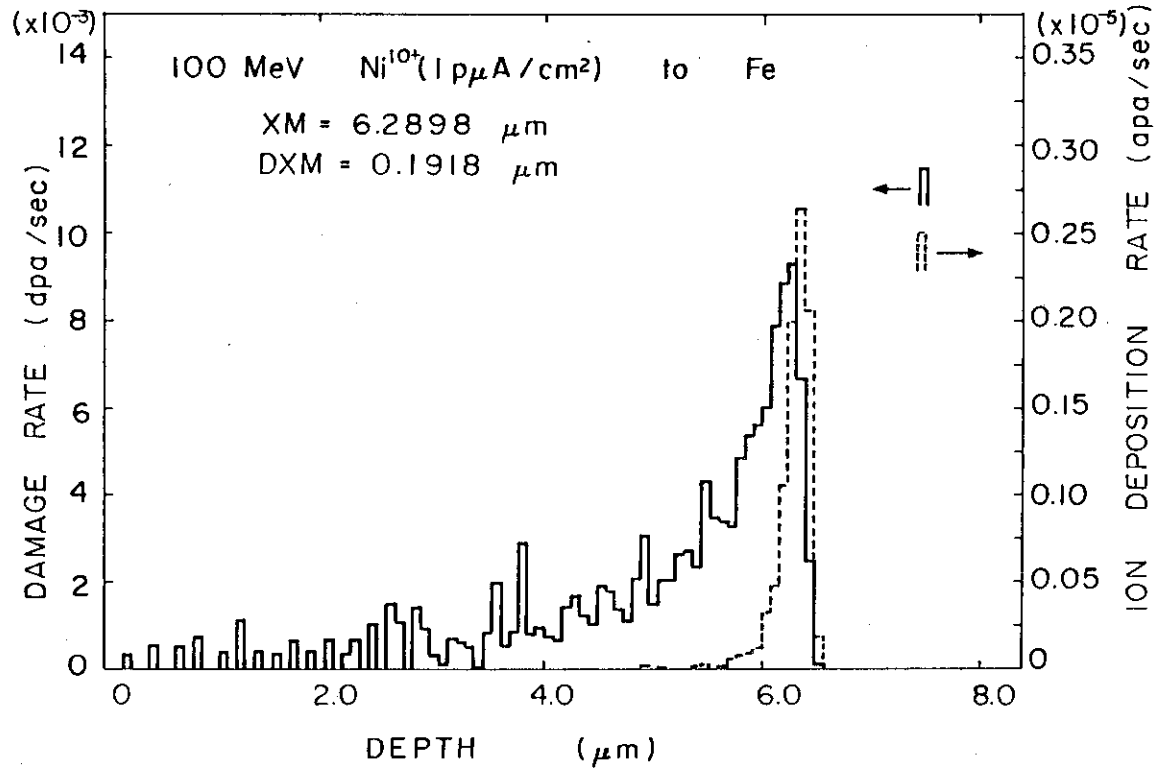

Fig. 1 Distribuion of damage and injected ions calculated by TRIM code for Fe specimen irradiated by 100 MeV Ni ions.

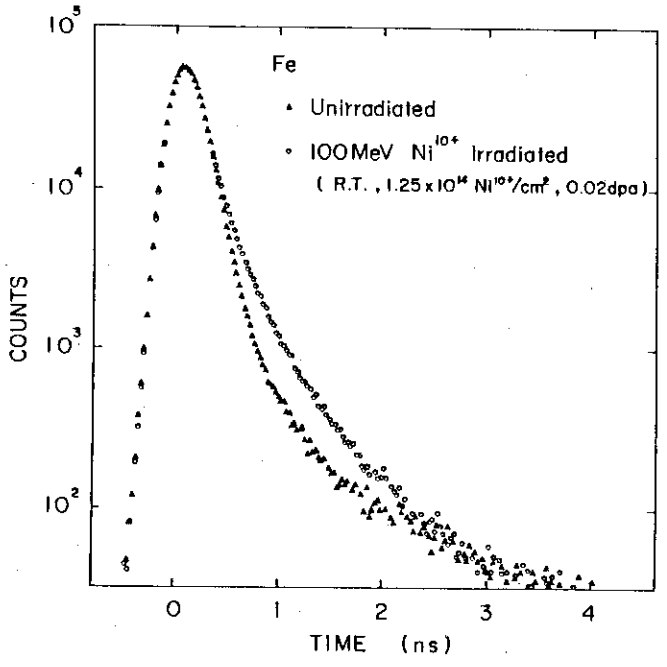

Fig. 2 Positron annihilation lifetime spectrum for Fe irradiated by 100 MeV Ni ions to a dose of 1.25×10^{14} Ni/cm^2 at R.T.

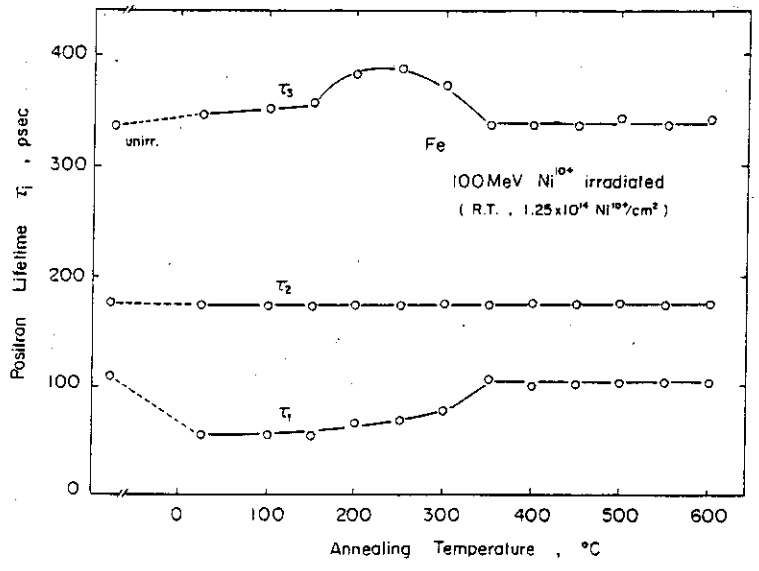

Fig. 3 Isochronal annealing curve of lifetime spectrum decomposed into three components for Fe irradiated by 100 MeV Ni ions to a dose of 1.25×10^{14} Ni/cm^2 at R.T.

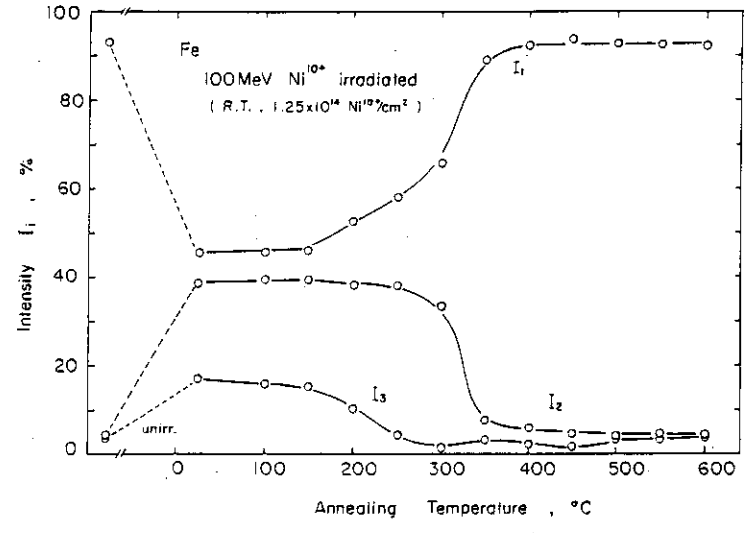

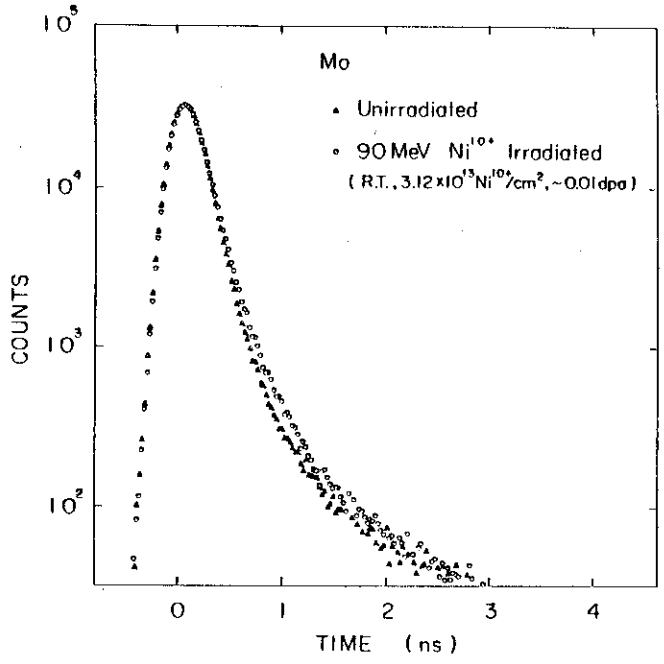

Fig. 4 Positron annihilation lifetime spectrum for Mo irradiated by 90 MeV Ni ions to a dose of 3.12×10^{13} Ni/cm^2 at R.T.

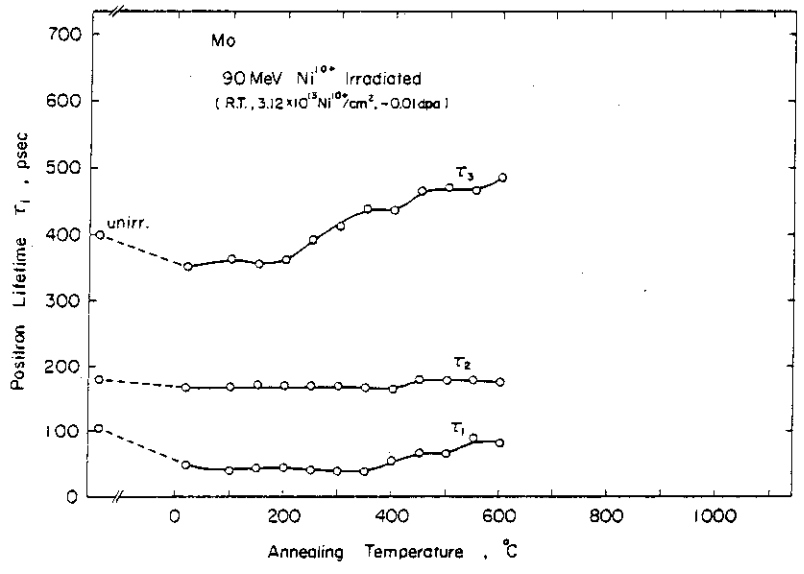

Fig. 5 Isochronal annealing curve of lifetime spectrum decomposed into three components for Mo irradiated by 90 MeV Ni ions to a dose of 3.12×10^{13} Ni/cm^2 at R.T.

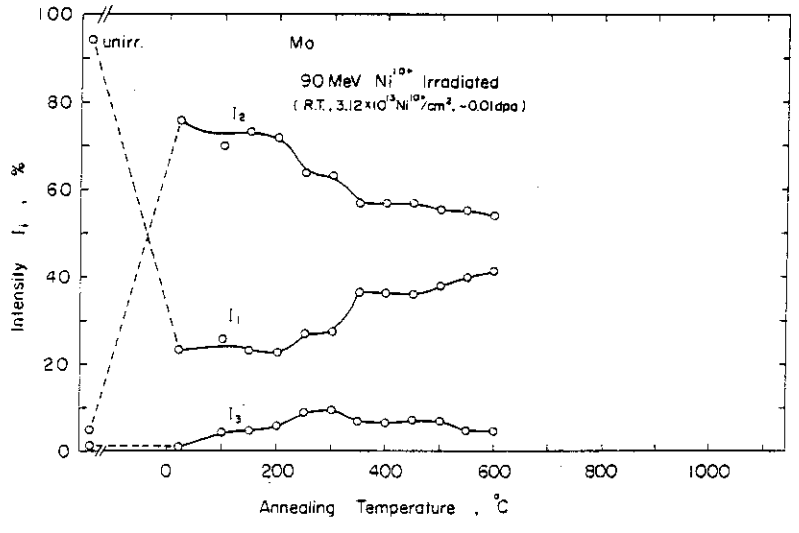

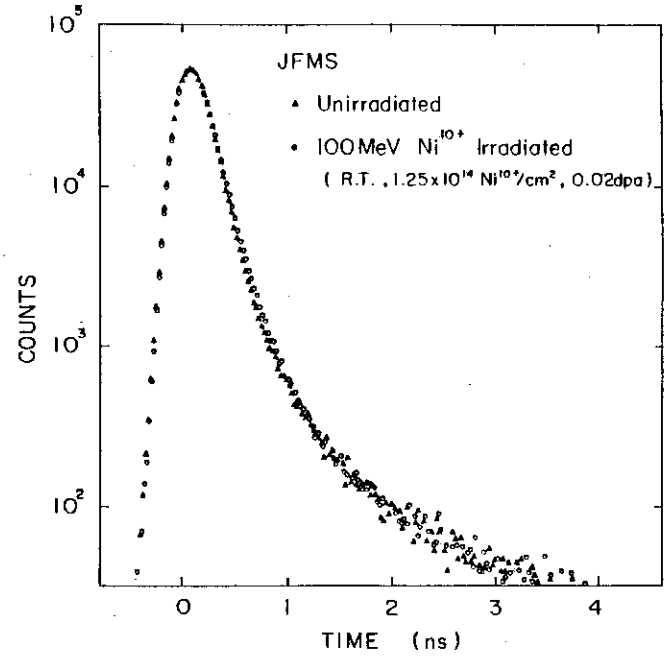

Fig. 6 Positron annihilation lifetime spectrum for JFMS irradiated by 100 MeV Ni ions to a dose of 1.25×10^{14} Ni/cm^2 at R.T.

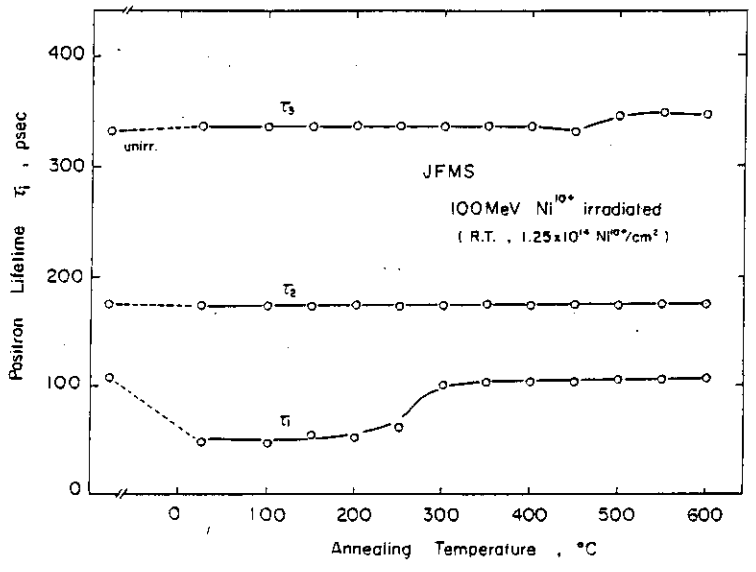

Fig. 7 Isochronal annealing curve of lifetime spectrum decomposed into three components for JFMS irradiated by 100 MeV Ni ions to a dose of 1.25×10^{14} Ni/cm^2 at R.T.

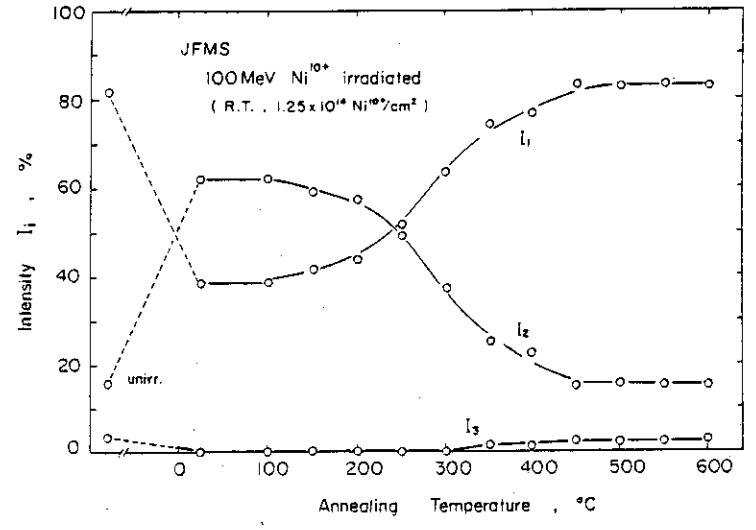

II.18 ON SELF-INTERSTITIAL ATOMS IN TA AND NB

Shigeo OKUDA and Hiroshi MIZUBAYASHI

Institute of Materials Science, University of Tsukuba
Sakura-mura, Ibaraki 305

§1. Introduction

From the recovery experiments of electrical resistivity after electron irradiation at low temperatures, H. Schultz suggested that self-interstitial atoms (SIA's) in Ta and Nb perform a long range free migration at least below 8K(1). This suggestion is, however, based on a rather indirect evidence and a more direct experimental evidence for the long range migration is desirable. For such a purpose, the experiments of dislocation pinning are very useful, because dislocation pinning is extremely sensitive to point defects arriving at dislocations and can provide a rather direct evidence. For Ta and Nb, however, a small amount of residual hydrogen atoms is difficult to remove and these hydrogen atoms seem to migrate a long distance even below about 5K (2). Therefore, the specimens must be very pure and any residual hydrogen should be carefully removed. Recently, Pd coating technique to remove residual hydrogen from Ta and Nb has been developed by Rodrigues and Kirchheim (3) and was used successfully in some internal friction experiments (4,5). In the present paper, our recent experimental results on internal friction in Ta and Nb after irradiation at low temperatures (6) will be presented and discussed together with a similar work made by other group (7).

§2. Experimentals and discussion

Specimens used in our work are wires of high purity Ta and Nb with residual resistivity ratio (RRR) ≒2000. Their surfaces were coated with Pd by vacuum evaporation and residual hydrogen in the specimens were carefully removed by ageing in the air. All the specimens were slightly deformed at RT prior to irradiation, in order to introduce dislocations which could work as sensors to pinners. With these treatments, Ta specimen showed the large α peak and no hydrogen cold work peak (HCWP). For Nb specimens, Nb-1 showed the large α peak and a trace of HCWP and Nb-2, the little smaller α peak and no HCWP. The α peak observed below 80K in Ta and Nb is

considered to consist of two peaks; the α_1 peak at ～20～30K which is associated with kink diffusion on screw dislocations and the α_2 peak at ～40～60K which associated with kink pair formation on non-screw dislocations (5). Further, it is known that a small amount of hydrogen introduced into the specimen can suppress this α peak and induce the large HCWP (5). Internal friction (IF) and vibrational period (P) were measured using a flexural resonant vibration at about 500Hz with strain amplitude of $\sim 10^{-6}$. The irradiation by 20MeV protons was made at 6K for the Ta and Nb-2 specimens and at ～25K for the Nb-1 specimen.

Fig. 1 shows changes in the IF and P observed in Ta below 80K. An IF peak observed at ～40K is the α peak. During these irradiations, decreases in both IF and P were observed and for heating to 60K following each irradiation, dislocation pinning effects were observed between 6K～20K and 40K～45K. The changes in P at 5K due to this pinning is shown in Fig. 2 where open and filled symbols denote P-values immediately after the each irradiation and those after the subsequent warm-up to 60K, respectively. Due to the pinning effects the IF and P at lower temperatures were suppressed strongly and the height of the α peak decreased monotonously without any change in the peak temperature.

Fig. 3 shows the results obtained for Nb-1 after irradiation at 25K. In Fig. 2, changes in P at 5K as mentioned before are shown for Nb-1 and also for Nb-2 which was irradiated at 6K. Comparing the results shown in Figs. 1 and 3, one can see that the peak height of the α peak before the irradiations were comparable for both the Ta and Nb-1, but as can be seen in Fig. 2, both dislocation pinning effects immediately after the irradiation and after the subsequent heating up cycles were much less for Nb than for Ta. Also, more than a 100 times larger dose was needed for Nb than Ta to obtain the same amount of pinning. For Nb-2 which exhibited a little smaller α peak due to the longer ageing necessary for the hydrogen degassing compared to Nb-1, the above mentioned tendency was clearly observed, i.e. the changes in P at 5K immediately after each irradiation at 6K were not a decrease but an increase probably due to a bulk effect of the irradiation induced defects. The results observed after the irradiation treatments described below were essentially the same for Nb-1 and -2 specimens. It is seen in Fig. 3 that below 300K, no pronounced dislocation pinning effects were observed but a close investigation of the results obtained in both Nb-1 and Nb-2 revealed very small pinning effects at about 10K and about 50K. Furthermore, the softening observed at ～100K

during heat-up after each irradiation treatment caused an increase in the the modulus defect associated with the α peak in the subsequent measurement runs. The latter feature is very similar to that observed in Ta. At low temperatures, the general features seen in Fig.3 are as follows.

Up to about 60K, the heating-up after each irradiation exposure brought about a decrease in the α peak height but an increase in its peak temperature. On the other hand, after heating-up above ～150K both the peak height and the peak temperature increased. The peak height increased particularly beyond that value before the irradiations. The tendency to observe increases in the peak height and peak temperature during higher temperature recoveries seemed to be similar to those in Ta. However in Nb, these changes of the α peak were also accompanied by a suppression of the low temperature side of the α peak which was not observed in Ta.

In Ta, as shown in Fig.1, dislocation pinning effects were clearly observed during the irradiation cycles at 6K and during heating-up to 60K following each irradiation cycle, respectively. As is seen in Fig.2, the observed amount of the pinning effect at 6K and during warm-up to 60K were about the same for a wide range of irradiation dosage. These results support the concept that SIA's in Ta can migrate below 6K and pin down dislocations or be trapped by impurity atoms. As regards the α peak, interesting observations concerning the pinning effects were obtained, i.e. the pinning achieved below 60K after the irradiation cycle decreased the α peak monotonously without any peak shift, but after the softening observed between 100K and 150K, the α peak grew and shifted to higher temperature. This can be understood in the following way. The α peak, more exactly the α_1 and α_2 peaks are composed of many constituent relaxations and for the pinning effects below 60K, these constituent relaxations are equally suppressed, but during the higher temperature recovery (which was observed as the softening between 100K and 150K) these peaks recovered differently from each other and more for the higher temperature components.

On the other hand, in Nb, only a small pinning was observed on IF and P during the irradiation and also during the warm-up to 60K, over a wide range of irradiation dosage. No pronounced pinning was observed even during the warm-up to 300K. The unusually small pinning effect observed in Nb might be considered to be associated with the fact that dislocations in the Nb specimens may have been almost completely pinned by impurities during the long ageing at 150°C for dehydrogenation. This idea cannot be accepted, however, since the α peak observed in these specimens was fairly

large and we know the α peak can be completely suppressed by introducing hydrogen atoms. Therefore, the present results suggest that in Nb, the SIA's arriving at dislocations during irradiation become absorbed into nodal points of the dislocation network or at other pre-existing stable pinning points. Only when the arrival rate of SIA's is high enough, some SIA's can combine together and possibly form stable pinning points. In fact, the small pinning effects observed at ～10K and ～50K during warm-ups could be due to this suggested mechanism of stable pinning. In more details, the pinning by SIA's seems to cause a suppression of the α_1 peak and a growth of the α_2 peak, i.e. a large part of SIA's arrived at dislocations seems not to work as pinners but possibly to convert screw dislocations to non-screw dislocations. It should be pointed out that since these effects were observed, the irradiations should have produced SIA's in Nb in the present experiments. Further, the present results are not in contradiction to the idea of long-range migration of SIA's in Nb below 8K or 6K suggested from the recovery of electrical resistivity after electron irradiation (1,7) and also from a theoretical study (8). In the present experiments, however, one can not specify the temperature of long range migration of SIA's in Nb.

In Figs.4 and 5, the results by Lauzier et al. (7) for similar experiments on Nb are shown. It is seen that the hardenings during irradiation below 4.7K were much smaller than the hardenings after warm-up to 20K and a pinning stage was found to start from～6K. From these results combined with the results of resistivity recovery, Lauzier et al. suggested that SIA's in Nb are already mobile below 4.7K but only one-dimensionally and change their migration mode to three-dimensional one at 6K (7).

At the present moment, the results of the two groups appear not to fit well to each other, but there seems to be no serious contradiction. To clarify the origin of the difference in the behavior of SIA's in Ta and Nb, further work is now in progress.

References

(1) H. Schultz: Point Defects and Defect Interactions in Metals, Yamada Conf. eds. J. Takamura, M. Doyama and M. Kiritani (Univ. of Tokyo Press, Tokyo 1983) pp. 183.

(2) H. Mizubayashi, T. Arai and S. Okuda: phys. stat. sol. (a) 76(1983) 165.

(3) J.A. Rodrigues and R. Kirchheim: Scripta Met. 17(1983) 159.

(4) G. Funk, M. Maul and H. Schultz: J. Physique 44(1983) C9-711.

(5) N. Kuramochi, H. Mizubayashi and S. Okuda: phys. stat. sol. (a), in press.

(6) T. Arai, H. Mizubayashi, S. Okuda, M. Okumura and S. Seki, Materials Science Forum (Trans. Tech. Pub. Switzerland) 15-18(1987) 261.

(7) J. Lauzier, J. Hillairet, J. Bauer, J. Petzold, G. Funk and H. Schultz, ibid. 267; J. Lauzier, J. Hillairet, G. Funk and H. Schultz: Scripta Met. 20(1986) 427.

(8) F. Ono and H. Maeta: J. Phys. Soc. Jpn. 53(1984) 2181.

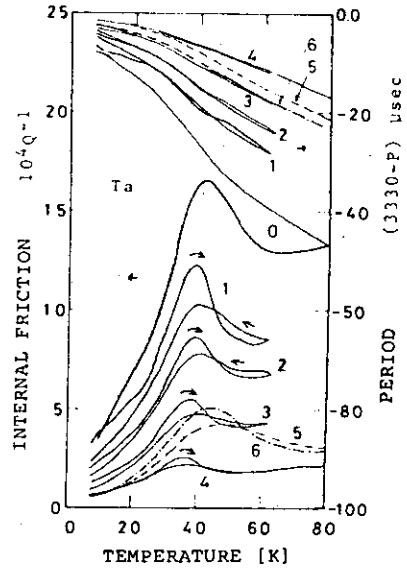

Fig. 1

Results of internal friction and vibrational period in Ta after irradiation by 20 MeV protons at 6K. 0: pre-irradiation, 1～4: after irradiation of 0.06, 0.11, 0.38 and 3.6×10^{15} p/cm^2, respectively, 5 and 6: after heating up to 240K and 300K following the curve 4 data, respectively.

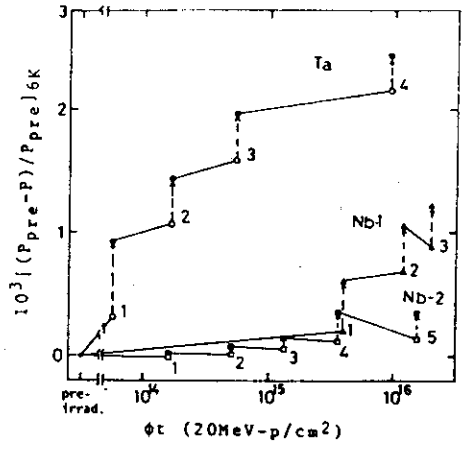

Fig. 2
Cnanges in P at 5K immediately after each irradiation cycle(open symbols) and after heating up to 60K or to higher temperatures following the each irradiation cycle(solid symbols) are plotted against the accumulated dose for Ta, Nb-1 and Nb-2.
The changes in P are given by $(P_{pre}-P)/P_{pre}$ where P_{pre} is the value for pre-irradiation.

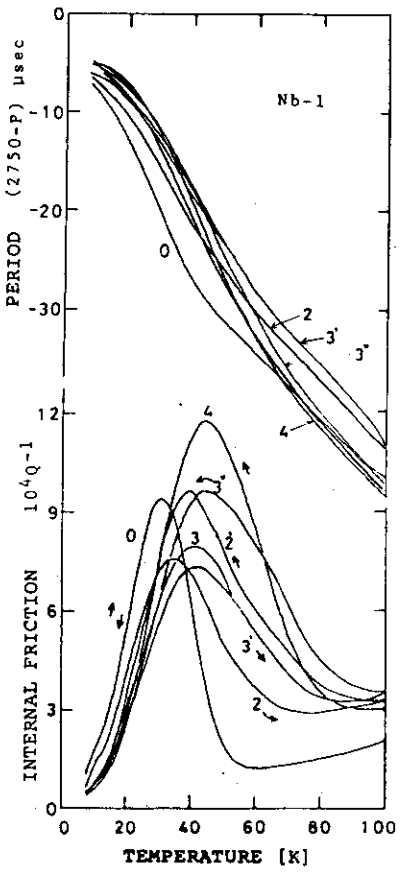

Fig. 3

Similar results as Fig . 1 but obtained for Nb-1.
0: pre-irradiation, 1～3: after irradiation (at ～25K) of 4, 8, 9×10^{15} p/cm^2 respectively.
Heating up to 50K, 180K and 60K in each run, respectively.
3', 3'' and 4: after heating up to 60K, 180K and 300K following the curve 3 data respectively.

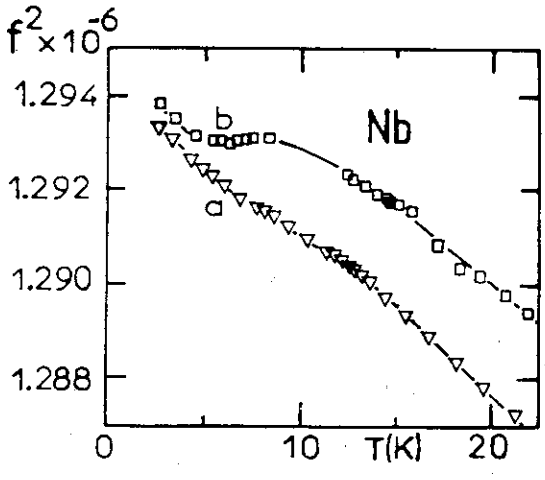

Fig.4 Resonant frequency as a function of temperature in pure niobium.
(a) unirradiated sample. (b) after 2 MeV electron irradiation at 2.6 K. Total dose: 2×10^{19} e.m^{-2}.

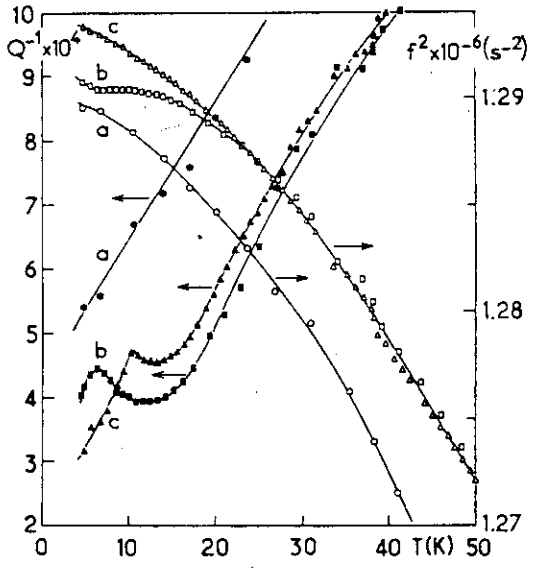

Fig.5 Temperature variation of resonant frequency and internal friction in niobium during successive heating runs between 4.7 K and 50 K. (a) unirradiated sample. (b) first heating run after the 2.3 MeV electron irradiation at 4.7 K. Total dose: 2×10^{20} e.m^{-2}. (c) Second heating run.

II.19 DAMAGE DISTRIBUTION OF HEAVY-ION IRRADIATION IN METALS STUDIED BY ELECTRICAL RESISTIVITY MEASUREMENT

Saburo TAKAMURA, Kiyotomo NAKATA*, Mamoru KOBIYAMA** and Takeo ARUGA***

Department of Physics, JAERI, * Hitachi Research Laboratory Hitachi Ltd., ** Faculty of Engineering,Ibaraki University, *** Department of Fuels and Materials, JAERI

1. Introduction

The heavy-ion irradiations are widely employed for the simulation of neutron irradiation in fusion and fission reactors. The radiation damage by ions has a strong gradient with the highly damaged region in the direction of depth of a sample. To know the precise depth distribution of damage is required for the irradiation experiment by ions.

In order to obtain the damage distribution by ion irradiation, theoretical calculations are applied, and two computer codes are currently used; one is the EDEP-1 code of analytical method(1), and the other is the TRIM code of Monte Carlo simulation(2). However, few experiments to determine the damage profile have been performed(3-4), and comparison of experiment with theory is rather limited.

In this study, C, Cl and Br ions at energies of 90-160 MeV are irradiated to multi-foil samples composed by pure metals at low temperature. The depth profile in the samples is obtained from a change in electrical resistivity of each the foil. Comparison of the experimental depth profiles with the theoretical predictions by the modified EDEP-1 and TRIM codes are performed.

2. Experimental procedure

Foils used in this study were pure Al(99.7 %), Fe(99.85 %), Ni(99.95 %), Cu(99.97 %), Ag(99.97 %) and Ta(99.9 %) with 1-50 μm in thickness, which were supplied by Goodfellow Metals Ltd.. Ratio of the resistivity at 4.2 K to that at room temperature(RRR) was about 10 in the foils. The foil thickness was determined precisely by a weighting method for the foils of 20×20 mm^2; the accuracy of the weighting was ±0.5 μg. More than ten foils cut to about 2 mm width were piled up on a sample holder to be perpendicullar to the direction of ion beam, and about ten foils with 1 μm thick were set around the damage peak as shown in Fig. 1.

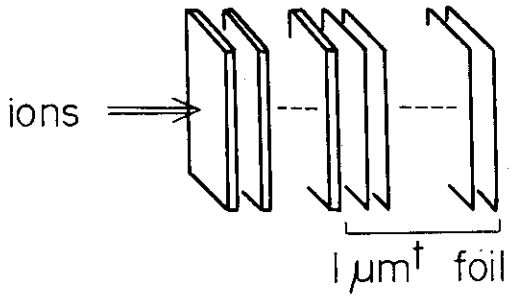

Fig. 1 Arrangement of foils.

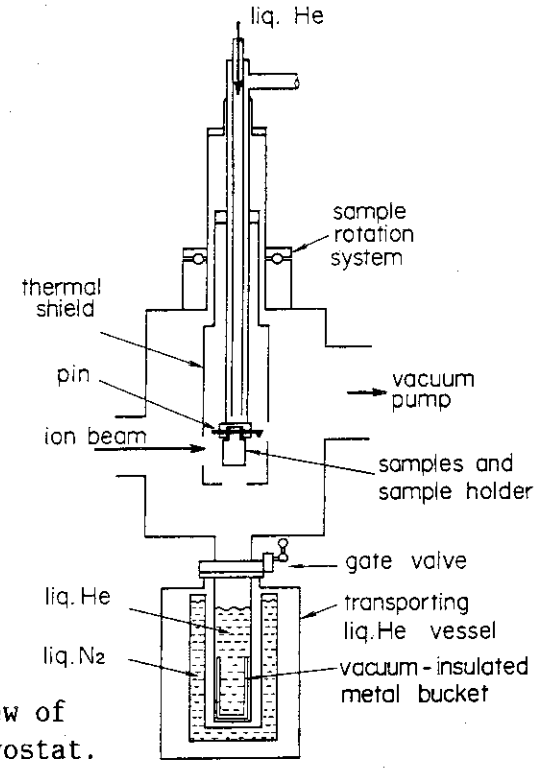

Fig. 2 Schematic cross sectional view of a low-temperature-ion-irradiation cryostat.

Ion irradiation was performed by 20 MV Tandem accelerator, cooling the samples by liquid He in a low-temperature-ion-irradiation cryostat. A schematic cross sectional view of the cryostat is shown in Fig. 2. The samples were set on five faces of the sample holder in the shape of hexagonal pillar. Through liquid He was flowed from the top of the cryostat, the samples were cooled below 10 K before ion irradiation. The sample holder could be rotated by using the sample rotation system, and the five samples were irradiated successively. After the irradiation, the sample holder with samples was dropped into the transporting liquid He vessel connected to the cryostat without warming. The ions used in the irradiation were 90 MeV C, 150 MeV Cl and 160 MeV Br. Fluctuation of accelerating voltage was within 0.1 %. The fluence was 2×10^{18} ions/m^2 for C and Cl ion irradiations, and 2×10^{17} ions/m^2 for Br irradiation. The temperature of the samples was not obviously determined during irradiation, but it seems to be held at a temperature below liquid N_2, because electrical resistivity of the irradiated samples decreased between 78 and 100 K anneals in isochronal curves as shown later.

The irradiated samples were removed from the sample holder, and thin copper lead wires were pressed at the ends of each the foil in liquid N_2 for electrical resistivity measurement. The electrical resistivity was measured in liquid He by the conventional four-probe potentiometric method.

For Ta foils, the measurement was carried out in magnetic field of 1 T to break the superconductive state at 4.2 K. The shape factor of the foil was calculated from the foil dimensions at room temperature. As the resistivity increase by size effect at liquid He temperature(5) was estimated to be less than 10 % of the resistivity of the foil, the size correction was not carried out for the resistivity measured. The uncertainty in resistivity variations was 0.5 pΩm.

In order to know the resistivity change caused by the radiation-produced defects, the irradiated foils were isochronally annealed for 300 s from 100 to 220 K by using an annealing copper box with electrical heater in the cryostat for electrical resistivity measurement. The annealing temperatures were controlled within an accuracy of ±0.5 K.

3. Results

Isochronal annealing curves in electrical resistivity of the foils set at various depth are shown in Fig. 3 for Al and Fe irradiated with C ions of 89.22 MeV. Large resistivity decrease is found in the foil set at 159.5 μm depth from the ion bombarded surface for Al, while a little resistivity change is observed in the foil at 152.2 μm. In the case of Fe, the large resistivity decrease is found in the foil at 67.1 μm. The difference between the resistivity at 78 K and that after the 220 K anneal($\Delta\rho$) is plotted against the depth of the samples. The typical result is presented in Fig. 4 for Al, Fe and Ni irradiated with C ions. The distribution of $\Delta\rho$ in the samples has a sharp peak at the specific depth; the peak depths are 159.5, 67.1 and 60.5 μm for Al, Fe and Ni,

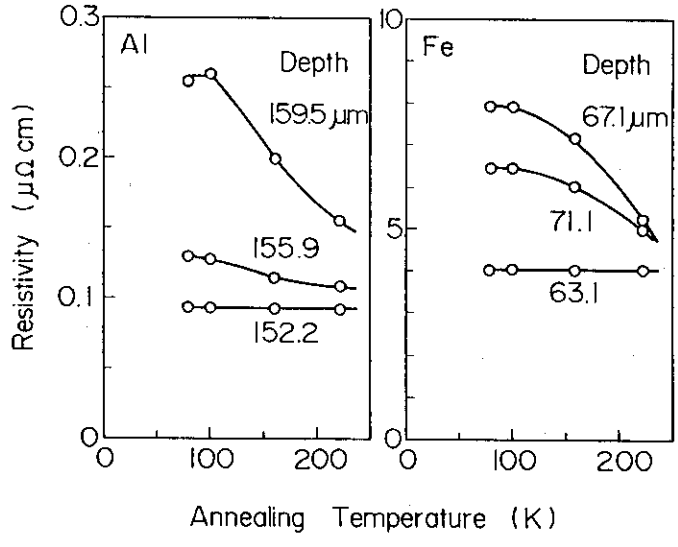

Fig. 3 Isochronal annealing curves in Al and Fe foils irradiated with C ions of 89.22 MeV up to a dose of 2×10^{18} ions/m².

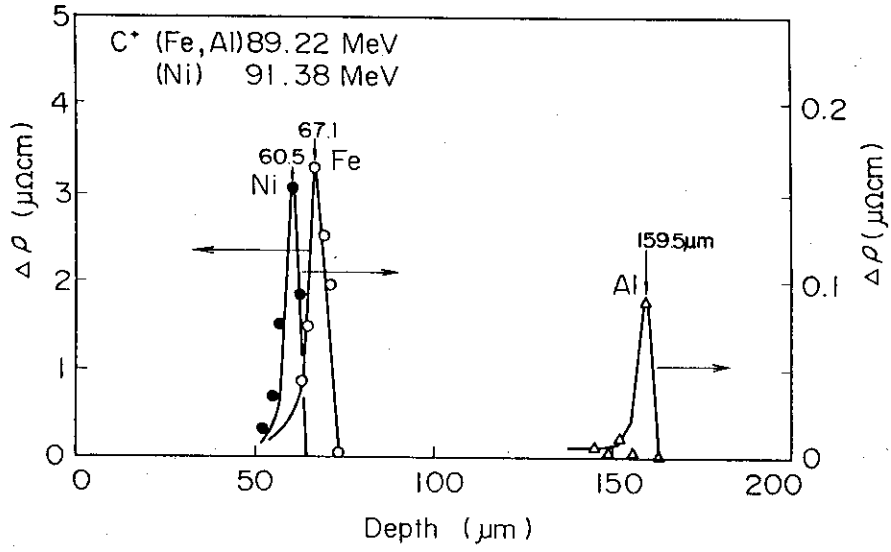

Fig. 4 The resistivity change between 78 and 220 K, $\Delta\rho$, as a function of depth of foils from the ion bombarded surface for Al, Fe and Ni irradiated with C ions.

Table 1 Damage peak depth and half-value width of damage distribution in the samples irradiated with C, Cl and Br ions.

Samples	Ions	Energies (MeV)	Damage peak (μm)	Half-value width (μm)
Al	C	90.30	161.2±0.2	5
Al		89.22	159.5±0.2	5
Fe		89.22	67.1±0.4	5
Ni		91.38	60.5±0.3	4
Cu		90.30	63.8±0.3	2
Ag		90.30	56.8±1.3	<5
Ta		90.30	45.5±0.4	3
Al	Cl	150.6	37.4±0.2	3
Al		149.7	36.6±0.2	3
Fe		150.6	15.8±0.3	2.5
Ni		149.7	14.4±0.3	2.5
Cu		149.7	14.9±0.3	1.5
Ag		150.6	15.0±0.4	6
Ta		149.7	13.4±0.4	3
Al	Br	160.0	21.2±0.2	2.5
Fe		160.0	8.5±0.3	2

respectively. As the resistivity change between 78 and 220 K seems to be caused only by migration and annhilation of ion irradiation-produced defects, the distribution of $\Delta\rho$ corresponds to the damage distribution in the samples. The damage peak depth and half-value width of the damage distribution summarized in Table 1 for all the samples examined in the cases of the C, Cl and Br ion irradiations. The error of damage peak depth due to the foil thickness is also shown in the table.

4. Discussion

The damage distribution in metals, such as peak depth and half-value width, is changed with thermal migration of irradiation-produced defects and an interaction between the defects and implanted ions(6). However, the damage peak obtained in this work is not altered by the defect migration because the piled thin foils are used and no defects diffuse between the foils. Futhermore, since the ion irradiation is performed at a temperature below liquid N_2 and the resistivity change of isochronal annealing below 220 K seems to be caused from the migration and annihilation of defects, the amount of defects estimated from the resistivity change in each the foil is unaffected by the implanted ions.

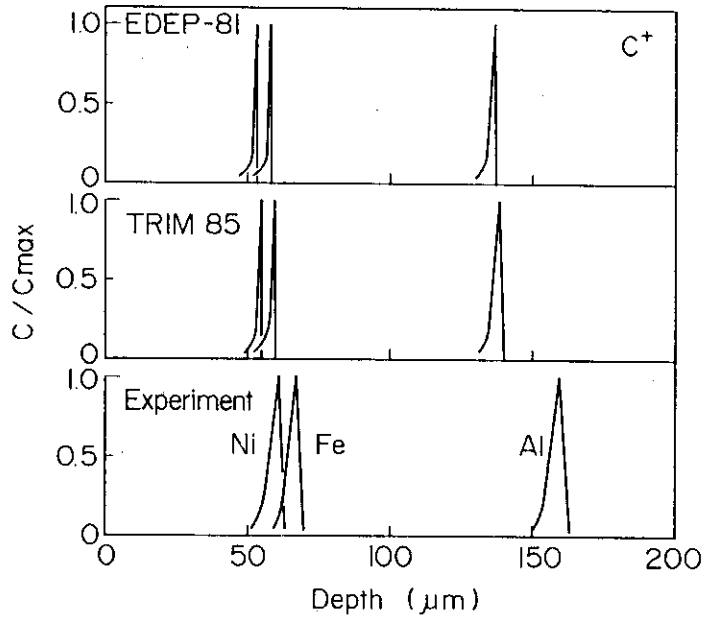

Fig. 5 The comparison between the experimenal damage profiles and calculated ones by EDEP-81 and TRIM 85 codes for Al, Fe and Ni irradiated with C ions at 90 MeV. Vertical axis means a ratio of resistivity or dpa at a depth to their maximum values.

The damage distridution with ion irradiation is also estimated by the theoretical calculations. The calculations take generally no account of the effect of thermal diffusion of the defects and implanted ions. Therefore, the results in this study are allowed to compare with the caluculated values. Fig. 5 shows the experimental damage profiles compared with the calculated ones by the modified EDEP-1, EDEP-81(7), and TRIM 85(8) codes for Al, Fe and Ni irradiated with C ions at 90 MeV. The depth of damage peak and half-value width calculated by the codes are smaller than that of experimental value in the samples. The comparison between the experimental and calculated damage profiles is shown in Fig. 6 for Fe irradiated with 160 MeV Br ions. In this case, the experimental damage profile is similar to the calculated one by the TRIM 85 code, although the peak depth calculated is slightly larger.

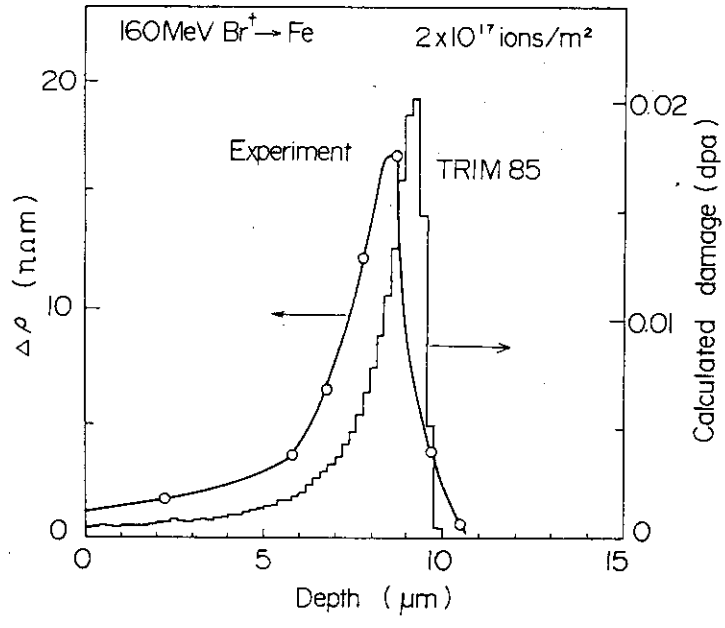

Fig. 6 The comparison between the experimental damage profile and TRIM 85 calculated one for Fe irradiated with Br ions at 160 MeV.

The difference between the calculated damage peak depth, Rcal, and experimental one, Rex, in the samples irradiated with C, Cl and Br ions is shown in Fig. 7 as a function of the atomic number of metals. In the irradiation with C ions, the experimental depths of damage peak are about 15 % larger than the calculated ones for the metals with small atomic number, such as Al, Fe, Ni and Cu, and show a good agreement with the calculated depths for Ag and Ta. On the other hand, the results in the Cl

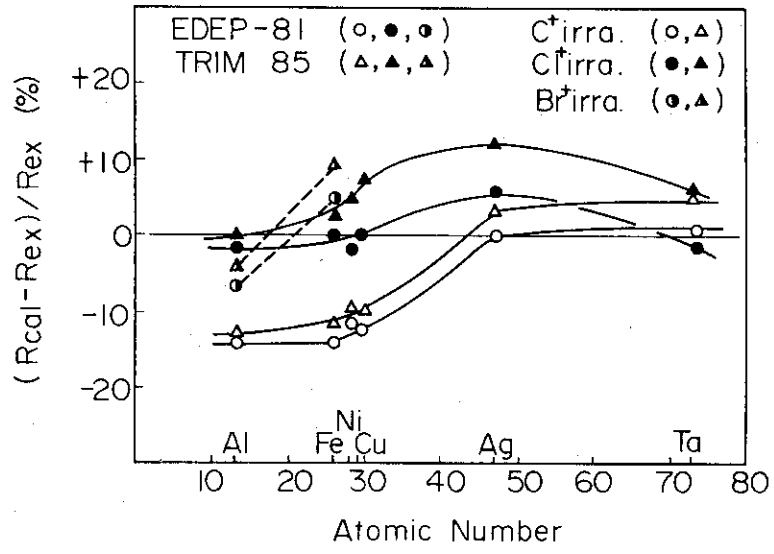

Fig. 7 The difference in percent between the calculated damage peak depth, Rcal, and experimental one, Rex, in the samples irradiated with C, Cl and Br ions as a function of the atomic number of samples.

ion irradiation indicate a good agreement between the damage peak depths obtained by the experiment and calculation using the EDEP-81 code, while the experimental value in Ag is slightly smaller than the calculated one. The damage peak depths are overestimated by the calculation using the TRIM 85 code for all the metals except Al in the Cl ion irradiation. The experimental peak depth of Al irradiated with Br ions is several percent larger than the calculated one, and that of Fe is inversely several percent smaller than the calculated one.

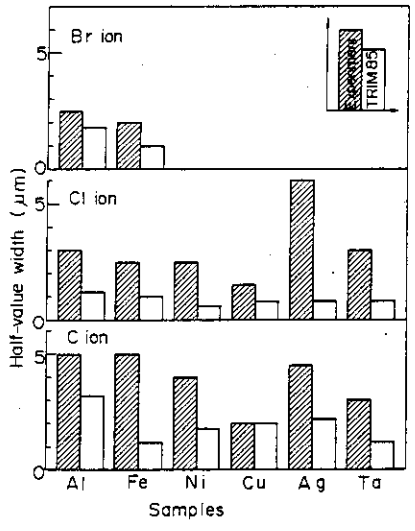

Fig. 8 The experimental and TRIM 85 calculated half-value widths of damage distribution in the samples irradiated with C, Cl and Br ions.

The experimental and TRIM 85 calculated half-value widths of the damage distribution are shown in Fig. 8 for the samples irradiated with C, Cl and Br ions. The experimental half-value widths are larger than the calculated ones in all the samples.

5. Summary

The piled thin foil samples of pure metals were irradiated with C, Cl and Br ions of 90 to 160 MeV at low temperature, and the damage

distribution in the samples studied by electrical resistivity measurement. The results were compared with the values of theoretical calculations. Main results are summarized as follows;

[1] The damage distribution with little variation caused by defect migration and implanted ions can be obtained for Al, Fe, Ni, Cu, Ag and Ta in this study.

[2] The difference between the experimental peak depth and the calculated one using EDEP-81 and TRIM 85 is correlated with atomic number of metals. The half-value width of the distribution obtained from the experiment is larger than the calculated half-value width in the samples.

References

(1) I. Manning and G. P. Mueller, Comp. Phys. Comm. 7 (1974) 85.
(2) J. P. Biersack and L. G. Haggmark, Nucl. Instr. and Meth. 174 (1980) 257.
(3) T. S. Noggle, B. R. Appleton, J. M. Williams, O. S. Oen, T. Iwata and G. W. Vogl, J. Nucl. Mater., 125 (1984) 330.
(4) S. Hamada, T. Sawai and K. Shiraishi, J. Nucl. Mater. 133&134 (1985) 370.
(5) F. Dworschak, W. Sassion, J. Wick and J. Wurn, KFA Report Jül-575-FN (1969).
(6) L. K. Mansur and M. H. Yoo, J. Nucl. Mater. 74 (1978) 228.
(7) T. Aruga, JAERI-M83-226 (1984) 1.
(8) J. F. Ziegler, J. P. Biersack and U. Littmark, The stopping and range of ions in solids, vol. 1 (Pergamon Press, New York, 1985).

II.20 ANOMALOUS REDUCTION OF STAGE I RECOVERY IN NICKEL IRRADIATED WITH HEAVY IONS IN THE ENERGY RANGE 100-120 MeV

Akihiro IWASE[*], Shigemi SASAKI[*], Tadao IWATA[*] and Takeshi NIHIRA[**]

[*]Department of Physics, Japan Atomic Energy Research Institute, [**]Faculty of Engineering, Ibaraki University

The defect recovery spectrum against the annealing temperature provides useful information about the structure of irradiation-produced defects, and many annealing experiments have been performed in metals using electrical resistivity(1). A lot of data have been acquired about the defect recoveries for electron-, neutron-, and low energy ion ($\lesssim$ 1 MeV)-irradiations. For high energy($>$100 MeV) ion-irradiations, however, there have been few measurements of the defect recovery. Here we report our measurements of the defect recovery, particularly focussing on the anomalous reduction of the stage I recovery in Ni irradiated with 100-120 MeV Si, Cl, Br, and I ions.

The specimens were nickel foils 0.23-0.25 μm thick which were grown onto the aluminum substrates by the vapor deposition at a pressure of 1.2×10^{-7}Torr. Before the vapor deposition, the aluminum substrates were coated with Al_2O_3 insulating layers about 0.2 μm thick by anode oxidation. The irradiations were performed in two energy regions. The irradiating ions in the high energy region were 84 MeV ^{12}C, 115 MeV ^{19}F, 120 MeV ^{28}Si, 120 MeV ^{35}Cl, 100 MeV ^{81}Br and 100 MeV ^{127}I ions from the JAERI tandem accelerator, and those in the low energy region were 0.5 MeV ^{1}H, 0.7 MeV ^{3}He, 1.5 MeV ^{4}He, 1.32 MeV ^{14}N and 1.8 MeV ^{40}Ar ions from 2MV Van de Graaff accelerator(2). The thickness of the specimens is much smaller than the projected ranges of ions. Therefore, ions pass completely through the specimens and the ratio of the energy loss of ions in the specimen ΔE to the initial ion energy E_0 satisfies the following condition: $\Delta E/E_0 \lesssim 0.07$ for the high energy ion irradiations and $\Delta E/E_0 \lesssim 0.38$ for the low energy ion irradiations. The temperature of the specimens during the irradiations were held at $<$14 K for the high energy ion irradiations and at $<$ 6 K for the low energy ion irradiations.

The annealing experiments were performed as follows;

Before and after irradiations, the resistivity of the specimen was measured as a function of temperature from 10 K to 300 K at a constant heating rate. The difference between the two measurements provides the electrical resistivity due to the residual defects as a function of the annealing temperature. The heating rate was 1.5 deg/min. Since the recovery curve depends on the initial concentration of defects, nearly the same concentration of defects was produced by each irradiation before annealing. The change in the resistivity by irradiation ,$\Delta\rho_0$, which is assumed to be proportional to the defect concentration, is shown in Table I for each irradiation. In Table I are also shown the ion fluence and the average ion beam current for each irradiation.

The effects of the mass and the energy of ions on the recovery mainly appear in the temperature region of the stage I recovery. Therefore, from now on, we confine the main discussion to the stage I recovery. Figures 1(a) and 1(b) show the recovery curves $\Delta\rho/\Delta\rho_0$ and the temperature derivatives of the recovery curves $-d(\Delta\rho/\Delta\rho_0)/dT$ as a function of the annealing temperature T in the low temperature region. All the recovery curves are not shown in the figure for clarity.

Energetic ions lose their energies by excitations of electrons in solid (inelastic collision) and by displacements of atoms from their normal crystal lattice sites(nuclear collision). In metals, it has been assumed so far that only the nuclear collision is responsible for the defect production and the radiation annealing process(3,4). If this assumption is correct, the initial state of irradiation damage in metals should be determined by the energy spectrum of the primary knock-on atoms(PKA). In the following, the amounts of the stage I recovery for ion irradiations at different energies and different projectile species are compared in terms of the spectra of PKA energy. As a parameter that characterizes a PKA energy spectrum, we have employed the PKA median energy $T_{1/2}$, which is defined by the following equation(5).

$$\int_{E_d}^{T_{1/2}} \nu(T)(d\sigma/dT)dT = (1/2) \int_{E_d}^{T_{max}} \nu(T)(d\sigma/dT)dT,$$

where T is the PKA energy, $d\sigma/dT$ the differential scattering cross section of nuclear collision(Winterbon's formula(6)), $\nu(T)$ the damage function based on the modified Kinchin-Pease model(7), E_d the average threshold energy and T_{max} the maximum transferred energy to recoil atoms. This

equation means that half of the displaced atoms result from PKAs with energies higher than $T_{1/2}$.

The amounts of the stage I recovery in Ni are plotted in Fig. 2(a) as a function of $T_{1/2}$, where we have assumed the recovery below 80K as the stage I for Ni. Since the stage I recovery is caused by the recombinations of the migrating single interstitials with lattice vacancies, the amount of the stage I recovery is a measure of a concentration of single interstitials, which can migrate freely in a lattice in the stage I temperature region. (This kind of interstitial is called the stage I interstitial here.)

As can be seen in Figs. 1 and 2(a), for the low energy ion irradiations and 84 MeV ^{12}C ion irradiation, the structure and the amount of the stage I recovery change systematically with increasing the PKA median energy $T_{1/2}$. The peaks of the substages I_B and I_C disappear gradually from the low temperature side with increasing $T_{1/2}$, and the total amount of the stage I recovery decreases smoothly as a function of $T_{1/2}$. The above behavior of the stage I recovery can be interpreted as due to two radiation-annealing effects by elastic collisions(2,3): (1) the close Frenkel pairs are too unstable to survive the displacement cascades started by higher energy PKAs; and (2) the lattice agitations by newly produced higher energy PKAs cause the more preferential annihilation of the already existing close Frenkel pairs.

For 100-120 MeV F, Si, Cl, Br and I ion irradiations, the behaviors of the stage I recovery are greatly different from those for the low energy ion irradiations and 84 MeV C ion irradiation. The amount of the stage I recovery for Si and Cl ion irradiations is greatly reduced. For I ion irradiation, the stage I peak nearly completely disappears, and moreover, even the recovery peak around 100 K disappears. For 115 MeV F irradiation, the reduction of the stage I recovery is observed though the amount of the reduction is not so large as for Si, Cl, Br and I ion irradiations. The stage I recoveries for Cl and I ion irradiations are only 0.15 times and 0.07 times the recovery for the low energy ion irradiations and 84 MeV C ion irradiation, as compared at the same PKA median energy.

Thus, the anomalous reduction of the stage I recovery for 100-120 MeV Si, Cl ,Br, and I ion irradiations is not related to the PKA median energy $T_{1/2}$ and it can not be explained within the framework of the defect production and the radiation-annealing by the nuclear collisions. The other mechanism besides the nuclear collision will enhance the

recombinations of the stage I interstitials with lattice vacancies during irradiations.

We also measured the stage I recovery in Cu, the next element of Ni in the periodic table, under the same experimental conditions as in Ni for irradiating ions and energies, specimen cooling and substrate. Fig. 2(b) shows the amount of the stage I recovery in Cu as a function of $T_{1/2}$. The irradiating ions and energies are indicated in the figure. The anomalous reduction of the stage I recovery is not observed in Cu . This result shows that the reduction of the stage I recovery depends not only on the mass and the energy of irradiating ion but also on the target metal.

High energy heavy ions cause the high density electron excitations along their ion paths in solids. The amount of electron excitations is given by the electronic stopping power, i.e. the energy transferred from the ion to electrons in the specimen per unit length of the ion path. In order to study the effect of the high density electron excitations on the stage I recovery, we plotted the amount of the stage I recovery in Ni as a function of the electronic stopping power value. We used the experimental electronic stopping power values for ^{12}C and ^{35}Cl ions(8) and the tabulated values of Northcliffe and Schilling(9) for the other ions. Figure 3 shows that the amount of the stage I recovery in Ni is strongly related to the electronic stopping power, and is drastically reduced when the electronic stopping power exceeds $\sim$3 MeV/(mg/cm^2). This result suggests that if the energy transferred from the ion to electrons, which causes electronic excitations, exceeds some value, this energy contributes to the reduction of the stage I recovery.

The energy of electron excitations can be transferred to the lattice atoms by the electron-phonon interaction. The energy transfer causes the lattice agitation, which leads to a small temperature increase effectively in a local region along the ion path. If the energy transferred from the ion to electrons is large and the electron-phonon interaction is strong, this temperature increase becomes large.

The anomalous reduction of stage I recovery in Ni can be explained as follows; for the low energy ion and 84 MeV C ion irradiations, due to the relatively small energy transfer from the ion to electrons, the local temperature increase along the ion path is small, so that the electron excitations have little influence on the stage I recovery. In these cases, the nuclear collision dominates the behavior of the stage I recovery, and as mentioned above, the structure and the amount of the stage I recovery can be well characterized as a function of the PKA median energy $T_{1/2}$. On

the other hand, for 120 MeV Si and Cl ion irradiations, due to the large energy transfer from the ion to the electrons and the subsequent electron-phonon interactions, the local temperature along the ion path reaches the stage I temperature region, and the recombinations of the stage I interstitials with the vacancies occur. These recombinations lead to the remarkable reduction of the stage I recovery. For 100 MeV I ion irradiation, the energy transferred to the electrons becomes much larger, and the local temperature along the ion path exceeds the stage I temperature. Due to this temperature increase, not only the stage I recovery peak but also the 100 K recovery peak nearly completely disappears.

It is worth noting here that before the defect recovery measurements, we measured the resistivity change by irradiation as a function of ion fluence. The results for the high energy heavy ion irradiations differ from those for the low energy ion irradiations(2) and are as follows; (1) the damage energy necessary to produce the same initial resistivity change ρ_0 is much larger and (2) the spontaneous recombination volume is much larger than for the low energy ion irradiations. These results show that the annihilations of the stage I interstitials occur during irradiation owing to the lattice agitation induced by high density electron excitations, and that the defect production rate becomes substantially smaller and the defect saturation becomes more remarkable than expected in nuclear collision process.

As mentioned above, the anomalous reduction of the stage I recovery is not found in Cu irradiated with high energy heavy ions, where nearly the same high density electron excitations as in Ni are expected to occur. The difference of the behaviors of the stage I recovery between the two metals can be explained by the strength of the electron-phonon interaction. The electron-phonon interactions in metals have been studied through the analysis, for instance, of lattice thermal conductivity and they are shown to be governed by the structure of electron energy bands, in particular by the density of states near the Fermi energy(10). As the density of states at Fermi energy in Ni is much larger than in Cu, the electron-phonon interactions in Ni are stronger than in Cu. Therefore, the effect of the electron-phonon interaction on the stage I recovery appears remarkably in Ni. But in Cu, due to the weak electron-phonon interaction, the local temperature increase along the ion path is insufficient for the reduction of the stage I recovery.

It is well known that in insulators the nuclear tracks are formed by the bombardment of energetic heavy ions such as fission fragments and that the track formation is originated from the high density electron excitations by ions(11). On the other hand, in metals, no nuclear tracks have been found except in very thin film. The reason is that the electron-phonon interactions are much weaker in metals than in insulators. The present experiment showed for the first time that the electron-phonon interactions in the high density electron excitations played an important role in the irradiation damage in metals.

The authors are thankful to the members of Accelerators Division, Department of Physics, Japan Atomic Energy Research Institute for operating the JAERI tandem accelerator.

References

(1)W. Schilling, G. Burger, K. Isebeck and H. Wenzl, in Vacancies and Interstitials in Metals, edited by A. Seeger, D. Schumacher, W. Schilling and J. Diehl(North-Holland, Amsterdam,1970), p. 255.

(2)A. Iwase, S. Sasaki, T. Iwata and T. Nihira, J. Nucl. Mater.,141-143, 786 (1986).

(3)R. S. Averback and K. L. Merkle, Phys. Rev. B16, 3860 (1977)

(4)R. S. Averback, R. Benedek and K. L. Merkle, J. Nucl. Mater., 75, 162 (1978).

(5)R. S. Averback, R. Benedek and K. L. Merkle, Phys. Rev. B18 4156 (1978).

(6)K. B. Winterbon, P. Sigmund and J. B. Sanders, K. Dan. Vidensk. Selsk. Mat. Fys. Medd. 37, No. 14 (1970)

(7)M. T. Robinson and I. M. Torrens, Phys. Rev. B9 5008 (1974).

(8)A. Iwase, S. Sasaki, T. Iwata and T. Nihira, J. Phys. Soc. Jpn. 54, 1750 (1985).

(9)L. C. Northcliffe and R. F. Schilling, Nucl. Data. Tables A7 233 (1970).

(10)W. H. Butler and R. K. Williams, Phys. Rev. B18 6483 (1978).

(11)R. L. Fleischer, P. B. Price and R. M. Walker, in Nuclear Tracks in Solids(University of California Press, Berkeley, 1975).

Table I Resistivity change by ion irradiation $\Delta\rho_0$ (nΩ cm), ion fluence Φ (cm^{-2}) and average ion beam current I (particle nA).

ion	0.5 MeV ^{1}H	0.7 MeV ^{3}He	1.5 MeV ^{4}He	1.32 MeV ^{14}N	1.8 MeV ^{40}Ar	84 MeV ^{12}C	115 MeV ^{19}F	120 MeV ^{28}Si	120 MeV ^{35}Cl	100 MeV ^{81}Br	100 MeV ^{127}I
$\Delta\rho_0$ (nΩ cm)	505	510	507	495	509	499	498	498	428	503	717
Φ (cm^{-2})	1.1×10^{16}	1.3×10^{15}	2.1×10^{15}	7.2×10^{13}	9.9×10^{12}	6.4×10^{15}	4.7×10^{15}	1.7×10^{15}	1.1×10^{15}	4.3×10^{14}	8.1×10^{14}
I (p nA)	41.5	21.3	28.1	6.0	1.9	3.6	1.6	1.0	1.0	1.3	0.9

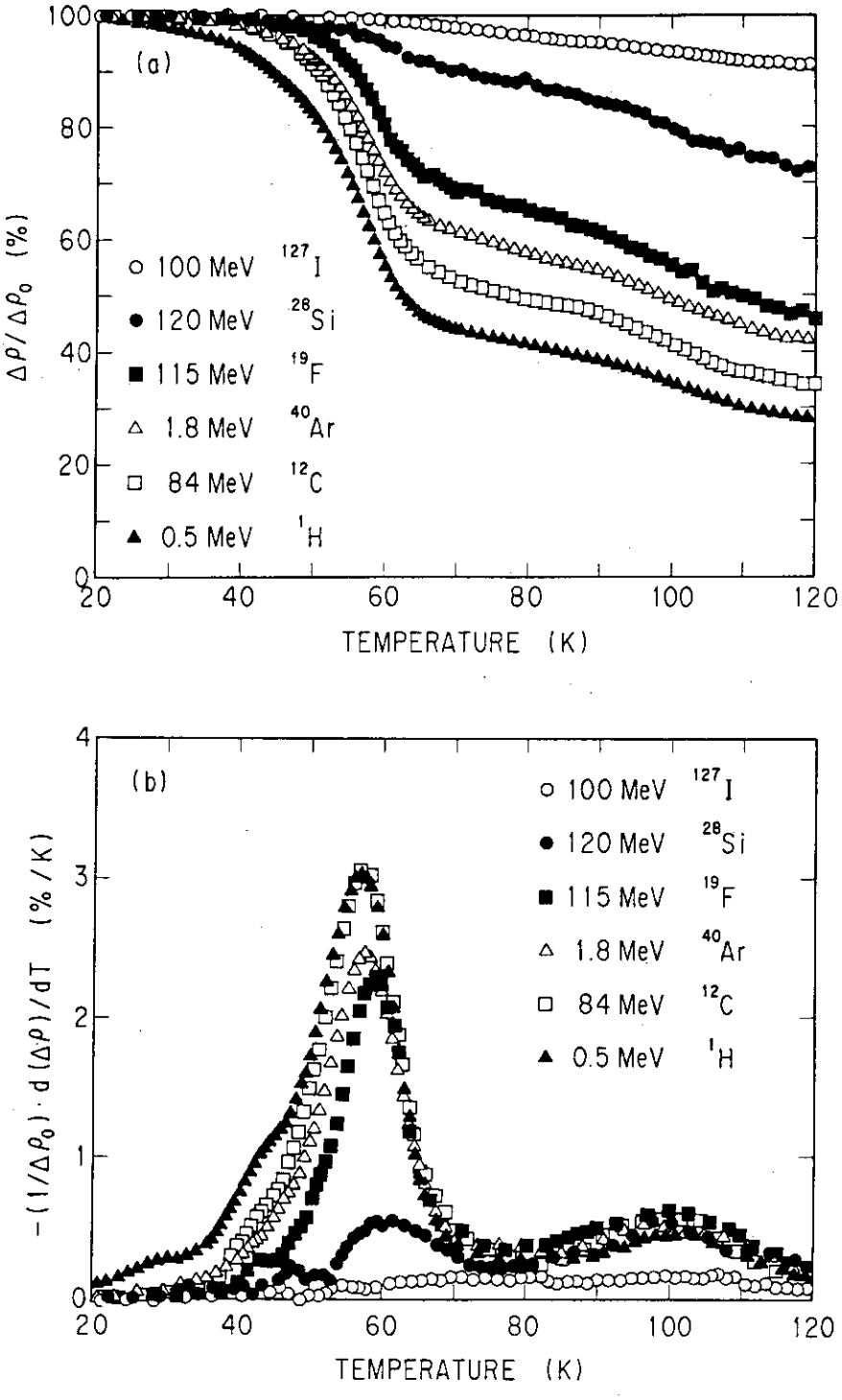

Fig. 1(a) and 1(b)

Recovery curves(a) and temperature derivatives of recovery curves(b) in Ni as a function of annealing temperature.

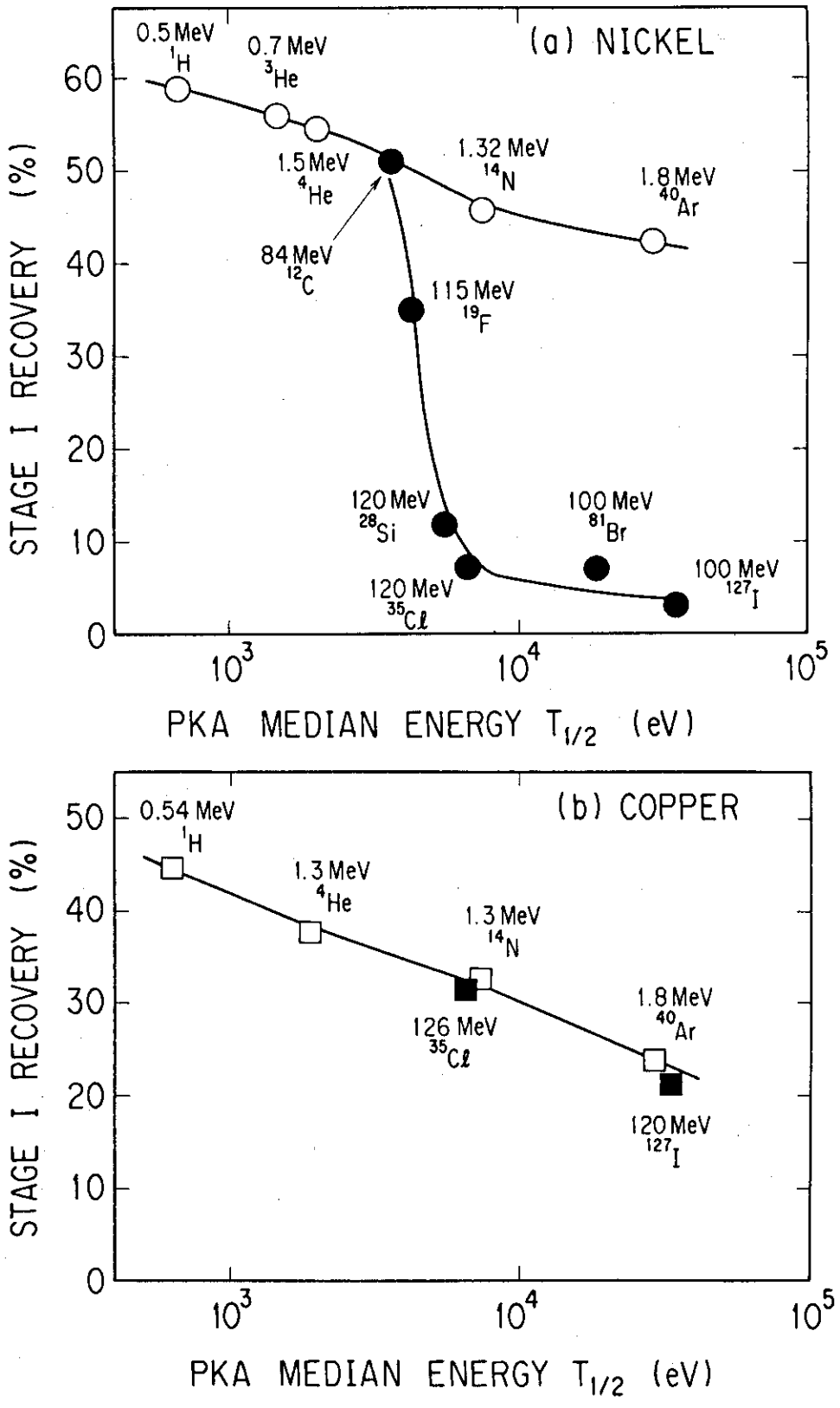

Fig. 2(a) and 2(b)

Amount of stage I recovery in Ni(a) and Cu(b) for low energy ion irradiations(open circles and open squares) and for high energy ion irradiations(solid circles and solid squares) as a function of PKA median energy $T_{1/2}$.

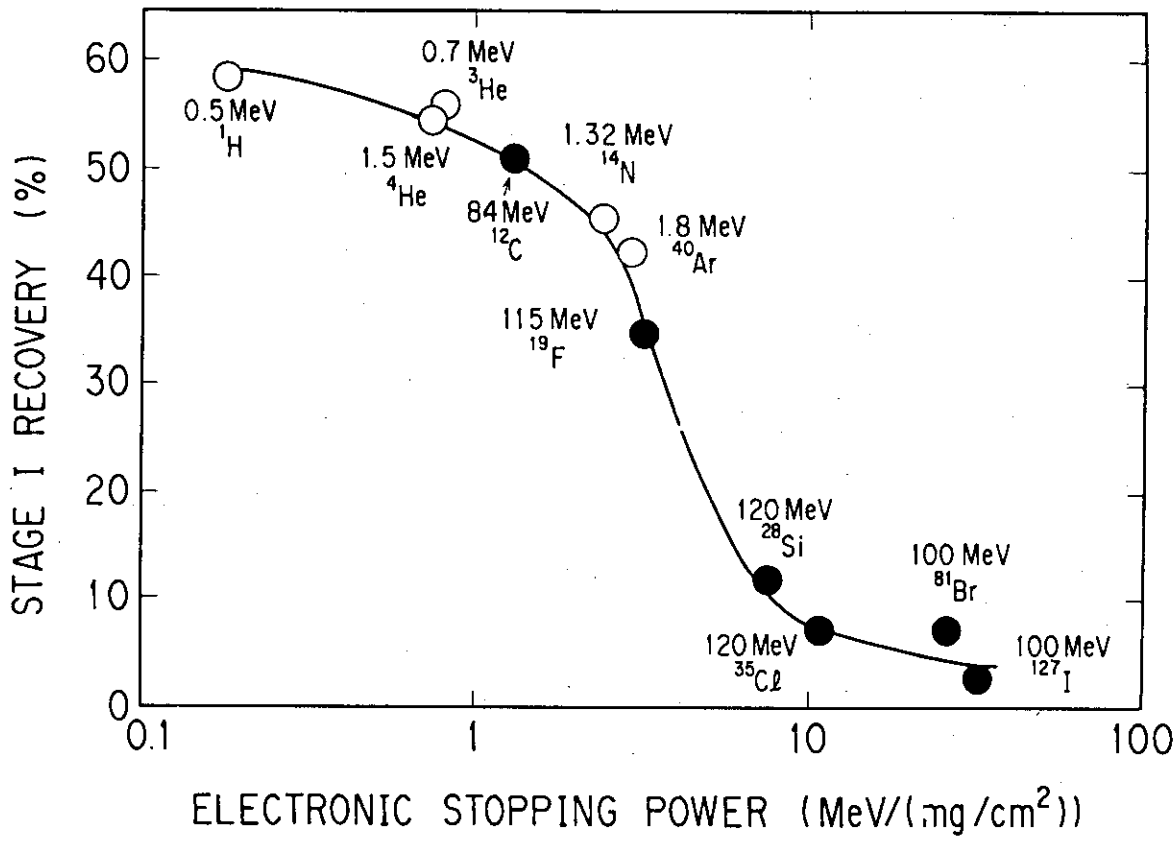

Fig. 3

Amount of stage I recovery in Ni for low energy ion irradiations(open circles) and for high energy ion irradiations(solid circles) as a function of electronic stopping power.